University of Washington
Department of Civil and Environmental Engineering

EFFECTS OF SPATIAL CONSTRAINTS ON CHANNEL NETWORK TOPOLOGY: IMPLICATIONS FOR GEOMORPHOLOGICAL INFERENCE

Mariza-Costa Cabral

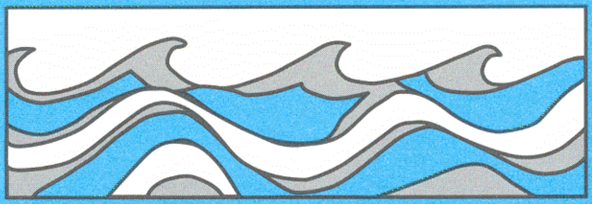

Water Resources Series
Technical Report No.157
March 1998

Seattle, Washington
98195

Department of Civil Engineering
University of Washington
Seattle, Washington 98195

EFFECTS OF SPATIAL CONSTRAINTS ON CHANNEL NETWORK TOPOLOGY: IMPLICATIONS FOR GEOMORPHOLOGICAL INFERENCE

Mariza-Costa Cabral

Water Resources Series
Technical Report No. 157

March 1998

ABSTRACT

In the fifty-two years since Robert Horton's 1945 pioneering quantitative description of channel network planform (or plan view morphology), no conclusive findings have been presented that permit inference of geomorphological processes from any measures of network planform. All measures of network planform studied exhibit limited geographic variability across different environments. Horton [1945], Langbein et al. [1947], Schumm [1956], Hack [1957], Melton [1958], and Gray [1961] established various "laws" of network planform, that is, statistical relationships between different variables which have limited variability. A wide variety of models which have been proposed to simulate the growth of channel networks in time over a landsurface are generally also in agreement with the above planform laws.

An explanation is proposed for the generality of channel network planform laws. Channel networks must be space filling, that is, they must extend over the landscape to drain every hillslope, leaving no large undrained areas, and with no crossing of channels, often achieving a roughly uniform drainage density in a given environment. It is shown that the space-filling constraint can reduce the sensitivity of planform variables to different network growth models, and it is proposed that this constraint may determine the planform laws.

The "Q model" of network growth of Van Pelt and Verwer [1985] is used to generate samples of networks. Sensitivity to the model parameter Q is markedly reduced when the networks generated are required to be space filling. For a wide variety of Q values, the space-filling networks are in approximate agreement with the various channel network planform laws. Additional constraints, including of energy efficiency, were not studied but may further reduce the variability of planform laws.

Inference of model parameter Q from network topology is successful only in networks not subject to spatial constraints. In space-filling networks, for a wide range of Q values, the maximal-likelihood Q parameter value is generally in the vicinity of 1/2, which yields topological randomness. it is proposed that space filling originates the appearance of randomness in channel network topology, and may cause difficulties to geomorphological inference from network planform.

Table of Contents

List of Figures

List of Tables

Acknowledgments

This report is based on the Doctoral thesis of the first author. Many people contributed greatly to this project. The comments by Ronald L. Shreve, of UCLA, on the contents of Chapter 2 were of such import that they contributed to a revised definition of the project objectives. Ronald's collegiality is very gratefully acknowledged. David R. Montgomery, of the UW Dep. of Geological Sciences provided much guidance and many fruitful discussions. His expertise in fluvial geomorphology was a most important resource for this work. James W. Kirchner, of UC Berkeley, contributed with his expertise at various stages of this project. His 1993 thought-provoking paper motivated the start of this project. Michael Woldenberg, of SUNY, Buffalo, and Tom Dunne of the UW Dep. of Geological Sciences (now at UC Santa Barbara), provided useful discussions and literature references. Useful comments on the contents of Chapter 2 were also contributed by Athol D. Abrahams, of SUNY, Buffalo, and David G. Tarboton, of Utah State U. Dennis P. Lettenmaier, Ronald E. Nece, and Catherine M. Petroff, of the UW Dep. of Civil Engineering, provided useful comments on content, and on presentation and writing.

Chapter 1

Introduction

1.1 Laws of Channel Network Planform

Landscape evolution by fluvial erosion is among the earth science phenomena that usually occur over time periods too long for observation, and study of the physical processes involved relies strongly on inference from landscape form [*Gilbert*, 1877]. The most striking morphologic feature of fluvially eroded landscapes is the land surface tiling by valleys nested within larger valleys, their bottoms forming a connected network with the appearance of a bifurcating arborization. Through the valley network extend the stream channels that carry flow and sediment from the landscape. That valley connectivity and continuity of slope show such "nice adjustment" that they appear designed to accommodate the network of channels testifies that the valley is "the work of the stream which flows in it" [*Playfair*, 1802, p. 102].

Early geomorphologists judged the configuration of channel networks as most worthy of study, even as "the key to landscape" [*Zernitz*, 1932, p. 68], and searched for patterns and regularities in such networks. Channel network morphology may reflect regional tectonics, local geologic structure, prevailing erosional mechanisms, and climate (see *Kirchner* [1993, p. 591]); and in turn it affects hydrologic processes and fluxes (e.g., *Taylor and Schwarz* [1952], *Surkan* [1969], *Kirkby* [1976], *Rodríguez-Iturbe and Valdés* [1979], and *Troutman and Karlinger* [1986]). With the current availability of digital elevation maps and satellite imagery, from which approximate representations of channel networks may be obtained, the ability to interpret network morphology could be useful for inference of geophysical processes and geologic properties at the planetary scale.

Early descriptions of channel network morphology were mainly qualitative (e.g., *Davis* [1909], *Zernitz* [1932]). Quantitative analyses based on centrifugal branch-ordering systems (that is, ordering of streams in the upstream direction, starting with the outlet stream) [*Gravelius*, 1914, cited by *Jarvis and Woldenberg*, 1984], borrowed from the life sciences, were unsuccessful at identifying regularities due to lack of correlation of centrifugal order with channel size. *Horton* [1932] revived quantitative analysis with the introduction of a centripetal branch-ordering system. Centripetal ordering, using rules by *Strahler* [1952] (described below), remains in current use in fluvial geomorphology, and has been adopted in studies of organic networks [*Jarvis and Woldenberg*, 1984, pp. 9-10 and 101]. For a detailed review of the history of branch-ordering systems, see *Woldenberg* [1997].

The Strahler ordering system defines "streams" of different orders, according to the following rules (Figure 1.1a). Source channels are streams of order 1. Where two streams of the same order, ω, join, both streams terminate and the receiving stream has order $\omega+1$. Where two streams of different orders join, the stream of lower order terminates and the stream of higher order continues through the junction. In result of these rules, the outlet stream of a basin has the highest order, Ω, which is also the "basin order." Strahler streams and orders are entirely determined by the network's topology, defined as the particular arrangement in which the channel branches connect to one another in the network (see Section 1.2, below). Strahler ordering is independent of metric properties such as channel lengths and orientation.

Horton [1945] found that the decrease in number, N_ω, and increase in mean length, L_ω, of streams with centripetal order, ω, is approximately geometric. *Horton* [1945] hypothesized that the increase in mean sub-basin area, A_ω, with ω may also be geometric, and this was confirmed by *Schumm* [1956]. These statistical relations are known as “Horton’s laws” of stream numbers, lengths, and areas. Their respective series ratios are designated the bifurcation, length and area ratios (R_B, R_L, and R_A). Horton’s laws are illustrated by semi-logarithmic plots of N_ω, L_ω, and A_ω versus ω, known as “Horton diagrams,” in Figures 1.1b and 1.2, and are represented by the following expressions,

$$N_\omega \approx R_B^{\Omega-\omega} \qquad (1.1)$$

$$L_\omega \approx L_1 R_L^{\omega-1} \qquad (1.2)$$

$$A_\omega \approx A_1 R_A^{\omega-1} \qquad (1.3)$$

where L_1 and A_1 are the mean length and area, respectively, of first-order streams (source channels).

Horton [1945] interpreted the three Horton’s laws, (1.1), (1.2) and (1.3), as reflecting a distinctive orderliness in the topological patterns of channel networks. In a reference to *Playfair*’s [1802] well-known remark (cited on page 1, above) on the “nice adjustment” of valley connectivity and continuity of slope, or “declivities,” *Horton* [1945, p. 291] wrote that “the nice adjustment goes far beyond the matter of declivities.” *Horton* [1945] noted that R_B and R_L, together with Ω, L_1, and the basin area, A, permit estimation of the drainage density, D, and the stream frequency, F_s (concepts also introduced by *Horton* [1932]), defined as the average length of channels and average number of streams per unit terrain area, respectively.

Much effort was subsequently expended to find other geomorphologic laws resulting from this perceived organization of channel network planform, and a number of empirical statistical laws were established. The best documented major laws are summarized below. Variable notation is summarized in Appendix A.

Langbein et al. [1947] studied the variation of a basin’s “distance-weighted area,” P, with basin area, A. P is defined as the sum of sub-basin areas weighted (that is, multiplied) by their channel distance to the basin outlet, and has dimension of length cubed. Representing the k^{th} individual portion of the basin area by a_k, and its channel distance to the basin outlet by l_k (Figure 1.3), P is given by:

$$P = \sum_k l_k \, a_k \tag{1.4}$$

Using data for 340 drainage basins in the Northeastern United States, *Langbein et al.* [1947] found the following relation:

$$P = \varepsilon A^{\phi} \tag{1.5}$$

Exponent ε and coefficient ϕ in (1.5) were estimated as 1.56 and 0.90, respectively, for P expressed in cubic miles and A in square miles, for Langbein's Northeastern study basins.

Hack [1957], *Gray* [1961], and *Mueller* [1973] established another scaling relation between the length of the mainstream channel, L, and basin area, A:

$$L = \kappa \, A^{\theta} \tag{1.6}$$

Exponent θ in (1.6) varies geographically, and generally takes values greater than 0.5. *Mueller* [1973] collected data for several thousand basins of all sizes in various parts of the world, and found that θ changed abruptly from 0.6 for basins of area smaller than 8,000 mi^2 (20,720 km^2), to 0.5 for basins between 8,000 and 100,000 mi^2 (20,720 - 259,000 km^2), and to 0.466 for basins larger than 100,000 mi^2.

The computed value of θ is subject to uncertainty. *Robert and Roy* [1990] (see also *Beer* [1991] and *Robert and Roy* [1991]) presented evidence of influence of cartographic scale on the estimated θ. *Montgomery and Dietrich* [1992] replaced stream lengths by basin lengths, measured along the main valley axis to the drainage divide, obtaining $\theta \approx 0.5$. These authors suggested that θ depends on the headward extent of the mainstream depicted on maps of different scale, as well as on downstream variations in channel sinuosity and drainage density.

Melton [1958, pp. 36-37] analyzed data for 156 basins of differing area, climate, relief, geology and vegetation, and found the ratio between stream frequency, F_s, and the square of the drainage density, D^2, (concepts defined on page 3, above) to be approximately constant:

$$\frac{F_s}{D^2} \approx 0.694 \tag{1.7}$$

Gray [1961] found that the channel distance from the outlet to the center of gravity of the network, defined as $L_{ca}=P/A$ (Figure 1.3), where P is given by (1.4) and A is basin area, is approximately equal to half of the mainstream length, L:

$$L_{ca} \approx 0.5\ L \tag{1.8}$$

While violations of each of the above laws have been documented for individual networks, they approximate the aggregate central tendency of published data [*Abrahams*, 1984]. These laws represent statistical tendencies in large populations rather than exact relationships in individual cases [*Shreve*, 1975]. The above laws are included under the network properties I through VII listed by *Shreve* [1975], and quoted in Section 1.2.1, below.

1.2 The Random Topology Model

Shreve [1966] and subsequent researchers dispelled the notion that the geomorphologic laws listed in Section 1.1, above, imply topologic orderliness or distinctive characteristics. This had been suggested earlier by *Leopold and Langbein* [1962], who demonstrated that networks generated by random walks on a square lattice were in accord with Horton's laws, leading *Milton* [1966] to dismiss these laws as "irrelevant" to geomorphology.

Shreve [1966] investigated Horton's law of stream numbers (1.1) with the intent of explaining the law's generality and insensitivity to environmental factors (first noted by *Horton* [1945, p. 303]). This law is purely topological, i.e., determined by the channel connectivity pattern, and to study it *Shreve* [1966] introduced the concept of "topologically distinct channel networks" (TDCN) with a given number of channel sources, or "network magnitude," μ (Figure 1.4). The number of TDCN that can be constructed having μ channel sources, $N(\mu)$, is given by the formula by *Cayley* [1859] (presented in *Shreve* [1966, Eqn. 13]):

$$N(\mu) = \frac{(2\mu-2)!}{(\mu-1)!\,\mu!} \qquad (1.9)$$

$N(\mu)$ increases rapidly with network magnitude. For magnitude 4, $N(4)$ equals 5 (Figure 1.4). For magnitudes 7, 10, and 50, $N(\mu)$ equals 132, 4,862, and about $2.52\text{x}10^{26}$, respectively.

Shreve found that Horton's law of stream numbers holds approximately for all TDCN that can be constructed with any given magnitude, hence is "inherent in the definition of stream order" [*Shreve*, 1966, p. 30]. *Shreve* [1966] further showed that most TDCN that can be constructed have R_B values in the range typically observed in nature, with a modal value of about 4. The generality of Horton's law of stream numbers is explained in detail in Chapter 2, Section 2.4.1.

Having disproved that Horton's law of stream numbers and typical R_B values require particular topologic patterns, Shreve then proposed the diametrically opposite hypothesis: that "in the absence of geologic controls [such as geologic fractures, for example] a natural population of channel networks will be topologically random," i.e., "all topologically distinct networks [TDCN] with given number of links are equally likely" [*Shreve*, 1966, p. 27]. Shreve's definition of network randomness concerns topology alone and is descriptive rather than causative, i.e., it assumes nothing regarding the processes of network formation.

1.2.1 Topologic analogs of channel network planform laws and the predictive ability of the random topology model

All channel network planform laws other than Horton's law of stream numbers (1.1) involve metric quantities, that is, lengths measured along channels, and values of basin or sub-basin area. The variability in these metric quantities has both topologic and metric components. For example, variability in the length of the mainstream channel is due partly to variability in the number of links (defined in Figure 1.4) comprising the mainstream, and partly to variability in individual link lengths. The number of links in a stream is designated the stream's "topologic length," and is the "topologic component" or "topologic analog" of stream length. Similarly, basin area is determined by the number of links and by the size of areas contributing flow to individual links. The number of links in a network is the topologic component of basin area, A. The number of links in any network of magnitude μ is $2\mu-1$, the topologic analog of A.

An approximately linear relation may be expected between each metric variable and its topologic component, especially for large numbers of links, provided that no significant correlations exist between link length or contributing area and topologic variables, such as link magnitude and Strahler order [*Shreve*, 1974]. For example, if mean link length increased with Strahler order, mainstream length would not vary linearly with topologic length.

The distribution of link lengths has been found to vary with Strahler order and other topologic variables in some river basins (e.g., *Smart* [1968], *Shreve* [1969], *James and Krumbein* [1969], *Smart* [1969, 1972, 1978, 1981], *Ghosh and Scheidegger* [1970], *Krumbein and Shreve* [1970], *Mock* [1971], *Abrahams and Campbell* [1976], and *Montgomery and Dietrich* [1989]), but this variation is unlikely to affect significantly the approximately linear relation between a metric variable and its topologic component for large numbers of links [*Kirchner*, 1993, p. 593]. Link length and area distributions (sampled by, e.g., *Strahler* [1954], *Schumm* [1956], and *Maxwell* [1960]) have only slight influence on linearity [*Shreve*, 1974]. Using the hypothesis of linearity, *Smart* [1968] obtained good correlations between observed stream lengths and topologic stream lengths predicted by the random topology model.

Under the assumption of linearity, we obtain topologic analogs of channel network planform laws by replacing each metric variable by its topologic component, or "analog" [*Shreve*, 1967]. Stream length is replaced by topologic length (number of links in the stream), and basin area is replaced by number of links in the channel network. Predictions of the random topology model for the topologic-analog laws, which in some cases were coupled with observed distributions of link lengths and areas, were shown to approximate the respective geomorphologic law, as summarized by *Shreve* [1975, p. 527] (edited):

> "Without any adjustable parameters and with no other input than the observed distributions of link lengths and associated areas, [the random

topology model] has successfully predicted quantitatively the following observed [properties]:

* [**Property I**]: the distributions and numerical values of R_B (*Shreve*, 1966), R_L (*Smart*, 1968; *Shreve*, 1967, 1969), and R_A (*Shreve*, 1969).

* [**Property II**]: the correlations between R_B and R_L and between stream numbers and stream lengths (*Smart*, 1968)

* [**Property III**]: the statistical distributions of second-order stream lengths, Schumm lengths, and areas (*Shreve*, 1969)

* [**Property IV**]: *Melton's* (1958) proportional relationship between stream frequency and the square of the drainage density (*Shreve*, 1967)

* [**Property V**]: *Hack's* (1957) variation of mainstream length with basin area (e.g. *Shreve*, 1974)

* [**Property VI**]: *Langbein et al.'s* (1947) relationship between distance-weighted area and basin area (*Werner and Smart*, 1973)

* [**Property VII**]: *Gray's* (1961) relationship between distance from outlet to 'centroid' and mainstream length (*Werner and Smart*, 1973)."

Property I incorporates Horton's laws given by (1.1), (1.2) and (1.3); properties II and III are not well established laws but are based on a limited number of observations; property IV is given by (1.7); property V is given by (1.6); property VI is given by (1.5); and property VII is given by (1.8).

1.2.2 Search for an explanation

An explanation of why the random topology (RT) model approximately predicts properties I-VII, above, remains far from established and subject to debate (e.g., *Watson*

[1966, 1969], *Thakur and Scheidegger* [1968], *Krumbein and Shreve* [1970], *Howard* [1972], *Smart* [1973], *Shreve* [1974, 1975], *Schumm* [1977], *Jarvis and Sham* [1981], *Abrahams* [1984, 1987], *Mesa and Gupta* [1987], *Kirchner* [1993], and *Rodríguez-Iturbe and Rinaldo* [1997]). What explains the RT model's predictive ability?

Shreve [1975, p. 529] proposed two inferences or explanations: (i) the topologic component of geomorphologic laws is dominant, and (ii) random factors dominate network development. Inference (i) is almost certainly correct, as agreement between metric and topologic-analog laws could hardly be coincidental (and supports the above assumption of linearity). Is explanation (ii) valid?

This question is crucial for the direction of future research and for the best usage of the RT model. If random factors dominate network development, then it is those empirical properties of natural networks that disagree with RT model predictions which may be geomorphically significant and merit our attention. The RT model may be useful in isolating those properties. Also, why the physical processes involved in network development might have dominantly random effects on network topology becomes a fundamental research question in geomorphology [*Kirkby*, 1976, p. 197].

The question of validity of inference (ii) has provoked three different approaches. One approach has been to oppose (ii) on the argument that physical processes are intrinsically deterministic (e.g., *Watson* [1966], *Howard* [1972], and *Schumm* [1977]); or to defend (ii) on the argument that physical processes are intrinsically random (e.g., *Leopold and Langbein* [1963], *Langbein* [1964], *Krauskopf* [1968], and *Mann* [1970]), or that process complexity and sensitivity to initial and boundary conditions preclude deterministic modeling (e.g., *Thakur and Scheidegger* [1968], *Krumbein and Shreve* [1970], *Smart* [1973], and *Shreve* [1975]). *Smart* [1979] classified these arguments as philosophical, for they cannot be tested by current scientific methods. These arguments address the legitimacy of the RT model rather than the quality of its predictions [*Shreve*, 1979, p. 170]. We note that if simple deterministic processes of channel development were influenced by physical factors not correlated with any topologic variables, such processes would appear as random in the topologic domain. Hence, topologic randomness does not preclude deterministic processes, nor does it imply complexity.

A second approach provoked by the question of validity of (ii) has been to devise progressively discriminating tests of the RT model, as argued for by *Kirkby* [1976]. The RT model has been tested often against collected data, and has rarely been rejected. Direct testing of TDCN frequencies is feasible only for small networks, with 6 or fewer source channels (e.g., *Werner and Smart* [1973]), because the number of TDCN increases rapidly with magnitude, as given by (1.9). For this reason, tests of the RT model have used topologic variables which individually have limited informational content (e.g., *Jarvis and Werrity* [1975], *Abrahams and Mark* [1986], *Uylings et al.* [1989], and *Verwer et al.* [1992]). However, the combined informational content of all topologic variables predicted by the RT model has not been evaluated. *Abrahams and Mark* [1986] argued that the small significance level of 5% used in most of these tests for rejection of the RT model has resulted in favorable bias for the model.

Despite their limitations, statistical tests have successfully identified systematic deviations in nature from RT model predictions. These deviations were reviewed by *Abrahams* [1984, 1987]. *Abrahams* [1987, p. 164] summarized evidence that each systematic deviation from the RT model results from either steep or low terrain slope, or from space-filling and geometric properties of channel networks.

The space-filling property is that by which a channel network extends over the land surface to drain every hillslope, leaving no undrained areas, and with no crossing of channels, and having an approximately uniform drainage density, defined as the mean length of channels per unit area [*Horton*, 1932]. Where conditions of geology, climate, climatic history, vegetation cover, etc, are approximately constant, hillslope size does not vary widely but is, to some approximation, constant, and the drainage density is approximately uniform.

Space filling and geometric constraints affect in particular the arrangement of tributaries along a mainstream. For example, the number of two consecutive tributaries that join the mainstream from opposite sides (right and left) is found usually to be higher than the number joining it from the same side (Figure 1.5), especially when one or both tributaries have large basin areas [*James and Krumbein*, 1969; *Flint*, 1980; *Abrahams*, 1984]. Therefore, the number of TRANS links (defined in Figure 1.5) is usually higher than the number of CIS links. The RT model predicts that these occurrences will be equally frequent, and the number of CIS and TRANS links in a basin will be approximately equal. Attempts at simulating and quantifying the topologic effects of space filling by simulation include those of *Karlinger and Troutman* [1989], *Goodchild and Mark* [1985], *Goodchild* [1988], and *Goodchild and Klinkenberg* [1993].

A third approach provoked by the question of validity of (ii) has been to question the sensitivity of channel network planform laws to topologic variability. RT model deviations due to space filling or other possible factors are not detected by any of the above planform laws (included under properties I-VII), and *Abrahams* [1987, p. 156] attributes this failure partly to insensitivity of these laws. One source of insensitivity is the aggregation of topologic data from networks with diverse physical conditions, such as slope and orientation, resulting in the "canceling out" of opposing properties (e.g, *Werritty* [1972], *Jarvis and Werritty* [1975], *Flint* [1980], and *Abrahams and Mark* [1986]). *Kirchner* [1993] raised the important question of insensitivity of the Horton ratios to topologic variability, as reviewed in Section 1.3, below.

1.3 Sensitivity of Channel Network Planform Laws to Network Topology

Kirchner [1993] investigated the sensitivity of the Horton ratios for non-topologically-random samples of networks, that is, network samples where the TDCN of any given magnitude do not have equal probability of occurrence. Kirchner created non-topologically-random samples by first generating an original topologically-random sample of networks, and then selecting from that original sample those networks having specified topologic characteristics. Kirchner selected networks having one given topologic variable (the "selection variable"), such as the maximum topologic length, or "diameter," larger than, or smaller than, the median value of the original topologically-random sample. For each selection variable, two sub-samples were created, one sub-sample containing networks having a value of the selection variable greater than the median in the original sample, the other sub-sample containing networks having a value of the selection variable smaller than the median. Kirchner demonstrated that for such non-topologically-random samples the distributions of the Horton ratios deviate little from those in the original topologically-random sample.

Kirchner concluded that the RT model's prediction of the typical values of the Horton ratios does not constitute evidence in favor of the RT model, because similar values are observed also in many non-topologically-random samples. *Kirchner*'s [1993] results reinforce the perception of the Horton ratios, and hypothetically some channel network planform laws, as being inevitable to some degree.

A different method for creating non-topologically-random test samples is to generate each network using a stochastic topologic model of network growth. In geomorphology, examples include the convergent-growth (merging of channels formed independently) model of *Leopold and Langbein* [1962], and the headward-growth (addition of tributaries to pre-existing channels) models of *Howard* [1971] and *Dacey and Krumbein* [1976], among others.

The models of *Dacey and Krumbein* [1976], developed for channel networks, were generalized into the variable-parameter "Q model" of *Van Pelt and Verwer* [1985] in the field of neuroanatomy. The Q model assigns a variable probability to development of tributaries in interior and exterior links, and will be described in detail in Chapter 2, Section 2.2. The model starts with one original link, and adds a new tributary link at each growth step. A network of magnitude μ is obtained after μ-1 growth steps or "branching events." Each new tributary link is appended to any one of the pre-existing links, chosen by comparison of a random variable with link branching probabilities. The branching probability of a link is p_i if the link is interior (i.e., not a channel source), and p_e if the link is exterior (a channel source). The model parameter is defined by $Q=p_i/(p_i+p_e)$, and takes values in the interval [0, 1].

Q parameter values greater than 1/2 ($p_i>p_e$) favor network growth by extension, and tend to generate elongate networks, with high bifurcation ratio, R_B. Q values smaller than 1/2 ($p_i<p_e$) increase the importance of development of side tributaries, and tend to generate compact networks, with low R_B. With Q=1/2, all links (or "segments") have equal branching probability, and this model is designated "segmental growth." This results in all TDCN having equal probability of being generated, and segmental growth yields topological randomness [*Dacey and Krumbein*, 1976]. The Q model is entirely topological, disregarding geometric properties of channel networks, such as link lengths, junction angles, and space-filling constraints.

By testing against simulation results, *Dacey and Krumbein* [1976] rejected the hypothesis that channel networks grow principally by tributary development on exterior links (source channels), corresponding to Q=0. This growth mechanism however predicts well the topologic properties of dendrites of non-pyramidal neurons [*Van Pelt et al.*, 1992]. Contrary to channel networks, the topologic properties of neuronal dendrites differ widely from RT model predictions [*Verwer and Van Pelt,* 1983]. This is also the case for various other organic networks. Growth models that predict the topologic properties of particular organic networks include those of *Harding* [1971], *Berry et al.* [1975], *Hollingworth and Berry* [1975], and *Van Pelt and Verwer* [1985, 1986]. *Van Pelt et al.* [1992] found that two types of neuronal dendrite have topologic properties well represented by best-fit Q parameter values.

The above results demonstrate that topologic variables are sensitive to some types of topologic distribution, as has been suggested by *Troutman and Karlinger* [1994], and provoke the question of whether the channel network planform laws (included under properties I-VII, listed in Section 1.2.1) are sensitive to the TDCN frequencies produced by these growth models. If these properties have limited sensitivity to the topologic variability created by models of network development, this may explain the limited range of variability observed in nature in the coefficients of properties I-VII. If this is the case, the success of the RT model in predicting these properties may not be geomorphologically meaningful. The question of sensitivity of properties I-VII to network development models is addressed in this dissertation.

1.4. Objectives and Thesis Structure

The objective of this dissertation is to propose and investigate a novel hypothesis for a common origin of the laws of channel network planform reviewed in Section 1.1. The proposed hypothesis is that these laws may arise from the constraint that all channel networks must be approximately space filling (Section 1.2).

To test the above hypothesis, I study the sensitivity of the topologic analogs of the various channel network planform laws to the parameter of the "Q model" of network growth, used as a test example. The Q model, introduced in Section 1.3, above, is described in detail in Chapter 2, Section 2.2. Network samples are generated using different Q parameter values. The properties of samples of networks not subject to any spatial constraints, and samples of networks that are constrained to be space filling, are compared.

In Chapter 2, test samples of networks are created using different Q parameter values. Only the topology of these networks is specified, and no consideration is given to either geometric or space-filling network properties. A variety of topologic variables are computed for the networks in the different test samples, and the coefficients of the topologic analogs of properties I-VII (listed in Section 1.2.1) are determined.

It is shown that properties I-VI are sensitive to the Q parameter, which can originate much wider variability in the laws' coefficients than which is found in nature. Only property VII exhibits limited sensitivity to Q. It is concluded that the limited variability of these coefficients in nature may not be due to insensitivity of these laws to topologic composition. Neither the origin of these laws nor the ability of the RT model in predicting their coefficients has so far been explained.

In Chapter 3, samples of networks are created which are space filling and have specified geometric properties. All networks are assigned a simple, idealized geometry. All links are straight lines and have unit length, and all link junctions have the same angle. The geometric properties considered (defined in Section 3.2.1) are (i) drainage pattern, δ (dendritic and trellis patterns are used); and (ii) junction angle, α.

The Q model (described in Section 2.2) is not amenable to creation of growth of networks embedded in space because it involves branching of both interior and exterior links. Creation of space-filling networks with specified geometric properties, such as link lengths, δ, and α, precludes branching of interior links, as explained in Section 3.3. In Chapter 3, a new model, designated "Q_E," is developed which is topologically equivalent to the Q model and is amenable to simulation of growth of networks embedded in space. The Q and Q_E models are said to be topologically equivalent because, in the absence of the space-filling constraint, that is, in a purely topologic mode of operation, any TDCN is equally likely to be generated by either model, for any given Q value.

The Q_E model is amenable to simulation of network growth in space because it involves addition of new tributary links exclusively to exterior links. This permits specification of link lengths, drainage pattern and junction angles. The probability of adding a tributary link to a given exterior link in the Q_E model is computed from expressions derived in Section 3.3.2.

In Chapter 4, the coefficients of the topologic analogs of properties I-VII are computed for the sample space-filling networks created by the Q_E model, using different Q parameter values. It is found that the variability of these coefficients is reduced to a much narrower range than for the case where space filling is not required. This range is influenced by the choice of junction angle, α, and by drainage pattern, δ, but in general it is situated close to the RT model's expectations. This is a possible and novel explanation for the predictive success of the RT model. It is also a possible explanation for the approximate agreement between the properties of all published simulation models of network growth in space. The remaining variability in these coefficients may be largely due to differences in junction angles and, to a lesser extent, in drainage pattern.

The space-filling constraint may have important influence on the inference of growth processes from observed morphologic properties. To illustrate this influence, in Section 4.4 it is attempted to infer the value of parameter Q from the morphology of space-filling networks generated by the Q_E model. Maximum-likelihood Q values (denoted "ML-Q") are computed and it is shown that the ML-Q of a space-filling network generally differs from the true Q value used in the creation of that network. The ML-Q is generally closer than the true Q to the value of 1/2, which yields topological randomness. The ML-Q is obtained by maximizing the log-likelihood of Q, denoted "Log-L(Q)". It is shown that errors in statistical testing may result, including errors of type I (rejection of the true Q value) and of type II (failure to reject values distant from the true Q). It is concluded that the failure to account for the space-filling constraint, junction angles, and drainage pattern, is a serious impediment to model inference from network morphology, giving rise to errors of type I and II in statistical testing.

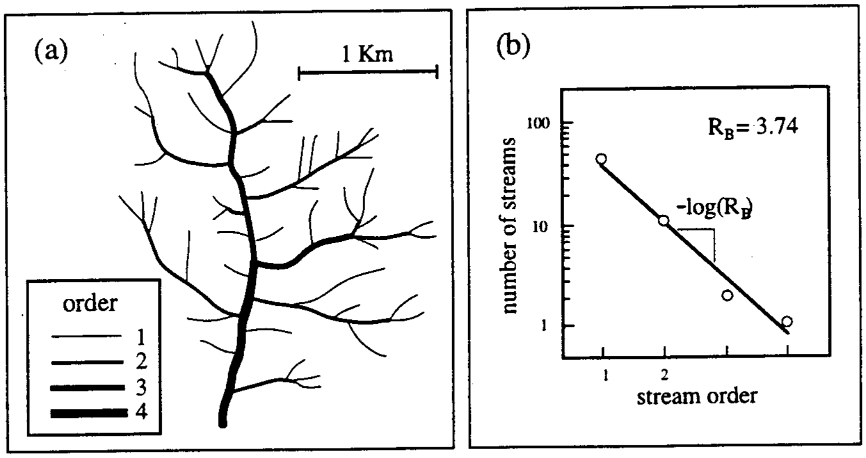

Figure 1.1. **(a)** Strahler streams of a fourth-order channel network that discharges into a fifth-order tributary stream of Old Man Creek, Iowa. Streams of orders 1 through 4 are drawn with increasing line thickness, as indicated in the figure legend. The number of streams of each order ω, N_ω, are N_1=46, N_2=11, N_3=2, N_4=1. The number of source streams, N_1, is designated the magnitude of the network, μ. **(b)** Horton diagram of stream numbers for the network in (a): $\log(N_\omega)$ is plotted against ω. The bifurcation ratio is R_B=3.74, obtained from the slope of the regression line, $(-\log(R_B))$.

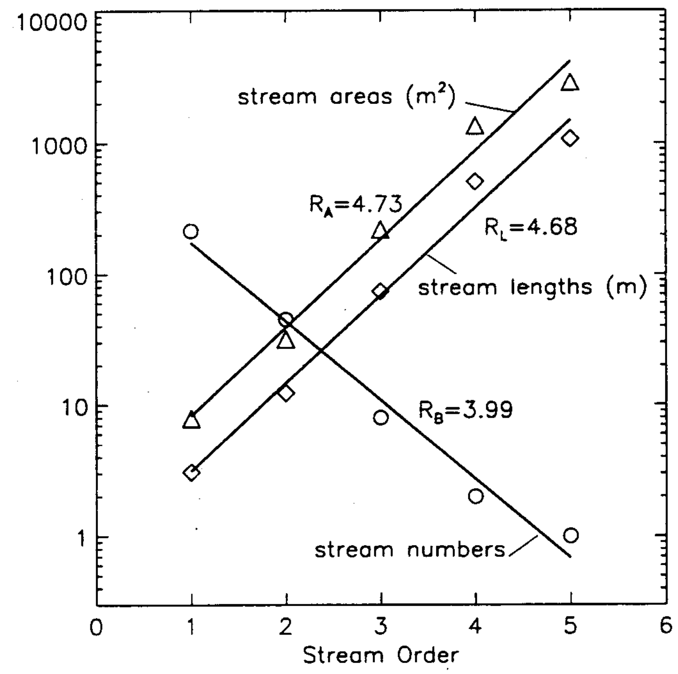

Figure 1.2. Horton diagrams of stream numbers, lengths, and areas, for the streams of Perth Amboy river basin, New Jersey (data of *Schumm* [1956]). Stream numbers are represented by circles, stream lengths are given in meters and represented by diamonds, and stream areas are given in square meters and represented by triangles. The Horton ratios R_B, R_L, and R_A, are obtained from the slopes of the regression lines, equal to $(-\log(R_B))$, $\log(R_L)$, and $\log(R_A)$.

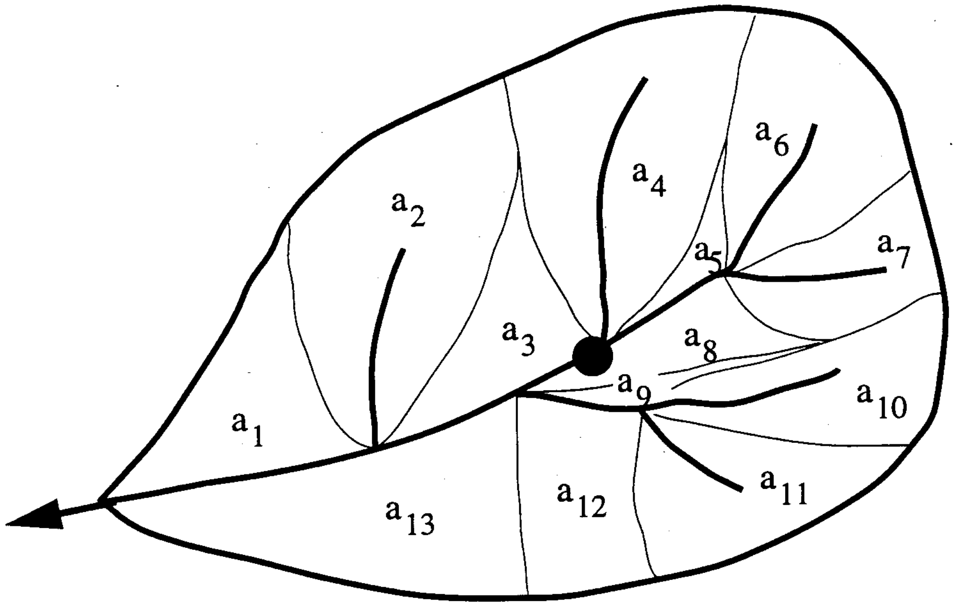

Figure 1.3. Definition of distance-weighted area, P. A basin's drainage divide and channel network are represented by bold lines. Thin lines define 13 sub-areas, designated a_1 through a_{13}. Thin lines are drawn by starting at a channel junction and moving upstream against contour lines (which are not shown) to the drainage divide. The channel distance to the outlet of sub-area a_k is designated l_k. The distance-weighted area, P, is defined as the sum of the product $a_k l_k$ for all k (1 through 13) (1.4). The circle in the figure indicates the location of the basin's center of gravity. The center of gravity is located at a channel distance L_{ca} from the basin outlet, where L_{ca} is given by the ratio P/A.

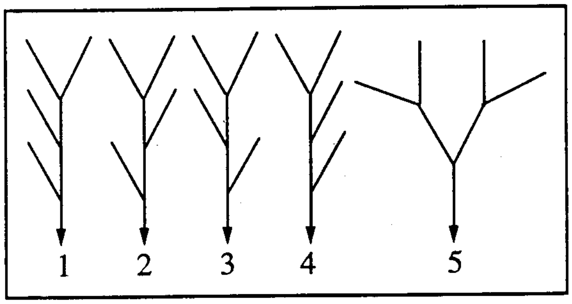

Figure 1.4. The five topologically distinct channel networks (TDCN) that can be constructed having four channel sources (magnitude μ=4). Each network is represented by a binary rooted tree graph [*Melton*, 1959], that is, a line graph drawn on a surface where no more that three segments, or "links," join at a point and that has a specified "root," or outlet location (here indicated by an arrowhead). "Nodes" are points of link confluence. "Exterior links" represent source channels, and "interior links" connect two nodes.

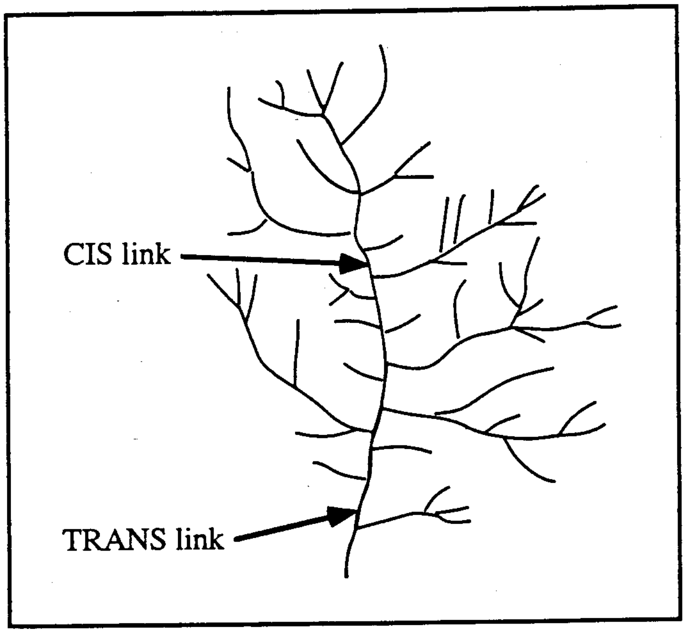

Figure 1.5. Definition of CIS and TRANS interior links. CIS links are interior links that are joined at their upper and lower nodes by exterior links joining it from the same side (left or right). TRANS links are interior links that are joined by exterior links from opposite sides.

Chapter 2

Sensitivity of Channel Network Planform Laws
To Network Growth Processes
In The Absence of Spatial Constraints

2.1 Objective

The objective of this chapter is to test the sensitivity of the channel network planform laws (properties I-VII in Section 1.2.1) to non-uniform TDCN distributions, in the absence of spatial constraints. The networks considered in this chapter have no specified geometric properties, such as link lengths, junction angles, or drainage pattern, and are not required to be space filling. Only their topologic properties are considered. Networks subject to spatial constraints are created in Chapter 3 and studied in Chapter 4.

Non-topologically random test network samples are generated and the parameters of the topologic-analogs of properties I-VII are computed for each sample. Two types of sample are tested. A sample of "type 1" is obtained by selection of networks with specified topologic properties from an original topologically-random sample. This is the method introduced by *Kirchner* [1993]. A sample of "type 2" is obtained by generating each network using a variable-parameter stochastic topologic model of network growth. The "Q model," referred in Chapter 1, is used as a test example.

The Q model is described in Section 2.2. The methods used to generate each test sample are described in Section 2.3. The coefficients of the topologic analogs of properties I-VII (above) are computed for each test sample in Section 2.4, and conclusions are presented in Section 2.5. The approximate size of a sub-sample required to distinguish statistically between topologically random and non-topologically-random test samples is not computed. Distinguishing between samples relies instead on the visual representation of the topologic-analogues of properties I-VII, and on the computed coefficients and standard deviations. Sample sizes required to distinguish between samples based on any of these properties will depend on the magnitudes of the networks sampled.

2.2 The Q Model of Network Growth

The Q model of network growth [*Van Pelt and Verwer*, 1985] was introduced in the field of neuroanatomy to represent possible growth mechanisms of neuronal dendrites of various types. The usefulness of such growth models for inference of natural growth mechanisms was argued for by *MacDonald* [1984]. The Q model is used here as a test example only.

2.2.1 Model description

The Q model represents network growth by sequential branching of links, i.e., by appending one new tributary link to one pre-existing link at each growth step. A magnitude-μ network is obtained after μ-1 growth steps. The choice of which link will branch (i.e., develop a new tributary) at each growth step is made stochastically. The probability of a given link branching is p_i if the link is interior, and p_e if the link is exterior. Model parameter Q relates p_i and p_e, and takes values in [0, 1]:

$$Q = \frac{p_i}{p_i + p_e} \tag{2.1}$$

Because one branching event must occur at each growth step, the sum of branching probabilities of all links in the growing network must equal unity. A network with μ exterior links (a magnitude-μ network) has μ-1 interior links, and we have:

$$\mu\, p_e + (\mu-1)\, p_i = 1 \tag{2.2}$$

Combining (2.1) and (2.2) yields:

$$p_i = \frac{Q}{\mu - Q} \tag{2.3a}$$

$$p_e = \frac{1-Q}{\mu - Q} \tag{2.3b}$$

For Q=1/2 (i.e., p_i=p_e), any link (or "segment"), be it interior or exterior, is equally likely to branch at each growth step, and the process is called "segmental growth." If when an interior link branches the probability of appending the new tributary link to the right or left-hand side of that link is the same, then segmental growth yields any TDCN of given magnitude with the same probability, and is a causative model of topologic randomness [*Dacey and Krumbein,* 1976, p. 157].

For Q=0 (i.e., p_i=0), only exterior (or "terminal") links branch, and the process is called "terminal growth." For Q=1 (i.e., p_i=1), only interior links branch, and this process yields exclusively order-two, i.e., "fishbone-shaped" networks. Any given TDCN can be produced using any value of Q (except for Q=1), however its probability of occurrence depends on Q. Lower Q values are more likely than higher Q values to produce high-order networks.

Models of either segmental or terminal growth have been used, e.g., by *Howard* [1971], *Smit et al.* [1972], *Berry et al.* [1975], *Berry and Bradley* [1976], and *Dacey and Krumbein* [1976]. The latter authors also used a growth model where p_i=2p_e, and the Q model is a generalization of their work to any p_i/p_e ratio.

The mean values of various topologic variables vary continuously with parameter Q (e.g., *Van Pelt and Verwer* [1985, 1986]). Comparing expected topologic measures with observed data, maximal-likelihood Q values can be determined, and some Q values may be ruled out at some confidence level. For example, *Van Pelt et al.* [1992] found the best-fit values Q=0.11 for Purkinje neuronal dendrites, and Q=0 for non-pyramidal dendrites. Inference of most likely growth parameters from network topology for networks embedded in space may, however, require consideration of spatial constraints, which have so far been neglected in such inference methods.

2.2.2 Computer code

A computer code, designated "Q.f," was written in Fortran to simulate network growth by the Q model. Networks were represented as binary strings, following Lukasiewicz's convention [*Berge*, 1958] (Figure 2.1a).

Growth of a network of magnitude μ starts with one initial link and requires a number μ-1 of branching events, or growth steps. Choice of which link will branch at each growth step is done by comparison of a random variable with the link branching probabilities, p_i (2.3a) for any interior link, and p_e (2.3b) for any exterior link. Once a link is chosen for branching, the new link is appended to the left or right-hand side of the branching link with equal probability, as determined by a random variable.

Figure 2.1b shows an example of five growth steps, or branching events. A branching event results in the addition of two new links: a new exterior link (appended to either the left or right-hand side of the branching link), and a new interior link that results from the partition of the branching link into two. Following each branching event, two digits representing these new links are added to the binary string that represents the network. If the new link is appended to the left-hand side of the branching link (as in steps 1, 3, and 4 in Figure 2.1b), the digits "01" are added preceding the digit representing the branching link. If the new link is appended to the right-hand side of the branching link (as in step 2 and 5 in Figure 2.1b), the digit "0" is added preceding the digit representing the branching link, and the digit "1" is added at the end of the sequence of digits (the "interval sequence") that represents the sub-network defined by the branching link. To find the end of the interval sequence, we start at its first digit (the digit representing the branching link) and move forward in the string counting the number of digits (links), n_t, and the number of "1" (exterior links), n_e. Because a network with n_e exterior links has a total of $2n_e$-1 links, the end of the interval sequence is found when n_t and n_e satisfy the equality $n_t=2n_e-1$. If the branching link is exterior, the interval sequence is the single digit "1" (as in step 2 of Figure 2.1b). In step 5 of Figure 2.1b, the end of the interval sequence "01011" is found when $n_t=5$ and $n_e=3$.

2.3 Test Network Samples

Two sets of test network samples are used: ten samples of networks of magnitude 50, including a topologically-random sample designated 0 and nine non-topologically-random samples designated A through I; and ten samples of networks of mixed magnitudes, including a topologically-random sample designated 0-mix and nine non-topologically-random samples designated A-mix through I-mix. Each sample contains 5,000 networks.

2.3.1 Samples of magnitude-50 networks

Sample 0 was constructed using the Q model computer code (Section 2.2), with

Q=1/2, for which all magnitude-50 TDCN are equally likely to be created. This sample is therefore drawn, with replacement, from a topologically-random population, and is here said to be a "topologically-random sample." A more efficient algorithm for drawing networks from a topologically-random population is given in *Shreve* [1974, p. 1172].

Non-topologically-random test samples are of type 1 (samples A through D) and type 2 (samples E through I). Test samples of type 1 were obtained by selection of networks having specified topologic properties, from an original topologically-random sample, a method introduced by *Kirchner* [1993]. Test samples of type 2 were obtained using the Q model computer code.

Test samples of type 1 are selected subsets of size 5,000 of an original topologically-random sample of size 10,000, which was obtained in the same manner as sample 0. Each of samples A through D contains all networks in the original random sample whose value of one specified "selection variable" is greater, or smaller, than the median of the original sample. To make up 5,000 networks it is necessary in some cases to include some of those networks with values equal to the median.

Sample A contains 5,000 networks whose R_B is smaller than or equal to the median value, $\tilde{R}_B$, in the original random sample. Samples B through D contain networks whose diameter (d), topologic width (w), and number of TS links (nTS), respectively, are greater than or equal to the median values of these variables in the original random sample. Variables d, w, and nTS are defined next.

The diameter, d, is the maximal number of links positioned in linear sequence from the outlet to a channel source (the longest topologic path). The topologic width, w, is the maximal number of links having the same topologic distance (path length) to the network outlet. nTS is the number of tributary-source (TS) links in the network, defined as source links (i.e., exterior links) that are tributary to a link of magnitude 3 or higher.

Test samples of type 2 were constructed using the Q model computer code (Section

2.2). Samples E through I were constructed with Q values of 0, 1/6, 1/3, 2/3, and 5/6, respectively. Samples E through I and sample 0 have Q values at intervals of 1/6. For $Q<1/2$, we have, from (2.1), $p_e>p_i$, i.e., tributary development on any one exterior link is more likely than on any one interior link. For example, in sample G, we have $Q=1/3$ and, from (2.1), $p_e=2p_i$. The resulting distribution of TDCN favors higher Strahler orders than in a topologically-random sample (Figure 2.2). For $Q>1/2$, we have, from (2.1), $p_i>p_e$. Sample H was constructed with $Q=2/3$, and from (2.1), we have $p_i=2p_e$. Values of Q larger than 1/2 favor more elongate networks, of lower Strahler orders (Figure 2.2).

2.3.2 Samples of mixed-magnitude networks

Study of the topologic analogs of geomorphologic laws that involve basin area requires a range of network magnitudes. Each mixed-magnitude test sample contains 10 networks of each magnitude in [1, 500]. These samples were created by methods analogous to those for the magnitude-50 samples *0*, and *A* through *I* (above), and are designated *0-mix*, and *A-mix* through *I-mix*, respectively.

Table 2.1 summarizes the method by which each test sample was created.

2.4 Topologic Analogs of Channel Network Planform Laws

In this section, the parameters of the topologic-analog of each geomorphologic law listed in Chapter 1 (properties I-VII) are computed for the test network samples described in Section 2.3. See Appendix A for variable notation.

A computer code, designated "topovars.f," was written in Fortran to compute the topologic variables from the binary strings representing networks.

2.4.1 Property I: Horton's laws and ratios

Horton's laws of stream numbers, lengths, and areas, were given by expressions (1.1), (1.2), and (1.3), respectively, in Chapter 1. Shreve showed that "no [TDCN] can depart indefinitely far from Horton's [law of stream numbers]," and in this sense this law is "inherent in the definition of stream order" [*Shreve*, 1966, p. 30]. Hence, this law may not be attributed "to either orderly evolution or random development" [*Bowden and Wallis*, 1964, p. 769]. Most TDCN also comply approximately with the topologic-analogs of Horton's laws of stream lengths and areas [*Shreve*, 1969].

The generality of Horton's laws among TDCN is most easily explained for the law of stream numbers, as follows. The first and last points in a Horton diagram of stream numbers (Figure 1.1b) are determined by network magnitude and order ($N_1=\mu$ and $N_\Omega=1$), while the intermediate points (N_ω, $1<\omega<\Omega$) have variable positions. Shreve showed that the domain of variation for these points is narrow, because "for every stream of given order, except the first, there must be at least two streams of the next lower order" [*Shreve*, 1966, p. 30]. This range is a narrow parallelogram whose diagonal represents a geometric series with ratio G_B (the geometric-mean bifurcation ratio) determined by μ and Ω (2.4a) [*Shreve,* 1969, p. 21]. R_B, obtained by regression, approximates G_B (2.4b).

$$G_B = \mu^{1/(\Omega-1)} \tag{2.4a}$$

$$R_B \approx G_B \tag{2.4b}$$

Given any set of stream numbers, we can arrange those streams to form a finite number of TDCN. *Shreve* [1966] demonstrated that those sets of stream numbers which approximate a geometric series with ratio 4.0 allow the largest number of TDCN. Therefore, in a topologically-random population of magnitude-μ networks, the most frequent, or modal order, $\Omega_M(\mu)$, is that for which G_B is closest to 4.0 [*Shreve*, 1966]. From (2.4):

$$\Omega_M(\mu) = \mathrm{Round}(\frac{\log \mu}{\log 4} + 1) \tag{2.5}$$

where "Round(·)" denotes the closest integer.

The topologic analogs of Horton's laws of stream lengths and areas substitute the number of links in a stream (the stream's "topologic length"), and in a network (the network's topologic "Schumm length"), for stream length and basin area, respectively. The topologic-analog length and area ratios are here indicated by R^t_L and R^t_A, and the geometric-mean ratios are G^t_L and G^t_A. For a network of order Ω, G^t_A depends on the total number of links, equal to 2μ-1 (2.6a), and G^t_L depends on the topologic length of the highest order stream, L^t_Ω (2.7a). Ratios R^t_L and R^t_A approximate G^t_L and G^t_A, respectively (2.6b and 2.7b):

$$G^t_A = (2\mu-1)^{1/(\Omega-1)} \tag{2.6a}$$

$$R^t_A \approx G^t_A \tag{2.6b}$$

$$G^t_L = {L^t_\Omega}^{1/(\Omega-1)} \tag{2.7a}$$

$$R^t_L \approx G^t_L \tag{2.7b}$$

Smart [1968, Eqn. 13a] derived an expression for the average topologic length of streams of order ω, $\bar{L}^t_\omega$, as a function of the set of stream numbers, $\{N_i, 1 \leq i \leq \omega\}$, under the assumption of topological randomness:

$$\bar{L}^t_\omega = \prod_{i=2}^{\omega} \frac{N_{i-1} - 1}{2N_i - 1} \tag{2.8}$$

For the RT model, the ratio N_{i-1}/N_i tends to 4 at large i, and equation (2.8) approximates Horton's law of stream lengths with R^t_L=2 [*Smart*, 1968].

Approximating the set of stream numbers by a geometric series with the ratio given by (2.4a), we obtain, using (2.8), the mean topologic length of the outlet stream of order-Ω networks, $\bar{L}^t_\Omega$, for the RT model:

$$\bar{L}^t_\Omega = \prod_{\omega=2}^{\Omega} \frac{\mu^{1-(\omega-2)/(\Omega-1)} - 1}{2\mu^{1-(\omega-1)/(\Omega-1)} - 1} \tag{2.9}$$

G^t_L for topologically-random samples is approximated by substituting $\bar{L}^t_\Omega$ in (2.9) for L^t_Ω in (2.7a).

The quality of approximations (2.4b), (2.6b) and (2.7b) can be appreciated from Figure 2.3. Deviations from (2.7b) are the most pronounced, especially for orders other than $\Omega_M(\mu)$. *Shreve* [1969] showed that topologic stream lengths often deviate markedly from a geometric series and, citing empirical studies, noted that natural networks also often violate Horton's law of stream lengths [*Shreve*, 1969, p. 407].

Holding network magnitude fixed in Figure 2.3, we obtain multimodal R_B, R^t_A, and R^t_L distributions. The R_B distribution for topologically-random magnitude-50 sample 0 is shown in Figure 2.4a. This distribution has an upper, central, and lower mode, corresponding to network orders 3, 4, and 5, respectively. Mode positions are at the value 7.07, and at the approximate values of 3.68, and 2.66, given by (2.4). The most frequent Strahler order, from (2.5), is 4. Sample 0 contains 2.0%, 87.2%, and 10.8% of networks of orders 3, 4, and 5, respectively, in close agreement with analytic predictions [*Shreve*, 1966, Table 2]. The minimum and maximum possible orders for magnitude 50 are 2 and 6, but no networks of these orders appear in sample 0; their probability of occurrence in a topologically-random sample of size 5,000 is only 1.21×10^{-4} (computed from *Shreve* [1966, Table 2]).

The R_B distribution of sample A (Figure 2.4a) represents a truncated distribution of a topologically-random sample, because the selection variable used in constructing this type-1 sample is R_B itself. Type-1 samples B, C, and D, selected for variables d, w, and nTS, respectively, have R_B distributions differing little from sample 0 (Figure 2.4a). These results agree with those of *Kirchner* [1993], who studied test samples of type 1.

Some magnitude-50 test samples of type 2 have R_B distributions markedly different from sample 0 (Figure 2.4a). The most frequent order is 5 for samples E and F, 4 for G and H, and 3 for I. Order-5 networks are more frequent in samples E, F, and G ($Q<1/2$), and less frequent in sample H ($Q>1/2$) than in sample 0. No order-5 networks appear in sample I (highest Q value tested, $Q=5/6$). Order-3 networks are less frequent in sample G ($Q<1/2$) and more frequent in samples H and I ($Q>1/2$) than in sample 0. No order-3 networks appear in samples E and F (lowest Q values tested, $Q=0$ and $Q=1/6$). Sample I ($Q=5/6$) includes four networks of order 2 (having $R_B=50$, which is above the plot axis range).

The positions of R_B, R^t_A and R^t_L distribution modes depend on network magnitude ((2.4), (2.6), (2.7) and (2.9)), hence mixed-magnitude distributions don't have separated modes (Figure 2.4b). Increasing Q values in type-2 samples, from $Q=0$ to $Q=5/6$ (E-mix through I-mix), yield higher R_B, R^t_A and R^t_L means and increased dispersion. This is shown for R_B in Figure 2.4b.

Results for the R^t_A and R^t_L distributions (not shown) are qualitatively similar to those for the R_B distributions shown in Figure 2.4. R_B, R^t_A and R^t_L means and standard deviations for the mixed-magnitude test samples are given in Table 2.2. Figure 2.5 shows the R_B, R^t_A and R^t_L means for the type-2 mixed-magnitude test samples, plotted against the Q parameter.

Horsfield et al. [1987] derived (2.10a) for the mean ratio between stream numbers of orders 1 and 2, $\bar{R}_{B_{1-2}}$, as a function of Q. For large magnitude, R_B approaches $\bar{R}_{B_{1-2}}$

(2.10b):

$$\bar{R}_{B_{1\text{-}2}} = 3 + \frac{Q}{1\text{-}Q} \qquad (2.10a)$$

$$R_B \approx \bar{R}_{B_{1\text{-}2}} \qquad , \mu \text{ large} \qquad (2.10b)$$

From (2.1), the ratio Q/(1-Q) in (2.10a) equals p_i/p_e.

The most frequent network order, $\Omega_M(\mu, Q)$, is given upon substitution of $\log(\bar{R}_{B_{1\text{-}2}})$, obtained from (2.10a), for log(4) in (2.5). Smaller Q values yield larger $\Omega_M(\mu, Q)$ values. The position of the principal R_B distribution mode is estimated using (2.4), by substituting $\Omega_M(\mu, Q)$ for Ω. The R_B value obtained from (2.4) oscillates above and below the value given by (2.10). The amplitude of these oscillations decreases with μ, and is larger for larger Q (see *Horsfield and Woldenberg* [1986] for an extensive discussion and related references). For the low range of magnitudes in our mixed-magnitude test samples, (2.10b) is not a good approximation, especially for large Q.

For Q=1/2 (yielding topological randomness), the R_B value predicted by (2.10) is 4.0. For the maximum magnitude used, 500, the order which gives R_B closest to 4.0 is, from (2.5), $\Omega_M(500)=5$. The R_B modal value for order 5, using (2.4), is 4.729. The principal modal value of R_B in a topologically-random population oscillates about the value of 4.0.

The published observed values of the Horton ratios include networks of various magnitudes and from different environments. R_B is usually in the range of 3 to 5, with a modal value near 4; R_L is in the range of 1.5 to 3.5, with a modal value near 2; and R_A is in the range of 3 to 6, with a modal value near 4 [*Chorley*, 1957; *Smart*, 1972; *Abrahams*, 1984]. Shreve remarked that for a topologically-random population of finite-magnitude networks, the R_B principal modal value and main range of variation coincide with the observed values [*Shreve*, 1966]; and that if all network links had the same length and drainage area, R_L and R_A would coincide with their topologic-analogs, $R^t{}_L$ and $R^t{}_A$, which for a uniform distribution of TDCN of finite magnitude exhibit a range of variation similar to observations [*Shreve*, 1967, p. 184]. Shreve interpreted these results as supportive evidence for the RT model [*Shreve*, 1966, p. 36; *Shreve*, 1969, p. 414].

Kirchner [1993] showed that distributions of the Horton ratios in non-topologically-random samples of type 1 do not deviate much from those in a random sample, and concluded that these ratios have little sensitivity to topological distribution, hence the RT model prediction of their typical empirical values does not provide evidence in support of the RT model. It has been shown here that the Horton ratios are sensitive to the Q parameter in type-2 test samples. It is possible that they are sensitive also to other models of network growth.

2.4.2 Property II: Correlations between Horton ratios, and between stream numbers and stream lengths

The topologic-analog Horton ratios depend strongly on magnitude, μ, and order, Ω ((2.4), (2.6), (2.7) and (2.9)). When μ is held fixed, the modal clusters corresponding to Ω (Figures 2.3 and 2.4a) are seen in plots of paired values of these ratios (Figures 2.6a and 2.7a for sample 0). Correlation coefficients between (R_B, $R^t{}_L$), (R_B, $R^t{}_A$), and ($R^t{}_L$, $R^t{}_A$) are determined largely by cluster positions, and are high in all test samples, especially for (R_B, $R^t{}_A$) (Table 2.3, magnitude-50 samples). When both μ and Ω are held constant, i.e., within a cluster, (R_B, $R^t{}_L$) are uncorrelated, and the (R_B, $R^t{}_A$) and ($R^t{}_L$, $R^t{}_A$) correlations drop considerably (see Table 2.3, (R_B, $R^t{}_A$) order-4 column, magnitude-50 samples).

In mixed-magnitude samples, clusters overlap and plots of paired values of R_B, $R^t{}_A$ and $R^t{}_L$ show stratification by Ω, most marked in the case of (R_B, $R^t{}_A$) (Figure 2.7b).

Correlation coefficients are high for all three pairs in all mixed-magnitude samples, especially for (R_B, R^t_A) (Table 2.3). Due to stratification by Ω, correlation coefficients are higher for Ω held fixed (see Table 2.3, order-4 columns, mixed-magnitude samples).

The mean ratios R^t_L/R_B, R^t_A/R_B and R^t_L/R^t_A are higher for sets of networks of lower Ω ((2.4), (2.6) and (2.7)). Ratio R^t_A/R_B for fixed Ω is approximately equal to $2^{1/(\Omega-1)}$ ((2.4) and (2.6)), and tends to 1 for large Ω (Figure 2.7b). Because higher Q values tend to originate a larger proportion of networks of lower Ω, ratios R^t_L/R_B, R^t_A/R_B and R^t_L/R^t_A increase with Q, i.e., from sample E to I, and from E-mix to I-mix (Table 2.3).

"Correlations between stream numbers and stream lengths," included by *Shreve* [1975] under Property II, refers to the prediction of the set of mean stream lengths, $\{\bar{L}_\omega\}$, from the set of stream numbers, $\{N_\omega\}$, via (2.8) for networks from topologically-random samples, under the assumption of linearity between measured and topologic lengths (Chapter 1). *Smart* [1968] showed that $\bar{L}^t_\omega$ from (2.8) provides an approximation to $\bar{L}_\omega/\bar{l}_i$, where $\bar{L}_\omega$ is the mean length of order-ω streams, and $\bar{l}_i$ is the mean link length. Correlation coefficients between predicted and observed $\bar{L}_\omega$ ranged from 0.69 to 0.90 for various ω in basins analyzed by *Smart* [1968].

Expression (2.8) was derived for the RT model and is not expected to provide approximate $\bar{L}^t_\omega$ predictions for non-topologically-random samples. A corresponding expression to (2.8) is not currently available for networks created by the Q model. To test the sensitivity of the relation between $\{\bar{L}^t_\omega\}$ and $\{N_\omega\}$, the values observed in each test sample, $\bar{L}^t_{\omega_{obs}}$, are compared to RT model predictions obtained from $\{N_\omega\}$ via (2.8), $\bar{L}^t_{\omega_{pred}}$, (Table 2.4).

In type-1 samples, (2.8) provides good predictions, comparable to those for sample 0 (Table 2.4). In type-2 samples, the mean ratio between $\bar{L}^t_{\omega_{obs}}$ and $\bar{L}^t_{\omega_{pred}}$ varies with Q and ω, while correlation coefficients are high (0.737-0.916) for all test samples and all ω.

Correlations increase with network magnitude (not shown). Figure 2.8 illustrates the high correlation between $\bar{L}^{t}_{2_{obs}}$ and $\bar{L}^{t}_{2_{pred}}$, for samples 0-mix and E-mix. The correlation for sample E-mix is even higher than for sample 0-mix, however the ratio $\bar{L}^{t}_{2_{obs}}/\bar{L}^{t}_{2_{pred}}$ is greater than 1 for sample E-mix. This ratio is greater than 1 for $Q<1/2$ and less than 1 for $Q>1/2$ for order 2; approximately equal to 1 for all Q for order 3; and less than 1 for $Q<1/2$ and greater than 1 for $Q>1/2$ for higher orders (Table 2.4).

2.4.3 Property III: Statistical distributions of second-order stream lengths, Schumm lengths, and areas

The topologic analog of stream length is the number of links in the stream, and the analog of both Schumm length (total channel length in the basin) and drainage area is the total number of links in the network. In sub-basins of order two, the total number of links equals $2L^{t}_{2}+1$, where L^{t}_{2} is the topologic length of the second-order stream.

Figure 2.9 shows the frequency distribution of L^{t}_{2} for all second-order streams in the networks of mixed-magnitude type-2 samples. Table 2.5 gives the mean and standard deviation for each test sample. For an infinite topologically-random network, the frequency distribution of topologic lengths of streams of any given order w is geometric [*Shreve*, 1969, Eqn. 9b], and the expected topologic stream length for successive orders is given by a geometric series of ratio 2 [*Shreve*, 1967, p. 184; *Shreve*, 1969, Eqn. 9c].

In type-1 samples, the L^{t}_{2} frequency distribution differs little from RT model predictions (Table 2.5), the largest deviation being for sample D-mix, selected for $nTS(\mu)$ higher than the median. In type-2 samples, this distribution differs from RT model predictions and is not geometric (Figure 2.9, Table 2.5).

2.4.4 Property IV: Proportional relationship between stream frequency and the square of drainage density

Stream frequency, F_s, and drainage density, D, are the average number of streams and average length of streams, respectively, per unit area in a drainage basin. *Melton* [1958, pp. 36-37] analyzed data for 156 basins of differing area, climate, relief, geology and vegetation, and found the ratio F_s/D^2 to be approximately constant:

$$\frac{F_s}{D^2} \approx 0.694 \tag{2.11}$$

Shreve [1967, pp. 184-185] showed that the topologic analog of F_s/D^2 is the ratio between the number of streams, S_s, and the number of links, 2μ-1. The ratio $S_s/(2\mu-1)$ is the reciprocal of the average number of links, or topologic length, per stream.

For large μ, expected stream numbers approximate a geometric series with ratio R_B, and the expected number of streams, S_s, is approximated by the sum of this series over orders 1 through Ω:

$$S_s = \sum_{\omega=1}^{\Omega} R_B^{\Omega-\omega} = \frac{1-R_B^{\Omega}}{1-R_B} \tag{2.12}$$

For large-μ topologically-random networks, we have $R_B \approx 4$, and substituting (2.5) for Ω in (2.12) yields $S_s \approx 4\mu/3$, and $S_s/(2\mu-1) \approx 2/3$ [*Shreve*, 1967, p. 185]. This value compares well with (2.11).

For large-μ networks generated by the Q model, substituting $\log(R_B)$ for $\log(4)$ in (2.5), we obtain from (2.12):

$$\frac{S_s}{2\mu-1} \approx \frac{R_B}{2(R_B-1)} \tag{2.13}$$

Substituting (2.10) into (2.13) yields:

$$\frac{S_s}{2\mu-1} \approx \frac{3-2Q}{4-2Q} \tag{2.14}$$

Table 2.6 gives the mean and standard deviation of $S_s/(2\mu-1)$ for each test sample. Mean values for type-1 samples are close to those of sample 0. Mean values for type-2 samples are in approximate agreement with (2.14). For the purpose of illustration, the $S_s/(2\mu-1)$ values in test samples 0-mix and E-mix are plotted against μ in Figure 2.10.

2.4.5 Property V: Variation of mainstream length with basin area

Hack [1957] found an exponential relation between mainstream length, L, and basin area, A, (also given in (1.6)):

$$L = \kappa A^{\theta} \tag{2.15}$$

Hack [1957] and *Gray* [1961] found the exponent θ to vary with geographic location, taking values larger than 0.5. *Mueller* [1973] collected data for several thousand basins of all sizes in various parts of the world, and found that θ changed abruptly from 0.6 for basins of area smaller than 8,000 mi^2, to 0.5 for basins between 8,000 and 100,000 mi^2, and to 0.466 for basins larger than 100,000 mi^2.

The computed value of θ is subject to uncertainty. *Robert and Roy* [1990] (see also *Beer* [1991] and *Robert and Roy* [1991]) presented evidence of influence of cartographic scale on the estimated θ. *Montgomery and Dietrich* [1992] replaced stream lengths by basin lengths, measured along the main valley axis to the basin divide, obtaining θ=0.5. These authors suggested that θ depends on the headward extent of the mainstream depicted on maps of different scale, as well as on downstream variations in channel sinuosity and drainage density.

The topologic-analogs of L and A are network diameter, d, and total number of links, 2μ-1, respectively. However, when data from basins of different drainage densities are lumped together, there is not a direct correspondence between L and A and their topologic analogs. Despite this limitation, (2.15) has been used to test the RT model using the topologic analogs.

Mesa and Gupta [1987, Eqn. 16] derived the approximate expression (2.16) for a for the RT model, under the assumption of independent, identically distributed (i.i.d.) exponential link lengths.

$$\theta(\mu) = \frac{1}{2}\frac{\pi + (\pi/\mu)^{1/2}}{\pi - (1/\mu)} \tag{2.16}$$

From (2.16), the RT model predicts that θ decreases continuously from about 0.6 for small magnitudes, μ, to the asymptotic value of 0.5 for large μ. Similar results had been obtained by Monte Carlo simulations by *Shreve* [1970] and *Werner and Smart* [1973].

Shreve [1974, pp. 1175-1176] showed that the observed deviations of θ from RT model predictions for large basin areas may be accounted for by channel sinuosity (see also *Smart and Surkan* [1967]). *Mesa and Gupta* [1987] remark that the abrupt changes of θ with basin size cannot be accounted for by the RT model. In our view, the above uncertainties concerning the computation of θ from observed data preclude any definite conclusions regarding the validity of the RT model. Moreover, the above computed values of θ most certainly include basins subject to strong geologic controls.

Figure 2.11b shows a log-log plot of diameter, d, versus the number of links, 2μ-1, for topologically-random sample 0-mix. The values of d in sample 0-mix lie within a narrow region inside the zone of possible values, and the variance does not decrease with magnitude, as shown analytically by *Mesa* [1986], cited by *Mesa and Gupta* [1987, Eqn. 27], so that $d(\mu)$ does not tend to almost-sure values at large μ. Figures 2.11a and 2.11c illustrate the influence of Q on the $d(\mu)$ distribution. The $d(\mu)$ distributions of samples F-mix and I-mix, pictured, do not overlap for μ larger than about 70.

Figure 2.12 shows similar plots, for test samples of type 1. Deviation from the RT model (Figure 2.11b) is small in all type-1 samples, excepting the sample obtained by selection of $d(\mu)$ larger than the median, $\tilde{d}(\mu)$. The reasons for the small deviation are addressed in Section 2.5.

The value of θ varies with μ in all samples. Table 2.7 gives the overall θ and κ values. Both θ and κ vary markedly with Q; θ varies from less than 0.3 for Q=0 (sample E-mix) to 1.0 for Q=1 (order-2 networks, represented by the upper boundary of the zone of possible values of $d(\mu)$ in Figures 2.11 and 2.12).

2.4.6 Property VI: Variation of basin distance-weighted area with basin area

Langbein et al. [1947] studied the relation between basin area, A, and the basin's "distance-weighted area," P, defined by

$$P = \sum_{k} l_k \, a_k \qquad (2.17)$$

where a_k is a portion of the basin area (a "partial area"), and l_k is the channel distance from the partial area to the outlet. P has dimension of length cubed. Using data for 340 drainage basins in the Northeastern U.S., *Langbein et al.* [1947] found the relation:

$$P = \varepsilon \, A^{\phi} \qquad (2.18)$$

where P and A are expressed in miles and square miles, respectively, and ε and ϕ have the respective values of 1.56 and 0.90.

The topologic path length of a link is the number of links composing the path that connects the link of interest to the root link, including the link of interest itself. The total topologic path length, p, of a network is the sum of topologic path lengths of all links composing the network. If we choose the a_k values in (2.17) to be the individual link areas, and under the assumption that a_k and l_k are uncorrelated, then p is the topologic analog of P [*Werner and Smart*, 1973, p. 292].

Werner and Smart [1973] found the following relation for a computer-generated sample of 200 topologically-random networks with magnitudes, μ, randomly selected from the range [20-200]:

$$p = 1.0\,(2\mu - 1)^{1.53} \qquad (2.19)$$

Mesa and Gupta [1987, Eqn. 25] derived for the RT model, under the assumption of i.i.d. exponentially distributed link lengths, the approximate expression for p at large μ:

$$p \approx 2\sqrt{\pi}\ \mu^{1.5} \qquad , \mu \text{ large} \qquad (2.20)$$

Figure 2.13 shows log-log plots of p versus 2μ-1, for sample 0-mix, and type-2 samples F-mix and I-mix. The p values in sample 0-mix (topologically random) lie within a narrow plot region within the zone of possible values (Figure 2.13b). Table 2.8 gives the overall exponent, ϕ, and coefficient, ε, in (2.19) for each test sample. Variation of ϕ and ε is slight for type-1 samples, but marked for type-2 samples. Both ϕ and ε vary with Q, and ϕ decreases from 1.242 for Q=0 (sample E-mix) to 1.803 for Q=5/6 (sample I-mix).

2.4.7 Property VII: Relation between distance from the basin outlet to centroid and mainstream length

Gray [1961] studied the relation between the channel distance from the outlet to the center of gravity (or "centroid") of the network, L_{ca}, and the mainstream length, L. L_{ca} is given by:

$$L_{ca} = P/A \tag{2.21}$$

where P is defined by (2.17). *Gray* [1961] found the relation (also given in (1.8)):

$$L_{ca} = 0.5\ L \tag{2.22}$$

The topologic analogs of L and L_{ca} are d and the mean topologic path length, $\overline{p}=p/(2\mu-1)$, respectively. *Werner and Smart* [1973, Eqn. 34] obtained the following regression relation for a computer-generated sample of 200 topologically-random networks with magnitudes μ randomly selected from the range [20-200]:

$$\overline{p} = 0.50\ d + 1.3 \tag{2.23}$$

Both $\overline{p}$ and d increase with μ, and for large μ, (23) is approximated by $\overline{p}=0.5d$, the topologic equivalent of (22). *Mesa and Gupta* [1987, Eqn. 26] derived for the RT model, at large μ, assuming i.i.d. exponentially distributed link lengths:

$$\overline{p} = 0.50\ d \qquad , \mu \text{ large} \tag{2.24}$$

Because there is uncertainty in both d and $\overline{p}$ for given μ, it is not appropriate to perform regression of $\overline{p}$ against d. Regression implicitly assumes there to be uncertainty only in the dependent variable (e.g., *Hirsch and Gilroy* [1984]). Instead, the mean and standard deviation of $\overline{p}/d$ was computed for each test sample (Table 2.9). Also given in Table 2.9 are the mean and standard deviation of $\overline{p}^*/d$, where $\overline{p}^*$ denotes the mean value of p^*, the "total modified topologic length," introduced here. The modified topologic length is here defined as the number of links forming the path that connects the link of interest and the root link, excluding the link of interest. The standard definition of topologic length includes the link of interest. We have:

$$p^* = p - (2\mu-1) \tag{2.25}$$

$$\overline{p}^* = \overline{p} - 1 \tag{2.26}$$

The reason for using p^* instead of p is that the ratio $\overline{p}^*/d$ shows dependency on μ only for very low μ values. Figure 2.14 depicts $\overline{p}^*/d$ plotted against μ for test samples F-mix, 0-mix, and I-mix. The mean $\overline{p}^*/d$ increases with Q, as does the standard deviation (Table 2.9). This increase is slight except for very low Q values.

For given d, variable $\overline{p}^*$ is determined by the network's shape. Networks having more links at higher than lower topologic distances from the root, said to be "top heavy," have high $\overline{p}^*$ values. "Bottom heavy" networks have more links at short topologic distances from the root, and have low $\overline{p}^*$ values. Networks produced with low Q values tend to be more compact, with lower bifurcation ratios. Because the maximum number of links at a given topologic distance from the root increases with distance, these compact networks tend to have more links at topologic distances higher than half the network's diameter, and hence are top-heavy. Networks produced with high Q values do not have a tendency to be either top or bottom heavy. For Q=1, which produces exclusively second-order networks, $\bar{p}^*/d$ tends to 0.5 for μ large.

2.5 Conclusions

The sensitivity of channel network planform laws (properties I-VII) to non-uniform TDCN frequencies was tested by computing the coefficients of each topologic-analog law for non-topologically-random test samples. Two types of test sample were used (Section 2.3). Samples of type 1 were obtained by selection of networks from an original topologically-random sample, based on threshold values of a specific topologic variable, located at the sample median. Samples of type 2 were obtained by constructing each network using the Q model of stochastic topologic growth (Section 2.2), where the probabilities of tributary development on an exterior link, and on an interior link, are allowed to vary.

Sensitivity of the topologic-analog laws is different for type-1 and type-2 test samples (Section 2.4). Sensitivity of all laws to type-1 samples (A through D and A-mix through D-mix) is limited. This is because the cutoff value for each selection variable was placed at the sample median. Given the sharply peaked distributions of the selection variables, a cutoff value equal to the sample median will not succeed in sampling away from the narrow distribution peak. The effects on topologic variables other than the selection variable depend on the correlations between variables, and are small for cutoff values placed at the sample median. Cutoff values corresponding to the upper or lower third, fourth, fifth, or any decile, would require larger sample sizes than those used here. Cutoff values located farther from the median would necessarily result in larger deviations from RT model predictions.

Parameter values of the Q model are well reflected in departures from RT model predictions for all topologic-analog laws. Only Gray's relation (property VII) shows very limited sensitivity to Q, except for low Q values. It is possible that properties I-VI are sensitive to other models of network growth as well.

Correlations between (R_B, $R^t{}_L$), (R_B, $R^t{}_A$), and ($R^t{}_L$, $R^t{}_A$) are largely determined by network magnitude and order. When both these variables are held fixed, correlations drop considerably, and are close to zero for (R_B, $R^t{}_L$). Given that observed correlations among these ratios [*Smart*, 1968] have not been studied conditionally for μ and Ω, the correlation values found do not establish well-defined geomorphologic laws. Conditional analysis of observed correlations and comparison with RT model predictions may constitute useful future work, especially since high correlations between R_B and $R^t{}_L$ in natural channel networks may be a result of the space-filling requirements of these networks. *Tarboton et al.* [1988], and *La Barbera and Rosso* [1989] have proposed that the ratio $\log(R_B)/\log(R^t{}_L)$ provides an estimate of a network's fractal dimension, in the vicinity of 2.

Given the sensitivity of channel network planform laws to at least one class of network growth models, represented by the Q parameter, it is concluded that the approximate agreement of these laws with the predictions of the RT model may be a distinctive property of channel networks rather than an inescapable result. The approximate agreement with the RT model remains unexplained. In attempting an explanation, one must be cautioned that all models used here to create non-topologically-random network samples are purely topological. Space-filling and geometric properties of channel networks were ignored, and could lead to different results. Samples of networks subject to space-filling and geometric constraints are created in Chapter 3. The sensitivity of the topologic analogs of properties I-VII in sample networks subject to space-filling and geometric constraints is the topic of Chapter 4.

Table 2.1. Development of test samples. The median, for given network magnitude, μ, of each selection variable in the original topologically random sample of 10,000 networks is indicated by a tilde.

Sample	*Threshold-selection criterion or Q model parameter:*
Topologically-random samples:	
0 and 0-mix	$Q = 1/2$
Type-1 samples:	
A and A-mix	$R_B(\mu) \leq \tilde{R}_B(\mu)$
B and B-mix	$d(\mu) \geq \tilde{d}(\mu)$
C and C-mix	$w(\mu) \geq \tilde{w}(\mu)$
D and D-mix	$nTS(\mu) \geq n\widetilde{TS}(\mu)$
Type-2 samples:	
E and E-mix	$Q = 0$
F and F-mix	$Q = 1/6$
G and G-mix	$Q = 1/3$
H and H-mix	$Q = 2/3$
I and I-mix	$Q = 5/6$

Table 2.2. Arithmetic means and standard deviations of R_B, R^t_A and R^t_L, for mixed-magnitude test samples.

Sample	R_B *mean*	R_B *s. d.*	R^t_A *mean*	R^t_A *s. d.*	R^t_L *mean*	R^t_L *s. d.*
Topologically-random sample:						
0-mix	3.767	0.605	4.448	0.940	2.005	0.531
Type-1 samples:						
A-mix(*)	3.448	0.356	4.029	0.549	1.792	0.357
B-mix	3.881	0.612	4.586	0.994	2.162	0.540
C-mix	3.614	0.488	4.249	0.701	1.857	0.399
D-mix	3.796	0.614	4.498	1.000	2.026	0.563
Type-2 samples:						
E-mix	3.006	0.291	3.422	0.470	1.219	0.220
F-mix	3.181	0.344	3.650	0.554	1.396	0.284
G-mix	3.405	0.445	3.951	0.737	1.631	0.396
H-mix	4.337	0.820	5.258	1.310	2.622	0.767
I-mix	5.704	1.647	7.289	2.643	4.043	1.623

(*) The selection variable used in constructing sample A-mix was R_B.

Table 2.3. Correlations, r(·, ·), between topologic-analog Horton ratios in test samples, and in subsets containing only those networks of order four; and mean ratios between these variables.

Sample	r(R_B, R^t_L)		r(R_B, R^t_A)		r(R^t_L, R^t_A)		R^t_L/R_B	R^t_A/R_B	R^t_L/R^t_A
	all	*order 4*	*all*	*order 4*	*all*	*order 4*	*mean*	*mean*	*mean*
Magnitude-50 samples:									
Topologically-random sample:									
0	0.829	-0.073	0.990	0.661	0.801	-0.406	0.546	1.239	0.441
Type-1 samples:									
A(*)	0.803	0.032	0.989	0.414	0.769	-0.261	0.547	1.169	0.484
B	0.850	-0.130	0.991	0.626	0.822	-0.493	0.579	1.243	0.467
C	0.706	-0.127	0.988	0.710	0.665	-0.392	0.521	1.233	0.423
D	0.844	-0.105	0.992	0.661	0.822	-0.398	0.542	1.248	0.435
Type-2 samples:									
E	0.894	-0.220	0.997	0.791	0.881	-0.386	0.432	1.199	0.360
F	0.881	-0.154	0.996	0.762	0.863	-0.426	0.465	1.205	0.386
G	0.817	-0.087	0.992	0.718	0.786	-0.392	0.506	1.221	0.415
H	0.935	-0.057	0.997	0.560	0.924	-0.417	0.593	1.275	0.466
I	0.959	0.108	0.990	0.420	0.952	-0.201	0.697	1.354	0.513
Mixed-magnitude samples:									
Topologically-random sample:									
0-mix	0.874	0.886	0.936	0.993	0.872	0.857	0.527	1.177	0.449
Type-1 samples:									
A-mix(*)	0.709	0.813	0.896	0.985	0.667	0.768	0.514	1.162	0.443
B-mix	0.879	0.865	0.940	0.988	0.898	0.836	0.558	1.176	0.476
C-mix	0.799	0.844	0.951	0.989	0.781	0.816	0.504	1.170	0.431
D-mix	0.888	0.854	0.943	0.990	0.876	0.820	0.528	1.178	0.449
Type-2 samples:									
E-mix	0.745	0.732	0.904	0.995	0.870	0.700	0.405	1.137	0.356
F-mix	0.778	0.796	0.908	0.992	0.858	0.762	0.437	1.145	0.382
G-mix	0.834	0.827	0.922	0.994	0.871	0.797	0.476	1.157	0.412
H-mix	0.900	0.904	0.936	0.991	0.880	0.869	0.598	1.206	0.497
I-mix	0.954	0.912	0.957	0.976	0.923	0.855	0.694	1.267	0.550

(*) The selection variable used in constructing samples A and A-mix was R_B.

Table 2.4. Mean ratio of observed, $\bar{L}^t_{\omega_{obs}}$, to predicted, $\bar{L}^t_{\omega_{pred}}$, mean topologic stream lengths, and corresponding correlations, $r(\cdot, \cdot)$, for mixed-magnitude test samples. $\bar{L}^t_{\omega_{pred}}$ is the value predicted by the RT model, using (2.8).

Sample	mean $\left(\frac{\bar{L}^t_{\omega_{obs}}}{\bar{L}^t_{\omega_{pred}}}\right)$				$r(\bar{L}^t_{\omega_{obs}}, \bar{L}^t_{\omega_{pred}})$			
	ω=2	*ω=3*	*ω=4*	*ω=5*	*ω=2*	*ω=3*	*ω=4*	*ω=5*
Topologically-random sample:								
0-mix	1.000	0.998	1.021	1.060	0.862	0.840	0.845	0.833
Type-1 samples:								
A-mix	1.012	1.010	1.016	1.083	0.853	0.815	0.850	0.810
B-mix	1.004	1.005	1.034	1.078	0.856	0.820	0.844	0.826
C-mix	0.997	0.992	0.996	0.989	0.849	0.823	0.837	0.822
D-mix	1.016	1.022	0.994	1.077	0.865	0.849	0.838	0.821
Type-2 samples:								
E-mix	1.187	1.015	0.740	0.544	0.878	0.738	0.737	0.782
F-mix	1.144	1.012	0.805	0.642	0.885	0.773	0.762	0.787
G-mix	1.083	1.012	0.886	0.809	0.878	0.792	0.793	0.811
H-mix	0.873	0.979	1.241	1.484	0.841	0.828	0.881	0.814
I-mix	0.671	1.017	1.744	2.075	0.787	0.870	0.916	0.818

Table 2.5. Arithmetic mean and standard deviation of the length of second-order streams, L^t_2, in the networks of mixed-magnitude test samples.

	L^t_2	
Sample	*mean*	*s. d.*
Topologically-random sample:		
0-mix	2.003	1.411
Type-1 samples:		
A-mix	1.996	1.298
B-mix	1.999	1.430
C-mix	1.991	1.301
D-mix	2.139	1.427
Type-2 samples:		
E-mix	1.792	0.999
F-mix	1.838	1.087
G-mix	1.905	1.217
H-mix	2.177	1.790
I-mix	2.802	2.386

Table 2.6. Mean and standard deviation of $S_S/(2\mu-1)$ for mixed-magnitude test samples.

Sample	$S_S/(2\mu-1)$ *mean*	*s. d.*
Topologically-random sample:		
0-mix	0.672	0.022
Type-1 samples:		
A-mix	0.672	0.022
B-mix	0.670	0.022
C-mix	0.672	0.022
D-mix	0.667	0.020
Type-2 samples:		
E-mix	0.751	0.020
F-mix	0.729	0.021
G-mix	0.703	0.022
H-mix	0.633	0.022
I-mix	0.582	0.022

Table 2.7. Values of exponent, κ, and coefficient, κ, in $d=\kappa(2\mu-1)^{\theta}$, for mixed-magnitude test samples, obtained by least-square linear regression of log(d) over log(2μ-1); and values of the standard deviation about the regression line, in units of log(d).

Sample	θ	κ	*s. d.*
Topologically-random sample:			
0-mix	0.560	1.538	0.207
Type-1 samples:			
A-mix	0.556	1.487	0.195
B-mix(*)	0.581	1.560	0.138
C-mix	0.551	1.488	0.181
D-mix	0.557	1.599	0.206
Type-2 samples:			
E-mix	0.272	3.227	0.110
F-mix	0.355	2.595	0.148
G-mix	0.451	2.016	0.183
H-mix	0.689	1.100	0.217
I-mix	0.832	0.772	0.191

(*) The selection variable used in constructing sample B-mix was d itself.

Table 2.8. Values of exponent, ϕ, and coefficient, ε, in $p=\varepsilon(2\mu-1)^{\phi}$, for mixed-magnitude test samples, obtained by least-square linear regression of log(p) over log(2μ-1); and values of the standard deviation about the regression line, in units of log(p).

Sample	ϕ	ε	*s. d.*
Topologically-random sample:			
0-mix	1.521	1.038	0.207
Type-1 samples:			
A-mix	1.515	1.021	0.201
B-mix	1.546	1.011	0.161
C-mix	1.510	1.023	0.192
D-mix	1.520	1.063	0.212
Type-2 samples:			
E-mix	1.242	2.255	0.072
F-mix	1.316	1.842	0.128
G-mix	1.410	1.410	0.174
H-mix	1.652	0.721	0.226
I-mix	1.803	0.476	0.199

Table 2.9. Mean and standard deviation of $\bar{p}/d$ and $\bar{p}^*/d$, for mixed-magnitude test samples.

Sample	$\bar{p}/d$		$\bar{p}^*/d$	
	mean	*s. d.*	*mean*	*s. d.*
Topologically-random sample:				
0-mix	0.539	0.057	0.509	0.052
Type-1 samples:				
A-mix	0.539	0.058	0.509	0.053
B-mix	0.532	0.055	0.507	0.052
C-mix	0.543	0.059	0.512	0.055
D-mix	0.536	0.055	0.508	0.051
Type-2 samples:				
E-mix	0.587	0.044	0.521	0.038
F-mix	0.566	0.051	0.514	0.045
G-mix	0.549	0.055	0.511	0.048
H-mix	0.529	0.054	0.508	0.050
I-mix	0.520	0.045	0.506	0.041

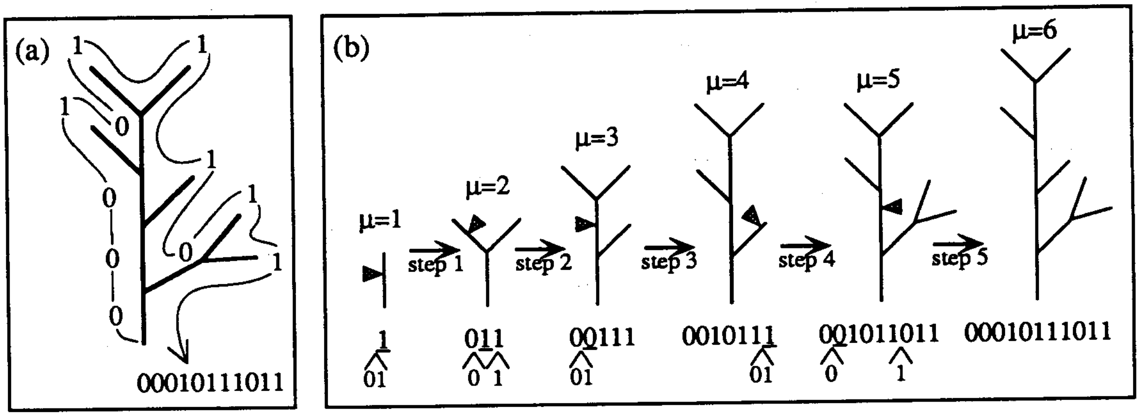

Figure 2.1. (**a**) Representation of a network's topology by a binary string, following Lukasiewicz's convention: interior and exterior links are represented by "0" and "1," respectively, and are listed in sequence starting with the root link and moving from left to right around the network. (**b**) Example sequence of five growth steps yielding the magnitude-six (μ=6) network in (a). The link chosen for branching, and the side (left or right) to which the new tributary link will be appended, is indicated by an arrow-head. The digit representing the link chosen is underlined in the binary string at the bottom, and the two new digits to be inserted are indicated.

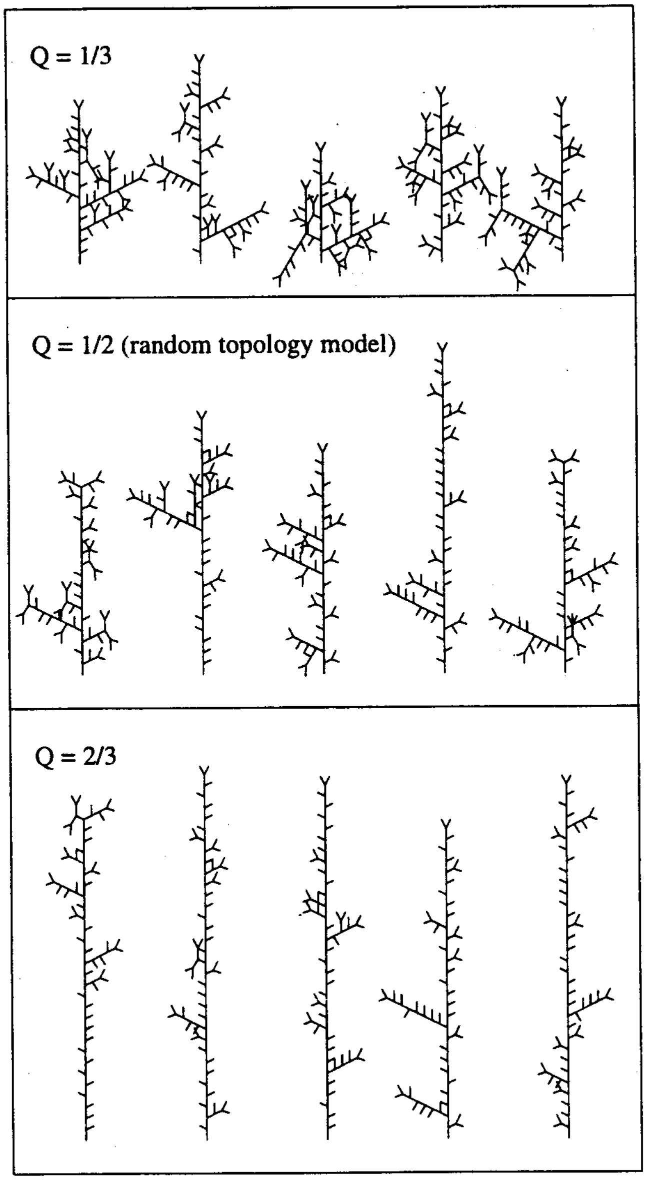

Figure 2.2. Five magnitude-50 networks drawn at random from test sample G (created with Q=1/3); test sample 0 (Q=1/2); and test sample H (Q=2/3). Five networks from each test sample suffice to illustrate network characteristics favored by different Q values.

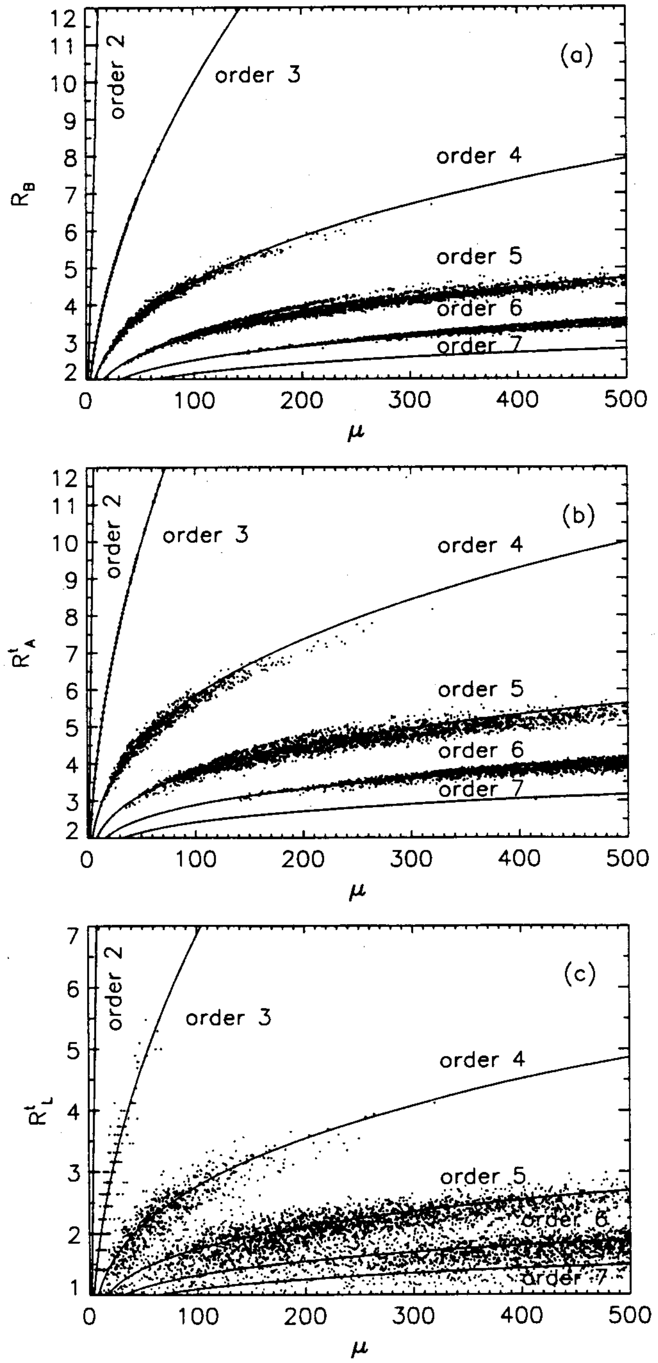

Figure 2.3. Topologic-analog Horton ratios plotted against network magnitude, μ, for topologically-random network sample 0-mix: **(a)** R_B; **(b)** R^t_A; **(c)** R^t_L. Curves are described by (2.4), (2.6), and (2.7) combined with (2.9), respectively. The most frequent order, $\Omega_M(\mu)$, is given by (2.5).

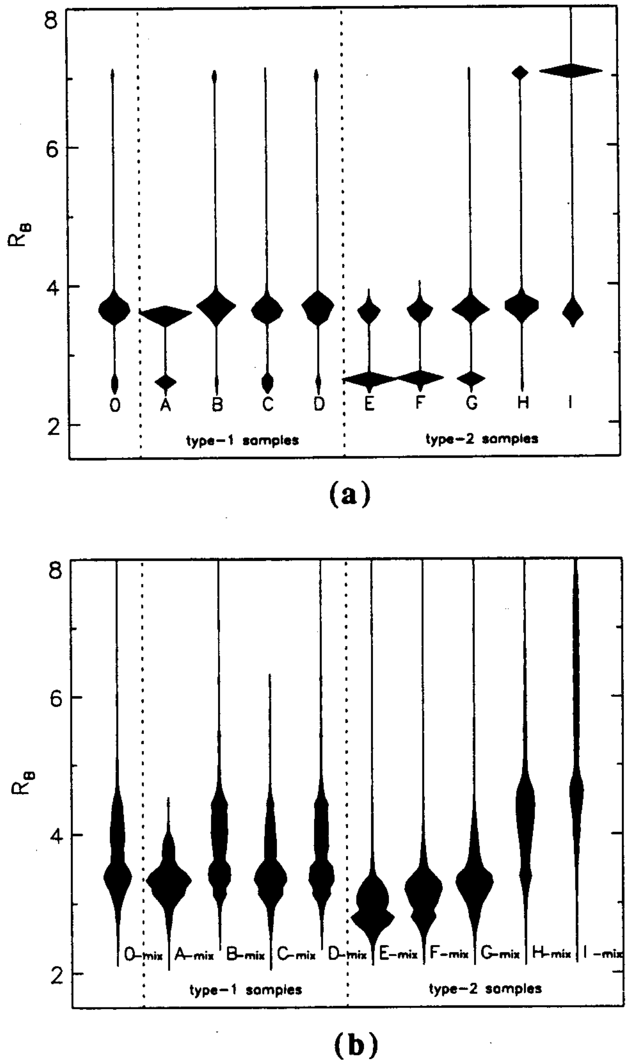

Figure 2.4. R_B distribution histograms for each test sample, using a bin size of 0.1. For each sample, the vertical reference axis extends from the minimum to maximum values observed, and the width about the axis is proportional to frequency. Where there is no thickness about the reference axis, there are no observed values. **(a)** magnitude-50 test samples; **(b)** mixed-magnitude test samples.

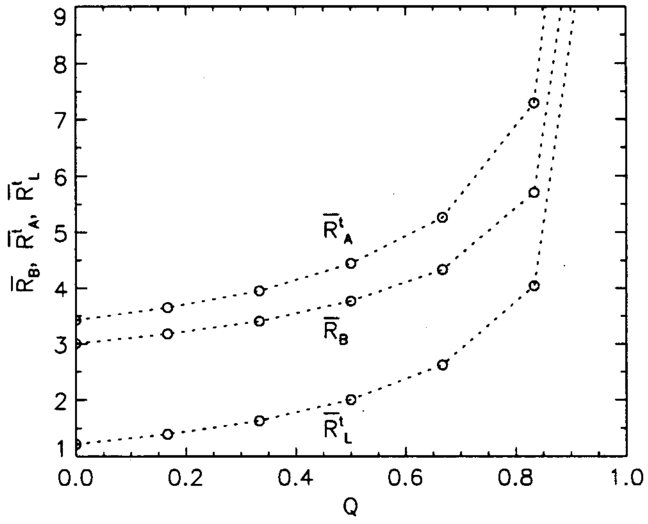

Figure 2.5. Mean values of the topologic-analog Horton ratios in mixed-magnitude test samples of type 2 and sample 0-mix, plotted against the respective Q parameter value: Q=0 (sample E-mix), Q=1/6 (F-mix), Q=1/3 (G-mix), Q=1/2 (0-mix), Q=2/3 (H-mix), and Q=5/6 (I-mix). For Q=1, only order-2 networks are created and, for the uniform mixture of magnitudes in [1, 500] used in our test samples, we have $\bar{R}_B$=252, $\bar{R}^t_A$=507, and $\bar{R}^t_L$=251. Curves were constructed by linear interpolation.

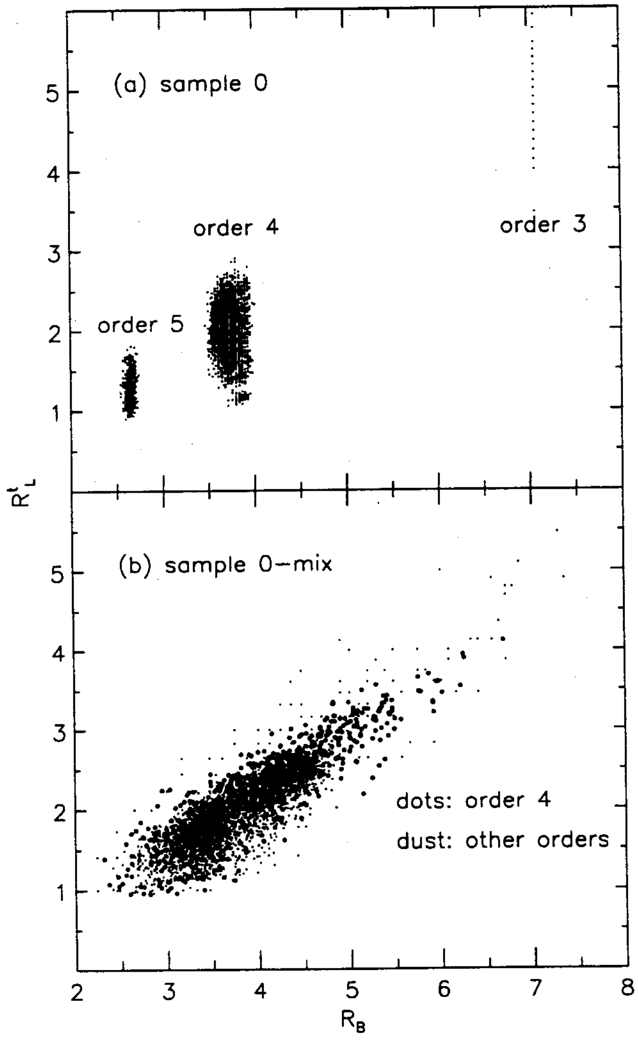

Figure 2.6. R^t_L plotted against R_B for each network in topologically-random test samples **(a)** 0 (μ=50) and **(b)** 0-mix ($1 \le \mu \le 500$).

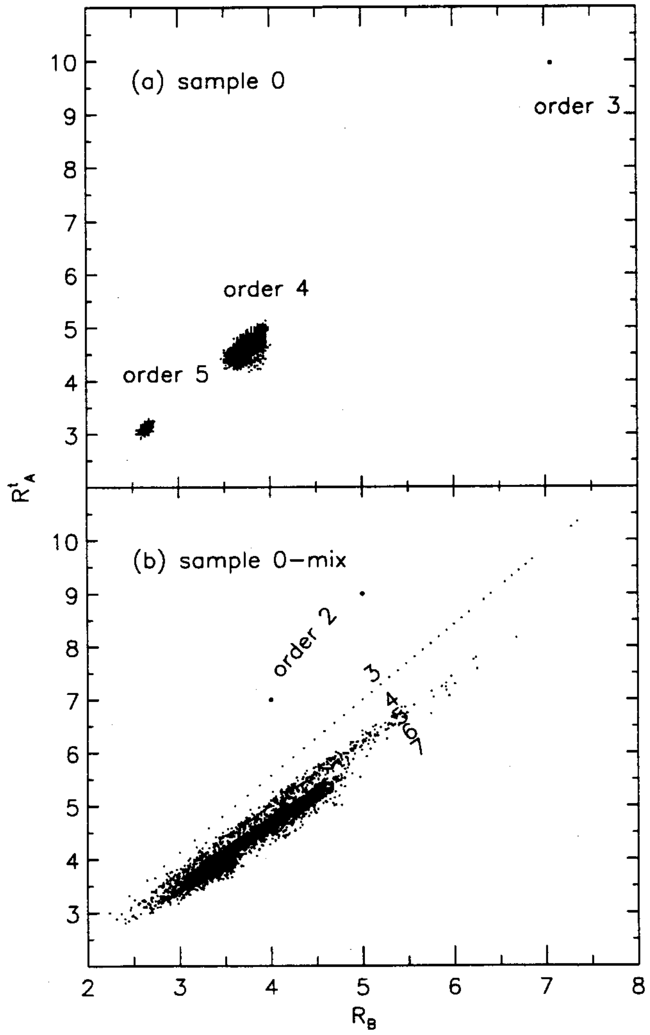

Figure 2.7. R^t_A plotted against R_B for each network in topologically-random test samples **(a)** 0 (μ=50) and **(b)** 0-mix ($1 \leq \mu \leq 500$). There is marked stratification by order in sample 0-mix.

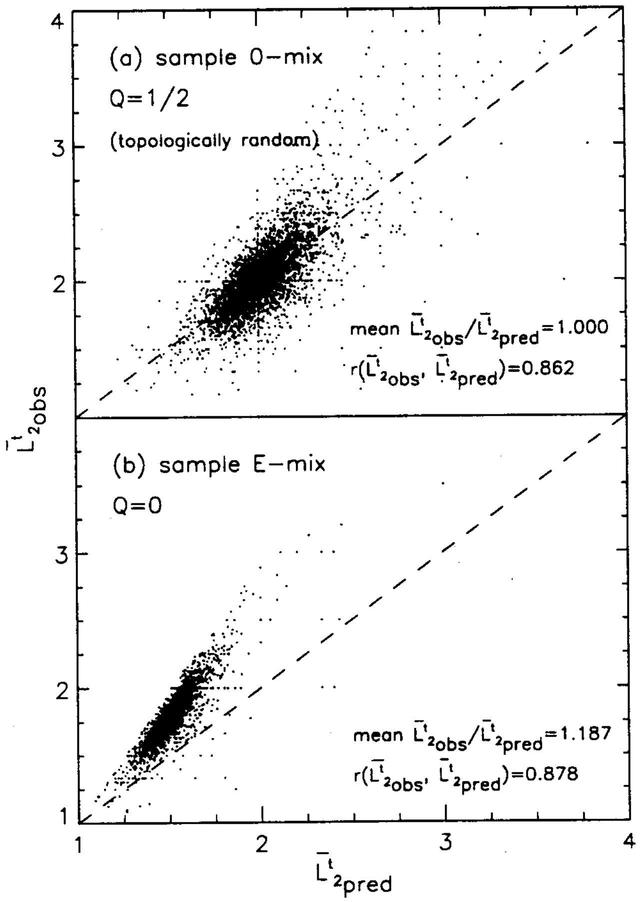

Figure 2.8. Average topologic length of second-order streams, $\bar{L}^t_{2_{obs}}$, plotted against RT model prediction, $\bar{L}^t_{2_{pred}}$, obtained from the stream number set using (2.8), for each network in samples **(a)** 0-mix and **(b)** E-mix.

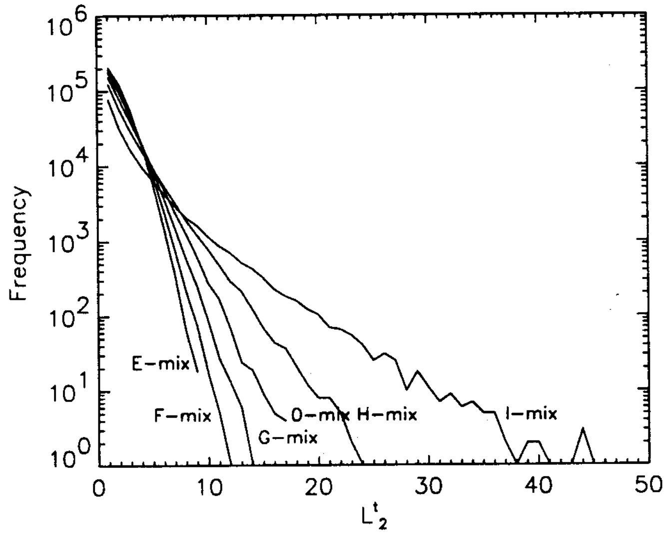

Figure 2.9. Frequency distribution of topologic length of second-order streams, L^t_2, for mixed-magnitude test samples of type 2.

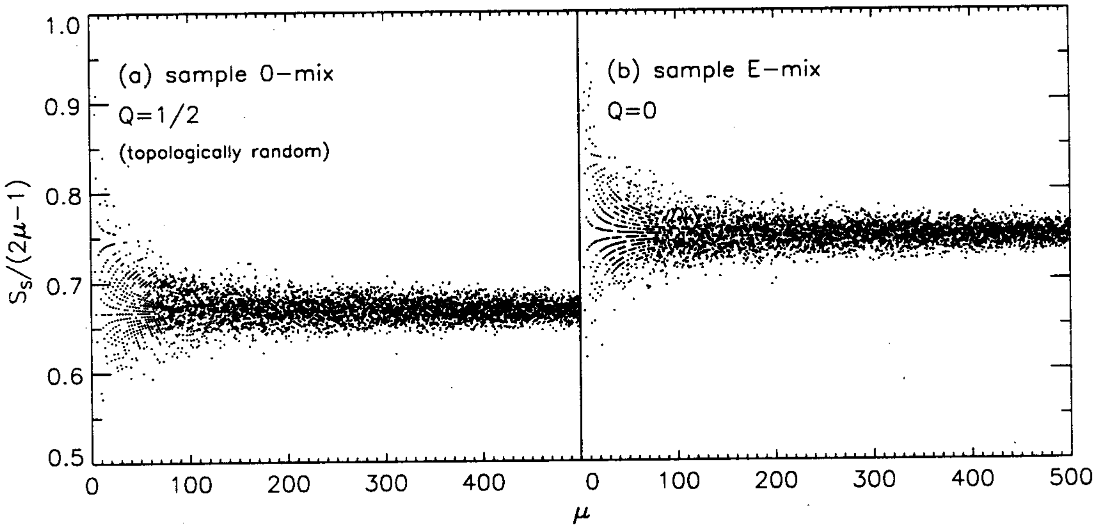

Figure 2.10. Number of streams, S_S, divided by number of links, 2μ-1, plotted against magnitude, μ, for test samples **(a)** 0-mix and **(b)** E-mix. For large μ, $S_S/(2\mu-1)$ is given by (2.14).

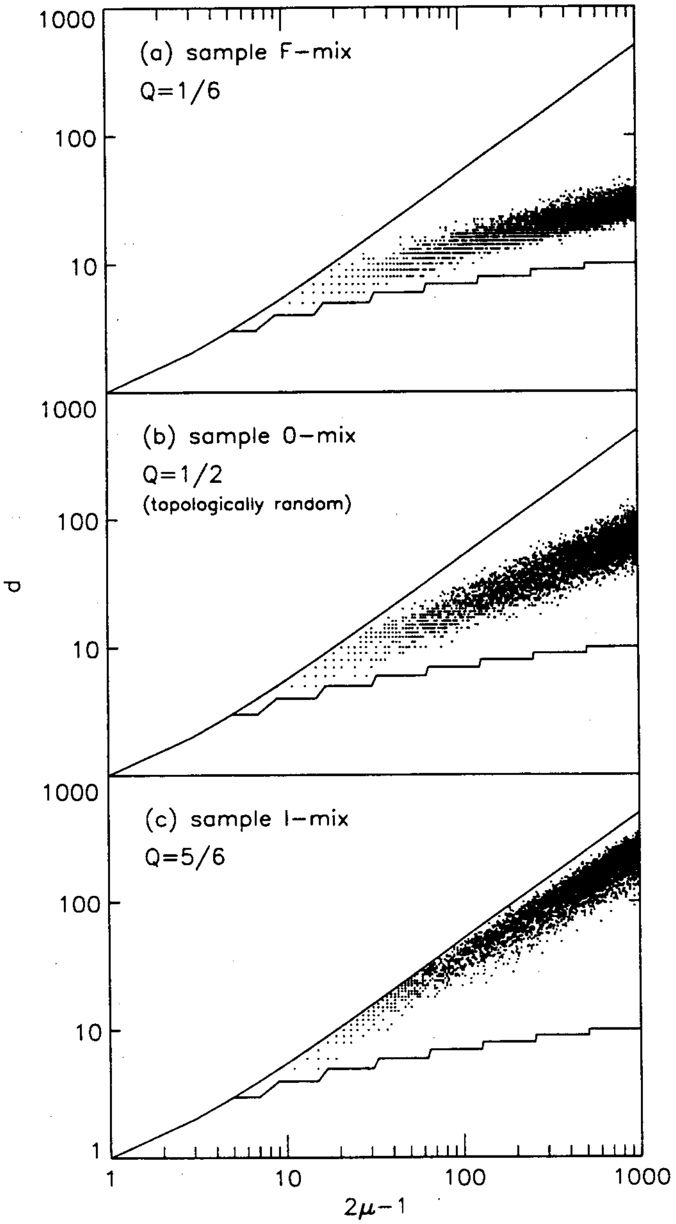

Figure 2.11. Diameter, d, plotted against number of links, 2μ-1, for samples **(a)** F-mix, **(b)** 0-mix, and **(c)** I-mix. Solid lines delineate zone of possible values.

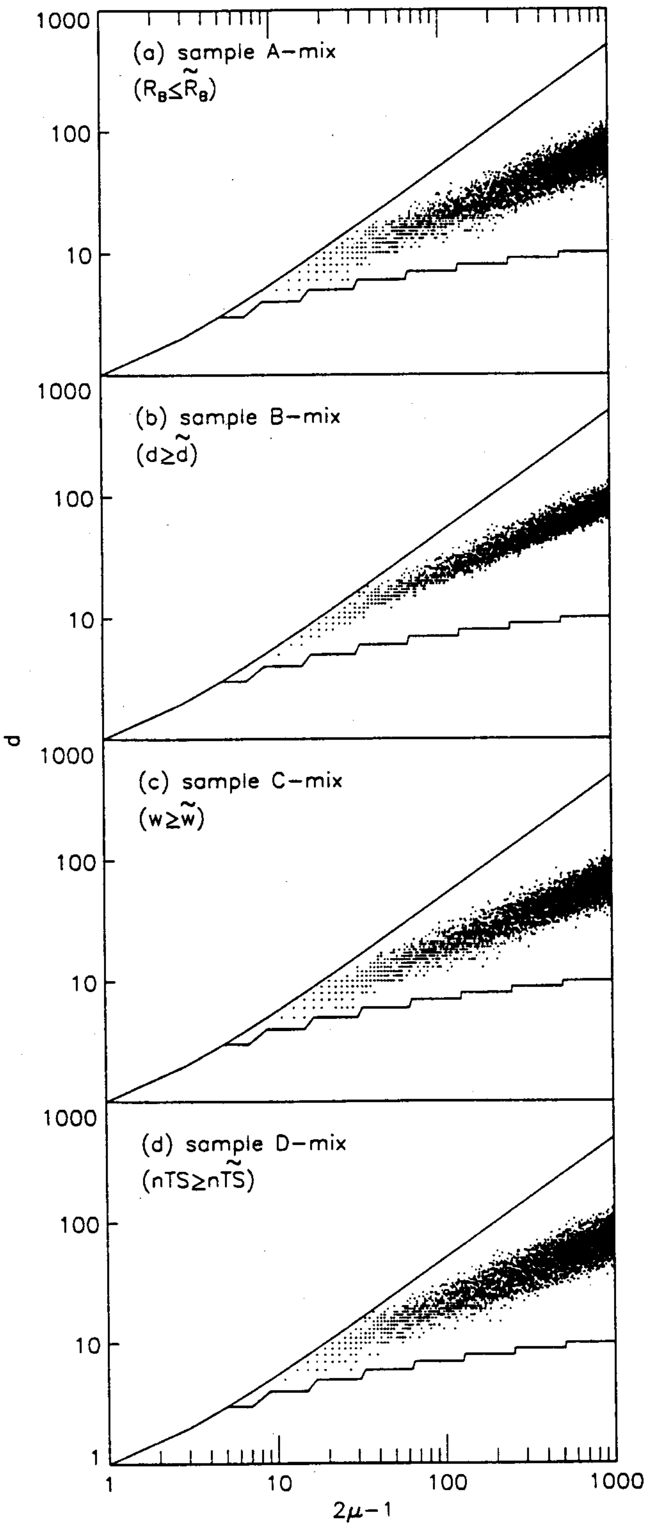

Figure 2.12. Diameter, d, plotted against number of links, 2μ-1, for samples of type-1: **(a)** A-mix, **(b)** B-mix, **(c)** C-mix, and **(d)** D-mix. The selection variable used to create sample B-mix was d itself. Solid lines delineate zone of possible values.

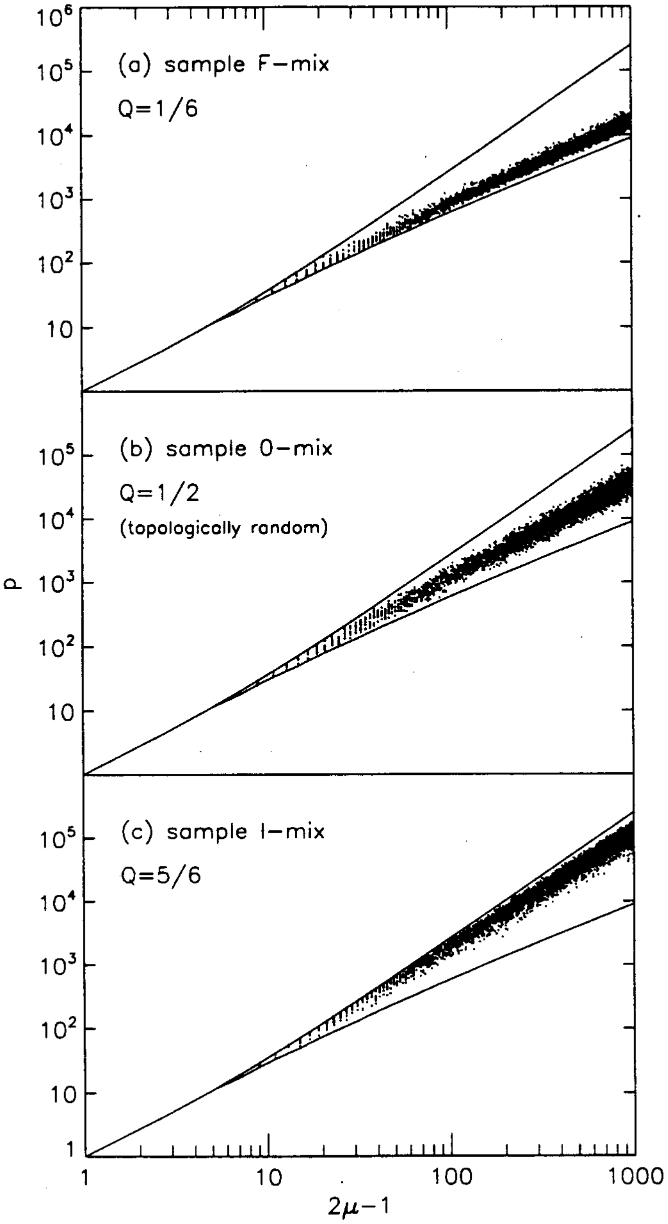

Figure 2.13. Total topologic path length, p, plotted against number of links, 2μ-1, for samples **(a)** F-mix, **(b)** 0-mix, and **(c)** I-mix. Solid lines delineate zone of possible values.

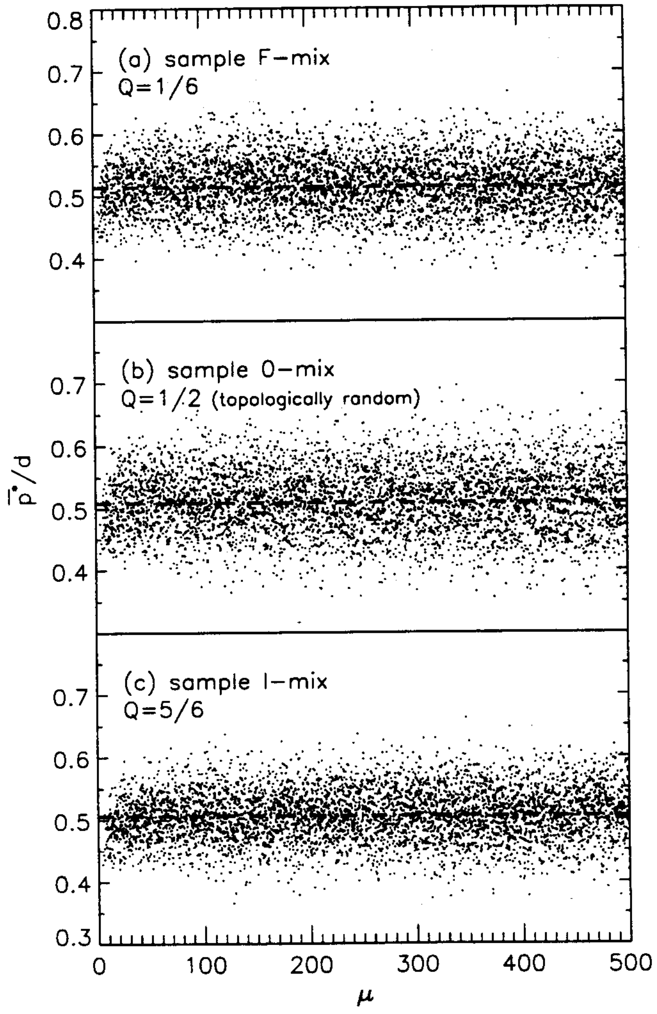

Figure 2.14. Ratio of mean modified total topologic length to diameter, $\bar{p}^*/d$, plotted against magnitude, μ, for each network in samples **(a)** F-mix, **(b)** 0-mix, and **(c)** I-mix. Dashed line represents the mean $\bar{p}^*/d$ value.

Chapter 3

Space Filling Networks

3.1 Introduction

The sample networks studied in Chapter 2 had no specified geometric properties, and were not required to be space filling. It was shown that, for such networks, the topologic analogs of properties I-VII (listed in Section 1.2.1) are sensitive to the parameter of the Q model of network growth. In this chapter, we create networks with specified geometric properties of drainage pattern, link lengths, and junction angles, and which fill a given drainage area, i.e., whose channels leave no undrained sub-areas, and maintain a minimum distance between them. Precise definitions of these terms are given in Section 3.2. The imposition of both geometric and space-filling requirements constrains network topology, that is, it precludes some TDCN. The sample networks created in this chapter will be used in Chapter 4 to investigate the sensitivity to the Q parameter of the topologic analogs of properties I-VII, and some additional topologic properties, under spatial constraints.

The Q model, described in Section 2.2, is not amenable to simulation of network growth under spatial constraints, as will be explained in Section 3.3. A topologically equivalent model, designated Q_E, is developed to generate networks under spatial constraints (Section 3.3). The Q_E model can operate in a topologic mode or in a space-filling mode. The Q and Q_E models are topologically equivalent because any TDCN is equally likely to be generated by either model for any given Q parameter value, in the absence of spatial constraints, i.e., when the Q_E model is operated in the topologic mode.

The Q_E model in the space-filling mode is used to create samples of space-filling networks, for a range of values of parameter Q (Section 3.4). Coefficients for the topologic analogs of properties I-VII will be computed for these network samples in Chapter 4.

All definitions presented in this chapter are novel, unless a literature reference is provided. These include definitions of terms and variables with no prior use in the field, as well as designations that are used here in a novel way.

3.2 Definitions

The geometric properties of the networks studied in this chapter are defined in Section 3.2.1. The terms "space-filling networks," "spatial constraints on network topology" and "random samples of space-filling networks" are defined in Section 3.2.2.

3.2.1 Network Geometry

The networks created in this chapter are required to have a well defined, idealized geometry. All links are straight lines and have unit length. The geometric properties of a network are its junction angle, α, and its drainage pattern, δ, defined next.

At any junction, two tributary links discharge into a receiving link. In the networks created in this chapter, the angle formed by the tributary links is the same at every junction, and is designated the junction angle, α. The drainage pattern, δ, is determined by the orientation of the tributary links relatively to their receiving link. The direction of the receiving link forms an angle α_1 with the tributary link to the left of the junction, and an angle α_2 with the tributary link to the right of the junction. The sum of angles α_1 and α_2 (designated the "semi-divide angles") equals α.

If α_1 and α_2 are equal, i.e., if junctions are shaped as symmetric "Y," the drainage pattern is "dendritic," and denoted by "δ=d" (Figure 3.1a). In "trellis" drainage patterns, denoted by "δ=t," some junctions have $\alpha_1=0$, and others have $\alpha_2=0$ (Figure 3.1b). According to the choice of $\alpha_1=0$ or $\alpha_2=0$ at each junction, trellis patterns may have different appearance. In the trellis patterns studied in this chapter, illustrated in Figure 3.1b, the following arbitrary rule is imposed. If the receiving link of the junction of interest forms a straight line with its own receiving link, then we have $\alpha_1=0$ or $\alpha_2=0$ at the junction of interest if we have $\alpha_2=0$ or $\alpha_1=0$ in the junction immediately downstream, respectively. If the receiving link of the junction of interest is at an angle with its own receiving link, then α_1 and α_2 at the junction of interest will be the same as at the junction immediately downstream.

The position and orientation of each link are described with reference to an orthogonal coordinate system by three variables: the spatial coordinates of the lower node, (x, y), and the orientation angle, β, formed by the directions of the link and the x axis, measured counter-clockwise from the positive x axis (Figure 3.2). The spatial coordinates of this link's tributary links are those of the junction node, (x', y'), and the orientation angles are β_1 for the tributary link to the left, and β_2 for the tributary to the right of the junction. Variables x', y', β_1, and β_2, are computed from α_1 and α_2, and from x, y, and β, from geometric considerations, as indicated in Figure 3.2.

3.2.2 Space-Filling Networks

A network is said to be space filling of an area $\mathcal{A}$ when the maximum distance between any point in $\mathcal{A}$ and the closest point on the network is not larger than a specified maximum, d_{max}, and when no two points on different network links are located at a distance shorter than a specified minimum, d_{min}, except at channel junctions.

Consider a specified drainage area, $\mathcal{A}$, and outlet link position, $\mathbf{O}$, defined by (x_0, y_0) and β_0, with (x_0, y_0) located on the boundary of $\mathcal{A}$, as shown in Figure 3.3. A network is said to be "space filling of $\mathcal{A}$ given $\mathbf{O}$ under δ and α" if, when all links are converted to straight lines of unit length, the outlet link is placed at position $\mathbf{O}$, and the network is assigned geometric properties δ and α, we have that: (i) every point in $\mathcal{A}$ is at a distance smaller than or equal to the specified maximum, d_{max}, from the closest point on the network; and (ii) the distance between each link and the link closest to it (excepting links joining it at a junction) is not smaller than the specified minimum, d_{min}, and no link intersects the boundary of $\mathcal{A}$. The distance between two links, X and Y, denoted d_{XY}, is defined as the smallest distance between a point in X and a point in Y (Figure 3.4). Figure 3.5 shows example space-filling and non-space-filling networks of $\mathcal{A}$ given $\mathbf{O}$ under particular geometric properties δ and α.

Space-filling requirements do not, on their own, preclude any network topologies. Any TDCN can be made space filling of $\mathcal{A}$ given $\mathbf{O}$, provided that its links are made sufficiently short or long and are shaped conveniently, and that its junction angles are chosen appropriately. When the space-filling requirement is combined with geometric requirements, such as those described in Section 3.2.1, some TDCN are precluded. For any given $\mathcal{A}$, $\mathbf{O}$, δ and α, only some TDCN are space filling. Other TDCN have links at too short a distance (smaller than d_{min}), or links that cross over each other, or leave sub-areas of $\mathcal{A}$ undrained (i.e., some points in $\mathcal{A}$ are at a distance larger than d_{max} from the closest point on the network), and are not space filling. These TDCN are precluded by the joint imposition of geometric and space-filling requirements, designated "spatial constraints."

Given a planform area $\mathcal{A}$ and a network outlet link location $\mathbf{O}$ (Section 3.2.2), there are in general multiple TDCN which, when their links are made to be straight lines of unit length and they are assigned geometric properties δ and α (Section 3.2.1), are space filling of $\mathcal{A}$. Figure 3.6 shows three different networks having δ=d and α=70° that are space filling of the drainage area $\mathcal{A}$ with the outlet link location $\mathbf{O}$ depicted in Figure 3.3b.

The set of all TDCN that are space-filling of $\mathcal{A}$ given $\mathbf{O}$ under δ and α, is denoted $S_{\mathcal{A},O,\delta,\alpha}$. A population of elements of $S_{\mathcal{A},O,\delta,\alpha}$ is said to be random if all elements of $S_{\mathcal{A},O,\delta,\alpha}$ occur with the same frequency in the population. A sample of elements of $S_{\mathcal{A},O,\delta,\alpha}$ is said to be random if the elements are drawn with replacement from a random population of $S_{\mathcal{A},O,\delta,\alpha}$.

3.3 The Q_E Model: A Topological Equivalent of the Q Model

The Q model of network growth, described in Section 2.2, involves sequential addition of tributary links to either exterior or interior links (Figure 2.1). Addition of tributary links to interior links is not amenable to creation of space-filling networks with pre-specified geometric properties, such as the networks illustrated in Figures 3.5a, 3.5c, and 3.6. When a new tributary link is appended to an interior link, this interior link is divided in two. If this interior link had length *l*, each of the two new interior links has a length less than *l*. If it is desired that all links have unit length, then the number of tributaries that a link will develop is established by the original length assigned to that link, which is an arbitrary decision. The three links that meet at the new node cannot form a symmetrical "Y" junction, because one of the tributary links will be aligned with the receiving link, and dendritic networks cannot be generated in this way.

For generation of space-filling networks with specified geometric properties, such as those described in Section 3.2.1, a model of network growth is needed which involves addition of tributaries only to exterior links. It is desired that this growth model be topologically equivalent to the Q model. Two growth models are said to be topologically equivalent if any TDCN is generated by both models with the same probability in the absence of spatial constraints, i.e., in a purely topologic mode of operation. A network growth model, designated Q_E, is introduced here which involves sequential branching of exterior links and is topologically equivalent to the Q model.

The Q_E model is described in Section 3.3.1. The expressions for computation of link branching probabilities are presented in Section 3.3.2. Sections 3.3.3 and 3.3.4 give example computations of link branching probabilities using these expressions, for the Q_E model in the topologic and space-filling modes of operation (defined in Section 3.3.1), respectively. The computer code of the Q_E model is described in Section 3.3.5.

3.3.1 Model Description

In the Q_E model, one exterior link branches at each growth step, becoming an interior link with two (new) exterior tributary links (Figure 3.7). We start with the root link and in the first growth step we add two tributary links to its upper node. The root link is said to "branch," and a network of magnitude 2 is produced. The root link thus becomes an interior link, and no more tributary links can be appended to it. In the second growth step, one of the two exterior links branches and a network of magnitude 3 is produced. In the third growth step, one of the three exterior links branches and a network of magnitude 4 is produced. A network of magnitude μ is attained after μ-1 growth steps.

At each growth step, the choice of which exterior link will branch is made stochastically, by comparison of a random variable to the branching probability assigned to each link. The branching probability of each link is determined by its topologic position in the network, as described in Section 3.3.2, and is a function of parameter Q.

The Q_E model has two "modes of operation:" a (purely) topologic mode, and a space-filling mode. In the topologic mode, no geometric variables are specified and there are no space-filling requirements. Link branching occurs without regard to network spatial layout and possible crossing of channels, or areas that remain undrained. This is the same mode in which the Q model operates (Chapter 2). Branching probabilities in the Q_E model (Section 3.3.2) are such that, in the topologic mode, the probability of any TDCN being generated by the Q_E and Q models is the same for given Q, and the two models are topologically equivalent.

In the space-filling mode, variables $\mathcal{A}$, $\mathbf{O}$, d_{min}, d_{max}, δ and α (defined in Sections 3.2.1 and 3.2.2) are specified. Network growth starts with the root link, positioned at $\mathbf{O}$, and proceeds in the same manner as in the topologic mode, described above, but with the following difference. If branching of a given link would result in one or two new links that violate spatial constraints (Section 3.2.2), the given link is not allowed to branch, and its branching probability is set to zero for all subsequent growth steps. This is further explained next.

When a link is chosen for branching, the spatial variables of its new tributary links are computed as indicated in Figure 3.2. These spatial variables are used to calculate the distance between each of these new links and any other link in the network, excepting each other and the branching link (Section 3.2.2), and to determine whether any of the new links crosses the boundary of $\mathcal{A}$. If the distance to the closest link is smaller than the specified minimum, d_{min}, or if one or both new links would cross the boundary of $\mathcal{A}$, these tributary links are not added. The link chosen is not allowed to branch, and its branching probability is permanently set to zero for all subsequent growth steps. Addition of tributaries to other links proceeds until addition of new tributary links to any exterior link would result in violation of spatial constraints. If no points in $\mathcal{A}$ are at a distance larger than d_{max} from the closest point on the network, then the network fills area $\mathcal{A}$.

3.3.2 Derivation of Link Branching Probabilities

Consider a network node, connecting a receiving link of magnitude μ and two tributary links, to the left and the right side of the node, having magnitudes a and b, respectively, where $a+b=\mu$. The magnitude of the receiving link, μ, is partitioned between its tributaries into a and b. The "partition" at this node is the pair of integers (a, b). Consider the partition at the node above a link of magnitude 6. This partition may be either (1, 5), (2, 4), (3, 3), (4, 2), or (5, 1). Partition (3, 3) is said to be "symmetric," while partitions (1, 5) and (5, 1) are the most "asymmetric" [e.g., *Van Pelt et al.,* 1992].

For fixed μ, the probability of a particular partition (a, b) depends on the growth model used to create the network. For the Q model, *Van Pelt and Verwer* [1985, Equations (18), (24), and (30)] derived expressions for the probability of partition (a, b) for given Q, denoted "p(a, b; Q)." These expressions can be combined as:

$$p(a, b; Q) = \prod_{i=2}^{a+b-1} \frac{1}{i-Q} \prod_{i=1}^{a-1} (i-Q) \prod_{i=1}^{b-1} (i-Q) \binom{a+b-2}{a-1} \left\{ 1+\frac{Q}{1-Q} \left(\frac{(a+b)(a+b-1)}{2ab} -1 \right) \right\} \quad \text{for } 0 \leq Q < 1 \qquad (3.1a)$$

$$p(a, b; 1) = \begin{cases} 0: & a \neq 1 \text{ and } b \neq 1 \\ \frac{1}{2}: & a=1 \text{ or } b=1 \end{cases} \quad \text{for } Q=1 \qquad (3.1b)$$

For Q=0, (3.1a) simplifies to:

$$p(a, b; 0) = \frac{1}{a+b-1} \qquad (3.2)$$

For Q=0, (3.2) gives the same probability for all partitions (a, b) for fixed μ ($\mu=a+b$), equal to the inverse of the number of partitions, a+b-1, or μ-1.

Given that branching probabilities in the Q model (Section 2.2.1) are independent of left or right tributary positioning, the probability of a partition (a, b) is equal to that of its left-right reverse, or mirror-image partition, (b, a), for any given Q:

$$p(a, b; Q) = p(b, a; Q) \tag{3.3}$$

Probabilities of symmetric partitions, i.e., where $b=a$ (if μ is even) or $b=a\pm1$ (if μ is odd), are higher for smaller Q values. Probabilities of strongly asymmetric partitions, such as $(1, \mu-1)$, are higher for larger Q values. For $Q=1$, from (3.1b), the only partitions that can occur are $(1, \mu-1)$ and $(\mu-1, 1)$, and the network has Strahler order 2.

Consider the outlet (or root) link of a network and its two tributary sub-networks. Let a and b be the magnitudes of the sub-networks on the left and right-hand sides of the outlet link, respectively. At each growth step of the Q_E model, an exterior link branches, and the magnitude of the network increases by one unit. If branching occurs somewhere in the sub-network on the left-hand side of the node, an event denoted "L," the original partition (a, b) changes to (a+1, b). If the branching occurs somewhere in the sub-network on the right-hand side, an event designated "R," the original partition changes to (a, b+1). The probabilities of events L and R, denoted $p(L| a, b; Q)$ and $p(R| a, b; Q)$, respectively, are designated the "partition-change probabilities." Either event L or R will occur at each growth step, i.e., their probabilities add to unity:

$$p(L| a, b; Q) + p(R| a, b; Q) = 1 \tag{3.4}$$

Because branching probabilities in the Q model do not depend on left or right tributary positioning, two mirror-image events, $(L| a, b)$ and $(R| b, a)$, have equal probability, for any given Q:

$$p(L| \, a, b; Q) = p(R| \, b, a; Q) \tag{3.5}$$

For any given Q (except Q=1), a partition (a, b) may have resulted from either event (L| a-1, b; Q) or (R| a, b-1; Q). Therefore, the probability of a partition (a, b) of magnitude μ (i.e., $a+b=\mu$), may be written as a function of partition probabilities and partition-change probabilities of magnitude μ-1:

$$p(a, b; Q) = p(L| \, a-1, b; Q) \, p(a-1, b; Q) + p(R| \, a, b-1; Q) \, p(a, b-1; Q) \tag{3.6}$$

Appendix B presents the derivation of expressions (3.7), from (3.6), using (3.3), (3.4), and (3.5).

$$p(L| \, 1, b; 1) = \begin{cases} 0: & b>1 \\ \frac{1}{2}: & b=1 \end{cases} \qquad \text{for } Q=1 \tag{3.7a}$$

$$p(L| \, a, b; Q) = \frac{1}{2} \qquad \text{for } a=b, \ 0 \leq Q < 1 \tag{3.7b}$$

$$p(L| \, a, b; Q) = \frac{1}{p(a, b; Q)} \left\{ (-1)^{|b-a|-1} \frac{1}{2} p(m, m; Q) - \sum_{i=1}^{|b-a|-1} (-1)^i \, p(a+\Delta a, b+\Delta b; Q) \right\}$$

$$\text{for } a \neq b, \ 0 \leq Q < 1 \tag{3.7c}$$

where:

$$m = \text{even}(b-a) \frac{a+b}{2} + \text{odd}(b-a) \frac{a+b+1}{2} \tag{3.7d}$$

$$\Delta a = \text{even}(i) \frac{i}{2} + \text{odd}(i) \frac{i+1}{2} \tag{3.7e}$$

$$\Delta b = -\, \text{even}(i) \frac{i}{2} - \text{odd}(i) \frac{i-1}{2} \tag{3.7f}$$

$$\text{even}(i) = \frac{1+(-1)^i}{2} = \begin{cases} 1: & i \text{ even} \\ 0: & i \text{ odd} \end{cases} \tag{3.7g}$$

$$\text{odd}(i) = 1\text{-even}(i) = \begin{cases} 0: i \text{ even} \\ 1: i \text{ odd} \end{cases} \qquad (3.7h)$$

For Q=1, it follows from (3.7a) that the only partitions that can occur are (1, b) and (a, 1), in agreement with (3.1b). Partition probabilities in (3.7c) are computed from (3.1).

In the Q_E model, a branching event results in change of the partition at each node located along the path from the branching link to the root link. At each of these nodes, the branching event will represent either an L or an R event. *Van Pelt and Verwer* [1984] showed that, in sequential growth models where branching probabilities do not depend on the topologic distance to the root (the topologic path length), the partitions at the various network nodes are independent. The Q and Q_E models meet this criterion. Therefore, the branching probability of a given link is given by the product of the probabilities of the corresponding L and R events at each of the affected nodes. These probabilities are computed from (3.7), combined with (3.4), (3.5) and (3.6).

An alternative and equivalent algorithm for the Q_E model treats the network as a decision tree. Starting at the junction at the upper node of the root link (the "first node"), a choice is made between the sub-tree to the left and to the right of the node, according to the partition change probabilities p(L| a, b; Q) and p(R| a, b; Q). We step to the first node of the chosen sub-tree and repeat the process. When an exterior link is reached, that link is chosen for branching. The probability of a given link being chosen for branching by this process equals the product of the corresponding partition change probabilities at each of the nodes visited, the same as in the algorithm presently described and that is used in this chapter.

Computation of branching probabilities in the Q_E model is illustrated below by four examples. Section 3.3.3 gives two examples for the topologic mode, and Section

3.3.4 gives two examples for the space-filling mode. All four examples use Q=1/2. Similar computations apply for any value of Q.

3.3.3 Example Computations of Link Branching Probabilities: Topologic Mode

This section presents two examples of computations of link branching probabilities for the Q_E model, in its topologic mode of operation. Example 1 (Section 3.3.3.1) presents detailed computations for a step in the growth of a network. Example 2 (Section 3.3.3.2) demonstrates how a topologically-random sample of TDCN is obtained by the Q_E model using Q=1/2.

3.3.3.1 Example 1

Consider the network of magnitude 8 depicted in Figure 3.8a. Its 8 exterior links are labelled A through H, and its nodes are numbered 1 through 7. We are to compute the branching probabilities for the Q_E model, for each of links A through H. These probabilities depend on Q, and are denoted p(A; Q) through p(H; Q). Choice of which of the eight exterior links will branch at the next growth step, yielding a network of magnitude 9, will be made by comparison of a random variable with the eight link branching probabilities.

Consider the branching probability of link H, p(H; Q) (Figure 3.8b). If link H is chosen for branching, the partitions of nodes 1 and 7, will be changed. The partition of node 1 will change from (6, 2) to (6, 3) (an R event), and the partition of node 7 will change from (1, 1) to (1, 2) (also an R event). The value of p(H; Q) is given by the product of the corresponding partition-change probabilities for nodes 1 and 7:

$$p(H; Q) = p(R \mid 6, 2; Q)\, p(R \mid 1, 1; Q) \tag{3.8}$$

Because (3.7) was written for L events, and for partitions (a, b) where $a \leq b$, to use (3.7) we must first write (3.8) as a function of L events with $a \leq b$, using (3.5):

$$p(H; Q) = p(L \mid 2, 6; Q)\, p(L \mid 1, 1; Q) \tag{3.9}$$

We can now use (3.7) to compute the partition-change probabilities in (3.9). For Q=1/2:

$$\begin{aligned} p(H; 1/2) &= p(L \mid 2, 6; 1/2)\, p(L \mid 1, 1; 1/2) \\ &= 0.7310 \times 0.5000 \\ &= 0.3655 \end{aligned} \tag{3.10}$$

Consider now the branching probability of link D (Figure 3.8c). If link D branches, five nodes, 1, 2, 3, 5, and 6, will experience a change in partition (Figure 3.8c), and we have:

$$p(D; Q) = p(L \mid 6, 2; Q)\, p(R \mid 1, 5; Q)\, p(R \mid 2, 3; Q)\, p(L \mid 2, 1; Q)\, p(L \mid 1, 1; Q) \tag{3.11}$$

To apply (3.7), the partition change probabilities in (3.11) must be written as functions of (L| a, b) partition change probabilities, with $a \leq b$. First using (3.4) and (3.5), then using (3.7), we obtain, for Q=1/2:

$$\begin{aligned} p(D; 1/2) = {} & p(L \mid 6, 2; 1/2)\, p(R \mid 1, 5; 1/2)\, p(R \mid 2, 3; 1/2)\, p(L \mid 2, 1; 1/2) \\ & p(L \mid 1, 1; 1/2) \end{aligned}$$

$$= [1 - p(L| 2, 6; 1/2)]\,[1 - p(L| 1, 5; 1/2)]\,[1 - p(L| 2, 3; 1/2)]$$

$$[1 - p(L| 1, 2; 1/2)]\,p(L| 1, 1; 1/2)$$

$$= 0.2690 \times 0.8994 \times 0.6667 \times 0.8000 \times 0.5000$$

$$= 0.0645 \tag{3.12}$$

Similar computations yield the branching probabilities for all exterior links, A through H, for Q=1/2:

$$p(A; 1/2) = 0.0271 \tag{3.13a}$$

$$p(B; 1/2) = 0.0403 \tag{3.13b}$$

$$p(C; 1/2) = 0.0403 \tag{3.13c}$$

$$p(D; 1/2) = 0.0645 \tag{3.13d}$$

$$p(E; 1/2) = 0.0645 \tag{3.13e}$$

$$p(F; 1/2) = 0.0323 \tag{3.13f}$$

$$p(G; 1/2) = 0.3655 \tag{3.13g}$$

$$p(H; 1/2) = 0.3655 \tag{3.13h}$$

The sum of (3.13a through h) equals unity. With Q=1/2, the next branching event is most likely to occur in link G or H, and least likely to occur in link A.

For Q=0, (3.2) indicates that all partitions of given μ have equal probability. From (3.7), this results in all exterior links having equal branching probability. For Q=0, each exterior link of the network in Figure 3.8a has a branching probability of 1/8. This growth model is designated "terminal growth" (Section 2.2). For Q=0, the Q and Q_E models are not just topologically equivalent, but are the same.

3.3.3.2 Example 2

Consider growth of a network by the Q_E model in its topologic mode, with Q=1/2. The network starts with its outlet link, which branches at the first growth step. At the second growth step, one of the two exterior links branches and a network of magnitude 3 is formed. At the third growth step, one of the three exterior links branches and a network of magnitude 4 is formed. The process continues until the desired network magnitude is attained. The branching probability of each exterior link at any time step is computed as illustrated in example 1 (Section 3.3.3.1).

In the topologic mode of the Q_E model, parameter value Q=1/2 draws networks with replacement from a topologically-random population, and is a causative model of topologic randomness (Section 2.2.1). As we generate an increasing number of networks of given magnitude μ, using Q=1/2, the frequency of each TDCN in the sample approches $1/N(\mu)$, where $N(\mu)$ is the number of TDCN of magnitude μ.

The present example illustrates the generation of a topologically-random sample of magnitude-6 networks from a topologically-random sample of magnitude-5 networks, by the Q_E model in its topologic mode. This example demonstrates that, if each TDCN of magnitude 5 has an expected frequency of 1/N(5), or 1/14, then all TDCN of magnitude 6 grown with Q=1/2 have an expected frequency equal to 1/N(6), or 1/42.

Figure 3.9 depicts the 14 TDCN of magnitude 5, numbered i through xiv, in the first matrix column. Any of the 5 exterior links of a magnitude-5 network may branch. Branching of one exterior link or another will generate different TDCN of magnitude 6, so that a magnitude-5 network can generate any of 5 magnitude-6 TDCN, depicted on the corresponding matrix row in Figure 3.9. Each magnitude-5 TDCN in Figure 3.9 is the "parent" of the five magnitude-6 TDCN in the same matrix row. For example, TDCN #i is the parent of TDCN #1 through 5.

There are N(6)=42 TDCN of magnitude 6, and the entries in Figure 3.9 are numbered 1 through 42 (by order of entry) on the upper left-hand corner of the corresponding matrix box. The total number of entries in Figure 3.9 is 14x5=70, as some of the 42 TDCN have multiple entries, i.e., they can be obtained from 2 or more magnitude-5 TDCN. For example, TDCN #1 may result from branching of either TDCN #i or xi. TDCN #37 may result from branching of either TDCN #ix, xi, or xii. The expected frequency of each branching event is indicated on the lower right-hand box corner. This frequency is obtained by multiplying the frequency of the parent TDCN of magnitude 5, equal to 1/14, by the corresponding link branching probability. Consider, for example, the branching of TDCN #i that results in TDCN #1. The probability of this branching event, denoted p(1| i; 1/2), is obtained from (3.7) as follows:

$$\begin{aligned} p(1|\, i;\, 1/2) &= p(L|\, 1, 4;\, 1/2) \\ &= \frac{1}{15} \end{aligned} \tag{3.14}$$

The product (1/15)x(1/14) yields a frequency 1/210 for this branching event. Consider now the branching of TDCN #xi that results in the same TDCN #1. This branching event has probability p(1| xi; 1/2), given by (using (3.4), (3.5) and (3.7)):

$$\begin{aligned} p(1|\, xi;\, 1/2) &= p(R|\, 2, 3;\, 1/2)\, p(R|\, 1, 2;\, 1/2)\, p(R|\, 1, 1;\, 1/2) \\ &= [1 - p(L|\, 2, 3;\, 1/2)]\, [1 - p(L|\, 1, 2;\, 1/2)]\, p(L|\, 1, 1;\, 1/2) \\ &= \frac{4}{15} \end{aligned} \tag{3.15}$$

The product (4/15)x(1/14) yields a frequency 2/105 for this branching event. The frequency of TDCN #1 is given by the sum of the frequencies of events (1|i) and (1|xi), equal to (1/210)+(2/105), or 1/42. It may be confirmed that all 42 TDCN in Figure 3.9 have the same frequency, 1/42.

3.3.4 Example Computations of Link Branching Probabilities: Space-Filling Mode

This section presents two examples of computations of link branching probabilities for the Q_E model, in its space-filling mode of operation. Example 3 (Section 3.3.4.1) presents detailed computations for a step in the growth of a network. Example 4 (Section 3.3.4.2) shows that Q=1/2 in the space-filling mode does not generate random samples of space-filling networks, as defined in Section 3.2.2.

3.3.4.1 Example 3

In this example, the branching probabilities are computed for the Q_E model, used in the space-filling mode, for the magnitude-8 network depicted in Figure 3.10, given $\mathcal{A}$, **O**, δ and α. In Section 3.3.3, these probabilities were computed for the topologic mode, for a topologically identical network (Figure 3.8). The network in Figure 3.10 has geometric properties δ=d and α=90° (defined in Section 3.2.1). Its outlet link is placed at location **O**, and all links have unit length. Tributary links are to be added to an exterior link of this network by the Q_E model at the next growth step. Addition of tributaries to links B, C, D, E or G is precluded, as they would result in violation of spatial constraints. These links are said to be "blocked," and are assigned zero branching probability. Addition of tributaries to links A, F or H would not result in violation of spatial constraints.

Branching probabilities in the space-filling mode are denoted $p^*(A; Q)$ through $p^*(H; Q)$. If no exterior links were blocked, branching probabilities $p^*(A; Q)$ through

$p^*(H; Q)$ in the space-filling mode would be equal to their counterparts $p(A; Q)$ through $p(H; Q)$ in the topologic mode. When one or more exterior link is blocked, the corresponding starred probabilities equal zero, and the positive branching probabilities must add to unity. In this example, we have:

$$p^*(A; Q) + p^*(F; Q) + p^*(H; Q) = 1 \tag{3.16}$$

Space-filling mode (SM) branching probabilities are obtained by setting the ratio between any two SM probabilities equal to their topologic-mode (TM) counterparts:

$$\frac{p^*(A; Q)}{p^*(F; Q)} = \frac{p(A; Q)}{p(F; Q)} \tag{3.17a}$$

$$\frac{p^*(F; Q)}{p^*(H; Q)} = \frac{p(F; Q)}{p(H; Q)} \tag{3.17b}$$

$$\frac{p^*(A; Q)}{p^*(H; Q)} = \frac{p(A; Q)}{p(H; Q)} \tag{3.17a}$$

Combining (3.16) and (3.17), yields:

$$p^*(A; Q) = \frac{p(A; Q)}{p(A; Q) + p(F; Q) + p(H; Q)} \tag{3.18a}$$

$$p^*(F; Q) = \frac{p(F; Q)}{p(A; Q) + p(F; Q) + p(H; Q)} \tag{3.18b}$$

$$p^*(H; Q) = \frac{p(H; Q)}{p(A; Q) + p(F; Q) + p(H; Q)} \tag{3.18c}$$

As in (3.18), all SM branching probabilities are obtained from their TM counterparts by normalization. For Q=1/2, (3.18a, b, and c) are computed by substitution of (3.13a, f, and h). The SM branching probabilities for Q=1/2 are:

$$p^*(A; Q) = 0.0638 \tag{3.19a}$$

$$p^*(B; Q) = 0. \tag{3.19b}$$

$$p^*(C; Q) = 0. \tag{3.19c}$$

$$p^*(D; Q) = 0. \tag{3.19d}$$

$$p^*(E; Q) = 0. \tag{3.19e}$$

$$p^*(F; Q) = 0.0760 \tag{3.19f}$$

$$p^*(G; Q) = 0. \tag{3.19g}$$

$$p^*(H; Q) = 0.8602 \tag{3.19h}$$

The sum of (3.19a through h) equals unity. It is most likely that link H will branch at the next time step. The SM probabilities in (3.19) differ greatly from the TM probabilities in (3.13), computed for a topologically identical network.

3.3.4.2 Example 4

Consider growth of a network by the Q_E model used in the space-filling mode, with Q=1/2. The network's geometric requirements are δ=d and α=90°, and all links have unit length. With these geometric properties, all TDCN of magnitude 5 or smaller respect the requirement that no two links (except links that join at a junction) be at a distance smaller than d_{min}=1.

For magnitude 6, under δ=d and α=90°, all TDCN except for one, numbered 42 in Figure 3.9, respect the minimum distance requirement for a small enough $d_{min}>0$. Under δ=d and α=90°, and for any value of α under δ=d, TDCN #42 has two links (that are not joined at a junction) that meet at a point (Figure 3.11a). Therefore, under δ=d, this TDCN does not meet the minimum distance requirement for any $d_{min}>0$. Regardless of the specified $\mathcal{A}$, $\mathbf{O}$, d_{min} and d_{max}, TDCN #42 always violates spatial constraints under

δ=d, and is precluded in the space-filling mode of the Q_E model. However, under δ=t, TDCN #42 does not violate the minimum distance requirement for small enough $d_{min}>0$. For example, under δ=t and $\alpha=90°$, this TDCN does not violate this requirement with $d_{min}=1$, as shown in Figure 3.11b.

Figure 3.12 represents all branching events leading from a magnitude-5 network to a magnitude-6 network, and the corresponding expected event frequencies in the space-filling mode of the Q_E model, with δ=d and $\alpha=90°$, assuming that only TDCN #42 is precluded. However, depending on $\mathcal{A}$, $\mathcal{O}$, d_{min} and d_{max}, other TDCN may also violate spatial constraints under δ=d and $\alpha=90°$. The TDCN are depicted in the figure without these geometric properties, for easier visualization and for comparison with Figure 3.9. Frequencies given in Figure 3.12 were computed in the same manner illustrated in example 3 (Section 3.3.4.1). These frequencies can be compared to those computed for the topologic mode (Section 3.3.3.2), given in Figure 3.9. The only differences arise in rows 12 (branching of TDCN #xii) and 14 (branching of TDCN #xiv). In these rows, the frequency of TDCN #42 is zero for the space-filling mode, as it violates spatial constraints (Figure 3.11a). The frequencies of the remainder branching events on these rows are higher than in the topologic mode (Figure 3.9). The sum of expected frequencies in each row equals 1/14, the frequency of each magnitude-5 TDCN in a topologically-random population.

In this example, there are 41 space-filling TDCN of magnitude 6, but they do not all have equal expected frequency, 1/41. For example, TDCN #37 has an expected frequency equal to 19/525, or 0.0362 (given by the sum of 1/105 from row 11 and 2/175 from row 12), greater than 1/41, or 0.0244. Most TDCN have an expected frequency of 1/42, while the TDCN on rows 12 and 14 (such as TDCN #37, above), have an expected frequency in excess of 1/41.

This example demonstrates that in the space-filling mode, Q=1/2 does not yield all space-filling TDCN of magnitude 6 (and higher) with the same likelihood. Therefore, Q=1/2 does not produce random samples of space-filling networks (defined in Section 3.2.2). Recall that, in the topologic mode, Q=1/2 yields topologically random samples of TDCN, as illustrated in example 2 (Section 3.3.3.2).

3.3.5 Computer Code

A computer code was written in Fortran which simulates network growth by the Q_E model. Networks are represented as binary strings, following Lukasiewicz's convention (Figure 2.1a). Growth of a network of magnitude μ starts with one initial link and requires a number μ-1 of sequential branching events, or growth steps (Section 3.3.1, Figure 3.7). Only exterior links may branch. At each growth step, a subroutine named "PROBABILITIES" computes the branching probability of each exterior link in the network, using (3.4), (3.5) and (3.7). Similar computations were presented in Sections 3.3.3 and 3.3.4 for the topologic and space-filling modes of operation, respectively. A subroutine named "RANDOM" selects a random number in [0, 1], and a subroutine named "CHOOSE" chooses which link will branch by comparison of this random number to the cummulative distribution of link branching probabilities.

In the topologic mode of operation, two new tributary links are appended to the link chosen for branching. In the space-filling mode of operation, these tributary links are added only if violation of spatial constraints does not result. A subroutine named "TEST_DMIN" computes the distance between each new tributary link and each other link in the network (excepting the branching link) and determines whether the new link would be at a distance smaller than d_{min} from another network link. If this spatial constraint is violated, then the new links are not added, and the branching probability of the chosen link is set to zero for all subsequent growth steps. The link is said to have been "blocked." If the above constraint is not violated, a subroutine named "TEST_BOUNDARIES" determines whether any of the new tributary links crosses the boundary line of drainage area $\mathcal{A}$. In this case, the chosen link is not allowed to branch, and is blocked.

If neither of the two spatial constraints above is violated, then two new tributary links are appended to the chosen link, according to geometric properties δ and α. A subroutine named "GEOMETRY" computes the spatial coordinates and orientation angle for the new links, as described in Figure 3.2. A subroutine named "ADD_LINKS" updates the binary string that defines the network, as described in Figure 3.7. The digit "1" representing the branching link in the binary string is changed to "0," because addition of the two tributary links makes the branching link become interior. Following this digit "0," two digits "1" are added to the binary string, representing the two new tributary links.

Network growth proceeds until all exterior links have been blocked. The final network may then fill the entire drainage area, $\mathcal{A}$. In some cases, there will be sub-areas which remain undrained. A subroutine named "TEST_DMAX" determines whether there are any points within drainage area $\mathcal{A}$ which are located at a distance greater than d_{max} from the closest point on the network. If this spatial constraint is not violated, the network is space-filling. If this constraint is violated, the entire network is discarded and a new program run is performed. An example of a non-space-filling network to which no more links may be added is given in Figure 3.13. Such networks occur rarely, except for low α and high Q values.

3.4 Test Network Samples

Test samples of space-filling networks were generated with the Q_E model using various Q values, and for different δ and α. All networks fill a square area, $\mathcal{A}$, of side measuring 50 length units, and have outlet link location, **O**, defined by $(x_0, y_0)=(0, 0)$ and $\beta_0=45^\circ$. $\mathcal{A}$ and **O** are represented in Figure 3.3c. Two examples of space-filling networks for this $\mathcal{A}$ and **O** are depicted in Figure 3.5a and c.

Due to the number of computations involved, computer generation of each space-filling network is time consuming. For smaller α, the network magnitude required to fill $\mathcal{A}$ is larger, and computer runs take considerably longer. For this reason, each test sample contains only one network. The influence of network magnitude on the various topologic variables is studied by considering all sub-networks of the complete network. Each network link is the outlet of a sub-network, and in a complete network of magnitude μ, sub-networks cover the range of magnitudes $[1, \mu]$, with μ-1 sub-networks having magnitude 2 or higher.

Test samples are denoted "(δ, α, Q)." For example, a dendritic network with junction angles 50° that was generated using Q=2/3 is denoted "(d, 50°, 2/3)," and a trellis network with junction angles 90° that was generated using Q=1/2, is designated "(t, 90°, 1/2)." Q parameter values are sampled at intervals of 1/6, similarly to Chapter 2, i.e., Q=0, 1/6, 1/3, 1/2, 2/3, and 5/6. Values of α are sampled at intervals of 20°, at the values of 30°, 50°, 70°, and 90°. These values of α are chosen for the purpose of illustration, however junction angles below 30° and above 90° also occur in nature. The value of d_{min} was set equal to $\sin(\alpha/2)$, i.e., half of the width of a junction, and d_{max} was set equal to 3.

Table 3.1 summarizes the space-filling sample networks created, and their principal topologic variables: magnitude (μ), Strahler order (Ω), diameter (d), total topologic path length (p), width (w), bifurcation ratio (R_B), and topologic area and length ratios (R^t_A and R^t_L). Dendritic test sample networks obtained with Q=0, 1/6, 1/3, 1/2, 2/3, and 5/6, are depicted in Figures 3.14 through 3.19, respectively. Apparent from these figures is the tendency for flow path convolution at large Q values. Figures 3.20 and 3.21

depict four stages in the growth of networks (d, 70°, 0) and (d, 70°, 5/6), respectively. These same networks are also depicted in Figures 3.14 and 3.19. For Q=0 (Figure 3.20), all exterior (or "terminal") links have equal branching probability at each growth step, and this model is designated "terminal growth." Terminal growth resembles a wave of dissection, where the area invaded by the network is fully or nearly filled with channels, i.e., network extension and elaboration (concepts introduced by *Glock* [1931]) are concurrent. For Q=5/6 (Figure 3.21), network extension precedes elaboration, i.e., the network extends in length until spatial constraints prevent further elongation, after which growth of tributary basins occurs in order to achieve space filling.

Trellis test sample networks were obtained with Q=0 and α=30°, 50°, 70°, and 90° (Figure 3.22); and with Q=0, 1/6, 1/3, 1/2, 2/3, and 5/6 for α=90° (Figure 3.23). Even if not immediately apparent to the eye in Figure 3.23, flow path convolution increases with Q, resulting in longer network diameters. The diameter paths in sample networks (t, 90°, 0) and (t, 90°, 5/6) are highlighted in Figure 3.24, for comparison.

For the purpose of comparison with space-filling networks, test sample networks were also created using the Q_E model computer code in the topologic mode of operation. The magnitude of each topologic-mode network was specified to be equal to that of the space-filling sample dendritic network having α=70° created with the same Q value (given in Table 3.1). For example, the topologic-mode network obtained with Q=0 has magnitude 1,111, which was chosen in order to be the same as the magnitude of the space-filling mode sample network (d, 70°, 0).

In Chapter 4, the coefficients of the topologic analogs of properties I-VII (listed in Section 1.2.1) are computed for all sample networks. The coefficients of topologic mode (TM) and space-filling mode (SM) networks created with the same Q values will be compared.

Table 3.1. Topologic properties of SM and TM test sample networks.

Sample	μ	Ω	d	p	w	R_B	$R^t{}_A$	$R^t{}_L$
SM sample networks: dendritic								
(d,30°,0)	2,179	7	75	183,615	120	3.847	4.192	1.645
(d,30°,1/6)	2,176	7	83	196,447	120	3.726	4.070	1.778
(d,30°,1/3)	2,175	7	138	275,447	80	3.724	4.109	1.728
(d,30°,1/2)	2,177	7	138	283,865	92	3.523	3.960	1.832
(d,30°,2/3)	2,187	7	195	551,101	70	3.845	4.084	2.192
(d,30°,5/6)	2.170	7	223	472,679	64	3.670	4.066	2.038
(d,50°,0)	1,391	7	79	129,255	78	3.502	3.812	1.809
(d,50°,1/6)	1,391	7	105	139,669	72	3.530	3.899	1.693
(d,50°,1/3)	1,396	6	89	157,035	68	4.229	4.714	2.246
(d,50°,1/2)	1,380	7	184	258,313	48	3.508	3.825	1.957
(d,50°,2/3)	1,389	6	200	299,739	38	4.637	5.023	2.550
(d,50°,5/6)	1,386	6	247	360,367	38	4.253	4.796	2.713
(d,70°,0)	1,111	6	83	105,281	62	4.431	5.109	1.606
(d,70°,1/6)	1,108	6	99	109,349	60	4.149	4.750	2.096
(d,70°,1/3)	1,099	6	117	155,549	54	4.263	4.708	2.323
(d,70°,1/2)	1,108	6	121	149,951	44	4.231	4.843	2.223
(d,70°,2/3)	1,100	5	231	282,079	26	5.593	6.439	3.551
(d,70°,5/6)	1,095	6	184	235,933	38	4.384	4.995	2.595
(d,90°,0)	1,045	6	111	123,323	46	4.166	4.771	2.100
(d,90°,1/6)	1,031	6	121	134,005	32	4.157	4.578	2.311
(d,90°,1/3)	1,036	6	105	128,505	48	4.160	4.797	2.169
(d,90°,1/2)	1,042	6	177	231,643	32	4.355	4.904	2.569
(d,90°,2/3)	1,032	6	232	242,707	30	4.322	5.038	2.486
(d,90°,5/6)	1,020	6	238	265,399	24	4.199	4.825	2.699
SM sample networks: trellis								
(t,30°,0)	2,134	7	82	204,667	120	3.883	4.130	1.796
(t,50°,0)	1,207	7	87	114,869	62	3.380	3.719	1.605
(t,70°,0)	931	6	85	92,479	54	4.030	4.658	1.914
(t,90°,0)	1,193	6	98	137,879	62	4.173	4.776	2.080
(t,90°,1/6)	1,193	6	110	142,135	56	4.183	4.790	2.033
(t,90°,1/3)	1,193	6	138	164,711	48	4.112	4.663	2.309
(t,90°,1/2)	1,193	7	156	224,415	42	3.330	3.708	1.928
(t,90°,2/3)	1,193	6	260	281,855	32	4.229	4.864	2.580
(t,90°,5/6)	1,193	6	385	434,951	18	4.184	4.766	2.909
TM sample networks:								
Q=0	1,111	7	22	28,605	264	3.107	3.405	1.243
Q=1/6	1,108	7	36	43,919	164	3.213	3.475	1.346
Q=1/3	1,099	6	57	71,915	78	4.061	4.466	1.948
Q=1/2	1,108	6	151	189,167	46	4.019	4.468	2.288
Q=2/3	1,100	6	284	304,921	28	4.133	4.597	2.542
Q=5/6	1,095	5	535	625,829	14	5.887	6.897	4.629

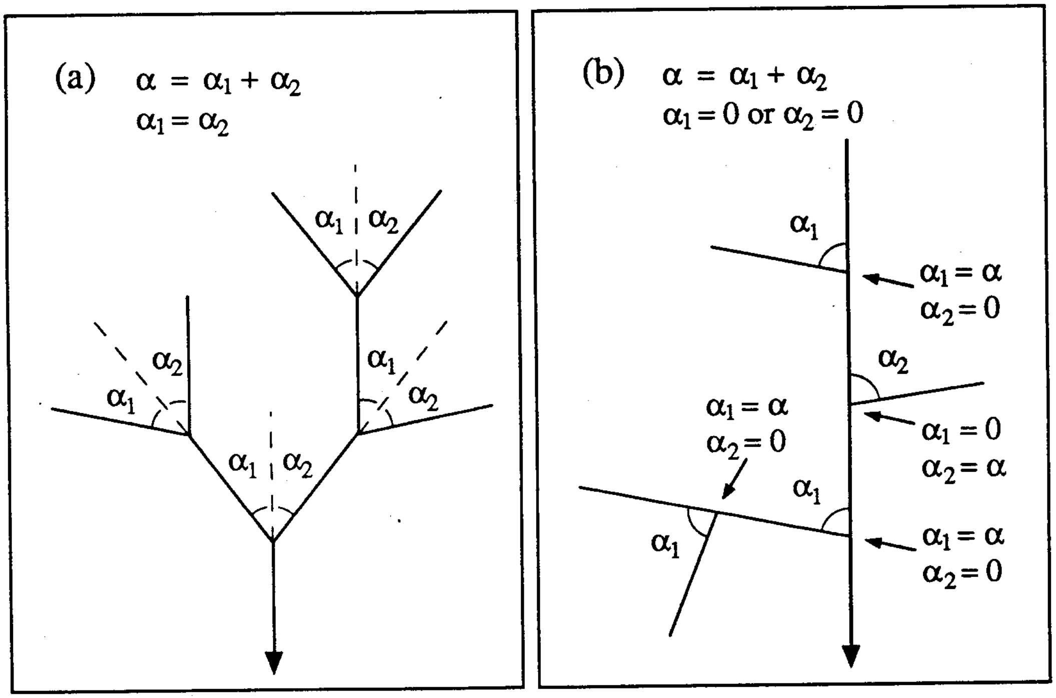

Figure 3.1. Two topologically identical networks with α=80°, and drainage pattern **(a)** dendritic (δ=d); **(b)** trellis (δ=t). The network outlet is indicated by an arrow head.

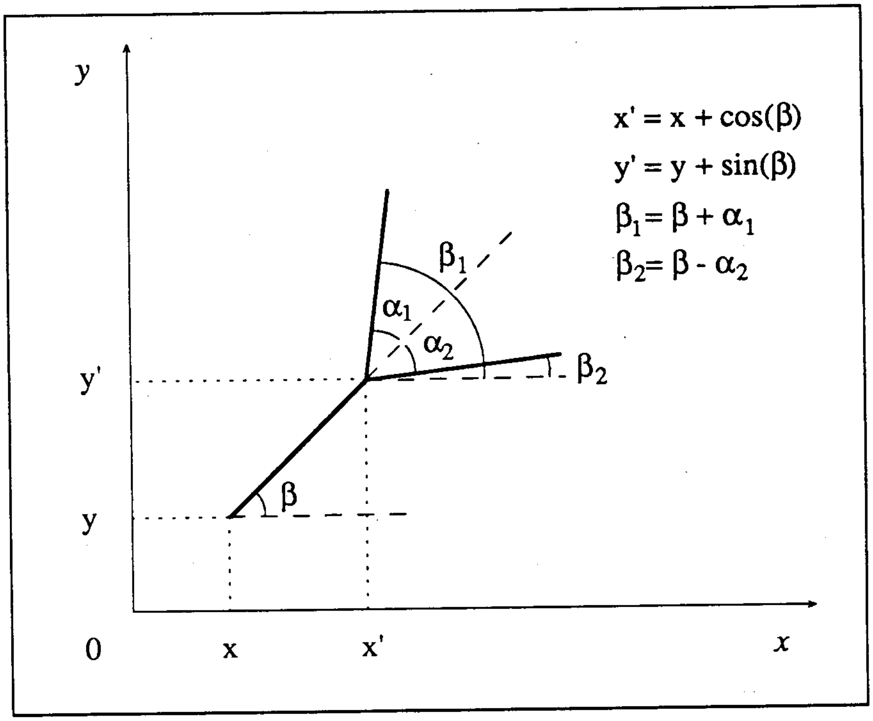

Figure 3.2. Spatial coordinates (x, y) and orientation angle, β, of a link. Computation of spatial coordinates (x', y') and orientation angles, β_1 and β_2, of its tributary links, from (x, y), β, and semidivide angles α_1 and α_2.

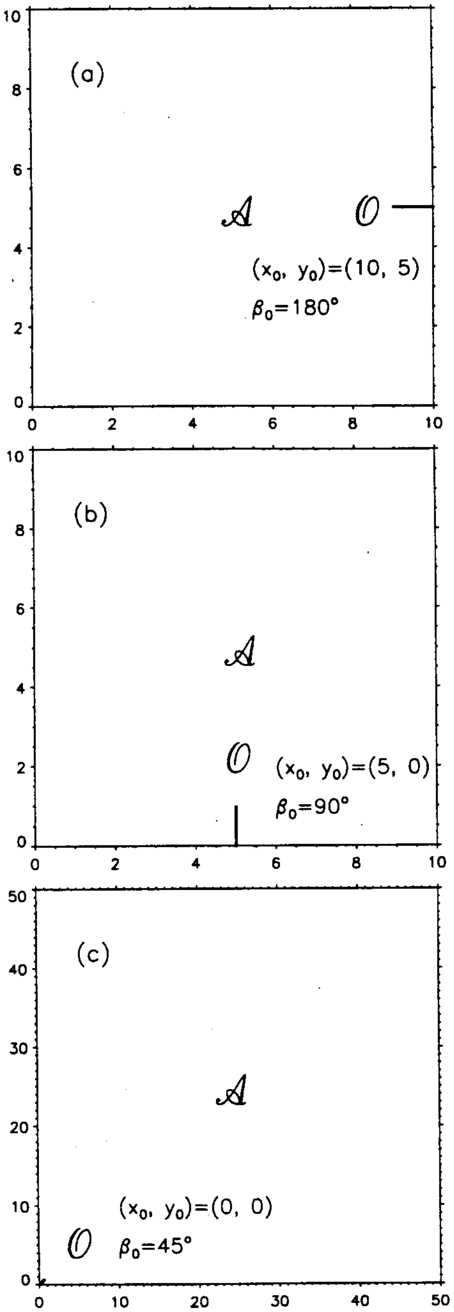

Figure 3.3. Examples of a specified drainage area, 𝒜, and outlet link location, O. 𝒜 is square in all three examples, but may have any shape, provided it has a single external boundary line. **(a)** 𝒜 is a square of side measuring 10 length units, and the outlet link location, O, is described by $(x_0, y_0)=(10, 5)$ and $\beta_0=180°$; **(b)** 𝒜 is a square of side measuring 10 length units, and O is described by $(x_0, y_0)=(5, 0)$ and $\beta_0=90°$; **(c)** 𝒜 is a square of side measuring 50 length units, and O is described by $(x_0, y_0)=(0, 0)$ and $\beta_0=45°$. Sample networks studied in this chapter are space filling of the area 𝒜 and have the outlet location O depicted in (c).

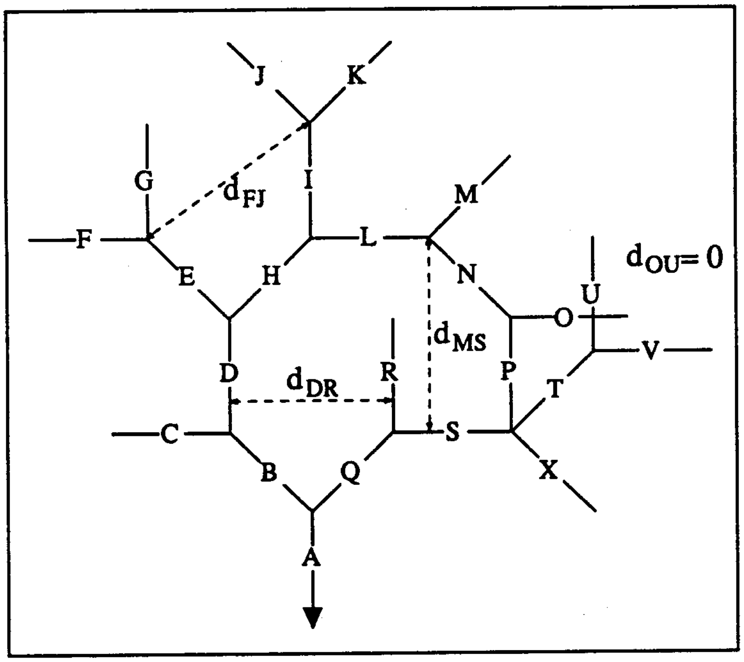

Figure 3.4. Definition of distance between two links. The links of the network depicted are labelled "A" through "X." The distance between links F and J, for example, denoted d_{FJ}, is equal to the length of the dashed line shown connecting the two links. Links O and U cross each other, therefore we have $d_{OU}=0$.

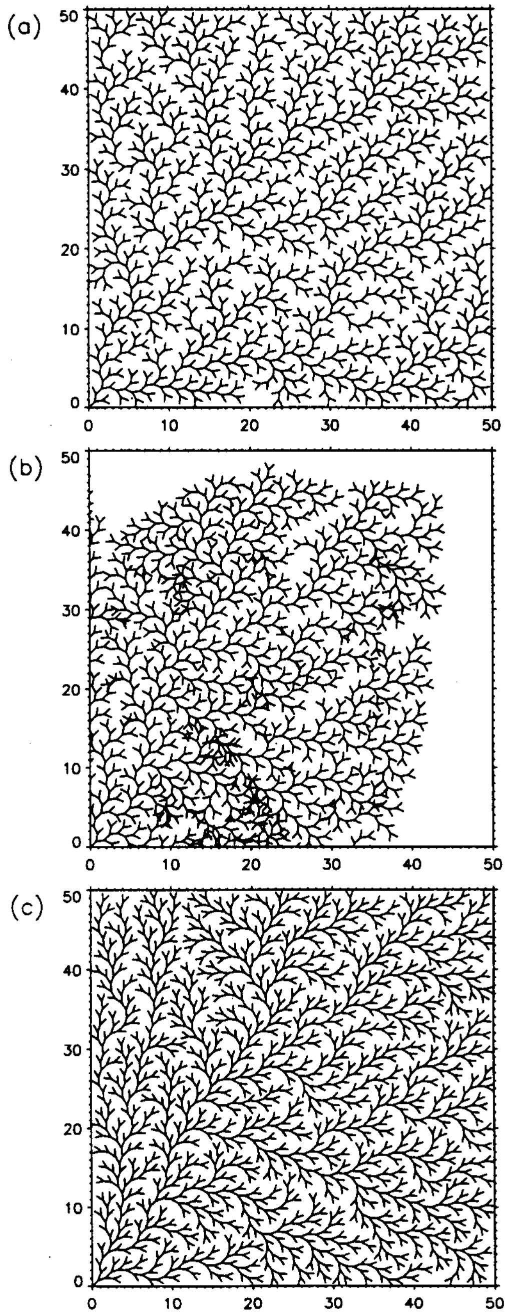

Figure 3.5. $\mathcal{A}$ and O are those depicted in Figure 3.4c. Values $d_{min}=0.2$ and $d_{max}=3$ are stipulated. **(a)** A network that is space filling of $\mathcal{A}$ given O, under $\delta=d$ and $\alpha=70°$. **(b)** A network that is not space filling of $\mathcal{A}$ given O under $\delta=d$ and $\alpha=70°$, because some links not joined at a junction are at a distance smaller than d_{min}, and because some points of $\mathcal{A}$ are at a distance larger than d_{max} from the closest point on the network. **(c)** A network that is topologically identical to the one in (b), but having geometric properties $\delta=d$ and $\alpha=50°$. The network topology in (b) and (c) is space-filling of $\mathcal{A}$ given O under $\delta=d$ and $\alpha=50°$ (shown in (c)) but not under $\delta=d$ and $\alpha=70°$ (shown in (b)).

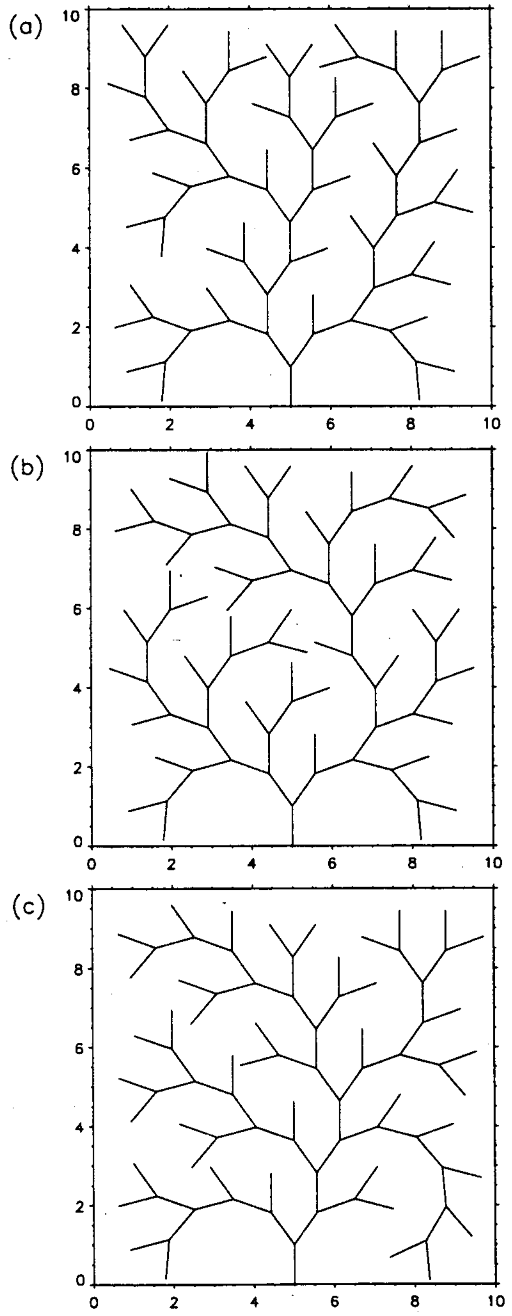

Figure 3.6. $\mathcal{A}$ and **O** are those depicted in Figure 3.3b. Values $d_{min}=0.1$ and $d_{max}=3$ are stipulated. The three topologically distinct networks are space-filling of $\mathcal{A}$ given **O**, under $\delta=d$ and $\alpha=40°$. The network in (a) has magnitude 41, and the networks in (b) and (c) have magnitude 42.

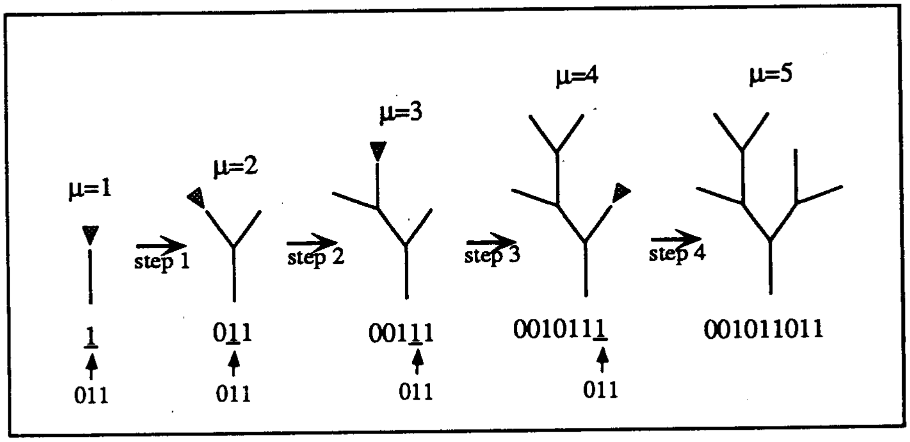

Figure 3.7. Example sequence of 4 growth steps of the Q_E model, yielding a network of magnitude 5. The link chosen for branching is indicated by an arrow head. The digit "1" representing the link chosen for branching is underlined in the binary string representing the network. In the computer code of the Q_E model, this digit "1" is replaced by the sequence "011" as indicated.

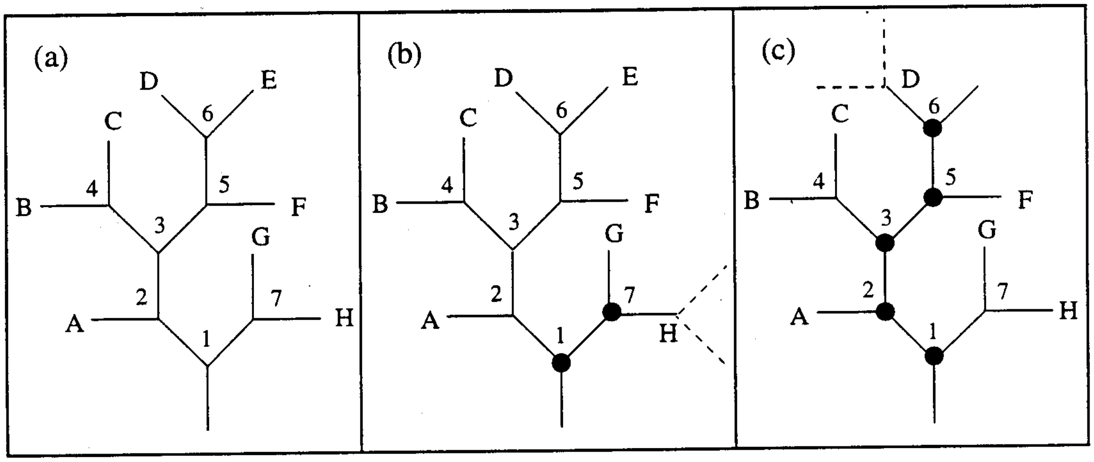

Figure 3.8. Example 1: **(a)** Network of magnitude 8. Exterior links are labelled A through H, and nodes are numbered 1 through 7. **(b)** Branching of link H will affect the partitions at nodes 1 and 7, encircled. **(c)** Branching of link D will affect the partitions at nodes 1, 2, 3, 4, and 6, encircled.

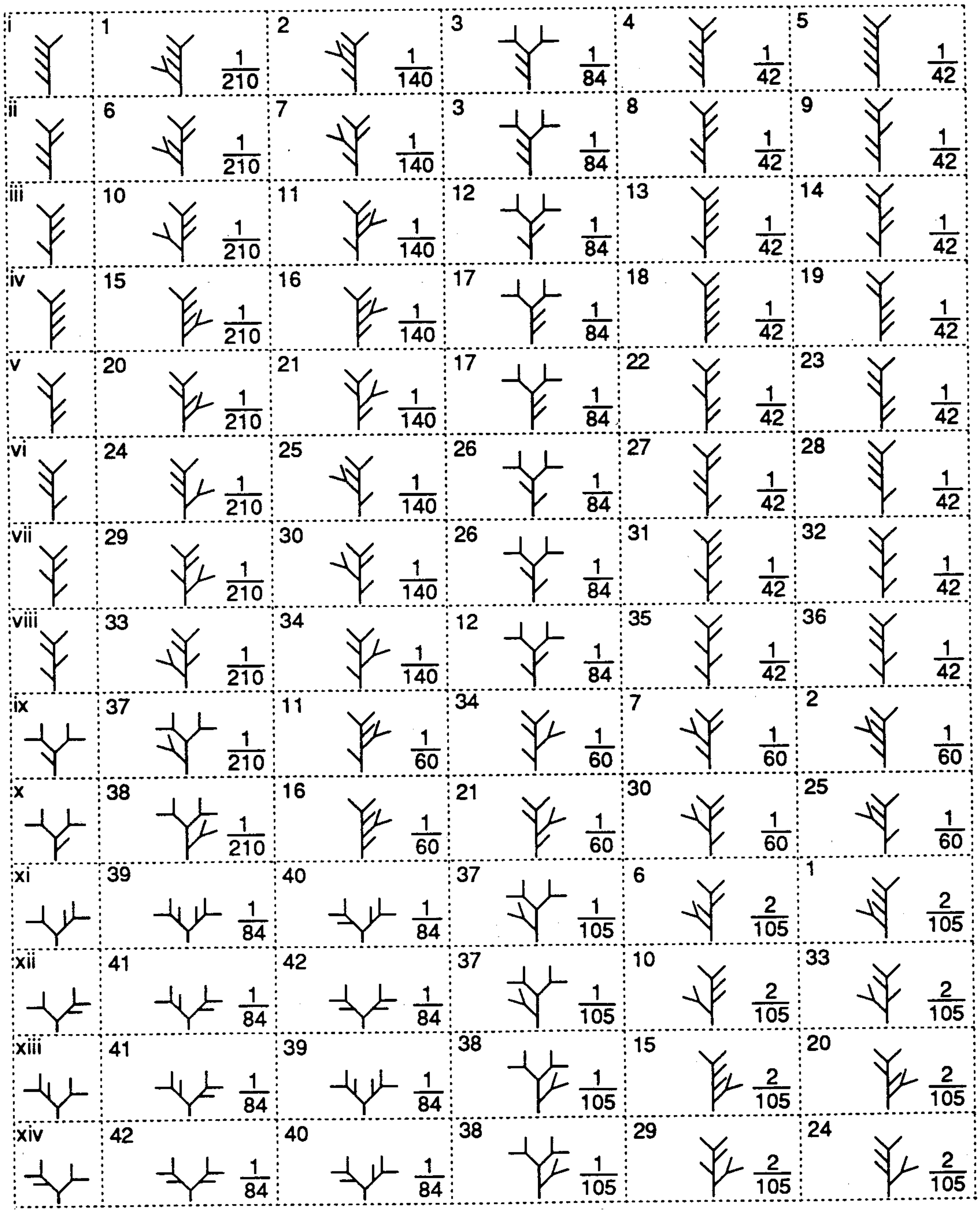

Figure 3.9. Example 2: Generation of the 42 TDCN of magnitude 6 (numbered in the upper left-hand corner of the corresponding box) from the 14 TDCN of magnitude 5 (numbered in Roman numerals) by the Q_E model in the space-filling mode, using Q=1/2. Each matrix box represents the outcome of branching of one external link of the magnitude-5 network in the same row, first column. The expected frequency of each branching event is indicated in the lower right-hand corner the corresponding box.

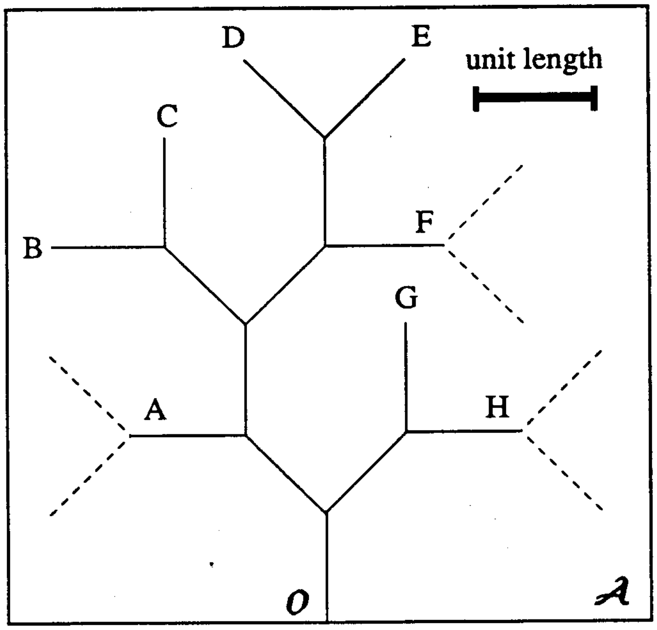

Figure 3.10. Example 3: A network under geometric properties δ=d and α=90°, and its outlet link positioned at O. This network is topologically identical to that in Figure 3.8. Exterior links are labelled A through H. Addition of new tributary links (represented by dashed lines) to exterior links A, F, and H will not result in violation of spatial constraints with, e.g., d_{min}=0.2 and d_{max}=2.

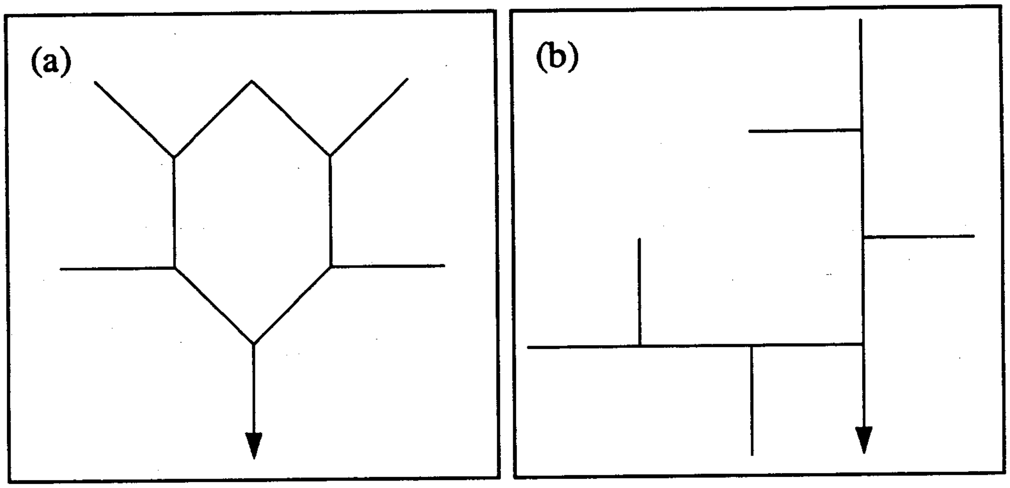

Figure 3.11. The TDCN numbered 42 in Figure 3.7, pictured with geometric properties **(a)** δ=d and α=90°, and **(b)** δ=t and α=90°. In (a), the requirement for a minimum distance between any two links not joined at a junction is violated for any specified $d_{min}>0$. In (b), this requirement is not violated for $d_{min}=1$ or smaller.

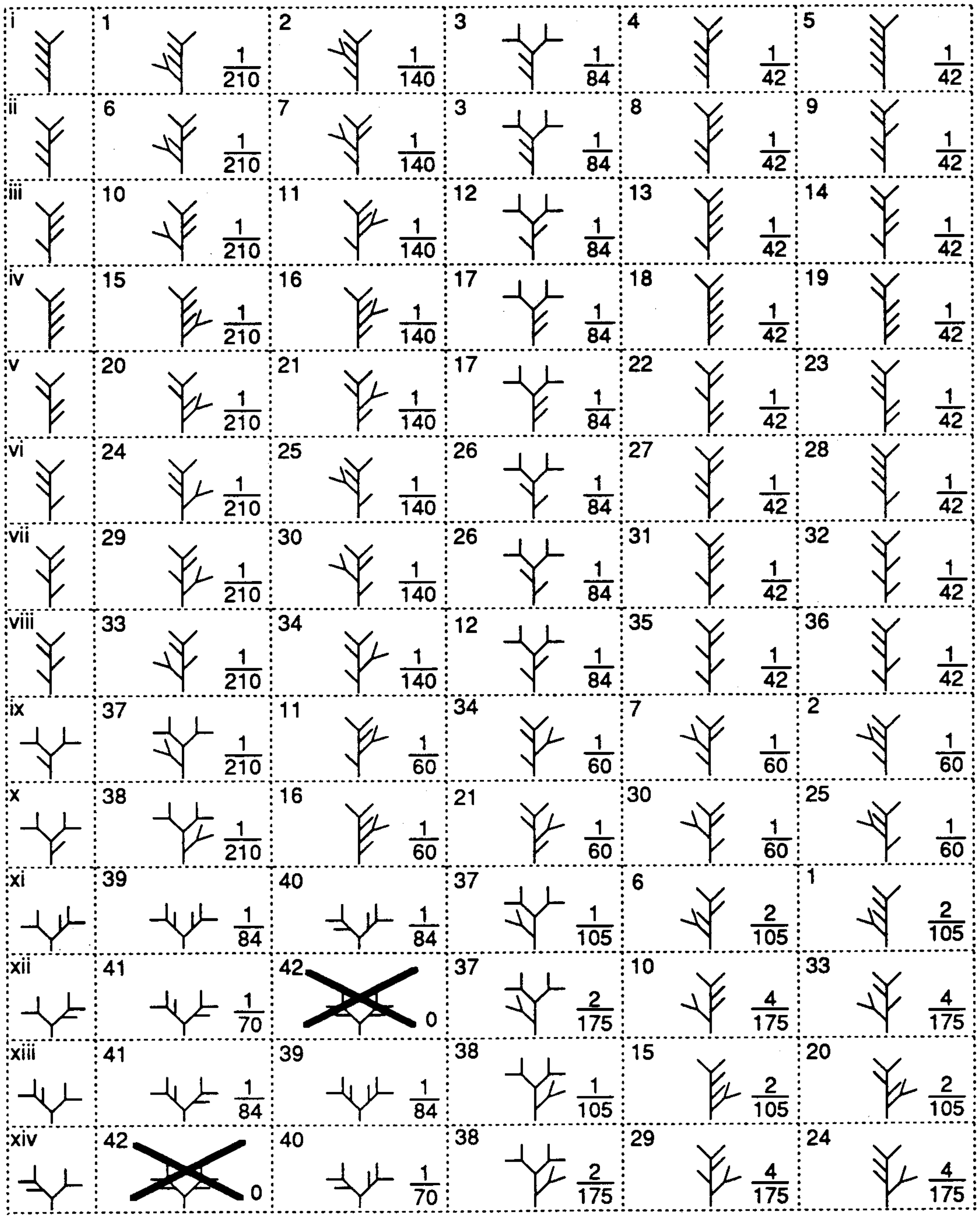

Figure 3.12. Example 4: Generation of TDCN of magnitude 6 (numbered in the upper left-hand corner of the corresponding box) from the 14 TDCN of magnitude 5 (numbered in Roman numerals) by the Q_E model in the space-filling mode, using Q=1/2, under δ=d and α=90°. TDCN #42 is precluded by spatial constraints. Expected frequencies (in the lower right-hand corner of each box) of TDCN #10, 24, 29, 33, 37, 38, 40, and 41, on the same matrix rows as #42, are increased relatively to the topologic mode (Figure 3.9).

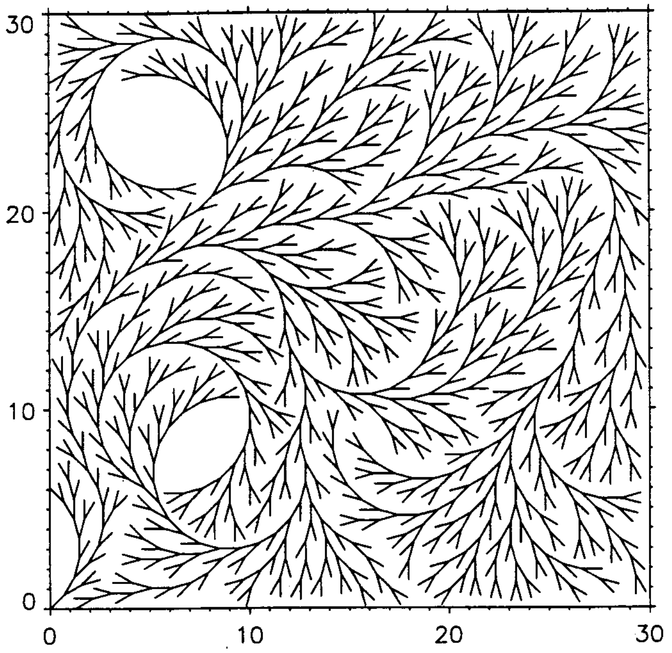

Figure 3.13. Drainage area, $\mathcal{A}$, is a square of side measuring 30 length units, and outlet link location, $\mathbf{O}$, is defined by $(x_0, y_0)=(0, 0)$ and $\beta_0=45°$. Variables $d_{min}=0.2$ and $d_{max}=3$ are specified. The network depicted has $\delta=d$ and $\alpha=30°$, and was obtained with the Q_E model using $Q=5/6$. Even though no more links may be added without either violation of the spatial constraint imposed by d_{min}, or crossing of the boundary line of $\mathcal{A}$, this network is not space-filling of $\mathcal{A}$ because the constraint imposed by d_{max} is violated in two sub-areas left undrained. The appearance of such undrained sub-areas is rare for larger α and for lower Q values.

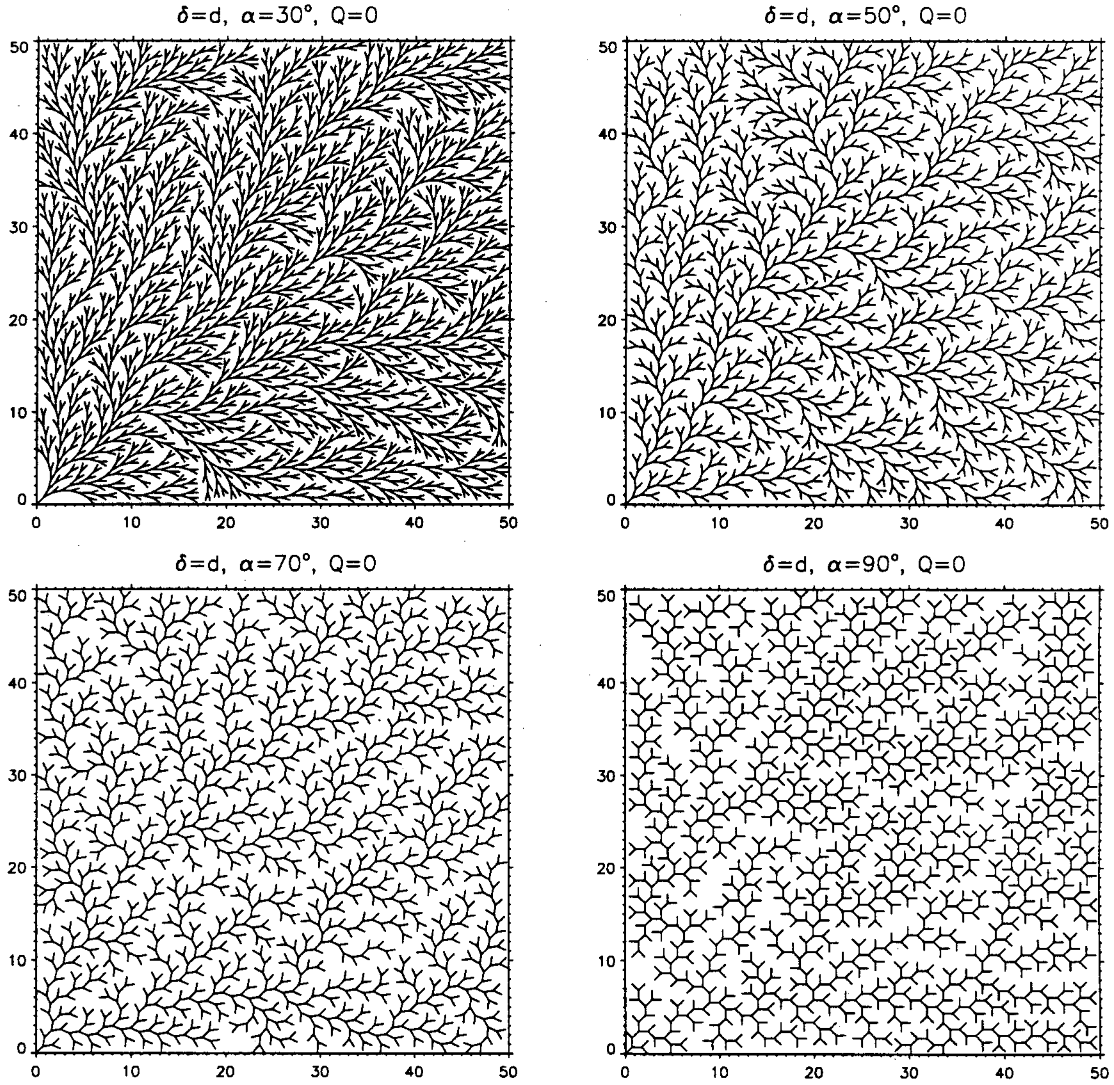

Figure 3.14. SM dendritic test sample networks created with the Q_E model, using Q=0, with various bifurcation angles, α: (d, 30°, 0), (d, 50°, 0), (d, 70°, 0), and (d, 90°, 0). These networks have magnitude 2,179, 1,391, 1,111, and 1,045, and diameter 75, 79, 83, and 111, respectively (Table 3.1).

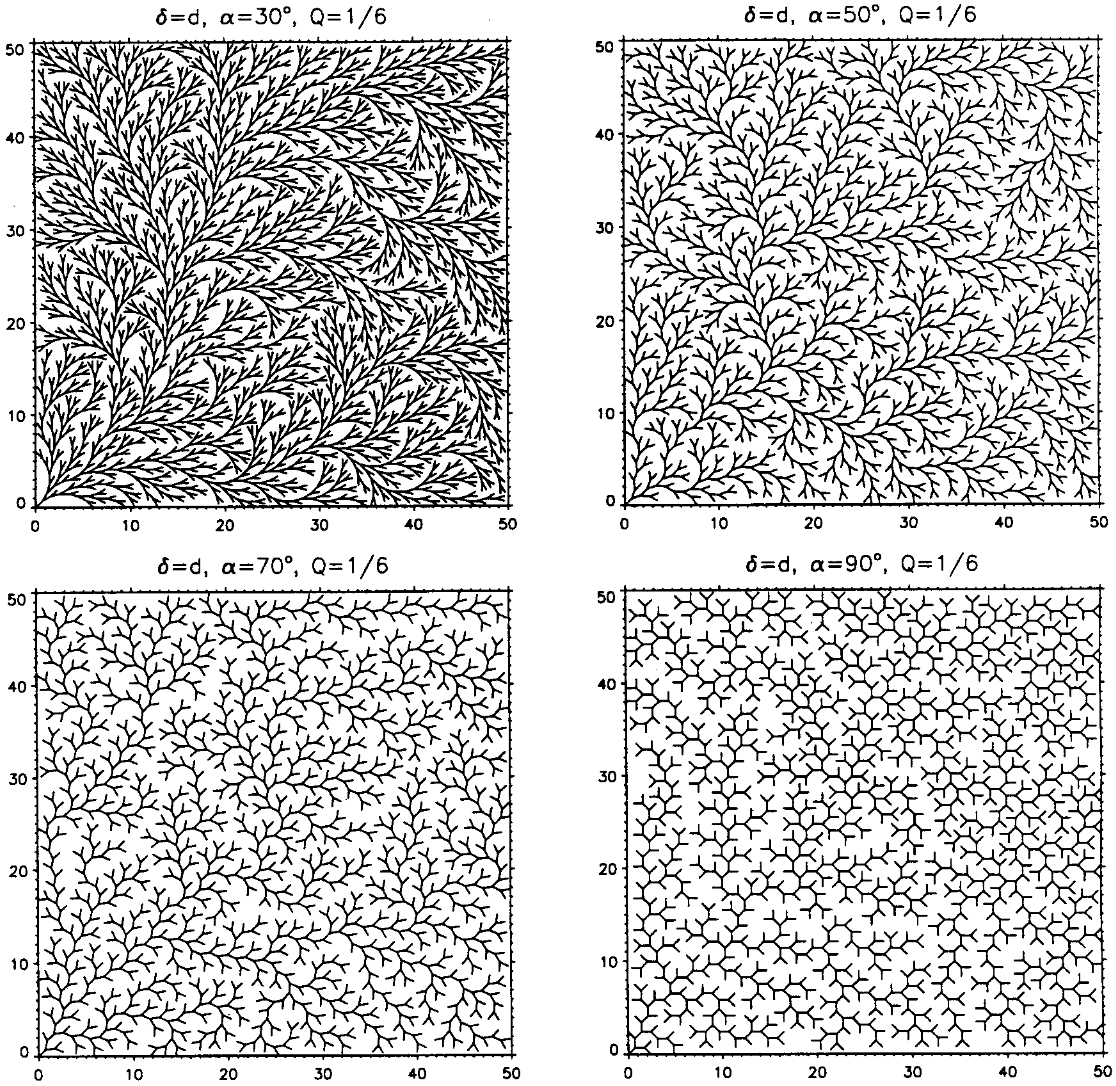

Figure 3.15. SM dendritic test sample networks created with the Q_E model, using Q=1/6, with various bifurcation angles, α: (d, 30°, 1/6), (d, 50°, 1/6), (d, 70°, 1/6), and (d, 90°, 1/6). These networks have magnitude 2,176, 1,391, 1,108, and 1,031, and diameter 83, 105, 99, and 121, respectively (Table 3.1).

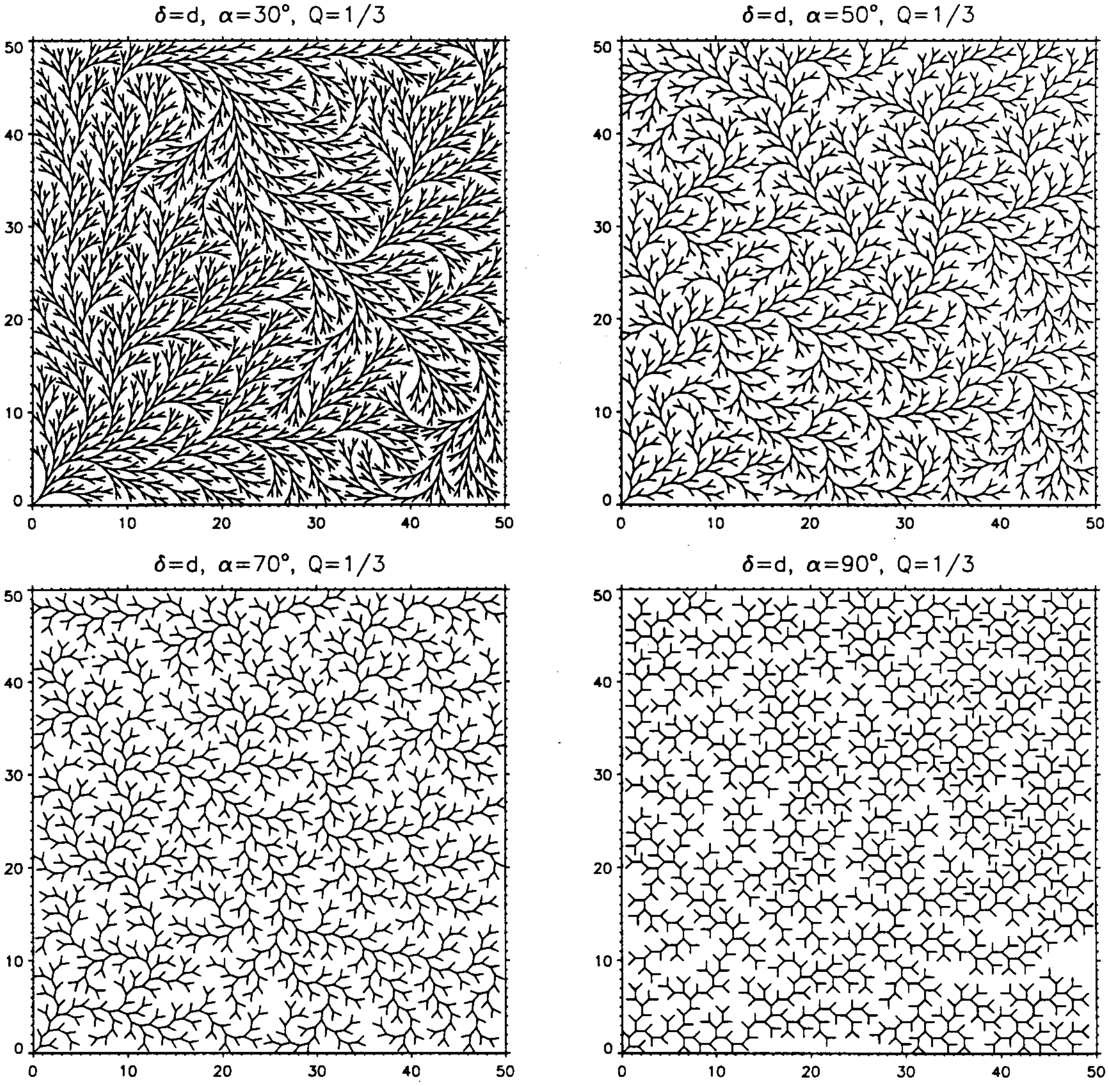

Figure 3.16. SM dendritic test sample networks created with the Q_E model, using Q=1/3, with various bifurcation angles, α: (d, 30°, 1/3), (d, 50°, 1/3), (d, 70°, 1/3), and (d, 90°, 1/3). These networks have magnitude 2,175, 1,396, 1,099, and 1,036, and diameter 138, 89, 117, and 105, respectively (Table 3.1).

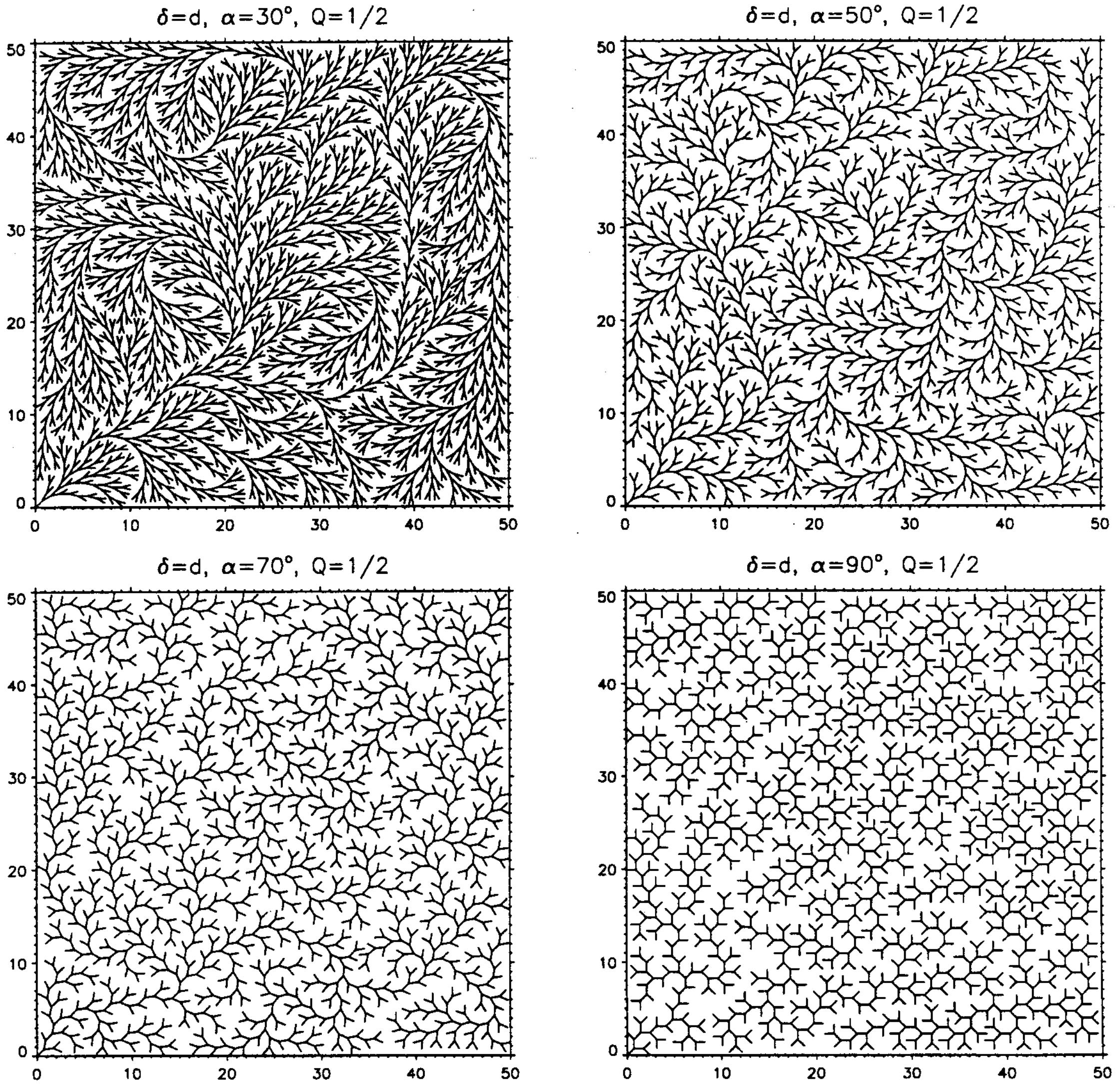
δ=d, α=30°, Q=1/2

δ=d, α=50°, Q=1/2

δ=d, α=70°, Q=1/2

δ=d, α=90°, Q=1/2

Figure 3.17. SM dendritic test sample networks created with the Q_E model, using Q=1/2, with various bifurcation angles, α: (d, 30^o, 1/2), (d, 50^o, 1/2), (d, 70^o, 1/2), and (d, 90^o, 1/2). These networks have magnitude 2,177, 1,380, 1,108, and 1,042, and diameter 138, 184, 121, and 177, respectively (Table 3.1).

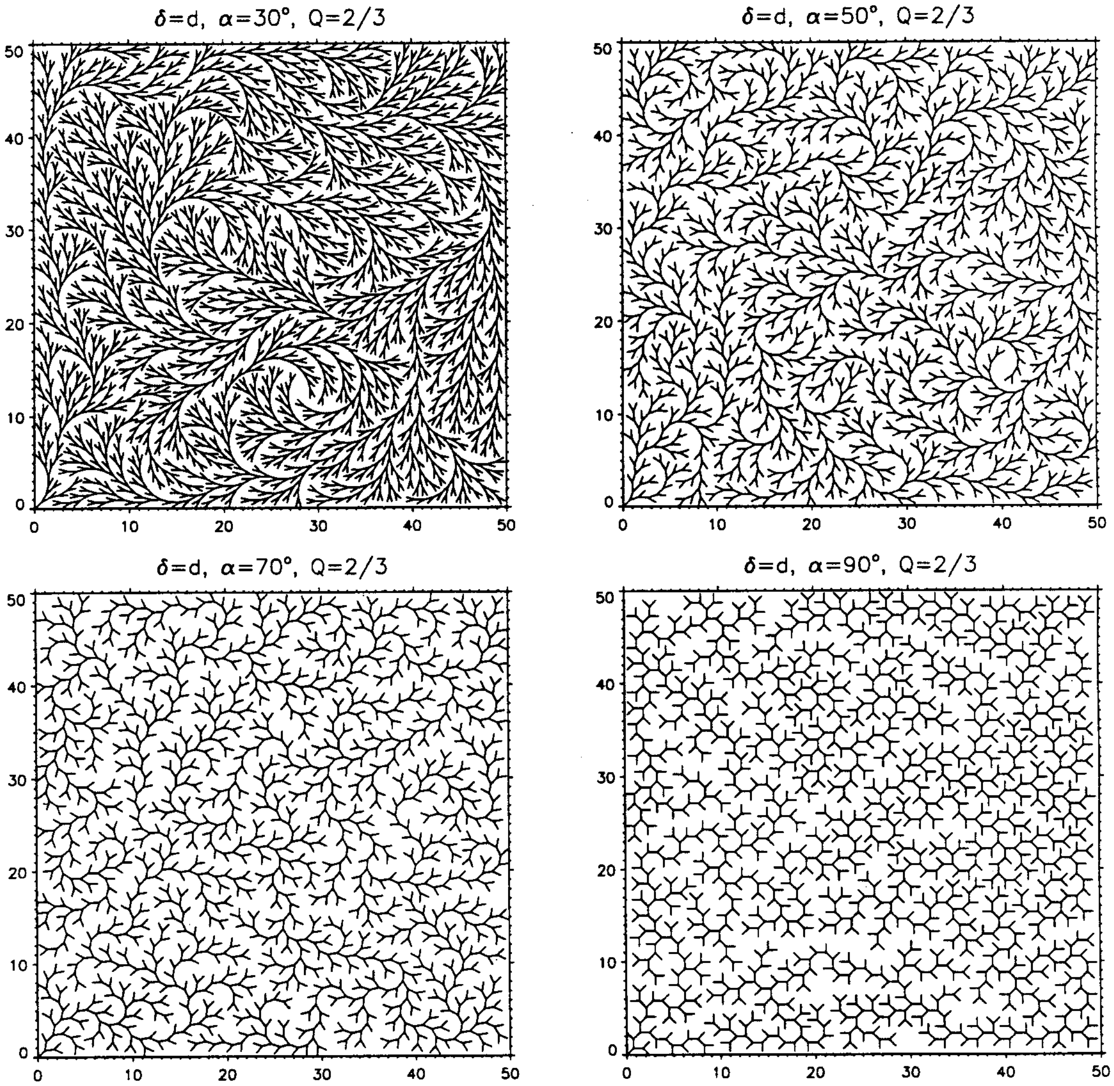

Figure 3.18. SM dendritic test sample networks created with the Q_E model, using Q=2/3, with various bifurcation angles, α: (d, 30°, 2/3), (d, 50°, 2/3), (d, 70°, 2/3), and (d, 90°, 2/3). These networks have magnitude 2,187, 1,389, 1,100, and 1,032, and diameter 195, 200, 231, and 232, respectively (Table 3.1).

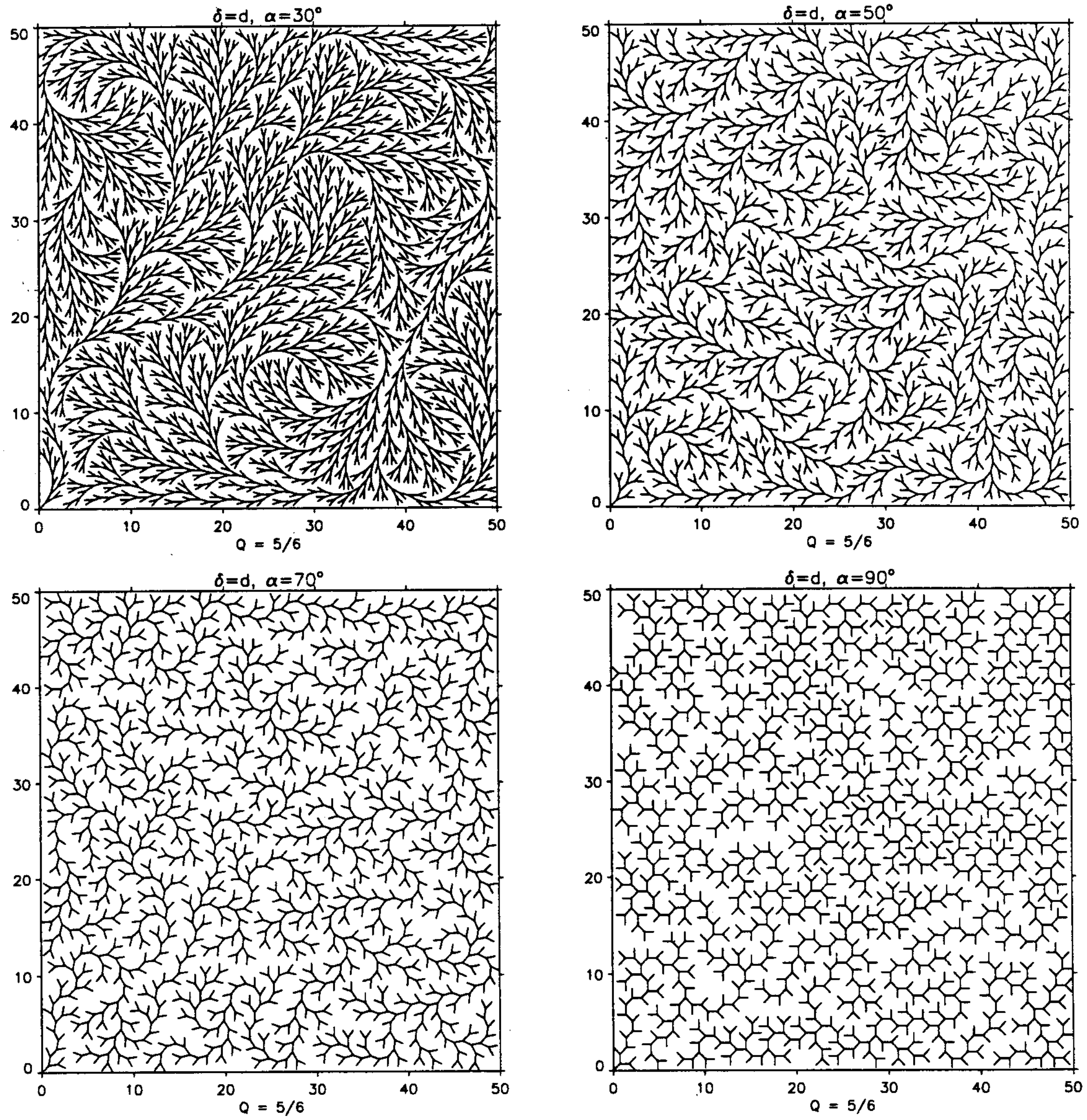

Figure 3.19. SM dendritic test sample networks created with the Q_E model, using Q=5/6, with various bifurcation angles, α: (d, 30°, 5/6), (d, 50°, 5/6), (d, 70°, 5/6), and (d, 90°, 5/6). These networks have magnitude 2,170, 1,386, 1,095, and 1,020, and diameter 223, 247, 184, and 238, respectively (Table 3.1).

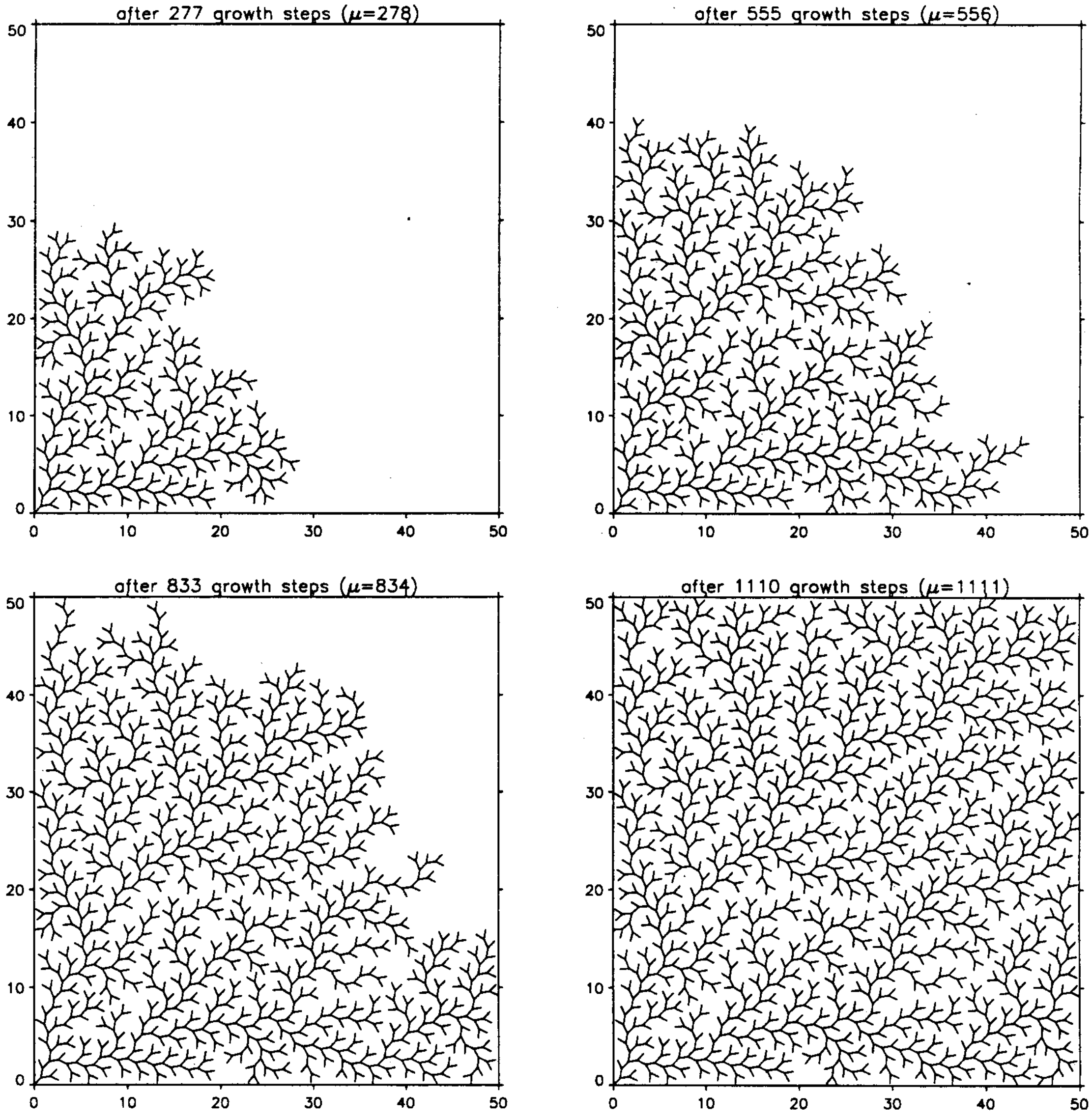

Figure 3.20. Four stages in the growth of test network (d, 70°, 0), depicted in Figure 3.14. The growing network is shown after 277, 555, 833, and 1,110 growth steps. The final network has magnitude 1,111. Growth with Q=0 resembles a wave of dissection, in which network elongation and elaboration occur concurrently.

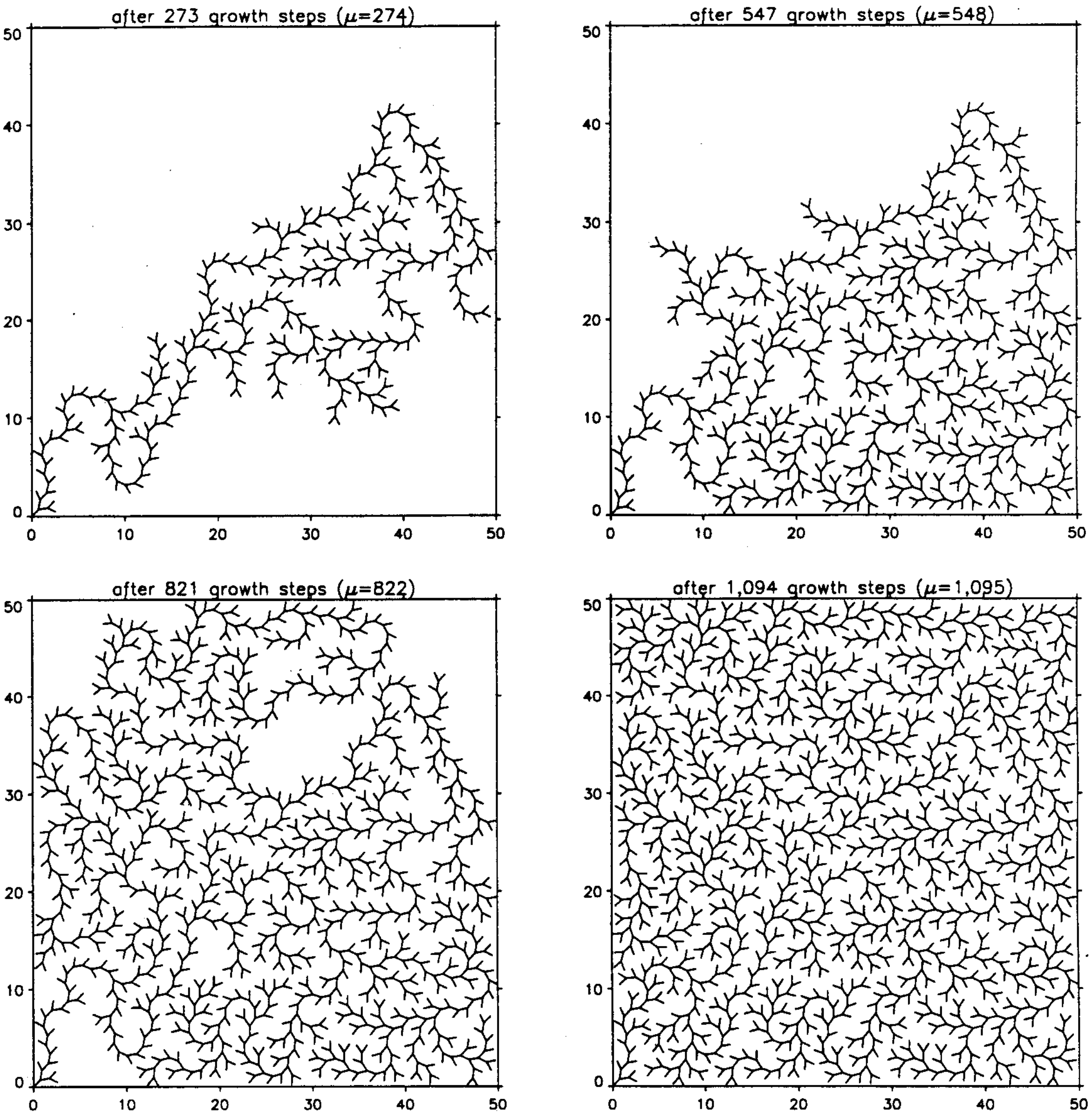

Figure 3.21. Four stages in the growth of test network (d, 70°, 5/6), depicted in Figure 3.19. The growing network is shown after 273, 547, 821, and 1,094 growth steps. The final network has magnitude 1,095. Growth with Q=5/6 favors network extension, followed by elaboration once spatial constraints prevent further extension.

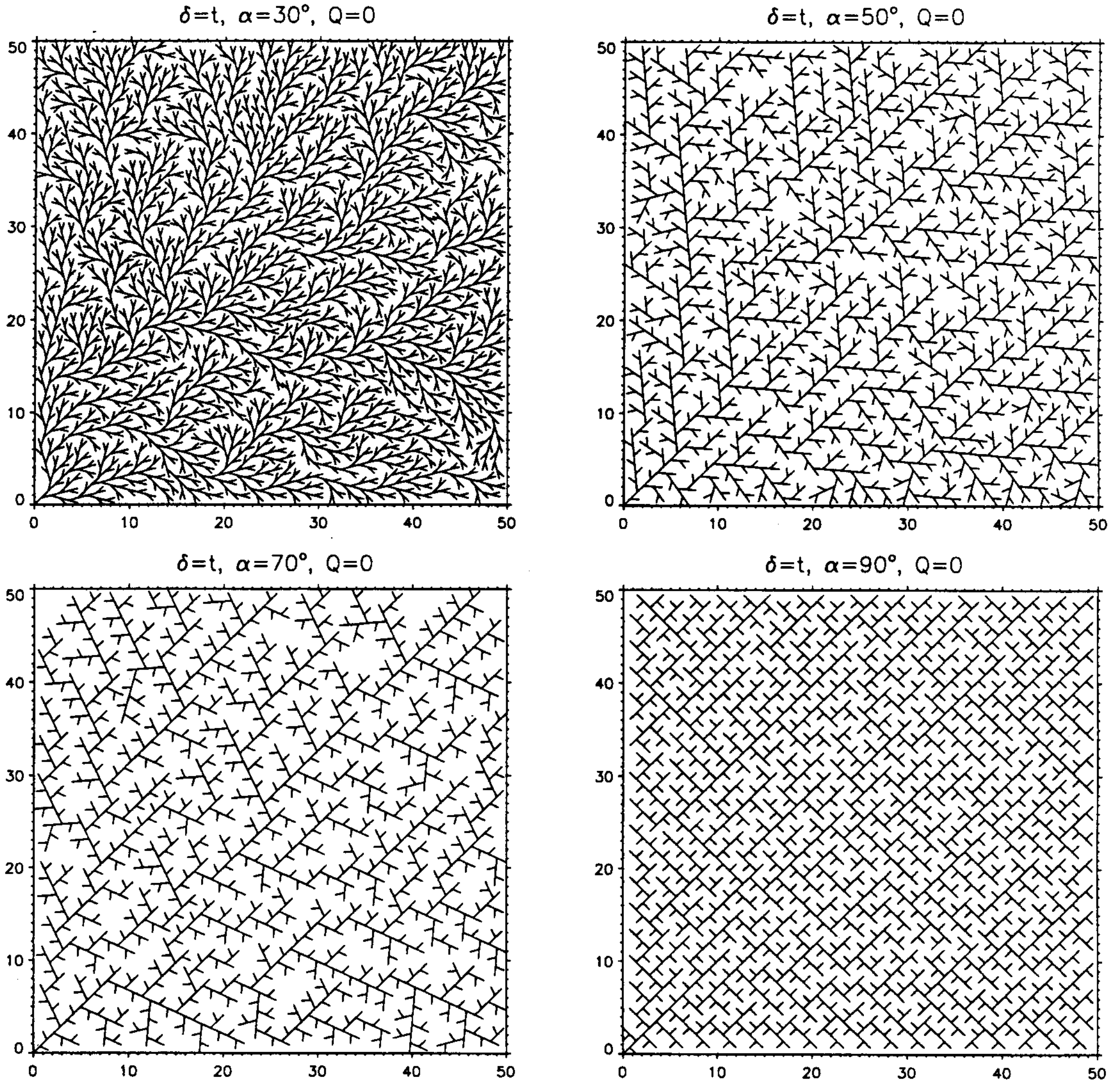

Figure 3.22. SM trellis test sample networks created with the Q_E model, using Q=0, with various bifurcation angles, α: (t, 30°, 0), (t, 50°, 0), (t, 70°, 0), and (t, 90°, 0). These networks have magnitude 2,134, 1,207, 931, and 1,193, and diameter 82, 87, 85, and 98, respectively (Table 3.1).

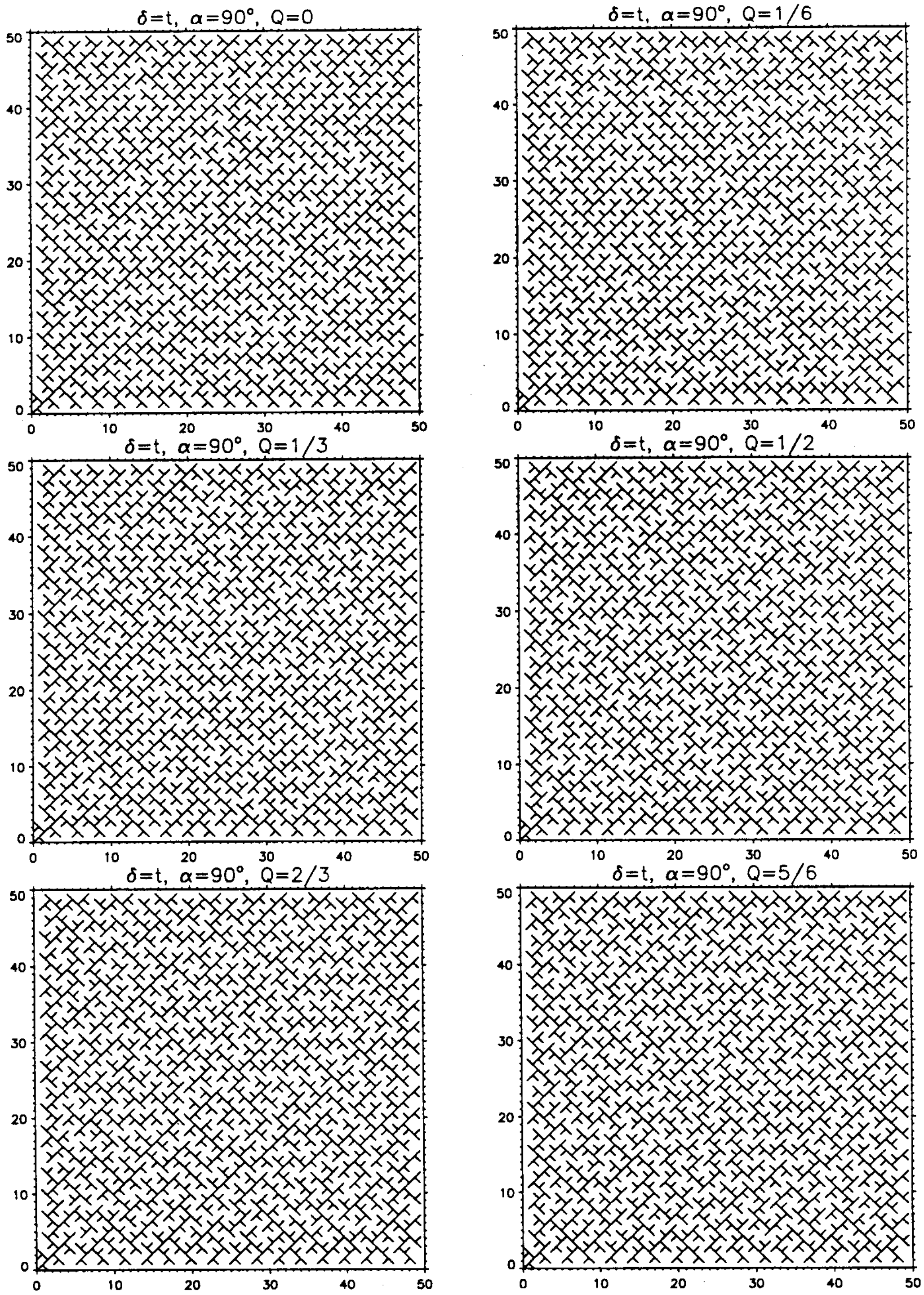

Figure 3.23. SM trellis test sample networks created with the Q_E model with α=90° (maze networks) using various Q values: (t, 90°, 0), (t, 90°, 1/6), (t, 90°, 1/3), (t, 90°, 1/2), (t, 90°, 2/3), and (t, 90°, 5/6). All of these networks have magnitude 1,193, and their diameters are 98, 110, 138, 156, 260, and 385, respectively (Table 3.1). The diameter paths for (t, 90°, 0) and (t, 90°, 5/6) are depicted in Figure 3.24.

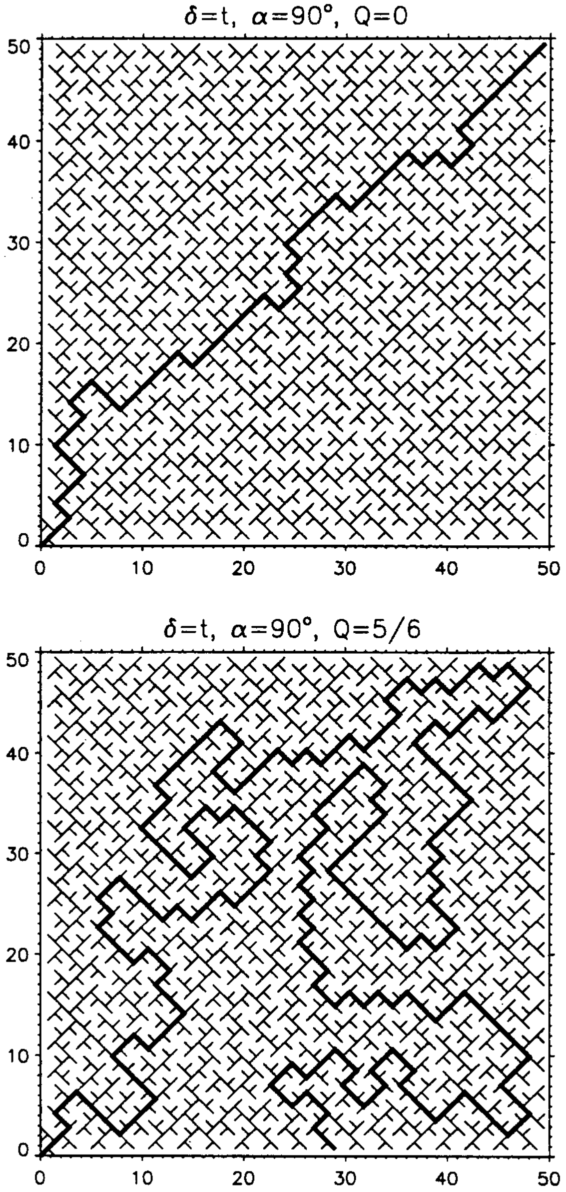

Figure 3.24. Diameter path of test sample networks (t, 90°, 0) and (t, 90°, 5/6), depicted in Figure 3.23. Diameters are 98 and 385, respectively. Higher Q values tend to originate convoluted flow paths and longer diameters.

Chapter 4

Sensitivity of Channel Network Planform Laws To Network Growth Processes Under Spatial Constraints

4.1 Introduction

The objective of this chapter is to test the sensitivity of the channel network planform laws (properties I-VII listed in Section 1.2.2) to the Q parameter, under spatial constraints. The coefficients of the topologic analogs of properties I-VII are computed for each sample network created with the Q_E model in Chapter 3 (Section 4.2). The sensitivity of these coefficients to Q is compared to that of sample networks subject to no constraints, similar to the networks studied in Chapter 2. Additional topologic properties are also compared (Section 4.3).

The probability of producing any given network depends on Q. The Q value that maximizes the likelihood of producing a given network in the absence of spatial constraints can be determined from the network's topology (Section 4.4). This value is designated the maximum-likelihood estimator of the Q parameter, and denoted "ML-Q." The ML-Q is computed for space-filling network samples and compared to the Q values that were used to create these samples (the "true Q") (Section 4.4). Differences between ML-Q and true Q values are caused by spatial constraints, and constitute a measure of the effect of these constraints on network topology.

4.2 Topologic Analogs of Channel Network Planform Laws

In this section, the parameters of the topologic-analog of each channel network law listed in Section 1.2.1 (properties I-VII) are computed for each sub-network of space-filling mode (SM) and topological mode (TM) sample networks described in Section 3.4 and listed in Table 3.1. Every link of a sample network is the outlet link of a sub-network. Thus, a sample network of magnitude μ contains $2\mu-1$ sub-networks. There is only one TDCN of magnitude 1 and one TDCN of magnitude 2, and two TDCN of magnitude 3 (differing only in left-right link orientation). Hence, only sub-networks of magnitude 4 or higher were considered. Topologic variables are computed from the binary strings representing the sample networks and their sub-networks, using the computer code "topovars.f," previously used in Chapter 2.

4.2.1 Property I: Horton's laws and ratios

Figure 4.1 shows the R_B distribution for the sub-networks of sample networks obtained with various Q values, including TM networks, and SM networks having $\delta=d$ and $\alpha=70^\circ$. The R_B means and standard deviations for all sample networks are given in Table 4.1. For any given Q, TM and SM networks have markedly different R_B distributions. The sensitivity of the R_B distribution to Q is greater in TM than in SM sample networks. Results are qualitatively similar for R^t_L and R^t_A distributions (Table 4.1).

Figures 4.2, 4.3 and 4.4 show the mean values $\bar{R}_B$, $\bar{R}^t_L$, and $\bar{R}^t_A$ plotted against Q for TM, SM dendritic, and SM trellis sample networks, respectively. There is marked increase in mean values with Q for TM sample networks, as was shown in Chapter 2 (Figure 2.5). In SM dendritic sample networks (Figure 4.3), there appears to be no sensitivity of $\bar{R}_B$, $\bar{R}^t_L$, and $\bar{R}^t_A$ to Q, except possibly some limited sensitivity for α=90°. To establish whether this apparent limited sensitivity to Q for α=90° is statistically significant would require a larger sample size. It suffices to conclude from our results that the sensitivity of $\bar{R}_B$, $\bar{R}^t_L$, and $\bar{R}^t_A$ is greatly reduced in SM dendritic networks relatively to TM networks. For TM sample networks, the interval of variation of $\bar{R}_B$ for the Q range sampled is [3.026, 5.200]. For SM dendritic sample networks, the $\bar{R}_B$ range is reduced to the narrower intervals of [3.202, 3.362] for α=30°, [3.359, 3.603] for α=50°, [3.677, 4.114] for Q=70°, and [3.988, 4.277] for α=90°.

In SM trellis networks, sensitivity of $\bar{R}_B$, $\bar{R}^t_L$ and $\bar{R}^t_A$ to Q for α=90° (Figure 4.4) appears to have a different tendency from either TM or SM dendritic networks. Minimum values of $\bar{R}_B$, $\bar{R}^t_L$ and $\bar{R}^t_A$ are reached at intermediate Q values, in the vicinity of 1/2. A larger sample size would be required to establish whether this behavior is statistically significant. In SM dendritic and trellis sample networks, the mean values $\bar{R}_B$, $\bar{R}^t_L$ and $\bar{R}^t_A$ are more sensitive to α than to Q (Table 4.1, Figures 4.3 and 4.4). Sensitivity to α is greater in trellis than in dendritic networks.

4.2.2 Property II: Correlations between Horton ratios

Table 4.2 lists the correlation values between topologic-analog Horton ratios in all test sample networks. These correlation values do not exhibit a consistent tendency to increase or decrease with either α or Q. Correlations of all three pairs, (R_B, R^t_L), (R_B, R^t_A), and (R^t_L, R^t_A), are generally higher in TM than in SM sample networks. The lower correlations in SM networks are partly due to the narrower range of variation of the three topologic-analog ratios (see Property I in Section 4.2.1).

Despite the generally lower correlations in SM networks, correlations between pairs (R_B, R^t_L) and (R^t_L, R^t_A) increase with network magnitude, μ, more rapidly than in

TM sample networks. This is demonstrated by the ratio $\log(R_B)/\log(R^t_L)$ plotted against μ in Figures 4.5, 4.6, and 4.7, for TM, SM dendritic, and SM trellis networks, respectively. For low Q values (sampled values $Q=0$ and $Q=1/6$), TM networks have a large scatter of this ratio, which narrows slowly with μ (Figure 4.5), while in SM networks this ratio converges quickly to values between 1 and 2 (Figures 4.6a and b, and 4.7a and b). For larger Q values, the conversion of this ratio is rapid for both TM and SM networks.

We conclude that the space-filling constraint causes the ratio $\log(R_B)/\log(R^t_L)$ to converge rapidly to a value between 1 and 2 with increasing network magnitude. A similar effect was observed for the ratio $\log(R^t_L)/\log(R^t_A)$ (not shown). The ratio $\log(R_B)/\log(R^t_L)$ provides an estimate of the contribution of topology to a network's fractal dimension [*Tarboton*, 1988; *La Barbera and Rosso*, 1989; *Liu*, 1992]. See *Liu* [1992] for a fractal interpretation of the function $2\log(R^t_L)/\log(R^t_A)$.

4.2.3 Property III: Statistical distributions of second-order stream lengths, Schumm lengths, and areas

The topologic analogs of second-order stream length and drainage area are the topologic length, L^t_2, and the total number of links, $2L^t_2+1$, respectively (Section 2.4.3). Table 3.4 gives the mean and standard deviation of L^t_2, for all test sample networks. The mean, $\bar{L}^t_2$, is higher in TM than in SM sample networks. The highest $\bar{L}^t_2$ value observed in SM networks is smaller than the lowest $\bar{L}^t_2$ value observed in TM networks.

Sensitivity of the mean, $\bar{L}^t_2$, to Q is higher in TM than in SM sample networks. In TM sample networks, $\bar{L}^t_2$ varies over the range [1.822, 2.552], which has amplitude 0.73. In all the SM sample networks in Table 3.4, $\bar{L}^t_2$ varies over the narrower range

[1.449, 1.680], which has only amplitude 0.231. For α equal to 0, 1/6, 1/3, 1/2, 2/3, and 5/6, the range of variation of L^t_2 is 0.079, 0.093, 0.207, and 0.043, respectively.

In SM sample networks, L^t_2 reveals no consistent tendency to increase or decrease with either Q or α (Table 4.3). The increase of L^t_2 standard deviation with α is possibly due to the decrease in network magnitude, μ, with α (Table 3.1). In TM sample networks, both the L^t_2 mean and standard deviation increase with Q.

Figures 4.8, 4.9, and 4.10 depict the exceedence probability function of L^t_2 for TM sample networks, SM dendritic networks, and SM trellis networks, respectively. The excedence probability changes markedly with Q for TM sample networks (Figure 4.8), but changes more slightly for SM sample networks (Figures 4.9 and 4.10). In TM sample networks, the form of this function in the semi-log plots is convex for low Q values, and concave for high Q values. In SM networks, the L^t_2 excedence probability takes the approximate form of a power function (Figures 4.9 and 4.10).

4.2.4 Property IV: Proportional relationship between stream frequency and the square of drainage density

The topologic analog of stream frequency, F_S, and drainage density, D, is the ratio of the number of streams, S_S, to the number of links, 2μ-1 (Section 2.4.4). Table 4.4 gives $S_S/(2\mu-1)$ for SM and TM networks. The range of variation of $S_S/(2\mu-1)$ with Q is larger in TM sample networks than in SM sample networks. The interval of variation with Q is [0.568, 0.750] in TM sample networks, [0.620, 0.644] in SM trellis sample networks having α=90°, and [0.632, 0.721] among all SM dendritic sample networks, that is, including all α. The amplitude of variation of $S_S/(2\mu-1)$ with Q is 0.182 in TM sample networks, but only 0.021 in SM trellis sample networks with α=90°, and 0.020, 0.024, 0.024, and 0.045 in SM dendritic sample networks with α equal to 30°, 50°, 70°, and 90°, respectively.

For fixed Q, $S_S/(2\mu-1)$ decreases with α in SM sample networks. For Q=0, $S_S/(2\mu-1)$ decreases from 0.718 for $\alpha=30°$ to 0.620 for $\alpha=90°$ in SM trellis sample networks (an amplitude of variation of 0.098), and from 0.711 for $\alpha=30°$ to 0.671 for $\alpha=90°$ in SM dendritic sample networks (an amplitude of variation of 0.040). Therefore, $S_S/(2\mu-1)$ in SM sample networks generally revealed greater sensitivity to α than to Q.

Figures 4.11, 4.12, and 4.13 depict $S_S/(2\mu-1)$ plotted against μ for TM sample networks, SM dendritic sample networks having $\alpha=70°$, and SM trellis sample networks having $\alpha=90°$, respectively. The reduced sensitivity of $S_S/(2\mu-1)$ to Q in SM networks relatively to TM networks is apparent from these figures. In general, $S_S/(2\mu-1)$ values for any Q value are closer to the prediction of the RT model in SM networks than in TM networks. Agreement with RT model predictions is better in SM networks with dendritic patterns than in those with trellis patterns.

4.2.5 Property V: Variation of mainstream length with basin area

The topologic analogs of mainstream length and basin area are the diameter, d, and the total number of links, $2\mu-1$, respectively (Section 2.4.5). Figures 4.14, 4.15, and 4.16 show logarithmic plots of d versus $2\mu-1$ for TM sample networks, SM dendritic sample networks having $\alpha=70°$, and SM trellis sample networks having $\alpha=90°$, respectively. It is apparent from these figures that the sensitivity of $d(\mu)$ to Q is smaller in SM networks than in TM networks. In general, $d(\mu)$ in SM networks is closer to the predictions of the RT model, shown in Figure 4.14d.

Table 4.5 gives the values of the exponent, θ, and the coefficient, κ, in $d=\kappa(2\mu-1)^{\theta}$, obtained by least-squares linear regression for the sub-networks of each sample network. Because the exponent varies with μ, also given in Table 4.5 are the values of θ and κ computed for the more restricted range of $\mu \geq 50$. While in TM sample networks θ increases with Q over a range of amplitude 0.456 (from 0.386 for Q=0 to 0.842 for Q=5/6), variation in SM dendritic networks is restricted to amplitudes of 0.105, 0.145, 0.115, and 0.137 for α equal to 30°, 50°, 70°, and 90°, respectively, and in SM trellis networks having α=90° this amplitude is 0.247.

In general, θ values in SM sample networks of any given Q different from 1/2, do not deviate largely from the RT model prediction of about 0.5-0.6, and are often closer to the RT model prediction than to the θ value of TM networks obtained with the same given Q. For example, the SM dendritic network, having α=70°, created with Q=0, has θ=0.579 (Table 4.5), closer to the value θ=0.621 of the TM network obtained with Q=1/2 than to the value θ=0.386 of the TM network obtained with Q=0. Also compare Figure 4.15a to Figures 4.14a and 4.14d.

4.2.6 Property VI: Variation of basin distance-weighted area with basin area

The topologic analogs of distance-weighted area and basin area are the total topologic path length, p, and the total number of links, 2μ-1, respectively (Section 2.4.6). Table 4.6 gives the values of the exponent, ϕ, and the coefficient, ε, in $p=\varepsilon(2\mu-1)^{\phi}$, obtained by least-squares linear regression for the sub-networks of each sample network.

Figures 4.17, 4.18, and 4.19 show logarithmic plots of p versus (2μ-1) for TM sample networks, SM dendritic sample networks having α=70°, and SM trellis sample networks having α=90°, respectively. Results are qualitatively similar to those of property V (Section 4.2.5). Variability of p(μ) with Q is reduced in SM networks relatively to TM networks. For Q values different from 1/2, results are generally not largely deviated from those for the TM sample network obtained with Q=1/2 (topologically random), as apparent from comparison of Figures 4.18 and 4.19 with Figure 4.17d.

4.2.7 Property VII: Relation between distance from the basin outlet to centroid and mainstream length

The topologic analog of the channel distance from the outlet to the basin centroid is the mean path length, $\bar{p}$, and the topologic analog of mainstream length is the diameter, d (Section 2.4.7). The modified mean path length, $\bar{p}^*$, defined as $\bar{p}^*=\bar{p}-1$, was introduced in Section 2.4.7.

Table 4.7 gives the mean and standard deviation of the ratio $\bar{p}^*/d$ for the sub-networks of each sample network. Figures 4.20, 4.21, and 4.22 show $\bar{p}^*/d$ plotted against network magnitude, μ, for TM sample networks, SM dendritic sample networks having $\alpha=70°$, and SM trellis sample networks having $\alpha=90°$, respectively. Mean $\bar{p}^*/d$ values are generally lower in SM networks than in TM networks created with the same Q, and is approximately equal to 0.5 in SM networks.

The mean ratio $\bar{p}^*/d$ does not consistenly increase or decrease with Q, in either TM and SM networks. In Chapter 2 (Section 2.4.6), property VI was shown to have very limited sensitivity to Q in TM networks.

4.3 Other Topologic Relations

In addition to the topologic analogs of properties I-VII studied in Section 3.5, in this section we compute a few other topologic variables, and use them to compare SM and TM networks. The topologic variables considered are the total "tree asymmetry" (Section 4.3.1), the fraction of "tributary-source" links (Section 4.3.2), the fraction of "CIS" links

(Section 4.3.3), the network's width (Section 4.3.4), and the width function (Section 4.3.5). Each of these variables is defined in the respective section.

4.3.1 Tree asymmetry

The variable designated "tree asymmetry," denoted A_t, was introduced by *Van Pelt et al.* [1992] to study the topology of neuronal dendrites, and is defined next. Consider the upper node of a link of magnitude μ. The tributary link on the left-hand side of this node has magnitude a, and that on the right-hand side has magnitude μ-a. The partition at this node (Section 3.3.2) is (a, μ-a). The "node asymmetry," A_p, is defined by:

$$A_p(a, \mu\text{-}a) = \begin{cases} \frac{\mu-2a}{\mu-2}: & a \leq \mu-a \\ \frac{a-\mu}{\mu-2}: & a > \mu-a \end{cases} \qquad \mu>2 \tag{4.1a}$$

$$A_p(1, 1) = 1 \qquad \mu=2 \tag{4.1b}$$

The "tree asymmetry," A_t, is the average of all nodes' asymmetry:

$$A_t = \frac{1}{\mu-1} \sum_{i=1}^{\mu-1} A_{pi} \tag{4.2}$$

A_t takes values in the interval [0, 1]. A_t equals 0 in networks where all nodes are symmetric, i.e., all node partitions of magnitude μ are (μ/2, μ/2). A_t equals 1 in networks where all node partitions of magnitude μ are either (1, μ-1) or (μ-1, 1), i.e., networks of Strahler order 2. *Van Pelt et al.* [1992] showed that A_t is sensitive to the Q parameter in the absence of spatial constraints, and that for a given Q, A_t converges to a constant value for large μ.

Table 4.8 gives A_t for each test sample network. A_t increases with Q in TM sample networks, from 0.464 for Q=0 to 0.965 for Q=5/6. The A_t range of variation is more restricted in SM networks. For example, in SM sample networks having $\alpha=70^\circ$, A_t varies from 0.602 for Q=0 to 0.652 for Q=5/6. This range is slightly below the value of A_t=0.657 of the TM network created with Q=1/2 (RT model). In SM trellis sample networks having $\alpha=90^\circ$, A_t values are higher than in dendritic sample networks created with the same Q. For fixed Q, A_t increases with α, especially in trellis sample networks.

4.3.2 Fraction of tributary-source links

Exterior links, or source links, that join an interior link downstream, i.e., that are tributary to a link of magnitude greater than 2, are designated “tributary-source” links, or TS links [*Mock*, 1971]. The number of TS links is denoted by “nTS,” and the fraction of TS links is nTS/μ. The RT model predicts that nTS/μ tends to 1/2 for large μ, however values much lower and much higher than 1/2 have often been observed in nature. *Abrahams* [1977] found a positive correlation between the percentage of TS links (nTS/μ x100%) and a basin’s relative relief.

Table 4.8 gives nTS/μ values for each test sample network. The fraction nTS/μ is strongly correlated with A_t and results are qualitatively similar to those reported in Section 4.3.1.

4.3.3 Fraction of CIS links

The number of CIS and TRANS links (defined in Figure 1.5) are denoted "nCIS" and "nTRANS," respectively. The fraction of CIS links, defined as nCIS/(nCIS + nTRANS), is insensitive to Q in TM networks, and has an expectation value of 0.5, that is, in the absence of spatial constraints, CIS and TRANS links appear with equal likelihood for any Q value. In the TM test sample networks, the fraction of CIS links ranges from 0.492 to 0.532 (Table 4.8), reflecting statistical variability. In the SM sample networks, the fraction of CIS links increases with Q for fixed α, and appears to have a tendency to decrease with α for fixed Q. For fixed Q and α, the fraction of CIS links is smaller in trellis than in dendritic networks.

The fraction of CIS links is the only variable studied which is insensitive to Q in the absence of spatial constraints; and the only variable studied which under spatial constraints gains some sensitivity to Q, hower limited. Low values of this variable have been observed and attributed to spatial constraints (as reviewed by *Abrahams* [1984]). The results obtained here corroborate this interpretation, and also indicate that the fraction of CIS links may depend on network geometry, being smaller for small junction angles, and being smaller in trellis than in dendritic drainage patterns.

4.3.4 Width

Network width, w, is defined as the maximum number of links having the same topologic path length (distance to the root). Table 4.9 gives the values of the exponent, γ, and the coefficient, χ, in (4.3), obtained by least-squares linear regression for the sub-networks of each sample network.

$$w=\chi(2\mu-1)^{\gamma} \tag{4.3}$$

While in TM sample networks γ decreases with Q over a range of amplitude 0.423 (from 0.773 for Q=0 to 0.350 for Q=5/6), variation in SM dendritic networks is restricted to amplitudes of 0.038, 0.101, 0.123, and 0.079 for α equal to 30°, 50°, 70°, and 90°, respectively, and in SM trellis networks having α=90° this amplitude is 0.220.

In general, γ values in SM sample networks of any given Q different from 1/2, do not deviate much from the value γ=0.531 obtained for the TM network created with Q=1/2 (RT model). For example, the SM dendritic network, having α=70°, created with Q=0, has γ=0.519 (Table 3.10), closer to the value γ=0.531 of the TM network created with Q=1/2 than to the value γ=0.773 of the TM network obtained with Q=0.

4.4 Inference of Model Parameter Q Using Maximum Likelihood

In this section, the most likely Q parameter value, designated "ML-Q," is inferred from the topology of sample networks, and compared to the Q value that was effectively used in creating those networks (the "true Q"). The probability of producing each sample network is computed for values of Q in [0, 1], sampled at intervals of amplitude 0.01 (that is, Q equal to 0, 0.01, 0.02, ..., 0.99, 1). This probability is the likelihood of Q. The ML-Q is the Q value sampled whose likelihood is maximal.

The likelihood of a given Q value is computed using the product of the probability p(a, b; Q) of each partition, (a, b), in the network, using (3.1). Due to the large number of TDCN that can be constructed with magnitudes in the range of our sample networks, the likelihood of producing a particular TDCN with any given Q is a very small number (roughly between 10^{-1300} and 10^{-4500}). Therefore, the logarithms of the likelihood values, denoted "Log-L(Q)," are reported instead of the likelihood values themselves.

Figure 4.23 shows the Log-L(Q) plotted against Q for networks created with Q=0. The left-hand column corresponds to SM dendritic sample networks (d, 30°, 0), (d, 50°, 0), (d, 70°, 0), (d, 90°, 0) and the right-hand column corresponds to TM sample networks. SM and TM networks on the same row have the same magnitude. The ML-Q value is indicated by a dashed line. The ML-Q of TM networks coincides with the true Q, equal to zero. The ML-Q of SM dendritic networks is very deviated from the true Q of zero, and varies from 0.34 (for α=30°) to 0.52 (for α=90°).

Figure 4.24 corresponds to networks created with Q=1/2. While TM networks have ML-Q values (dashed line) close to the true Q value (dotted line, marking Q=1/2), SM dendritic networks have ML-Q values lower than 1/2 for small α, and higher than 1/2 for large α.

Figure 4.25 summarizes the correspondence between ML-Q and true Q for SM dendritic networks. The space-filling constraint has restricted the range of variation of ML-Q to a much narrowed interval than the range of true Q. The location of this narrow range depends on junction angle, α, but is in general not situated far from Q=1/2, the parameter value which originates topological randomness. It is possible that this effect is responsible for the success of the random topology model in predicting many topologic properties of channel networks.

In attempting to infer growth model parameter values from maximum-likelihood estimators, or tests of hypotheses, the deviation of maximum-likelihood parameter values from the true parameter values may originate errors in statistical testing, including errors of type I (rejection of the true Q value) and of type II (failure to reject values distant from the true Q). A likely error of type II is the failure to reject the RT model (Q=1/2) even for networks which may have developed by headward growth (Q=0), or other different processes. It is concluded that the failure to account for the space-filling constraint, for junction angles and drainage pattern, may be a serious impediment to model inference from network morphology.

Table 4.1. Arithmetic means and standard deviations of R_B, R^t_A and R^t_L, for the subnetworks of SM and TM test sample networks.

Sample	R_B		R^t_A		R^t_L	
	mean	*st.dev.*	*mean*	*st.dev.*	*mean*	*st.dev.*
SM sample networks: dendritic						
(d,30°,0)	3.362	0.813	4.605	1.546	1.944	0.772
(d,30°,1/6)	3.119	0.744	4.246	1.524	1.782	0.740
(d,30°,1/3)	3.279	0.825	4.491	1.658	1.910	0.806
(d,30°,1/2)	3.202	0.777	4.318	1.506	1.842	0.734
(d,30°,2/3)	3.216	0.734	4.338	1.553	1.853	0.687
(d,30°,5/6)	3.260	0.802	4.376	1.646	1.913	0.809
(d,50°,0)	3.381	0.797	4.533	1.529	1.949	0.775
(d,50°,1/6)	3.359	0.811	4.565	1.572	1.971	0.785
(d,50°,1/3)	3.486	0.962	4.792	1.887	2.084	0.933
(d,50°,1/2)	3.455	0.819	4.648	1.601	2.041	0.784
(d,50°,2/3)	3.823	0.971	5.146	1.604	2.288	0.837
(d,50°,5/6)	3.603	0.829	4.645	1.374	2.182	0.756
(d,70°,0)	3.860	1.050	5.321	2.004	2.310	1.016
(d,70°,1/6)	3.702	0.966	5.025	1.674	2.212	0.886
(d,70°,1/3)	3.726	0.881	5.113	1.753	2.219	0.882
(d,70°,1/2)	3.677	0.915	4.930	1.792	2.255	0.918
(d,70°,2/3)	4.114	1.083	5.387	1.662	2.560	0.927
(d,70°,5/6)	4.107	1.087	5.400	1.647	2.540	0.910
(d,90°,0)	3.988	1.048	5.532	2.034	2.449	1.053
(d,90°,1/6)	3.563	0.850	4.849	1.735	2.177	0.869
(d,90°,1/3)	3.848	1.013	5.226	1.841	2.364	0.926
(d,90°,1/2)	4.001	0.975	5.337	1.726	2.438	0.905
(d,90°,2/3)	4.299	1.136	5.731	1.810	2.699	1.016
(d,90°,5/6)	4.227	1.258	5.672	2.310	2.774	1.288
SM sample networks: trellis						
(t,30°,0)	3.307	0.904	4.537	1.840	1.889	0.902
(t,50°,0)	3.685	1.206	5.073	2.492	2.252	1.229
(t,70°,0)	4.026	1.192	5.662	2.472	2.494	1.256
(t,90°,0)	4.324	1.346	6.457	3.007	2.803	1.492
(t,90°,1/6)	4.352	1.452	6.341	3.001	2.805	1.531
(t,90°,1/3)	3.916	1.283	5.549	2.722	2.522	1.302
(t,90°,1/2)	3.793	1.122	5.378	2.510	2.404	1.224
(t,90°,2/3)	3.871	0.981	5.210	1.866	2.474	0.983
(t,90°,5/6)	4.028	1.003	5.341	1.873	2.637	0.976
TM sample networks:						
Q=0	3.026	0.851	4.361	1.929	1.726	0.948
Q=1/6	3.263	0.929	4.728	2.065	1.912	1.023
Q=1/3	3.498	1.153	5.067	2.541	2.139	1.243
Q=1/2	3.930	1.301	5.590	2.805	2.451	1.385
Q=2/3	4.131	1.413	5.815	2.905	2.682	1.469
Q=5/6	5.200	1.592	7.116	3.394	3.886	1.656

Table 4.2. Correlations, r(·, ·), between topologic-analog Horton ratios for the subnetworks of SM and TM test sample networks.

Sample	$r(R_B, R^t_L)$	$r(R_B, R^t_A)$	$r(R^t_L, R^t_A)$
SM sample networks: dendritic			
(d,30°,0)	0.866	0.871	0.953
(d,30°,1/6)	0.892	0.903	0.960
(d,30°,1/3)	0.889	0.897	0.960
(d,30°,1/2)	0.892	0.879	0.951
(d,30°,2/3)	0.885	0.852	0.939
(d,30°,5/6)	0.925	0.888	0.950
(d,50°,0)	0.875	0.893	0.939
(d,50°,1/6)	0.873	0.888	0.951
(d,50°,1/3)	0.913	0.909	0.965
(d,50°,1/2)	0.894	0.871	0.940
(d,50°,2/3)	0.869	0.852	0.936
(d,50°,5/6)	0.928	0.795	0.884
(d,70°,0)	0.889	0.893	0.966
(d,70°,1/6)	0.881	0.890	0.940
(d,70°,1/3)	0.888	0.877	0.953
(d,70°,1/2)	0.916	0.875	0.934
(d,70°,2/3)	0.918	0.841	0.927
(d,70°,5/6)	0.915	0.900	0.936
(d,90°,0)	0.894	0.895	0.958
(d,90°,1/6)	0.922	0.894	0.949
(d,90°,1/3)	0.896	0.880	0.938
(d,90°,1/2)	0.907	0.858	0.943
(d,90°,2/3)	0.911	0.856	0.924
(d,90°,5/6)	0.958	0.928	0.939
SM sample networks: trellis			
(t,30°,0)	0.917	0.914	0.970
(t,50°,0)	0.954	0.943	0.974
(t,70°,0)	0.939	0.938	0.974
(t,90°,0)	0.936	0.942	0.983
(t,90°,1/6)	0.939	0.942	0.973
(t,90°,1/3)	0.939	0.943	0.965
(t,90°,1/2)	0.945	0.941	0.969
(t,90°,2/3)	0.932	0.882	0.925
(t,90°,5/6)	0.929	0.883	0.902
TM sample networks:			
Q=0	0.944	0.974	0.977
Q=1/6	0.937	0.962	0.979
Q=1/3	0.950	0.962	0.981
Q=1/2	0.928	0.925	0.960
Q=2/3	0.961	0.935	0.968
Q=5/6	0.965	0.932	0.920

Table 4.3. Arithmetic mean and standard deviation of L^t_2 for the subnetworks of SM and TM test sample networks.

Sample	L^t_2	
	mean	*s.d.*
SM sample networks: dendritic		
(d,30°,0)	1.656	0.944
(d,30°,1/6)	1.560	0.897
(d,30°,1/3)	1.614	0.968
(d,30°,1/2)	1.590	0.903
(d,30°,2/3)	1.539	0.855
(d,30°,5/6)	1.598	0.986
(d,50°,0)	1.565	0.872
(d,50°,1/6)	1.626	0.930
(d,50°,1/3)	1.701	1.038
(d,50°,1/2)	1.652	0.949
(d,50°,2/3)	1.678	0.993
(d,50°,5/6)	1.637	0.929
(d,70°,0)	1.642	1.113
(d,70°,1/6)	1.574	0.963
(d,70°,1/3)	1.656	1.061
(d,70°,1/2)	1.614	1.061
(d,70°,2/3)	1.550	0.985
(d,70°,5/6)	1.449	0.895
(d,90°,0)	1.678	1.221
(d,90°,1/6)	1.654	1.087
(d,90°,1/3)	1.709	1.126
(d,90°,1/2)	1.637	1.059
(d,90°,2/3)	1.687	1.177
(d,90°,5/6)	1.680	1.283
SM sample networks: trellis		
(t,30°,0)	1.711	0.973
(t,50°,0)	1.723	1.202
(t,70°,0)	1.785	1.426
(t,90°,0)	2.803	1.960
(t,90°,1/6)	2.372	1.771
(t,90°,1/3)	2.124	1.586
(t,90°,1/2)	2.120	1.613
(t,90°,2/3)	1.759	1.242
(t,90°,5/6)	1.866	1.289
TM sample networks:		
Q=0	1.822	1.013
Q=1/6	1.895	1.111
Q=1/3	1.864	1.333
Q=1/2	1.982	1.517
Q=2/3	2.162	1.695
Q=5/6	2.552	2.671

Table 4.4. Value of $S_S/(2\mu-1)$ for SM and TM test sample networks.

Sample	$S_S/(2\mu-1)$
SM sample networks: dendritic	
(d,30°,0)	0.711
(d,30°,1/6)	0.721
(d,30°,1/3)	0.709
(d,30°,1/2)	0.712
(d,30°,2/3)	0.710
(d,30°,5/6)	0.701
(d,50°,0)	0.699
(d,50°,1/6)	0.698
(d,50°,1/3)	0.694
(d,50°,1/2)	0.690
(d,50°,2/3)	0.675
(d,50°,5/6)	0.675
(d,70°,0)	0.686
(d,70°,1/6)	0.688
(d,70°,1/3)	0.685
(d,70°,1/2)	0.682
(d,70°,2/3)	0.675
(d,70°,5/6)	0.664
(d,90°,0)	0.671
(d,90°,1/6)	0.677
(d,90°,1/3)	0.666
(d,90°,1/2)	0.663
(d,90°,2/3)	0.651
(d,90°,5/6)	0.632
SM sample networks: trellis	
(t,30°,0)	0.718
(t,50°,0)	0.679
(t,70°,0)	0.656
(t,90°,0)	0.620
(t,90°,1/6)	0.629
(t,90°,1/3)	0.643
(t,90°,1/2)	0.644
(t,90°,2/3)	0.641
(t,90°,5/6)	0.623
TM sample networks:	
Q=0	0.750
Q=1/6	0.720
Q=1/3	0.702
Q=1/2	0.664
Q=2/3	0.635
Q=5/6	0.568

Table 4.5. Exponent, θ, and coefficient, κ, in $d=\kappa(2\mu-1)^{\theta}$ for the sub-networks of SM and TM test sample networks, obtained by least-square linear regression of log(d) on log(2μ-1); and standard deviation about the regression line.

	Full μ range			*$\mu \geq 50$*		
Sample	θ	κ	*s.d.*	θ	κ	*s.d.*
SM sample networks: dendritic						
(d,30°,0)	0.528	0.319	0.154	0.454	0.749	0.160
(d,30°,1/6)	0.514	0.327	0.137	0.447	0.711	0.116
(d,30°,1/3)	0.552	0.232	0.143	0.573	0.092	0.154
(d,30°,1/2)	0.577	0.142	0.158	0.636	-0.229	0.201
(d,30°,2/3)	0.577	0.148	0.152	0.595	0.027	0.164
(d,30°,5/6)	0.619	0.028	0.176	0.753	-0.857	0.142
(d,50°,0)	0.550	0.306	0.167	0.376	1.328	0.155
(d,50°,1/6)	0.571	0.229	0.139	0.517	0.553	0.157
(d,50°,1/3)	0.547	0.304	0.168	0.451	0.870	0.170
(d,50°,1/2)	0.634	0.066	0.146	0.686	-0.280	0.123
(d,50°,2/3)	0.652	0.024	0.165	0.629	0.175	0.178
(d,50°,5/6)	0.692	-0.109	0.162	0.748	-0.462	0.170
(d,70°,0)	0.579	0.261	0.137	0.485	0.806	0.129
(d,70°,1/6)	0.611	0.181	0.169	0.521	0.697	0.173
(d,70°,1/3)	0.577	0.284	0.135	0.389	0.818	0.109
(d,70°,1/2)	0.651	0.089	0.160	0.565	0.622	0.173
(d,70°,2/3)	0.693	-0.042	0.139	0.676	0.077	0.116
(d,70°,5/6)	0.692	-0.041	0.148	0.641	0.287	0.148
(d,90°,0)	0.597	0.273	0.148	0.545	0.554	0.101
(d,90°,1/6)	0.600	0.226	0.153	0.535	0.597	0.128
(d,90°,1/3)	0.623	0.174	0.159	0.507	0.867	0.158
(d,90°,1/2)	0.664	0.020	0.162	0.732	-0.425	0.148
(d,90°,2/3)	0.734	-0.120	0.154	0.734	-0.118	0.173
(d,90°,5/6)	0.727	-0.078	0.166	0.661	0.349	0.164
SM sample networks: trellis						
(t,30°,0)	0.508	0.363	0.159	0.420	0.877	0.154
(t,50°,0)	0.603	0.188	0.152	0.517	0.683	0.150
(t,70°,0)	0.598	0.274	0.185	0.533	0.612	0.195
(t,90°,0)	0.560	0.374	0.161	0.509	0.661	0.165
(t,90°,1/6)	0.599	0.305	0.186	0.453	1.141	0.136
(t,90°,1/3)	0.639	0.145	0.191	0.528	0.816	0.223
(t,90°,1/2)	0.616	0.208	0.140	0.500	1.008	0.083
(t,90°,2/3)	0.747	-0.162	0.161	0.771	-0.354	0.177
(t,90°,5/6)	0.807	-0.353	0.147	0.842	-0.577	0.098
TM sample networks:						
Q=0	0.386	0.634	0.142	0.205	1.527	0.083
Q=1/6	0.437	0.545	0.163	0.289	1.290	0.163
Q=1/3	0.491	0.464	0.167	0.346	1.257	0.127
Q=1/2	0.621	0.185	0.190	0.554	0.601	0.204
Q=2/3	0.736	-0.146	0.176	0.871	-1.047	0.128
Q=5/6	0.842	-0.289	0.108	0.825	-0.163	0.095

Table 4.6. Exponent, ϕ, and coefficient, ε, in $p=\varepsilon(2\mu-1)^{\phi}$ for the sub-networks of SM and TM test sample networks, obtained by least-square linear regression of log(p) on log(2μ-1); and standard deviation about the regression line.

Sample	ϕ	ε	*s.d.*
	SM sample networks: dendritic		
(d,30°,0)	1.481	0.038	0.113
(d,30°,1/6)	1.461	0.076	0.097
(d,30°,1/3)	1.493	0.006	0.111
(d,30°,1/2)	1.525	-0.104	0.149
(d,30°,2/3)	1.539	-0.139	0.139
(d,30°,5/6)	1.568	-0.222	0.160
(d,50°,0)	1.506	0.003	0.130
(d,50°,1/6)	1.499	0.010	0.111
(d,50°,1/3)	1.507	-0.007	0.118
(d,50°,1/2)	1.573	0.195	0.135
(d,50°,2/3)	1.593	0.234	0.152
(d,50°,5/6)	1.646	0.405	0.167
(d,70°,0)	1.530	-0.049	0.103
(d,70°,1/6)	1.547	-0.086	0.131
(d,70°,1/3)	1.531	-0.049	0.113
(d,70°,1/2)	1.593	-0.209	0.121
(d,70°,2/3)	1.645	-0.362	0.132
(d,70°,5/6)	1.662	-0.412	0.151
(d,90°,0)	1.546	-0.055	0.120
(d,90°,1/6)	1.554	-0.096	0.113
(d,90°,1/3)	1.581	-0.167	0.137
(d,90°,1/2)	1.639	-0.357	0.147
(d,90°,2/3)	1.670	-0.401	0.150
(d,90°,5/6)	1.686	-0.424	0.165
	SM sample networks: trellis		
(t,30°,0)	1.466	0.069	0.115
(t,50°,0)	1.550	-0.101	0.130
(t,70°,0)	1.559	-0.087	0.125
(t,90°,0)	1.531	-0.002	0.123
(t,90°,1/6)	1.537	0.008	0.148
(t,90°,1/3)	1.583	-0.143	0.151
(t,90°,1/2)	1.572	-0.125	0.114
(t,90°,2/3)	1.662	-0.378	0.148
(t,90°,5/6)	1.744	-0.617	0.156
	TM sample networks:		
Q=0	1.362	1.340	0.088
Q=1/6	1.379	0.292	0.106
Q=1/3	1.438	0.176	0.113
Q=1/2	1.579	-0.161	0.161
Q=2/3	1.683	-0.443	0.161
Q=5/6	1.803	-0.681	0.136

Table 4.7. Mean and standard deviation of $\overline{p}^*/d$, for the subnetworks of SM and TM test sample networks.

Sample	$\overline{p}^*/d$ *mean*	*s.d.*
	SM sample networks: dendritic	
(d,30°,0)	0.497	0.049
(d,30°,1/6)	0.497	0.044
(d,30°,1/3)	0.502	0.048
(d,30°,1/2)	0.505	0.053
(d,30°,2/3)	0.510	0.050
(d,30°,5/6)	0.505	0.051
(d,50°,0)	0.503	0.048
(d,50°,1/6)	0.487	0.038
(d,50°,1/3)	0.492	0.048
(d,50°,1/2)	0.488	0.043
(d,50°,2/3)	0.512	0.042
(d,50°,5/6)	0.509	0.048
(d,70°,0)	0.494	0.041
(d,70°,1/6)	0.491	0.046
(d,70°,1/3)	0.489	0.041
(d,70°,1/2)	0.485	0.037
(d,70°,2/3)	0.498	0.037
(d,70°,5/6)	0.521	0.053
(d,90°,0)	0.487	0.036
(d,90°,1/6)	0.496	0.044
(d,90°,1/3)	0.502	0.046
(d,90°,1/2)	0.522	0.059
(d,90°,2/3)	0.491	0.039
(d,90°,5/6)	0.516	0.050
	SM sample networks: trellis	
(t,30°,0)	0.497	0.049
(t,50°,0)	0.499	0.042
(t,70°,0)	0.499	0.053
(t,90°,0)	0.497	0.052
(t,90°,1/6)	0.484	0.042
(t,90°,1/3)	0.496	0.047
(t,90°,1/2)	0.495	0.045
(t,90°,2/3)	0.487	0.048
(t,90°,5/6)	0.497	0.043
	TM sample networks:	
Q=0	0.540	0.041
Q=1/6	0.523	0.041
Q=1/3	0.557	0.043
Q=1/2	0.559	0.051
Q=2/3	0.485	0.046
Q=5/6	0.533	0.037

Table 4.8. A_t, fraction of CIS links, and fraction of TS links for SM and TM test sample networks.

Sample	A_t	nTS/μ	$nCIS/(nCIS+nTRANS)$
SM sample networks: dendritic			
(d,30°,0)	0.557	0.369	0.431
(d,30°,1/6)	0.520	0.337	0.483
(d,30°,1/3)	0.541	0.357	0.457
(d,30°,1/2)	0.538	0.362	0.497
(d,30°,2/3)	0.542	0.357	0.511
(d,30°,5/6)	0.563	0.392	0.538
(d,50°,0)	0.573	0.352	0.452
(d,50°,1/6)	0.573	0.377	0.481
(d,50°,1/3)	0.584	0.391	0.578
(d,50°,1/2)	0.598	0.391	0.514
(d,50°,2/3)	0.619	0.431	0.535
(d,50°,5/6)	0.636	0.436	0.508
(d,70°,0)	0.602	0.381	0.400
(d,70°,1/6)	0.604	0.390	0.428
(d,70°,1/3)	0.607	0.387	0.485
(d,70°,1/2)	0.625	0.401	0.463
(d,70°,2/3)	0.640	0.415	0.512
(d,70°,5/6)	0.652	0.443	0.520
(d,90°,0)	0.642	0.430	0.358
(d,90°,1/6)	0.630	0.434	0.393
(d,90°,1/3)	0.652	0.456	0.416
(d,90°,1/2)	0.652	0.455	0.444
(d,90°,2/3)	0.690	0.498	0.479
(d,90°,5/6)	0.726	0.559	0.451
SM sample networks: trellis			
(t,30°,0)	0.533	0.351	0.376
(t,50°,0)	0.618	0.420	0.325
(t,70°,0)	0.670	0.491	0.252
(t,90°,0)	0.738	0.618	0.228
(t,90°,1/6)	0.723	0.586	0.285
(t,90°,1/3)	0.698	0.552	0.281
(t,90°,1/2)	0.702	0.552	0.306
(t,90°,2/3)	0.703	0.554	0.300
(t,90°,5/6)	0.746	0.599	0.321
TM sample networks:			
Q=0	0.464	0.343	0.510
Q=1/6	0.522	0.381	0.508
Q=1/3	0.567	0.399	0.492
Q=1/2	0.657	0.487	0.500
Q=2/3	0.722	0.583	0.524
Q=5/6	0.865	0.772	0.532

Table 4.9. Exponent, γ, and coefficient, χ, in $w=\chi(2\mu-1)^{\gamma}$ for the sub-networks of SM and TM test sample networks, obtained by least-square linear regression of log(w) on log(2μ-1); and standard deviation about the regression line.

Sample	γ	χ	*s.d.*
SM sample networks: dendritic			
(d,30°,0)	0.555	-0.098	0.241
(d,30°,1/6)	0.571	-0.086	0.231
(d,30°,1/3)	0.571	-0.123	0.247
(d,30°,1/2)	0.531	0.023	0.261
(d,30°,2/3)	0.517	0.073	0.235
(d,30°,5/6)	0.543	-0.030	0.247
(d,50°,0)	0.534	-0.075	0.275
(d,50°,1/6)	0.521	-0.021	0.233
(d,50°,1/3)	0.541	-0.096	0.256
(d,50°,1/2)	0.514	-0.034	0.232
(d,50°,2/3)	0.468	0.106	0.240
(d,50°,5/6)	0.440	0.178	0.220
(d,70°,0)	0.519	-0.125	0.231
(d,70°,1/6)	0.488	-0.021	0.244
(d,70°,1/3)	0.542	-0.194	0.215
(d,70°,1/2)	0.464	0.051	0.247
(d,70°,2/3)	0.419	0.167	0.211
(d,70°,5/6)	0.473	0.053	0.232
(d,90°,0)	0.500	-0.130	0.225
(d,90°,1/6)	0.470	0.038	0.220
(d,90°,1/3)	0.499	-0.085	0.220
(d,90°,1/2)	0.459	0.109	0.255
(d,90°,2/3)	0.422	0.102	0.210
(d,90°,5/6)	0.421	0.128	0.237
SM sample networks: trellis			
(t,30°,0)	0.587	-0.146	0.257
(t,50°,0)	0.515	-0.065	0.253
(t,70°,0)	0.521	-0.179	0.259
(t,90°,0)	0.577	-0.437	0.248
(t,90°,1/6)	0.530	-0.280	0.261
(t,90°,1/3)	0.502	-0.127	0.263
(t,90°,1/2)	0.502	-0.134	0.246
(t,90°,2/3)	0.416	0.149	0.254
(t,90°,5/6)	0.357	0.338	0.235
TM sample networks:			
Q=0	0.773	-0.595	0.253
Q=1/6	0.712	-0.503	0.254
Q=1/3	0.631	-0.353	0.265
Q=1/2	0.531	-0.203	0.290
Q=2/3	0.499	0.042	0.299
Q=5/6	0.350	0.133	0.237

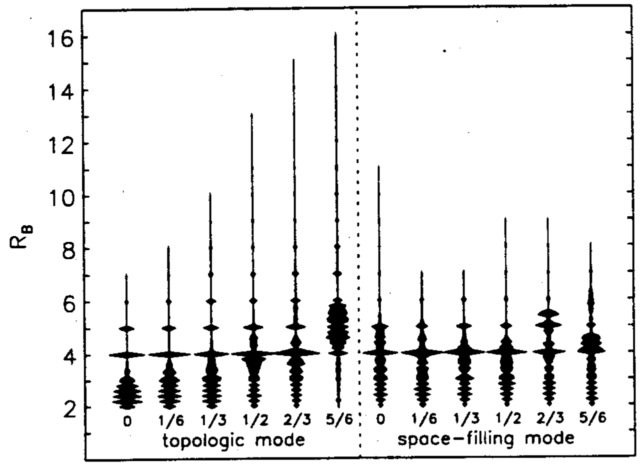

Figure 4.1. R_B distribution histograms for TM and SM dendritic test sample networks, using a bin size of 0.1. For each sample, the vertical reference axis extends from the minimum to maximum values observed, and the width about the axis is proportional to frequency. Where there is no thickness about the reference axis, there are no observed values. The corresponding Q value is indicated at the bottom of each histogram. Sensitivity to Q is marked in the TM sample networks, as shown in Chapter 2, but slight in SM dendritic sample networks. The R_B mean and standard deviation for each sample is given in Table 4.1.

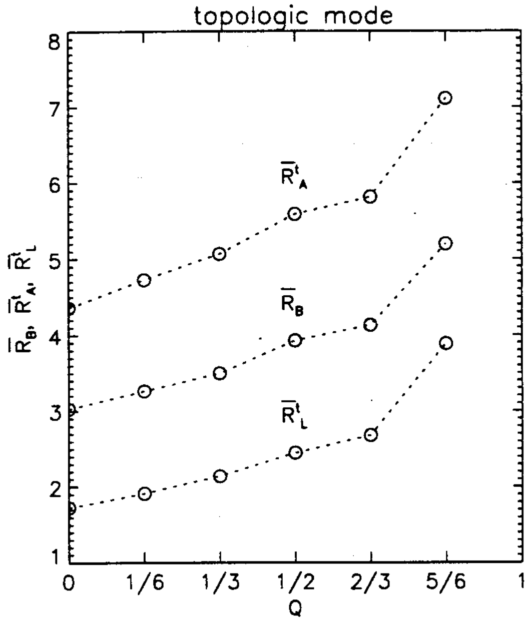

Figure 4.2. Mean values of topologic-analog Horton ratios for the subnetworks of TM test sample networks, plotted against Q. $\bar{R}_B$, $\bar{R}^t_L$ and $\bar{R}^t_A$ are markedly sensitive to Q in TM networks, as shown in Chapter 2. These mean values and corresponding standard deviations are given in Table 4.1.

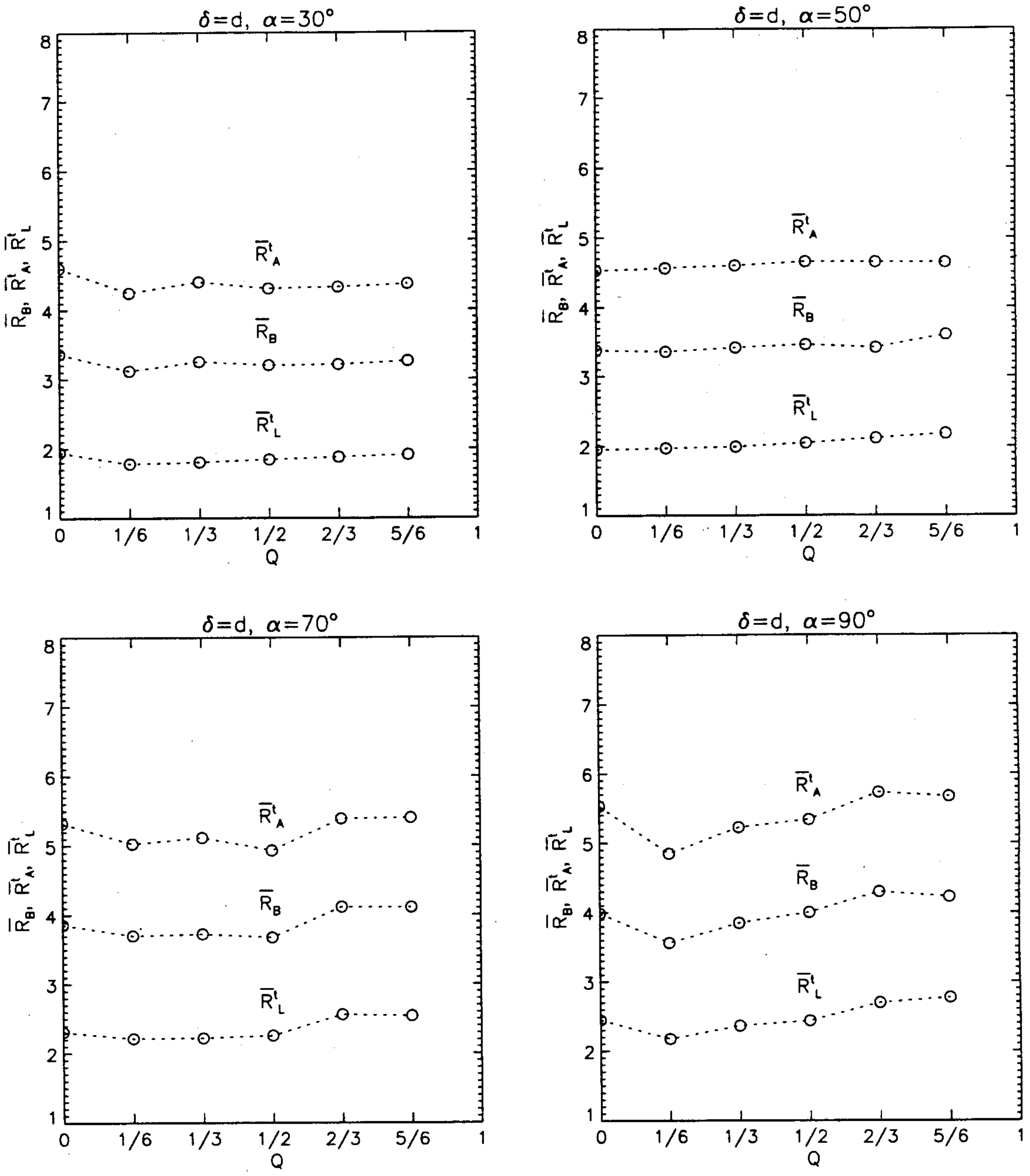

Figure 4.3. Mean values of topologic-analog Horton ratios for the subnetworks of SM dendritic test sample networks, plotted against Q. Sensitivity of $\bar{R}_B$, $\bar{R}^t_L$ and $\bar{R}^t_A$ to Q, if any, is markedly lesser than in TM networks (Figure 4.2). Sensitivity to α is greater than to Q. These mean values and corresponding standard deviations are given in Table 4.1.

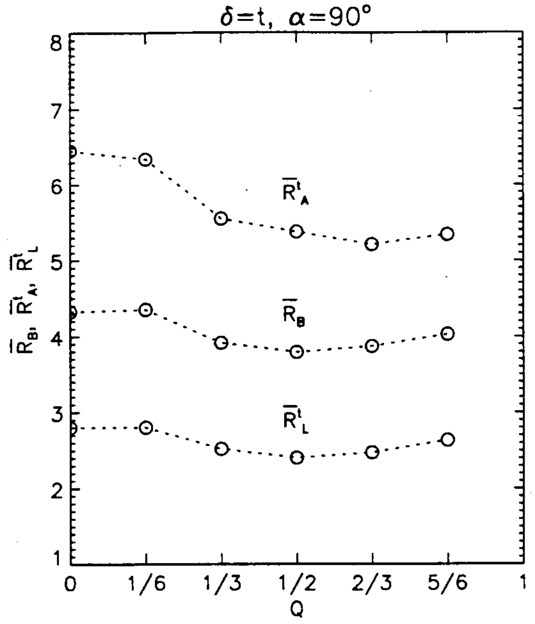

Figure 4.4. Mean values of topologic-analog Horton ratios for the subnetworks of SM trellis test sample networks, plotted against Q. Sensitivity of $\bar{R}_B$, $\bar{R}^t_L$ and $\bar{R}^t_A$ to Q is markedly different than in TM networks and also in SM dendritic networks (Figures 4.2 and 4.3, respectively). These mean values and corresponding standard deviations are given in Table 4.1.

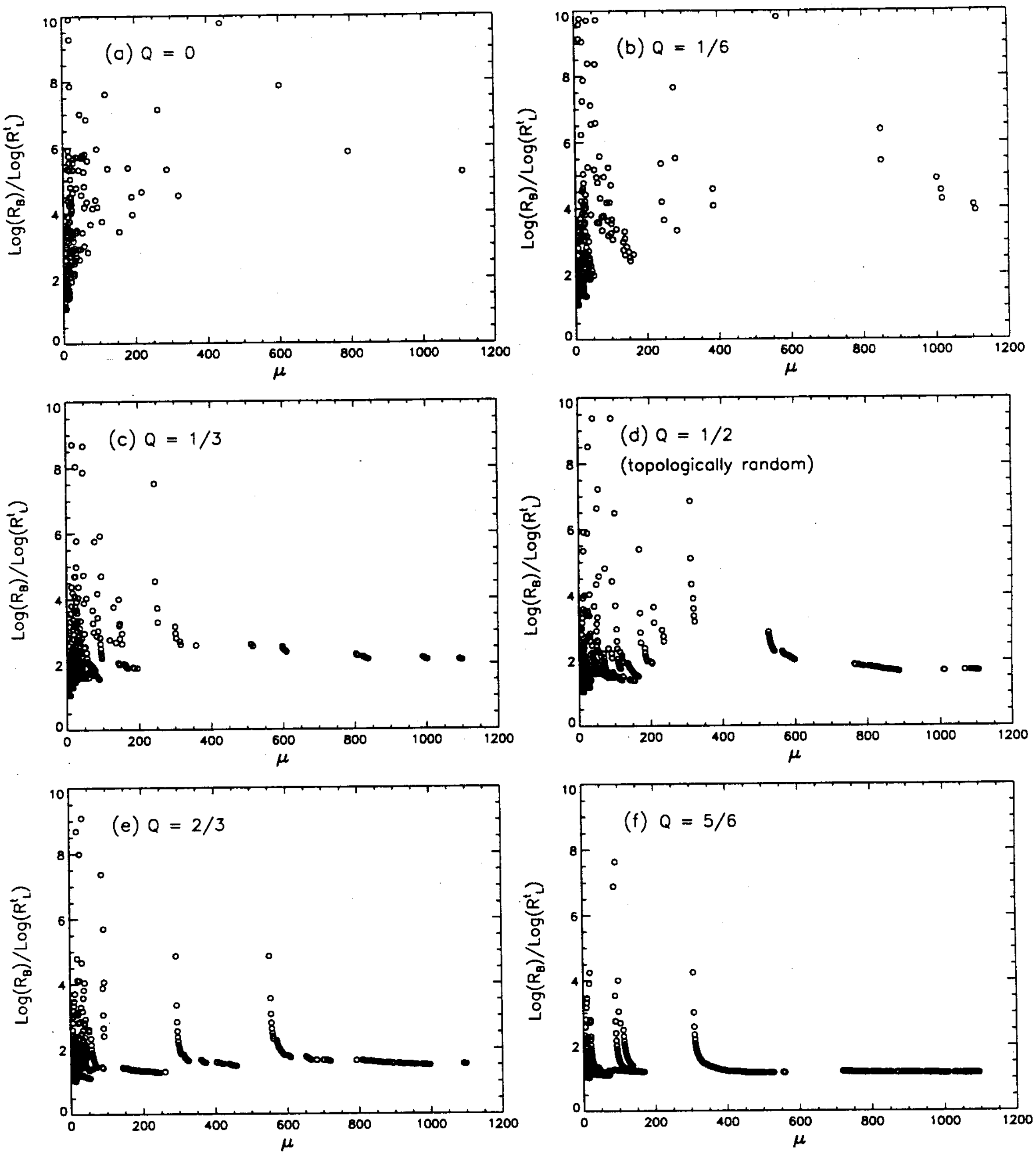

Figure 4.5. $\mathrm{Log}(R_B)/\mathrm{Log}(R^t_L)$ for each subnetwork of TM test sample networks created with various Q values, plotted against subnetwork magnitude, μ. This ratio approaches a value between 1 and 2 for large μ for higher Q values.

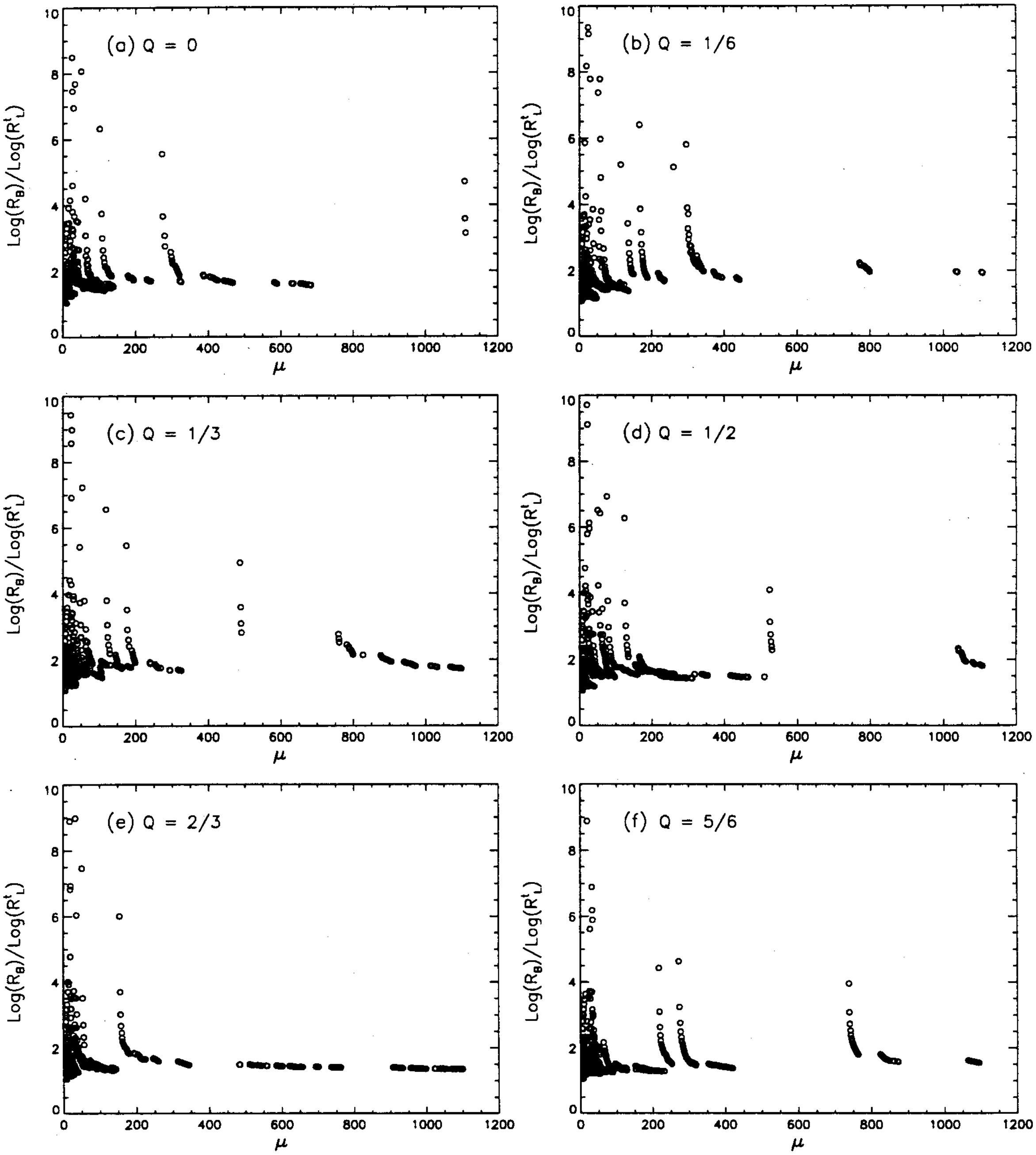

Figure 4.6. Log(R_B)/Log(R^t_L) for each subnetwork of SM dendritic test sample networks having α=70°, created with various Q values, plotted against subnetwork magnitude, μ. This ratio approaches a value between 1 and 2 for large μ for all Q values sampled.

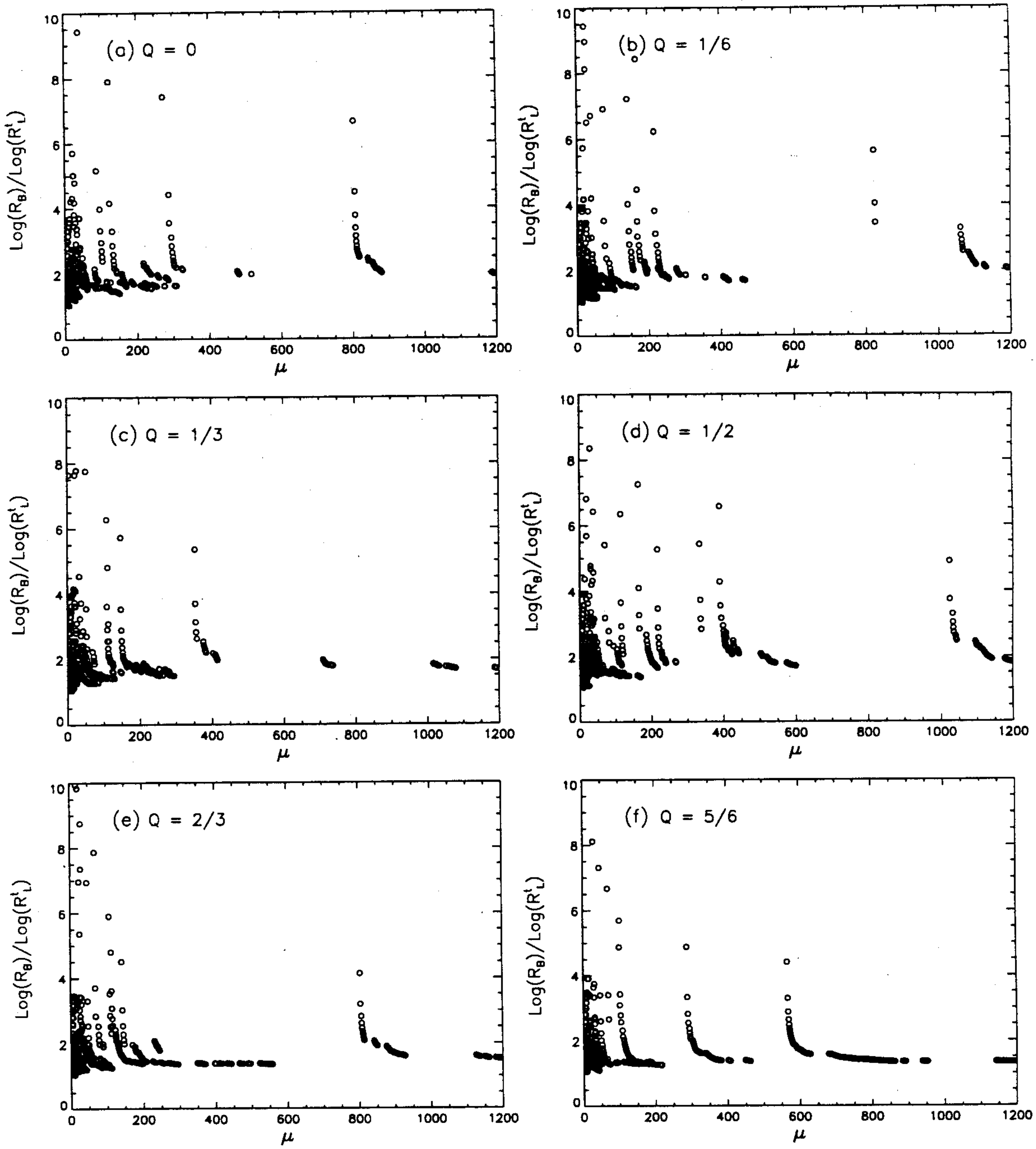

Figure 4.7. Log(R$_B$)/Log(R^t_L) for each subnetwork of SM trellis test sample networks having α=90°, created with various Q values, plotted against subnetwork magnitude, μ. This ratio approaches a value between 1 and 2 for large μ for all Q values sampled.

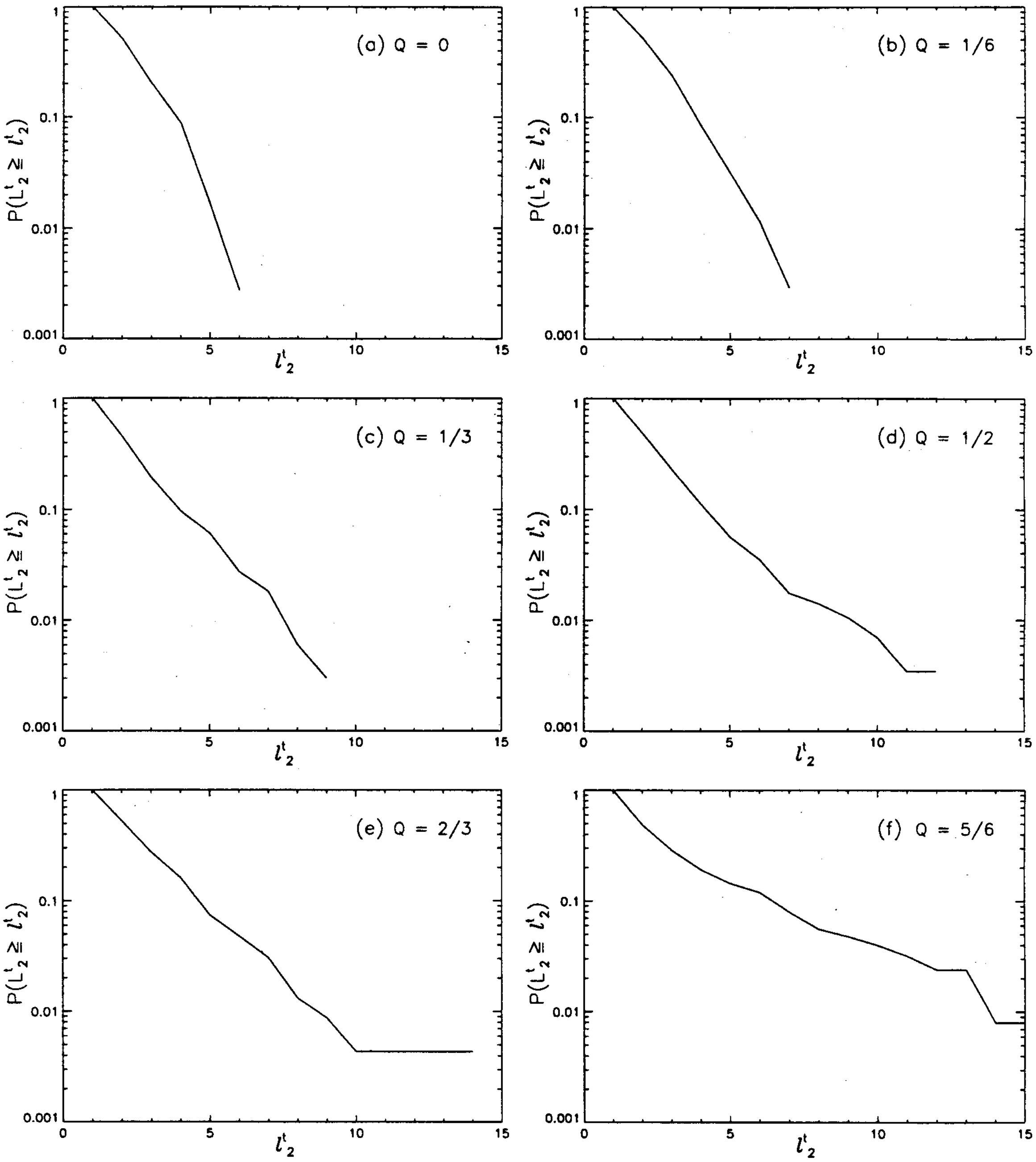

Figure 4.8. L^t_2 exceedence probability for each subnetwork of TM test sample networks created with various Q values, plotted against subnetwork magnitude, μ. The probability of exceedence of any given value is generally higher for larger Q values. L^t_2 means and standard deviations are given in Table 4.3.

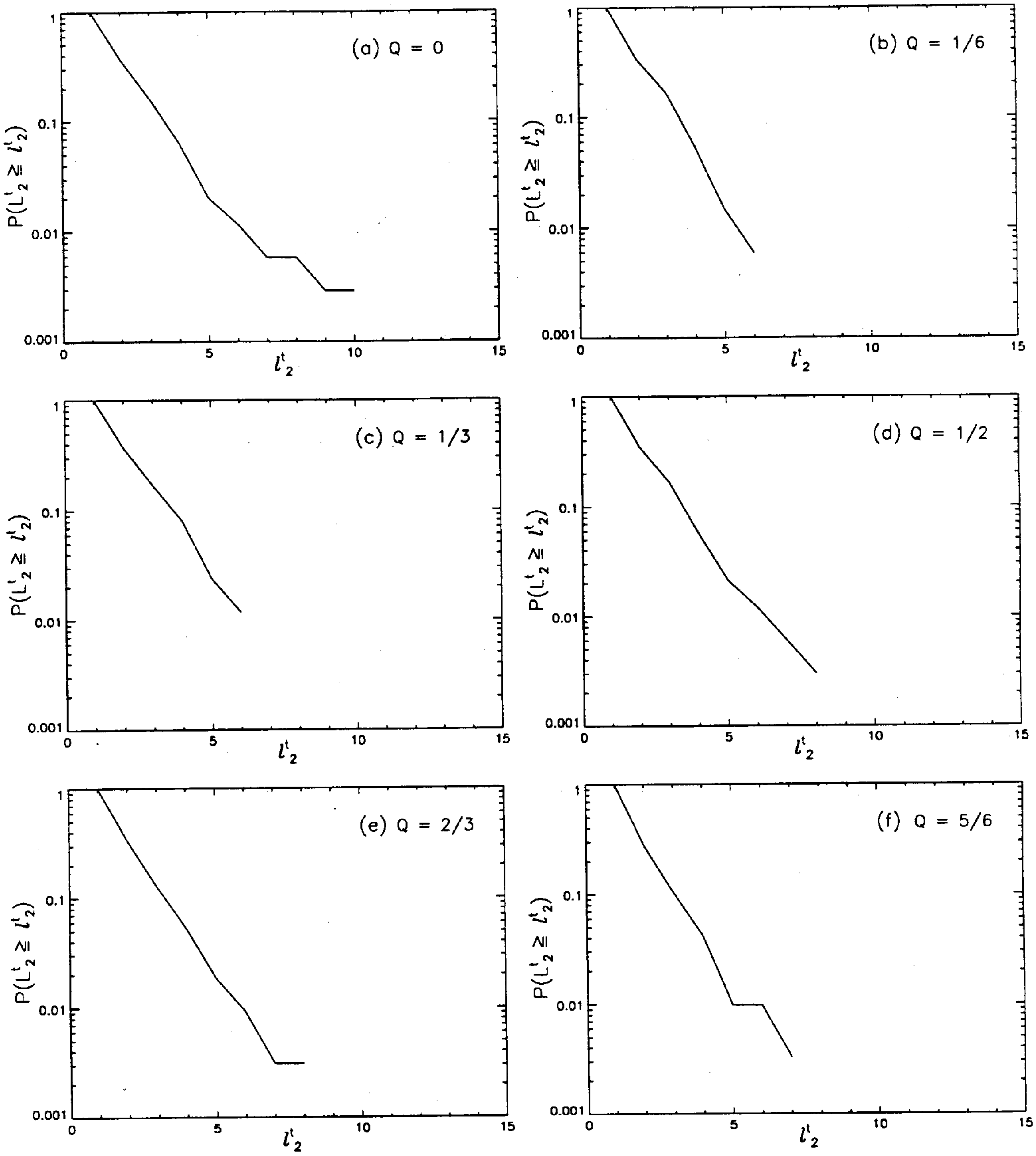

Figure 4.9. L^t_2 exceedence probability for each subnetwork of SM dendritic test sample networks having α=70°, created with various Q values, plotted against subnetwork magnitude, μ. The probability of exceedence of any given value shows no clear variation with Q. L^t_2 means and standard deviations are given in Table 4.3.

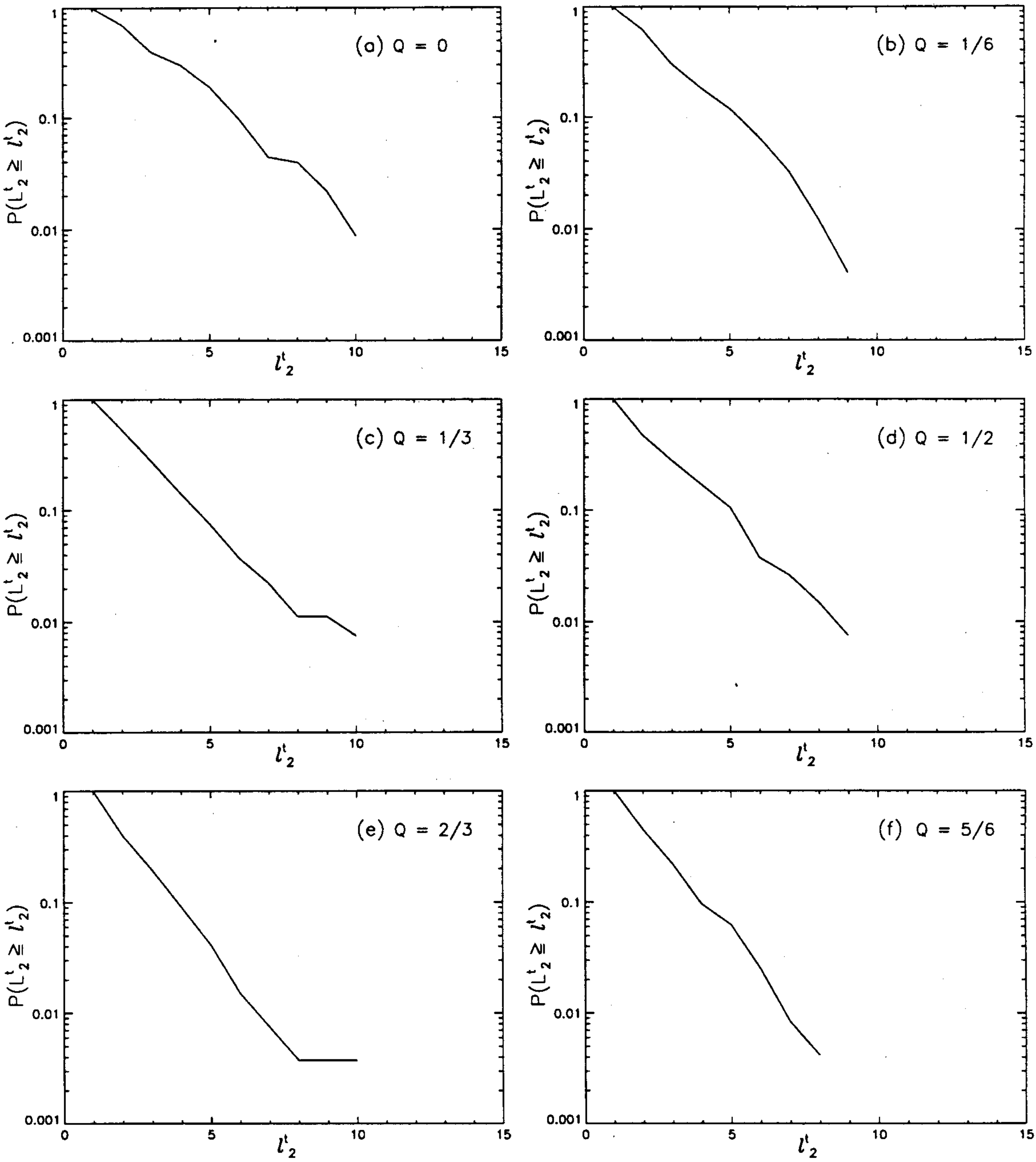

Figure 4.10. L^t_2 exceedence probability for each subnetwork of SM trellis test sample networks having α=90°, created with various Q values, plotted against subnetwork magnitude, μ. The probability of exceedence of any given value shows no clear variation with Q. L^t_2 means and standard deviations are given in Table 4.3.

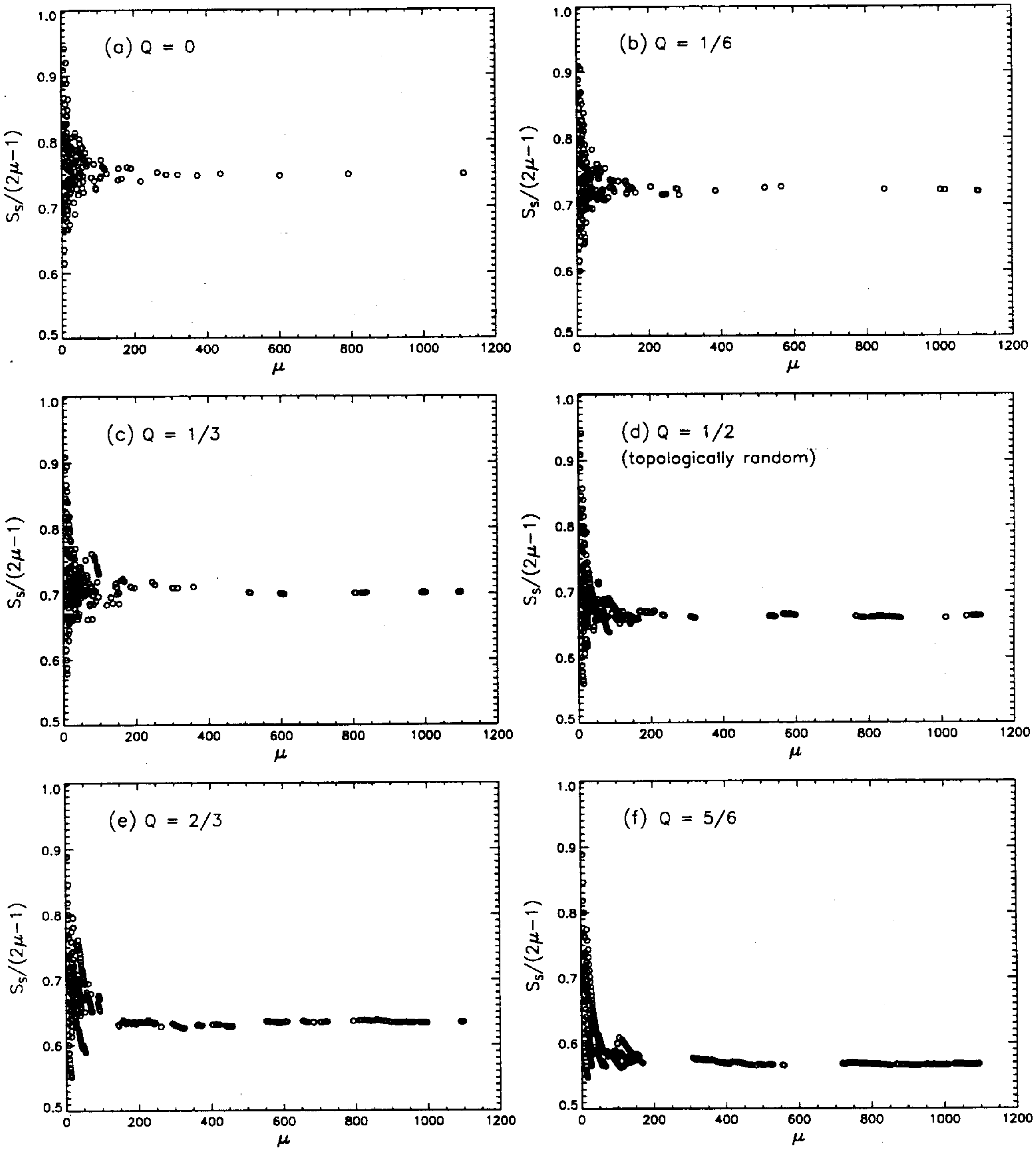

Figure 4.11. Number of streams, S_S, divided by number of links, $2\mu-1$, in each subnetwork of TM test sample networks created with various Q values, plotted against subnetwork magnitude, μ. Ratio $S_S/(2\mu-1)$ decreases from 0.750 for the complete network created with Q=0, to 0.568 for the complete network created with Q=5/6 (Table 4.4).

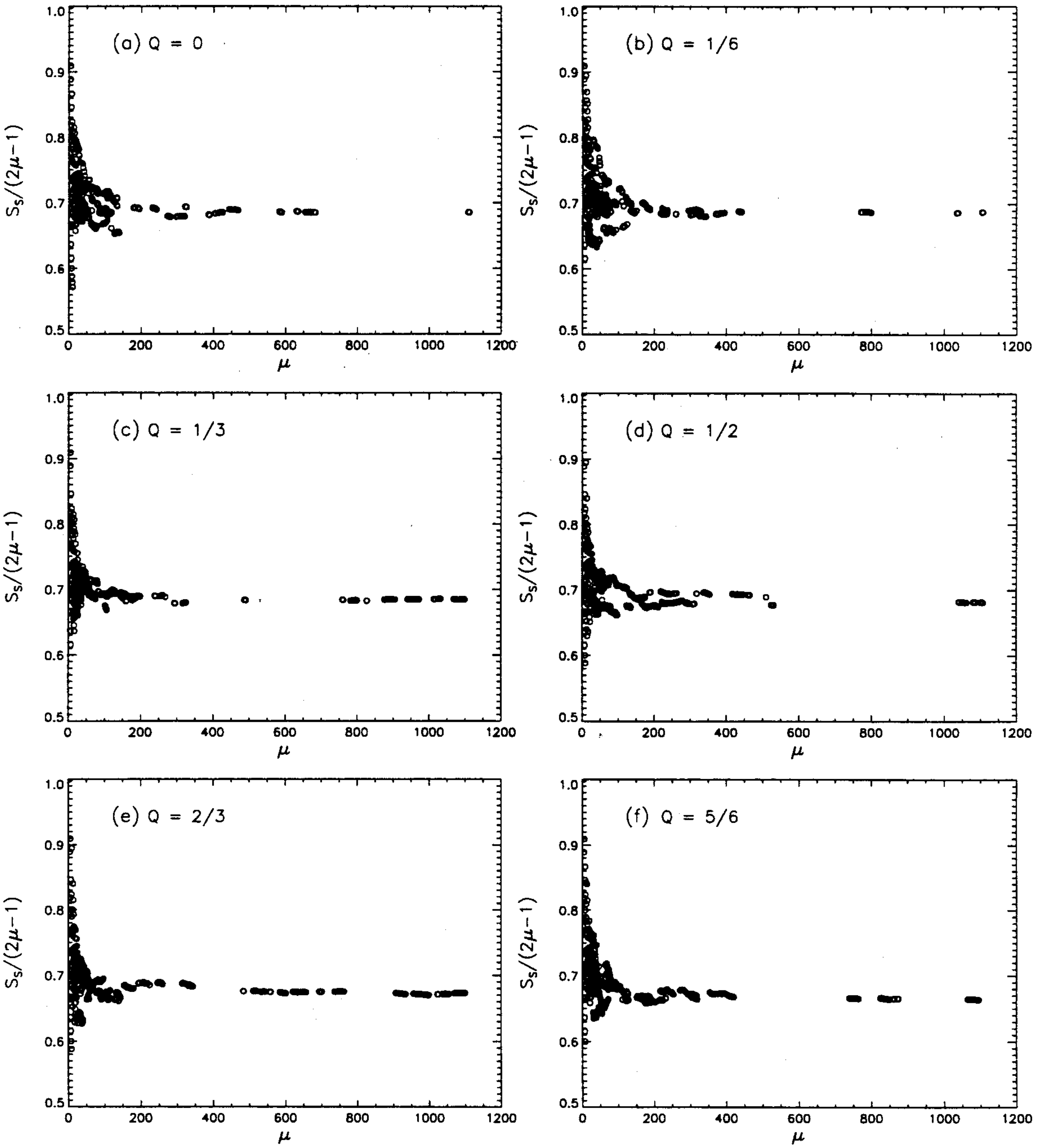

Figure 4.12. Number of streams, S_S, divided by number of links, 2μ-1, in each subnetwork of SM dendritic test sample networks having α=70°, created with various Q values, plotted against subnetwork magnitude, μ. Ratio $S_S/(2\mu-1)$ decreases from 0.686 for the complete network created with Q=0, to 0.664 for the complete network created with Q=5/6 (Table 4.4).

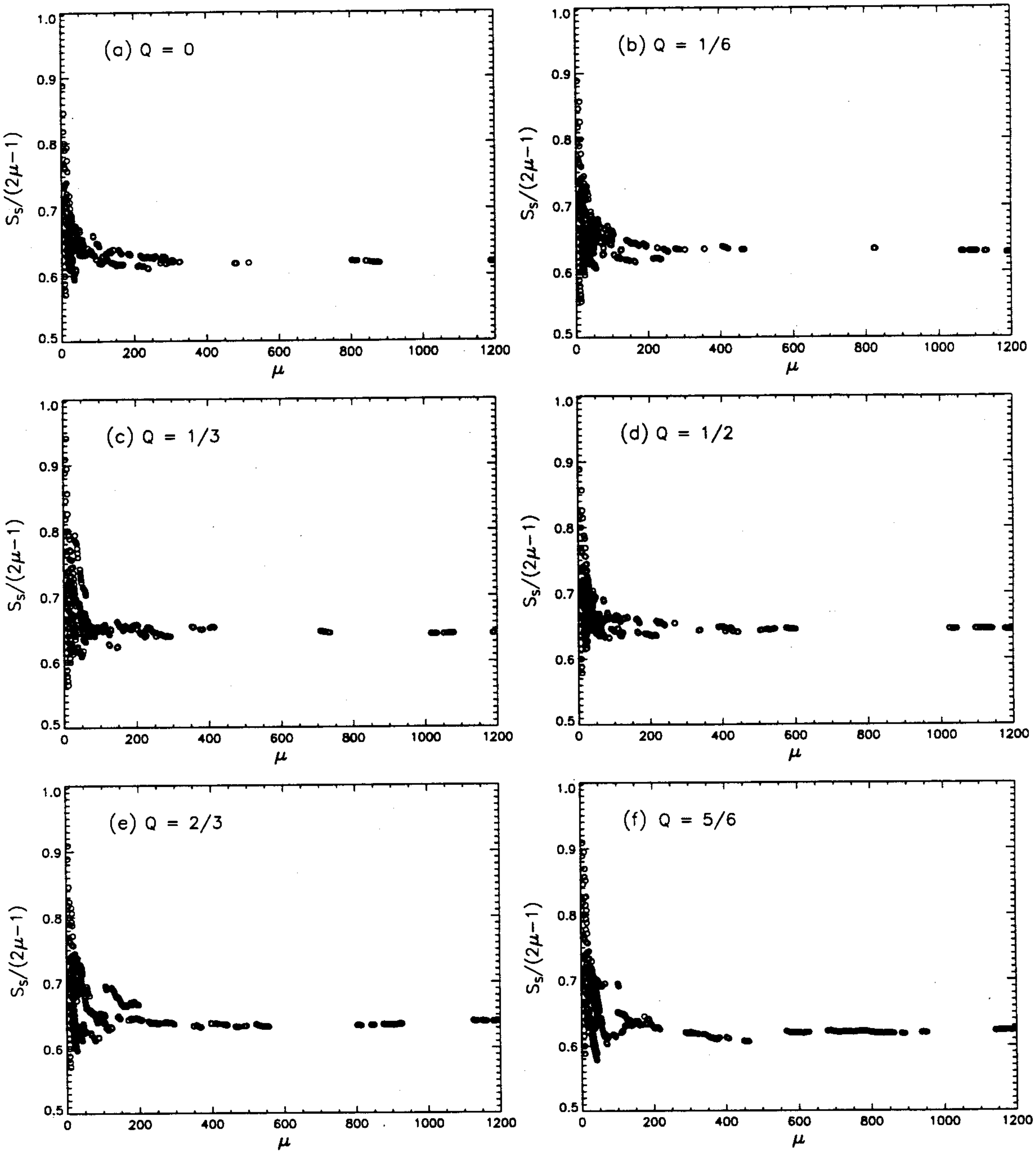

Figure 4.13. Number of streams, S_S, divided by number of links, 2μ-1, in each subnetwork of SM trellis test sample networks, created with various Q values, plotted against subnetwork magnitude, μ. Ratio $S_S/(2\mu-1)$ in the complete sample networks shows no consistent tendency with Q, and varies in the range [0.623, 0.644] (Table 4.4).

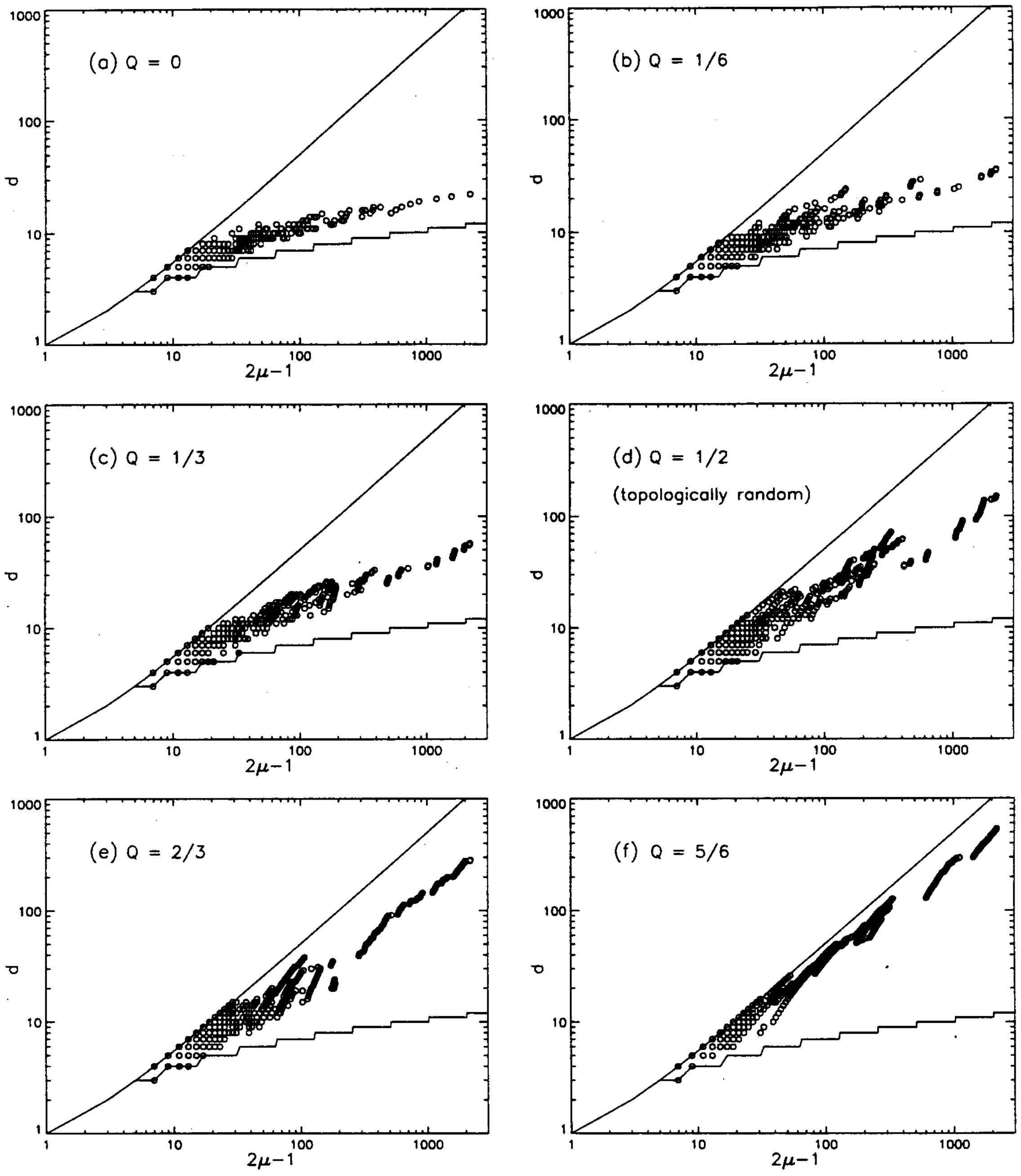

Figure 4.14. Logarithmic plot of diameter, d, of each subnetwork of TM test sample networks created with various Q values, plotted against number of links, 2μ-1. The $d(\mu)$ distribution is sensitive to Q, as shown in Chapter 2. Computed values of the slope and intercept, that is, best fit values of the exponent, θ, and coefficient, κ, in $d=\kappa(2\mu-1)^{\theta}$, are given in Table 4.5.

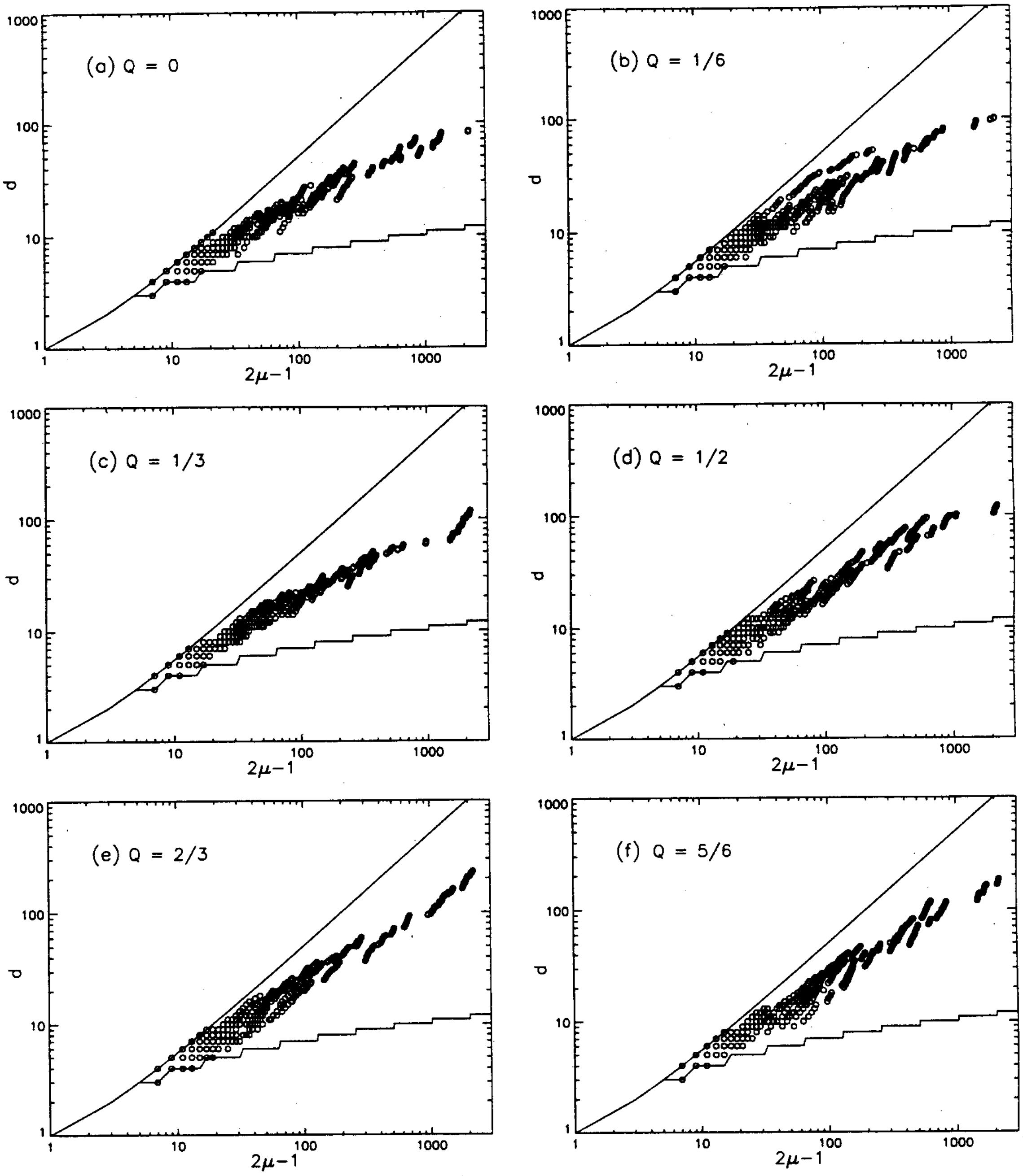

Figure 4.15. Logarithmic plot of diameter, d, of each subnetwork of SM dendritic test sample networks having α=70°, created with various Q values, plotted against number of links, $2\mu-1$. The $d(\mu)$ distribution has limited sensitivity to Q. Computed values of the slope and intercept, that is, best fit values of the exponent, θ, and coefficient, κ, in $d=\kappa(2\mu-1)^{\theta}$, are given in Table 4.5.

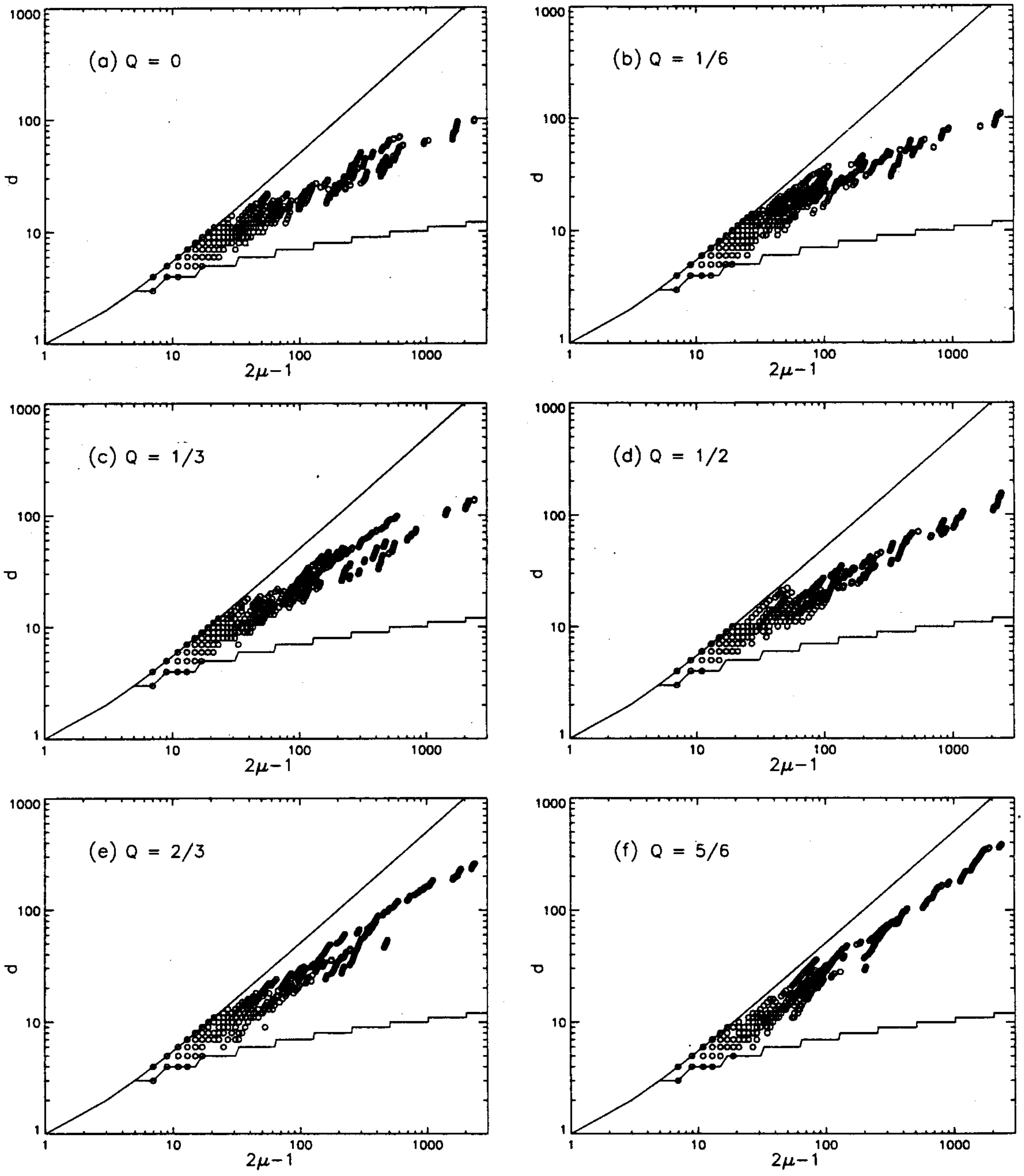

Figure 4.16. Logarithmic plot of diameter, d, of each subnetwork of SM trellis test sample networks having $\alpha=90^{\circ}$, created with various Q values, plotted against number of links, 2μ-1. The $d(\mu)$ distribution has limited sensitivity to Q, except for higher Q values. Computed values of the slope and intercept, that is, best fit values of the exponent, θ, and coefficient, κ, in $d=\kappa(2\mu-1)^{\theta}$, are given in Table 4.5.

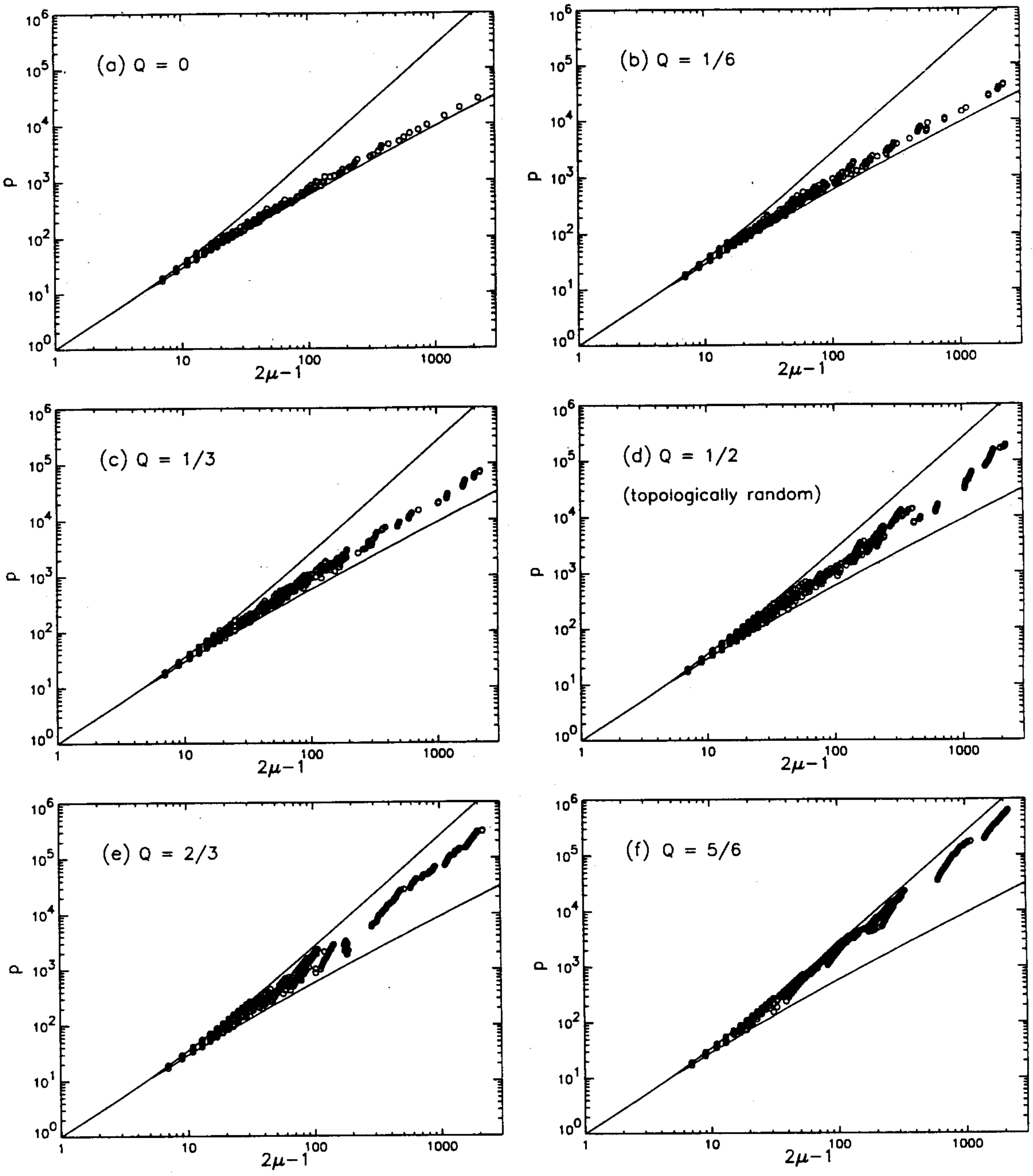

Figure 4.17. Logarithmic plot of total path length, p, of each subnetwork of TM test sample networks created with various Q values, plotted against number of links, 2μ-1. The p(μ) distribution is sensitive to Q, as shown in Chapter 2. Computed values of the slope and intercept, that is, best fit values of the exponent, ϕ, and coefficient, ε, in $p=\varepsilon(2\mu-1)^{\phi}$, are given in Table 4.6.

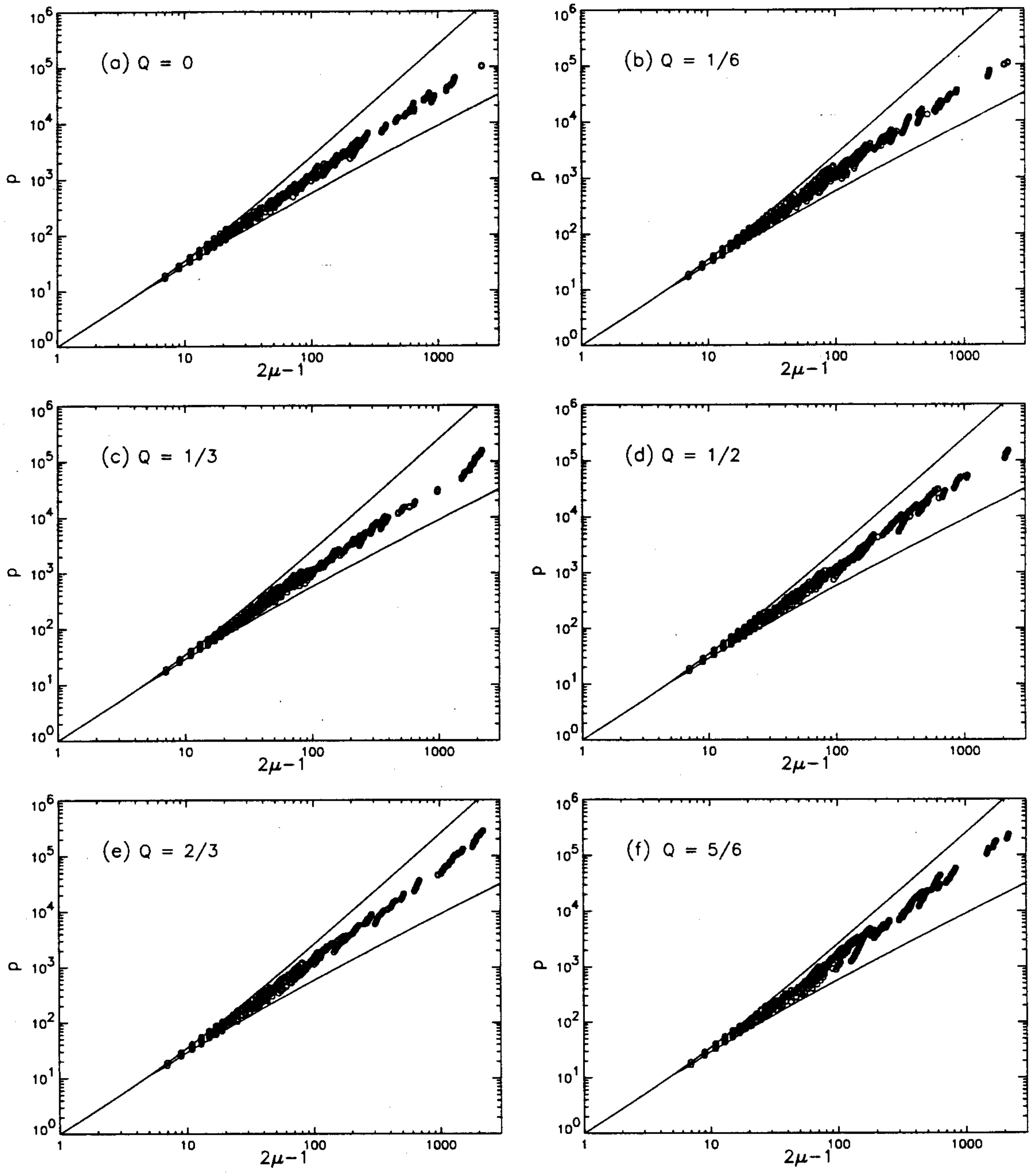

Figure 4.18. Logarithmic plot of total path length, p, of each subnetwork of SM dendritic test sample networks having α=70°, created with various Q values, plotted against number of links, 2μ-1. The p(μ) distribution has limited sensitivity to Q. Computed values of the slope and intercept, that is, best fit values of the exponent, ϕ, and coefficient, ε, in $p=\varepsilon(2\mu-1)^{\phi}$, are given in Table 4.6.

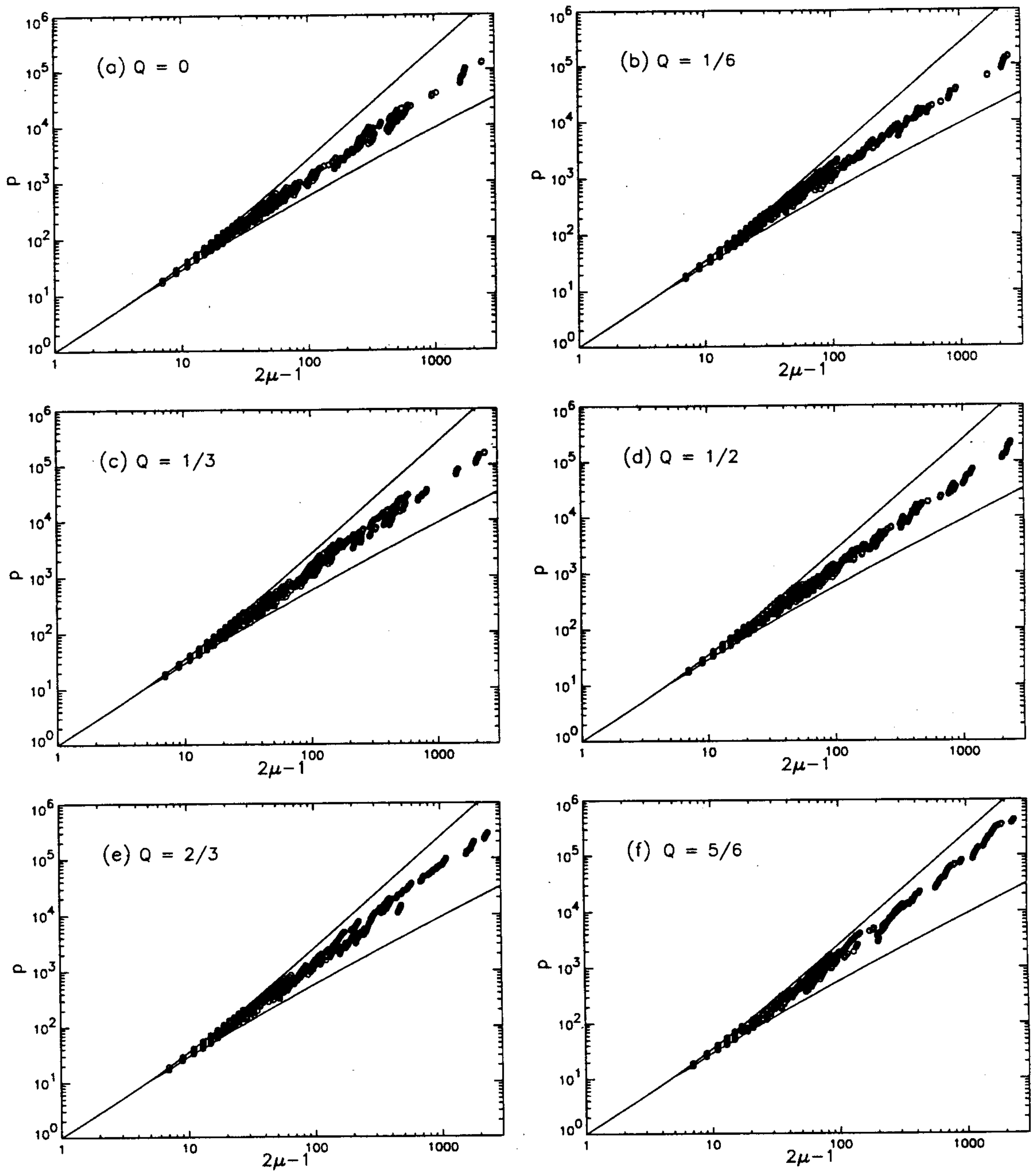

Figure 4.19. Logarithmic plot of total path length, p, of each subnetwork of SM trellis test sample networks having α=90°, created with various Q values, plotted against number of links, 2μ-1. The p(μ) distribution has limited sensitivity to Q, except for higher Q values. Computed values of the slope and intercept, that is, best fit values of the exponent, ϕ, and coefficient, ε, in $p=\varepsilon(2\mu-1)^{\phi}$, are given in Table 4.6.

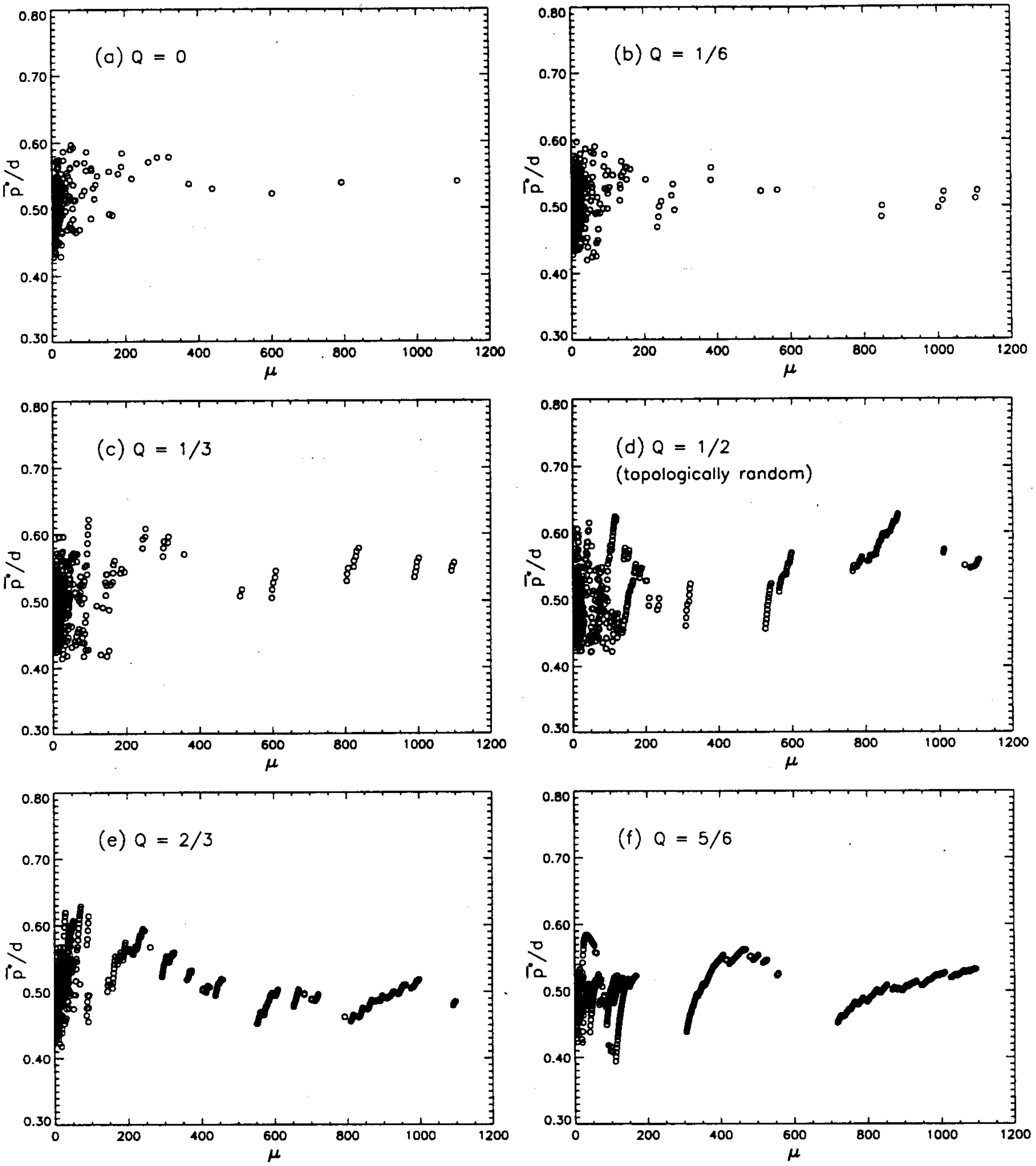

Figure 4.20. Ratio of mean modified path length, $\bar{p}^*$ to diameter, d, for each subnetwork of TM test sample networks created with various Q values, plotted against network magnitude, μ. Ratio $\bar{p}^*/d$ has very limited sensitivity to Q, as shown in Chapter 2. Values of $\bar{p}^*/d$ mean and standard deviation are given in Table 4.7.

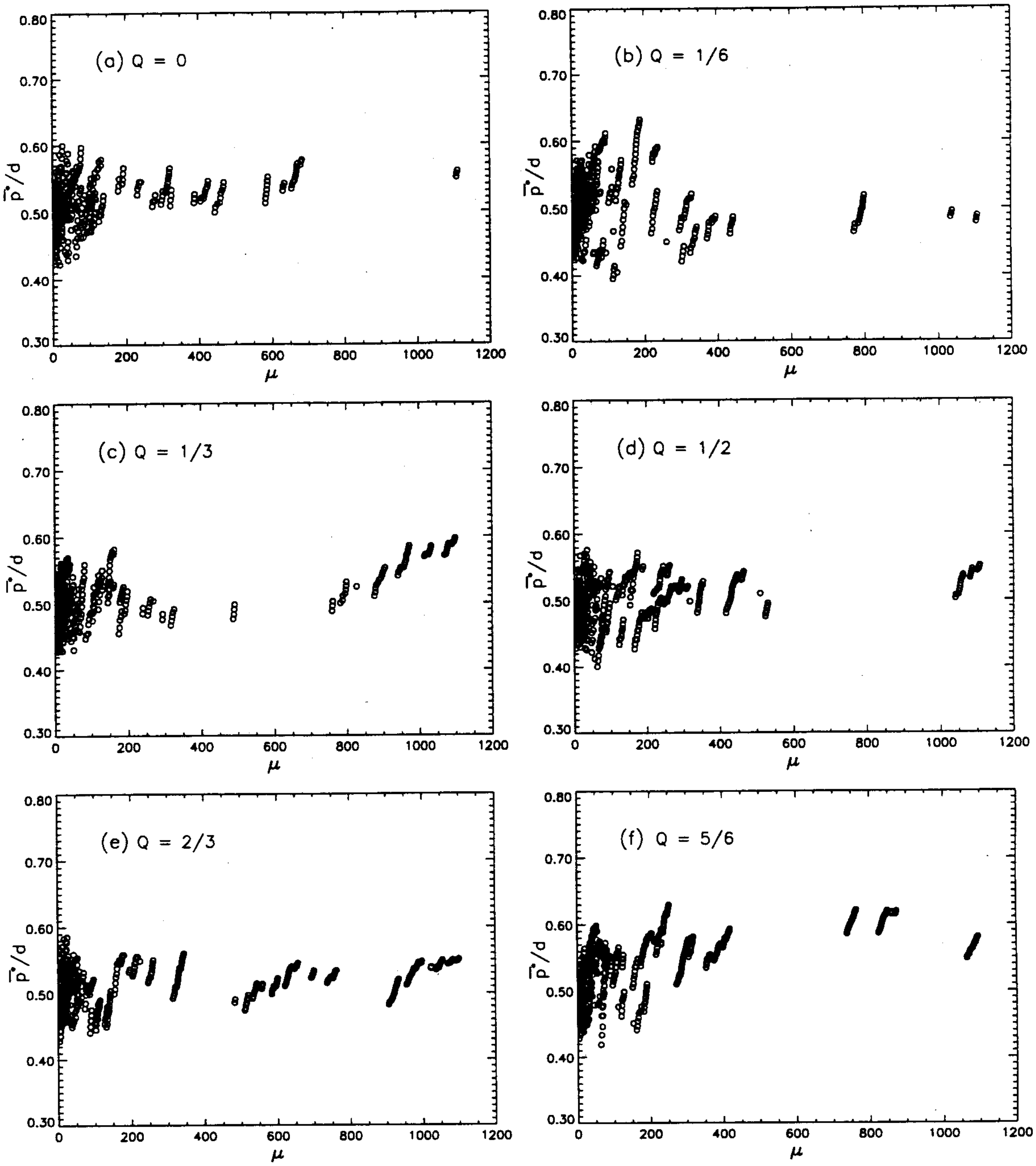

Figure 4.21. Ratio of mean modified path length, $\bar{p}^*$ to diameter, d, for each subnetwork of SM dendritic test sample networks having α=70°, created with various Q values, plotted against network magnitude, μ. Ratio $\bar{p}^*/d$ does not exhibit consistent variation with Q. Values of $\bar{p}^*/d$ mean and standard deviation are given in Table 4.7.

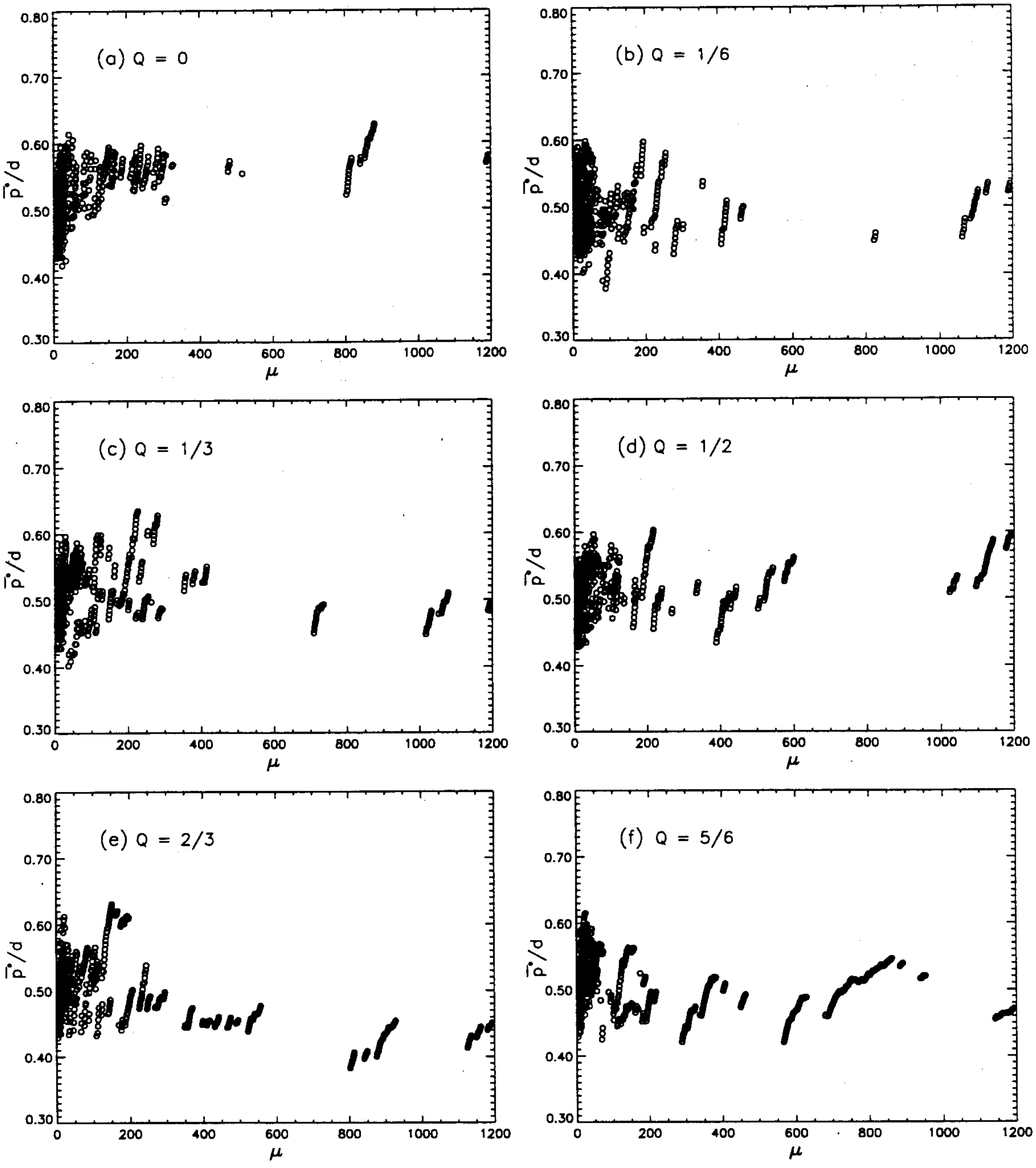

Figure 4.22. Ratio of mean modified path length, $\overline{p}^*$ to diameter, d, for each subnetwork of SM trellis test sample networks having α=90°, created with various Q values, plotted against network magnitude, μ. Ratio $\overline{p}^*/d$ does not exhibit consistent variation with Q. Values of $\overline{p}^*/d$ mean and standard deviation are given in Table 4.7.

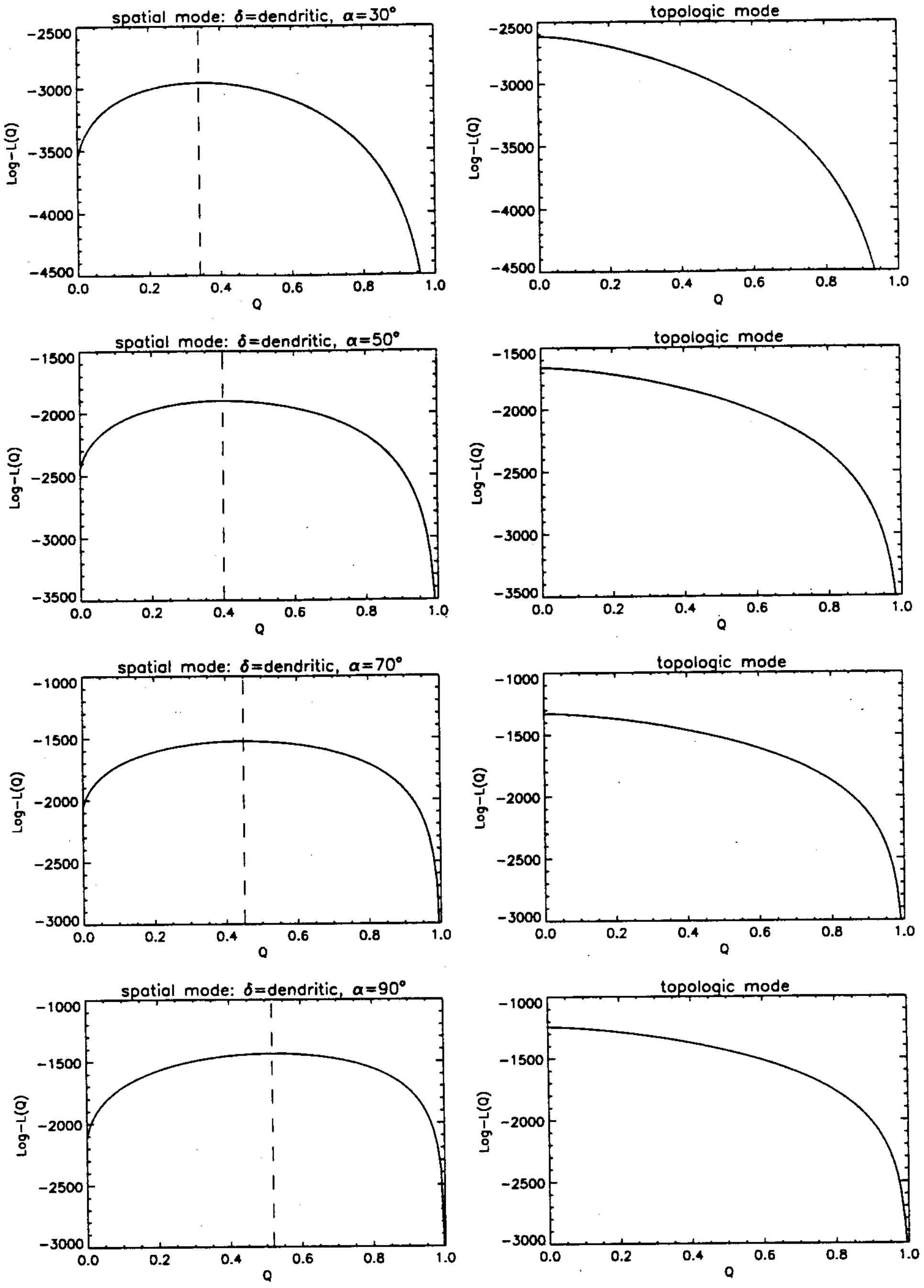

Figure 4.23. Value of Log-Likelihood function, Log-L(Q), plotted against Q, for SM dendritic test sample networks having α equal to 30°, 50°, 70°, and 90° (left-hand column), and TM test sample networks (right-hand column). All networks represented were created with Q=0 (their true Q value). The magnitude of an SM and a TM network on the same row is the same. Dashed line indicates the maximum likelihood Q value (ML-Q). For TM networks, the ML-Q is zero, equal to their true Q value. For SM networks, the ML-Q is deviated from the true Q and increases with α (Table 4.10).

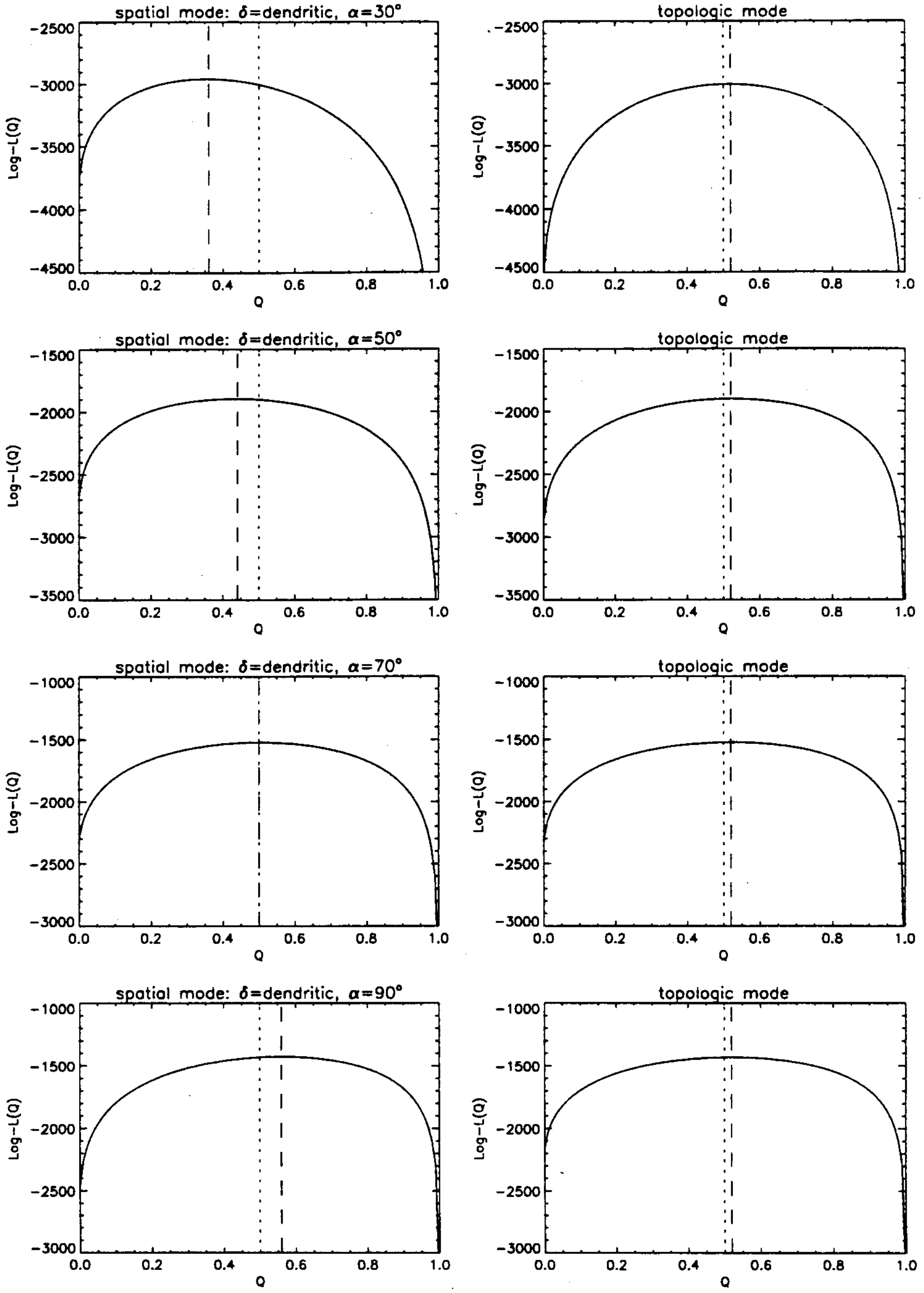

Figure 4.24. Value of Log-Likelihood function, Log-L(Q), plotted against Q, for SM dendritic test sample networks having α equal to 30°, 50°, 70°, and 90° (left-hand column), and TM test sample networks (right-hand column). All networks represented were created with Q=0.5 (their true Q value), indicated by a dotted line. The magnitude of an SM and a TM network on the same row is the same. Dashed line indicates the maximum likelihood Q value (ML-Q). For TM networks, the ML-Q is zero, equal to their true Q value. For SM networks, the ML-Q increases with α, and is deviated from the true Q for all α except α=70° (Table 4.10).

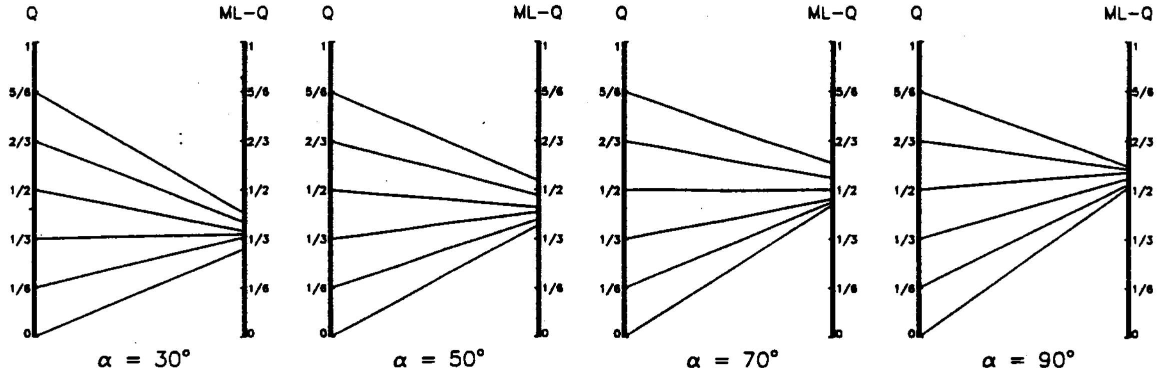

α = 30° α = 50° α = 70° α = 90°

Figure 4.25. Correspondence between the true Q (denoted "Q") and the maximum-likelihood Q (denoted "ML-Q") for SM test sample networks with variable α. For any given Q, the corresponding ML-Q increases with α. The range of variation of ML-Q is much narrower than that of Q, and is not very distant from 1/2 for any of these α values.

Chapter 5

Conclusions

The sensitivity of the coefficients of topologic analogs of channel network planform laws to the parameter of the Q model of network growth [*Van Pelt and Verwer,* 1985] was tested in the absence and in the presence of spatial constraints (Chapters 2 and 4, respectively), yielding different results. Sensitivity to Q was in general more limited in space-filling networks, and showed dependency on the geometric properties of drainage pattern and junction angle. Model inference from network planform requires consideration of space filling and geometric properties.

In Chapter 2, the purely topological version of the Q model was considered, without regard for spatial constraints. All geometric properties such as link lengths, junction angles, drainage pattern, etc., were ignored. It was shown that, in the absence of spatial constraints, the coefficients of the topologic analogs of properties I through VI (listed in Section 1.2) are markedly sensitive to the Q parameter. Only property VII revealed little sensitivity to Q, except for low Q values.

The comparatively small variability of these coefficients in nature, as well as in a variety of models of network growth over a two-dimensional surface, provoked the question, introduced in Chapter 1, of whether there may be a common factor shared by all networks which reduces their topologic sensitivity to growth models. It was hypothesized that such a possible shared factor may be the constraint that all natural networks must, to some approximation, be space filling of a two-dimensional area.

In Chapter 3, a model designated Q_E was introduced (Section 3.3) which is topologically equivalent to the Q model but is capable of generating space-filling networks over a plane surface, with specified properties of link lengths, junction angles, drainage pattern, etc. The Q and Q_E models are topologically equivalent because any given TDCN is equally likely to be produced by either model, in the absence of spatial or other constraints. Test sample space-filling networks were generated (Section 3.4), and the coefficients of the topologic-analogs of properties I through VII, and other additional properties, were computed for these networks (Sections 4.2 and 4.3).

It was shown that the sensitivity of the coefficients of the topologic-analog properties to parameter Q is reduced in space-filling networks comparatively to networks which are not constrained to be space filling. Under the space-filling constraint, the distribution of all topologic variables analyzed, except for the fraction of CIS links, including variables R_B, $R^t{}_L$, $R^t{}_A$, $\log(R_B)/\log(R^t{}_L)$, $L^t{}_2$, $S_s/(2\mu-1)$, d, p, p^*/d, A_t, nTS/μ, w, and p, were sensitive to Q but varied over a restricted range, considerably narrower than the range of variation observed in the absence of space filling (Chapter 2).

The restricted range of variation with Q of topologic variables under the space-filling constraint depends on drainage pattern (dendritic and trellis), δ, and on junction angle, α, and in general is not situated far from the value predicted by the random topology model (RT model) [*Shreve,* 1966]. This is a possible and novel explanation for the predictive success of the RT model. It is also a possible explanation for the approximate agreement between the outcome of a variety of models of network formation that have been published in the literature, noted, e.g., by *Howard* [1972] and *Rodríguez-Iturbe and Rinaldo* [1997].

The fraction of CIS links, nCIS/(nCIS+nTRANS), is the only variable analyzed which is not sensitive to Q in the absence of space filling. The expectation value of this variable is 0.5 for all Q values in the purely topologic mode of operation. Under the space-filling constraint, however, the fraction of CIS links increases significantly with Q for fixed δ and α. For fixed Q and α, the fraction of CIS links is smaller for a trellis than for a dendritic drainage pattern, and for fixed Q and δ, the fraction of CIS links decreases with α.

Maximum-likelihood Q values (ML-Q) were computed (Section 4.4) for the test sample space-filling networks created with the Q_E model with various Q parameter values. ML-Q values were also computed for test sample networks obtained with the same Q values but which were not required to be space filling. The ML-Q of the unconstrained sample networks corresponded closely with the true Q used in creating the networks. The ML-Q of the space-filling sample networks, however, often deviated markedly from the true Q used in the creating the networks. The ML-Q of space-filling networks varied over a much narrower range than the true Q. This narrow range of variation depends on δ and α, but in general is not situated far from the value $Q=1/2$, yielding topological randomness.

Inference of the Q parameter based on maximum likelihood estimates will often lead to erroneous conclusions. Under the space-filling constraint, a given Q value may generate a network which would have very low probability of being generated with that Q value in a purely topological mode of operation of the Q model. Statistical testing of hypotheses using the likelihood values computed without regard for the effects of spatial constraints is likely to lead to errors of type I and type II in statistical testing.

Disagreement between the properties of networks generated by a same given model when operated under the space-filling constraint, and without constraints, was found previously by *Howard* [1971]. Howard did not interpret these results correctly. Noting that the properties of networks generated by different models under the space-filling constraint were in approximate agreement, Howard proposed the explanation that the random component present in all of these models dominates model results. However, the same random component is present in the purely topological mode of operation of these same models, and yet the properties of the resulting networks are clearly distinguishable between models. It is the space-filling constraint, not the stochastic component, which is responsible for the convergence of network properties produced by different models.

It is doubtful that any proposed model of network development in space can be validated based on comparison of any of the measures of network planform studied here with those extracted from natural networks. The agreement between model outcomes and natural channel morphology may be a result of limited sensitivity of these measures to network growth models. In physically-based models of network development [e.g., *Wilgoose et al.*, 1989; *Howard*, 1994], it may be more fruitful to compare geometric measures of simulated networks against observations. Geometric measures of potential interest are the distribution of link lengths, junction angles, and the spatial layout of the network, that is, whether the drainage area to the left and to the right of a mainstream tend to differ little, as is often observed, and whether there is a tendency for tributaries to curve upstream towards the mainstream, as is also often observed [*Abrahams*, 1984], etc.

It has been proposed [e.g., *Abrahams*, 1984] that space-filling constraints originate deviations from the RT model, such as reflected by the fraction of CIS links and the fraction of TS links. I have shown that space-filling constraints not only originate deviations from the RT model but also, and more importantly, that they may be responsible as well for the vast body of agreement of observations with the RT model. Space filling reduces the sensitivity of a large number of topologic variables to network growth processes, restricting their variability to a narrow range that changes with geometric factors, but is generally located close to RT model predictions.

The space-filling constraint and the geometric properties of channel networks are most important determinants of measures of channel network planform. Failure to account for these spatial factors results in errors in model inference from network morphology. It is possible that additional constraints impose further restrictions on measures of channel network planform. In particular, the effects of principles of efficient transport, that is, of minimal energy expenditure, must be considered. Efficient transport may exclude networks with tortuous flow paths, such as those obtained in Chapter 3 using large values of Q, which are not observed in nature.

The results of this research provide an explanation for the predictive ability of the random topology model for channel networks, and for the agreement between the outcomes of widely different models of network formation over a two-dimensional surface. We conclude that current measures of channel network plan view morphology ought not be used for model validation. These results also indicate that model inference from the plan view morphology of space-filling networks in diverse fields of science may be erroneous because the most likely inferred models and parameters may differ from the models and parameters that have produced the network.

References

Abrahams, A. D., The factor of relief in the evolution of channel networks in mature drainage basins, *Am. J. Sci.*, 277, 626-645, 1977.

Abrahams, A. D., Channel networks: a geomorphological perspective, *Water Resour. Res., 20 (2),* 161-188, 1984.

Abrahams, A. D., Channel network topology: regular or random?, in International Geomorphology 1986 Part II, edited by V. Gardner, John Wiley & Sons, Chichester, pp. 145-158, 1987.

Abrahams, A. D., and R. N. Campbell, Source and tributary-source link lengths in natural channel networks, *Bull. Geol. Soc. Amer., 87,* 1016-1020, 1976.

Abrahams, A. D., and D. M. Mark, Acceptance of the random topology model of channel networks: bias in statistical tests, *The Professional Geographer, 38,* 77-81, 1986.

Beer, T., Comment on "On the fractal interpretation of the mainstream length-drainage area relationship" by A. Robert and A. G. Roy, *Water Resour. Res., 27(9),* 2487-2488, 1991.

Berge, C., Théorie des graphes et ses applications, Dunod, Paris, 1958.

Berry, M., T. Hollingworth, E. M. Anderson, and R. M. Flinn, Application of network analysis to the study of the branching patterns of dendritic fields, in *Advances in Neurology, 12,* edited by G. W. Kreutzberg, Raven Press, New York, pp. 217-245, 1975.

Berry, M., and P. M. Bradley, The application of network analysis to the study of branching patterns of large dendritic fields, *Brain Res., 109,* 111-132, 1976.

Bowden, K. L., and J. R. Wallis, Effect of stream-ordering technique on Horton's laws of drainage composition, *Geol. Soc. Am. Bull., 75,* 767-774, 1964.

Cayley, A., On the analytical forms called trees, Second Part, London, Edinburgh, *Dublin Philos. Mag. Jour. Sci., 18,* 374-378, 1859. (Reprinted by Cambridge University Press, *Collected mathematical papers, 4,* 1891.)

Chorley, R. J., Illustrating the laws of morphometry, *Geological Magazine, 94,* 140-150, 1957.

Dacey, M. F., and W. C. Krumbein, Three growth models for stream channel networks, *J. Geol., 84,* 153-163, 1976.

Davis, W. M., Geographical essays, Ginn and Company, Boston, 1909. (Reprinted by Dover, New York, 1954.)

Flint, J. J., Tributary arrangements in fluvial systems, *American J.of Sci., 280,* 26-45, 1980.

Ghosh, A. K., and A. E. Scheidegger, Dependence of stream link lengths and drainage areas on stream order, *Water Resour. Res., 6(2),* 336-340, 1970.

Gilbert, G. K., Report on the Geology of the Henry Mountains, U.S. Geological Survey Rocky Mountain Region, Government Printing Office, Washington, D.C., 1877.

Glock, W. S., The development of drainage systems: a synoptic view, *Geog. Rev., 21,* 475-482, 1931.

Goodchild, M. F., Lakes on fractal surfaces: A null hypothesis for lake-rich landscapes, *Math. Geol., 20(6),,* 615-629, 1988.

Goodchild, M. F., and D. M. Mark, Statistics of hydrologic networks on fractional Brownian surfaces, in *Modeling and Simulation, 16* (Proceedings of the 16th annual Pittsburgh conference), 317-323, Instrument Society of America, Pittsburgh, 1985.

Goodchild, M. F., and B. Klinkenberg, Statistics of channel networks on fractional Brownian surfaces, in *Fractals in Geography,* edited by N. Lam and L. de Cola, pp. 122-141, Prentice Hall, NJ, 1993.

Gravelius, H., Flüsskunde, Band I, Goschenesche Verlag, Berlin and Leipzig, 176 pp., 1914.

Gray, D. M., Interrelationships of watershed characteristics, *J. Geophysical Research, 66,* 1215-1223, 1961.

Hack, J. T., Studies of longitudinal stream profiles in Virginia and Maryland, *U.S. Geol. Surv. Professional Paper 294-B,* 1957.

Harding, E. F., The probabilities of rooted tree-shapes generated by random bifurcation, *J. Appl. Prob., 3,* 44-77, 1971.

Hirsch, R. M., and E. J. Gilroy, Methods of fitting a straight line to data: Examples in water resources, *Water Resour. Bull., 20(5),* 705-711, 1984.

Hollingworth, T., and M. Berry, Network analysis of dendritic fields of Pyramidal cells in neocortex and Purkinje cells in the cerebellum of the rat, *Phil. Trans. R. Soc., B270,* 227-264, 1975.

Horsfield, K., and M. J. Woldenberg, Branching ratio and growth of tree-like structures, *Respiratory Physiology, 63,* 97-107, 1986.

Horsfield, K., M. J. Woldenberg, and C. L. Bowes, Sequential and synchronous growth models related to vertex analysis and branching ratios, *Bull. Math. Biol., 49(4),* 413-429, 1987.

Horton, R. E., Drainage basin characteristics, *Trans. Am. Geoph. U., 13,* 350-361, 1932.

Horton, R. E., Erosional development of streams and their drainage basins: Hydrophysical approach to quantitative morphology, *Geol. Soc. Amer. Bull., 56,* 275-370, 1945.

Howard, A. D., Simulation of stream networks by headward growth and branching, *Geograph. Anal., 3,* 29-50, 1971.

Howard, A. D., Problems of interpretation and simulation models of geologic processes, in *Quantitative geomorphology: Some aspects and applications,* edited by M. Morisawa, pp. 63-82, Binghampton, New York, 1972.

James, W. R., and W. C. Krumbein, Frequency distributions of stream link lengths, *J. Geol., 77*, 544-565, 1969.

Jarvis, R. S., and C. H. Sham, Drainage network structure and diameter-magnitude relation, *Water Resour. Res., 17(4),* 1019-1027, 1981.

Jarvis, R. S., and A. Werritty, Some comments on testing random topology stream network models, *Water Resour. Res., 11(2),* 309-318, 1975.

Jarvis, R. S., and M. J. Woldenberg, Ed., River Networks, ***Benchmark papers in Geology, 80,*** Hutchison Ross Publ., 386 p., 1984.

Karlinger, M. R., and B. M. Troutman, A random spatial network model based on elementary postulates, *Water Resour. Res., 25(5)*, 793-798, 1989.

Kirchner, J. W., Statistical inevitability of Horton's laws and the apparent randomness of stream channel networks, *Geology, 21(7),* 591-594, 1993.

Kirkby, M. J., Tests of the random network model, and its application to basin hydrology, *Earth Surface Proc., 1,* 197-212, 1976.

Krauskopf, K. B., A tale of ten plutons, *Bull. Geol. Soc. Amer., 79,* 1-18, 1968.

Krumbein, W. C., and R. L. Shreve, Some statistical properties of dendritic channel networks, Tech. Rep. 13, Dep. Geol. Sci., Northwestern Univ., 1970.

La Barbera, P., and R. Rosso, On the fractal dimension of stream networks, *Water Resour. Res., 25(4),* 735-741, 1989.

Langbein, W. B., Geometry of river channels, *J. Hydraul. Div., Amer. Soc. Civ. Eng., 90* (HY2), 301-312, 1964.

Langbein, W. B., et al., Topographic characteristics of drainage basins, *U.S. Geol. Surv. Water Supply Paper 968-C,* 1947.

Leopold, L. B., and W. B. Langbein, The concept of entropy in landscape evolution, *U.S. Geol. Surv. Professional Paper 500-A,* 20 p., 1962.

Leopold, L. B., and W. B. Langbein, Association and indeterminacy in geomorphology, in *The fabric of geology*, edited by C. C. Albritton, Jr., pp. 184-192, Addison Wesley, Reading, Mass., 1963.

Liu, T., Fractal structure and properties of stream networks, *Water Resour. Res.*, 28(11), 1992.

MacDonald, N., The usefulness of growth models for trees, letter to the editor, *J. Theor. Biol., 111,* 419-423, 1984.

Mann, C. J., Randomness in nature, *Bull. Geol. Soc. Amer., 81,* 95-104, 1970.

Maxwell, J. C., Quantitative geomorphology of the San Dimas National Forest, California, Proj. NR 389-042, Tech. Rep. 19, Dep. Geology, Columbia Univ., NY, 1960.

Melton, M. A., Geometric properties of mature drainage systems and their representation in an E_4 phase space, *J. Geol., 66(1),* 35-56, 1958.

Melton, M. A., A derivation of Strahler's channel-ordering system, *J. Geol., 67,* 345-346, 1959.

Mesa, O., Analysis of channel networks parameterized by elevation, Ph.D. dissertation, Dep. Civil Eng., Univ. Mississippi, 1986.

Mesa, O. J., and V. K. Gupta, On the main channel-length area relationship for channel networks, *Water Resour. Res., 23(11),* 2119-2122, 1987.

Milton, L. E., The geomorphic irrelevance of some drainage net laws, *Australian Geographical Studies, 4,* 89-95, 1966.

Mock, S. J., A classification of channel links in stream networks, *Water Resour. Res., 7(6),* 1558-1566, 1971.

Montgomery, D. R., and W. E. Dietrich, Source areas, drainage density, and channel initiation, *Water Resour. Res., 25(8),* 1907-1918, 1989.

Montgomery, D. R., and W. E. Dietrich, Channel initiation and the problem of landscape scale, *Science, 255,* 826-830, 1992.

Mueller, J. E., Re-evaluation of the relationship of master streams and drainage basins: Reply, *Geol. Soc. Amer. Bull., 84,* 3127-3130, 1973.

Playfair, J., Illustrations of the Huttonian theory of the Earth, Cadell and Davies, London, 528 p., 1802 (Reprinted by Dover, New York, 1956).

Robert, A. and Roy, A. G., On the fractal interpretation of the mainstream length-drainage area relationship, *Water Resour. Res., 26(5),* 839-842, 1990.

Robert, A. and Roy, A. G., Reply (to T. Beer, Comment on "On the fractal interpretation of the mainstream length-drainage area relationship", same issue), *Water Resour. Res., 27(9),* 2489-2490, 1991.

Rodríguez-Iturbe, I., and J. B. Valdés, The geomorphologic structure of hydrologic response, *Water Resour. Res., 15(6),* 1409-1420, 1979.

Rodríguez-Iturbe, I., and A. Rinaldo, Fractal river basins: Chance and self organization, Cambridge Univ. Press, U.K., 547 pp., 1997.

Scheidegger, A. E., Stochastic branching processes and the law of stream orders, *Water Resour. Res., 2(2),* 199-203, 1966.

Schumm, S. A., Evolution of drainage systems and slopes in badlands at Perth Amboy, New Jersey, *Geol. Soc. Am. Bull., 67,* 597-646, 1956.

Schumm, S. A., The fluvial system, John Wiley & Sons, New York, 338 pp., 1977.

Shreve, R. L., Statistical law of stream numbers, *J. Geol., 74,* 17-37, 1966.

Shreve, R. L., Infinite topologically random channel networks, *J. Geol., 75,* 178-186, 1967.

Shreve, R. L., Stream lengths and basin areas in topologically random channel networks, *J. Geol., 77,* 397-414, 1969.

Shreve, R. L., Mainstream length versus basin area in topologically random channel networks (abstract), *Geol. Soc. Amer. Abstr. Programs, 2,* 682, 1970.

Shreve, R. L., Variation of mainstream length with basin area in river networks, *Water Resour. Res., 10(6),* 1167-1177, 1974.

Shreve, R. L., The probabilistic-topologic approach to drainage-basin geomorphology, *Geology, 3,* 527-529, 1975.

Shreve, R. L., Models for prediction in fluvial geomorphology, *Math. Geol., 11(2),* 165-174, 1979.

Smart, J. S., Statistical properties of stream lengths, *Water Resour. Res., 4(5),* 1001-1014, 1968.

Smart, J. S., Distribution of interior link length in natural channel networks, *Water Resour. Res., 5(6),* 1337-1342, 1969.

Smart, J. S., Channel networks, *Advances in Hydroscience, 8,* 305-346, 1972.

Smart, J. S., The random model in fluvial geomorphology, in *Fluvial Geomorphology,* edited by M. Morisawa, pp. 26-49, Binghampton, New York, 1973.

Smart, J. S., The analysis of drainage network composition, *Earth Surface Proc., 3,* 129-171, 1978.

Smart, J. S., Determinism and randomness in fluvial geomorphology, *Eos Trans. AGU, 60(36),* 651-655, 1979.

Smart, J. S., Link length and channel network topology, *Earth Surface Proc. and Landforms, 6,* 77-79, 1981.

Smart, J. S., and A. J. Surkan, The relation between mainstream length and area in drainage basins, *Water Resour. Res., 3(4),* 963-974, 1967.

Smit, G. J., H. B. M. Uylings, and L. Veldmaat-Wansink, The branching pattern in dendrites of cortical neurons, *Acta Morphol. Neerl. Scand., 9,* 253-274, 1972.

Strahler, A. N., Hypsometric analysis of erosional topography, *Bull. Geol. Soc. Am., 63,* 117-1142, 1952.

Strahler, A. N., Statistical analysis in geomorphic research, *J. Geol., 62,* 1-25, 1954.

Surkan, A. J., Synthetic hydrographs: Effects of network geometry, *Water Resour. Res., 5(1),* 112-128, 1969.

Tarboton, D. G., R. L. Bras, and I. Rodríguez-Iturbe, The fractal nature of river networks, *Water Resour. Res., 24(8),* 1317-1322, 1988.

Taylor, A. B., and H. E. Schwarz, Unit hydrograph lag and peak flow related to basin characteristics, *Trans. Am. Geoph. U., 33,* 235-246, 1952.

Thakur, T. R., and A. E. Scheidegger, A test of the statistical theory of meander formation, *Water Resour. Res., 4(2),* 317-329, 1968.

Troutman, B. M., and M. R. Karlinger, Averaging properties of channel networks using methods in stochastic branching theory, in *Scale Problems in Hydrology,* edited by V. K. Gupta, I. Rodríguez-Iturbe, and E. F. Wood, pp. 185-216, D. Reindel, Norwell, Mass., 1986.

Troutman, B. M., and M. R. Karlinger, Comment on: Statistical inevitability of Horton's laws and the apparent randomness of stream channel networks (by J. W. Kirchner, Geology, *21(7)*, 1993), *Geology, 22(6),* 573-574, 1994.

Uylings, H. B. M., J. Van Pelt, and R. W. H. Verwer, Topological analysis of individual neurons, in *Computer Techniques in Neuroanatomy,* edited by J. J. Capowski, Plenum, 1989.

Van Pelt, J., and R. W. H. Verwer, Growth models (including terminal and segmental branching) for topological binary trees, *Bull. Math. Biol., 47 (3),* 323-336, 1985.

Van Pelt, J., and R. W. H. Verwer, Topological properties of binary trees grown with order-dependent branching probabilities, *Bull. Math. Biol., 48(2),* 197-211, 1986.

Van Pelt, J., H. B. M. Uylings, R. W. H. Verwer, R. J. Pentney, and M. J. Woldenberg, Tree asymmetry - a sensitive and practical measure for binary topological trees, *Bull. Math. Biol., 54(5),* 759-784, 1992.

Verwer, R. W. H., and J. Van Pelt, A new method for the topological analysis of neuronal tree structures, *J. Neurosci. Metods, 8,* 335-351, 1983.

Verwer, R. W. H., J. Van Pelt, and H. B. M. Uylings, An introduction to topological analysis of neurones, in *Quantitative Meth. in Neuroanatomy,* edited by M. G. Stewart, John Wiley & Sons, 1992.

Watson, R. A., Discussion: Is geology different: A critical discussion of 'The Fabric of Geology,' *Phil. Sci., 33,* 172-185, 1966.

Watson, R. A., Explanation and prediction in geology, *J. Geol., 77,* 488-494, 1969.

Werner, C., and J. S. Smart, Some new methods of topologic classification of channel networks, *Geogr. Anal., 5,* 271-295, 1973.

Werritty, A., The topology of stream networks, in *Spatial Analysis in Geomorphology,* edited by R. J. Chorley, pp. 167-196, Methuen, London, 1972.

Woldenberg, M. J., James Keill (1708) and the morphometry of the microcosm: geometric progression laws in arterial trees, in *Process and Form in Geomorphology,* edited by D. R. Stoddart, Routledge, New York, 1997.

Zernitz, E. R., Drainage patterns and their significance, *J. Geol., 40,* 498-521, 1932.

Appendix A

Notation

A	basin area.
A_ω	area of a basin of order ω.
A_t	total asymmetry of a network.
A^t_ω	topologic analog of A_ω: number of links in a network of order ω.
d	diameter.
D	drainage density.
F	link frequency.
F_s	stream frequency.
G_B, G^t_L, G^t_A	geometric-mean bifurcation ratio, and topologic-analog length, and area ratios.
L	mainstream length.
L_{ca}	channel distance from outlet to network center of gravity.
L_ω	length of a stream of order ω.
L^t_ω	topologic analog of L_ω: number of links in a stream of order ω.
N_ω	number of streams of order ω.
nCIS	number of CIS links in a network.
nTRANS	number of TRANS links in a network.
nTS	number of tributary-source links in a network.
P	distance-weighted basin area.
p, p^*	standard and modified total topologic length in a network.

p_i, p_e	branching probability of an interior and an exterior link in the Q model.
Q	parameter of the Q and Q_E models.
R_B, R_L, R_A	arithmetic-mean bifurcation, length, and area ratios
$R^t{}_L$, $R^t{}_A$	topologic analogs of R_L and R_A.
RT model	random topology model.
S_s	number of Strahler streams in a network.
SM network	network obtained by the Q_E model in the space-filling mode of operation.
TDCN	topologically distinct channel networks.
TM network	network obtained by the Q model or the Q_E model in the topologic mode of operation.
w	network width.
α	junction angle.
δ	drainage pattern.
ε, ϕ	exponent and coefficient in property V
κ, θ	exponent and coefficient in property VI
μ	network magnitude.
Ω	network Strahler order.
$\Omega_M(\mu)$	most frequent Strahler order among TDCN of magnitude μ.
ω	Strahler order of a link, Strahler stream, or network.

Appendix B

Derivation of Equation (3.7)

Equation (3.7a) follows directly from (3.1b). Equation (3.7b) follows directly from (3.4) and (3.5). Equations (3.7a through h) are derived recursively as follows.

For the case where b=a, we obtain from (3.6):

$$p(a, a; Q) = p(L| a\text{-}1, a; Q)\, p(a\text{-}1, a; Q) + p(R| a, a\text{-}1; Q)\, p(a, a\text{-}1; Q) \qquad \text{(B1)}$$

Using (3.3) and (3.5), and rearranging (B1):

$$p(L| a\text{-}1, a; Q) = \frac{1}{2} \frac{p(a, a; Q)}{p(a\text{-}1, a; Q)} \qquad \text{(B2)}$$

The partition probabilities in (B2) can be computed from (3.1).

For the case where b=a+1, we obtain from (3.6):

$$p(a, a{+}1; Q) = p(L| a\text{-}1, a{+}1; Q)\, p(a\text{-}1, a{+}1; Q) + p(R| a, a; Q)\, p(a, a; Q) \qquad \text{(B3)}$$

Using (3.4) and (3.5), and rearranging (B3):

$$p(L| a\text{-}1, a{+}1; Q) = \frac{1}{p(a\text{-}1, a{+}1; Q)} \left\{p(a, a{+}1; Q) - \frac{1}{2} p(a, a; Q)\right\} \qquad \text{(B4)}$$

For the case where b=a+2, we obtain from (3.6):

$$p(a-1, a+1; Q) = p(L|\, a-2, a+1; Q)\, p(a-2, a+1; Q) + p(R|\, a-1, a; Q)\, p(a-1, a; Q) \quad (B5)$$

Using (3.5) and (B2), and rearranging (B5):

$$p(L|\, a-2, a+1; Q) = \frac{1}{p(a-2,\ a+1;\ Q)} \{p(a-1, a+1; Q) - p(a-1, a; Q) + \frac{1}{2} p(a, a; Q)\} \quad (B6)$$

Similarly, for the case where b=a+3:

$$p(a-1, a+2; Q) = p(L|\, a-2, a+2; Q)\, p(a-2, a+2; Q) + p(R|\, a-1, a+1; Q)\, p(a-1, a+1; Q) \quad (B7)$$

Using (3.4) and (B4), and rearranging (B7):

$$p(L|\, a-2, a+2; Q) = \frac{1}{p(a-2,\ a+2;\ Q)} (p(a-1, a+2; Q) - p(a-1, a+1; Q) + p(a, a+1; Q) - \frac{1}{2} p(a, a; Q)) \quad (B8)$$

Similarly, for the case where b=a+4:

$$p(a-2, a+2; Q) = p(L|\, a-3, a+2; Q)\, p(a-3, a+2; Q) + p(R|\, a-2, a+1; Q)\, p(a-2, a+1; Q) \quad (B9)$$

Using (3.5) and rearranging (B9):

$$p(L|\,a\text{-}3, a\text{+}2; Q) = \frac{1}{p(a\text{-}3, a\text{+}2; Q)}\big(p(a\text{-}2, a\text{+}2; Q)\text{-}p(a\text{-}2, a\text{+}1; Q) \\ +p(a\text{-}1, a; Q)+\frac{1}{2}p(a, a; Q)\big) \qquad \text{(B10)}$$

From (B2), (B4), (B6), (B8), and (B10), we obtain by induction the general expression (B11), also given as (3.7c):

$$p(L|\,a, b; Q) = \frac{1}{p(a, b; Q)}\left\{ (-1)^{|b-a|-1}\,\frac{1}{2}\,p(m, m; Q) - \sum_{i=1}^{|b-a|-1}(-1)^{i}\,p(a+\Delta a, b+\Delta b; Q)\right\}$$

$$\text{for } a<b,\ 0\leq Q<1 \qquad \text{(B11)}$$

where m, Δa and Δb are given by (3.7d through h).

Appendix C

Plots of topologic variables

Plots of topologic relations studied in Section 4.3 are included in this appendix. Summary statistics of the variables represented in these plots were given in Chapter 4, Table 4.8.

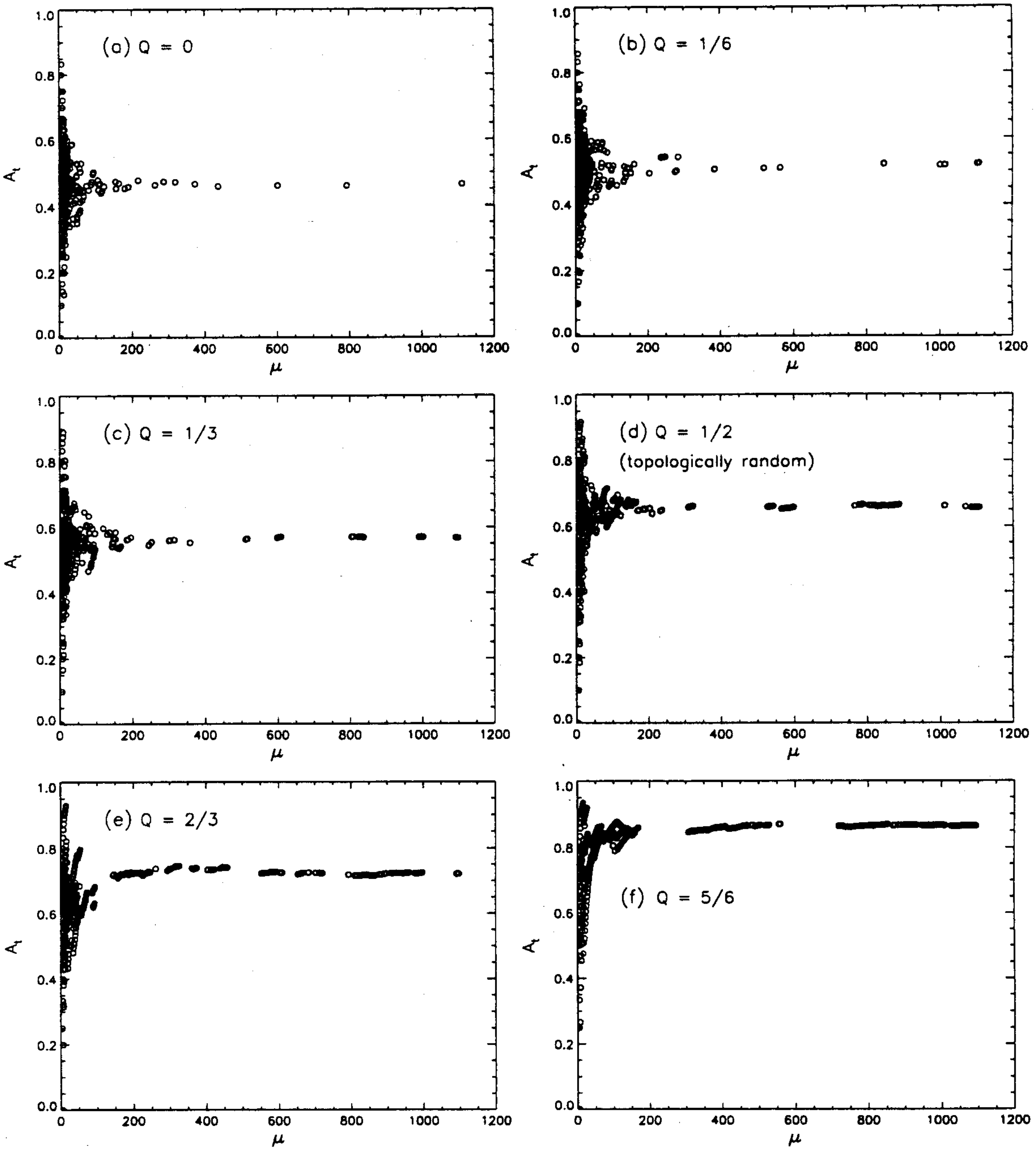

Figure C.1. Total asymmetry, A_t, for each subnetwork of TM test sample networks created with various Q values, plotted against network magnitude, μ. A_t increases from 0.464 for the complete network created with Q=0, to 0.865 for the complete network created with Q=5/6 (Table 3.9).

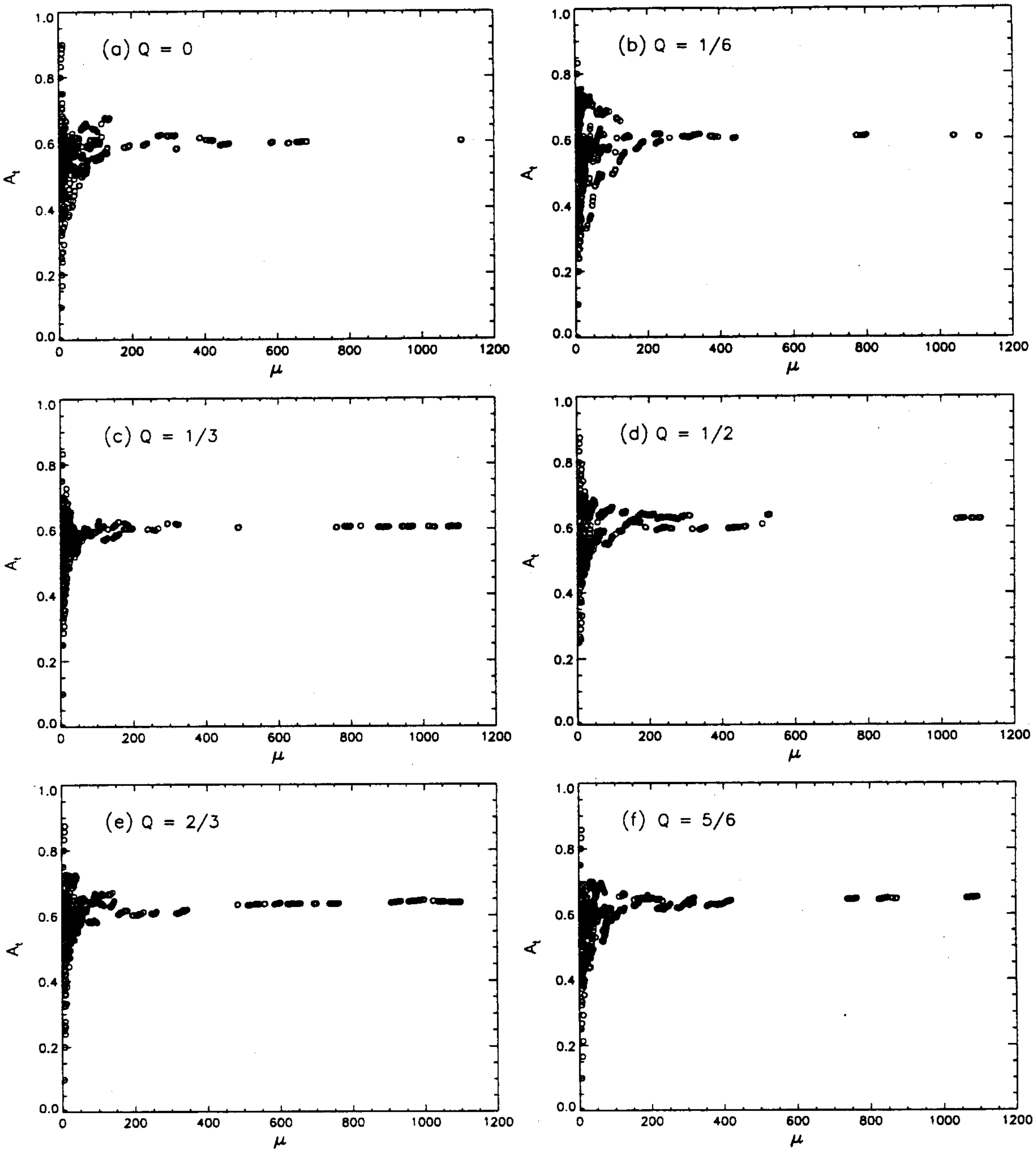

Figure C.2. Total asymmetry, A_t, for each subnetwork of SM dendritic test sample networks having α=70°, created with various Q values, plotted against network magnitude, μ. A_t increases from 0.602 for the complete network created with Q=0, to 0.652 for the complete network created with Q=5/6 (Table 3.9).

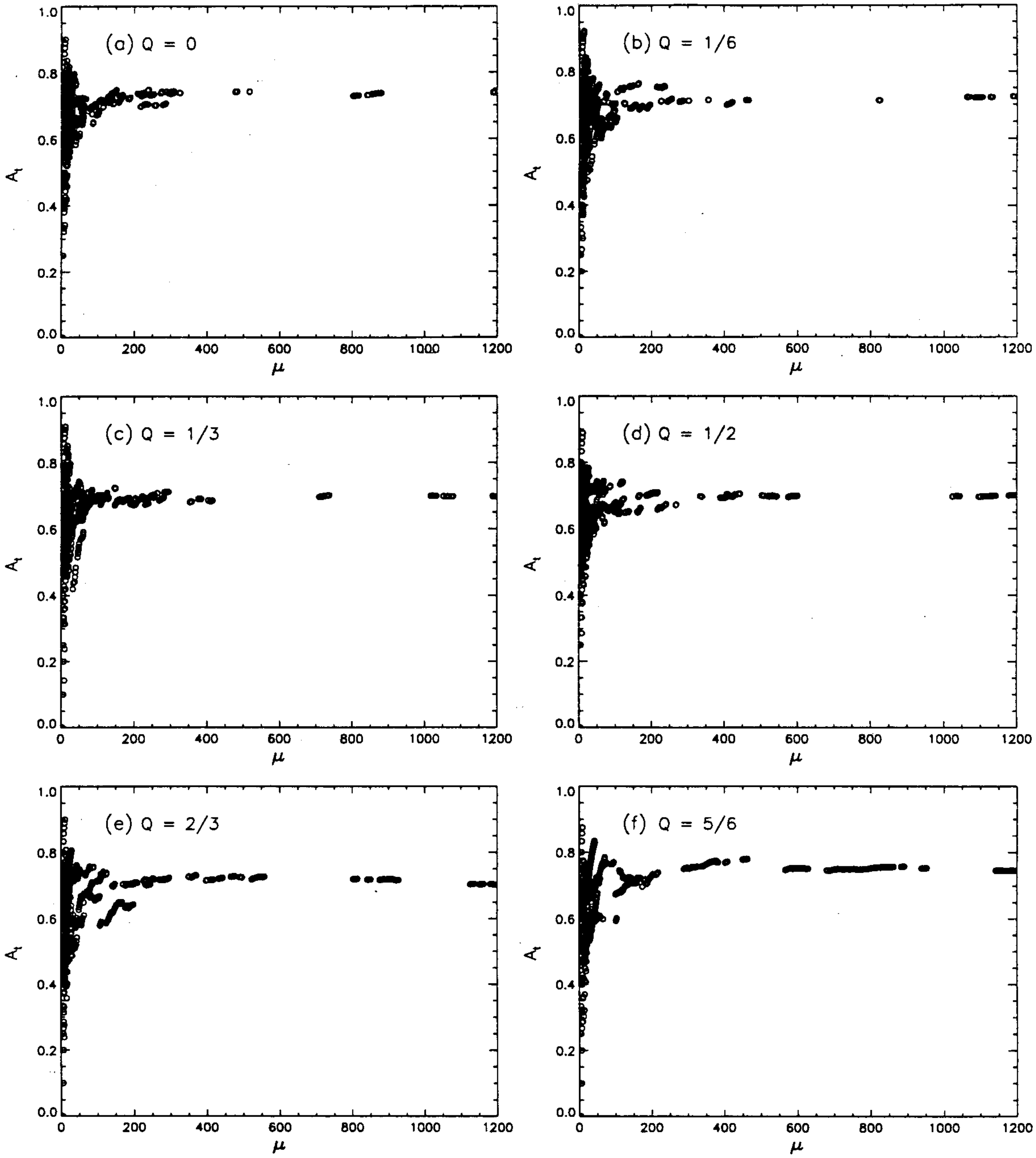

Figure C.3. Total asymmetry, A_t, for each subnetwork of SM trellis test sample networks having α=90°, created with various Q values, plotted against network magnitude, μ. A_t does not exhibit consistent variation with Q (Table 3.9).

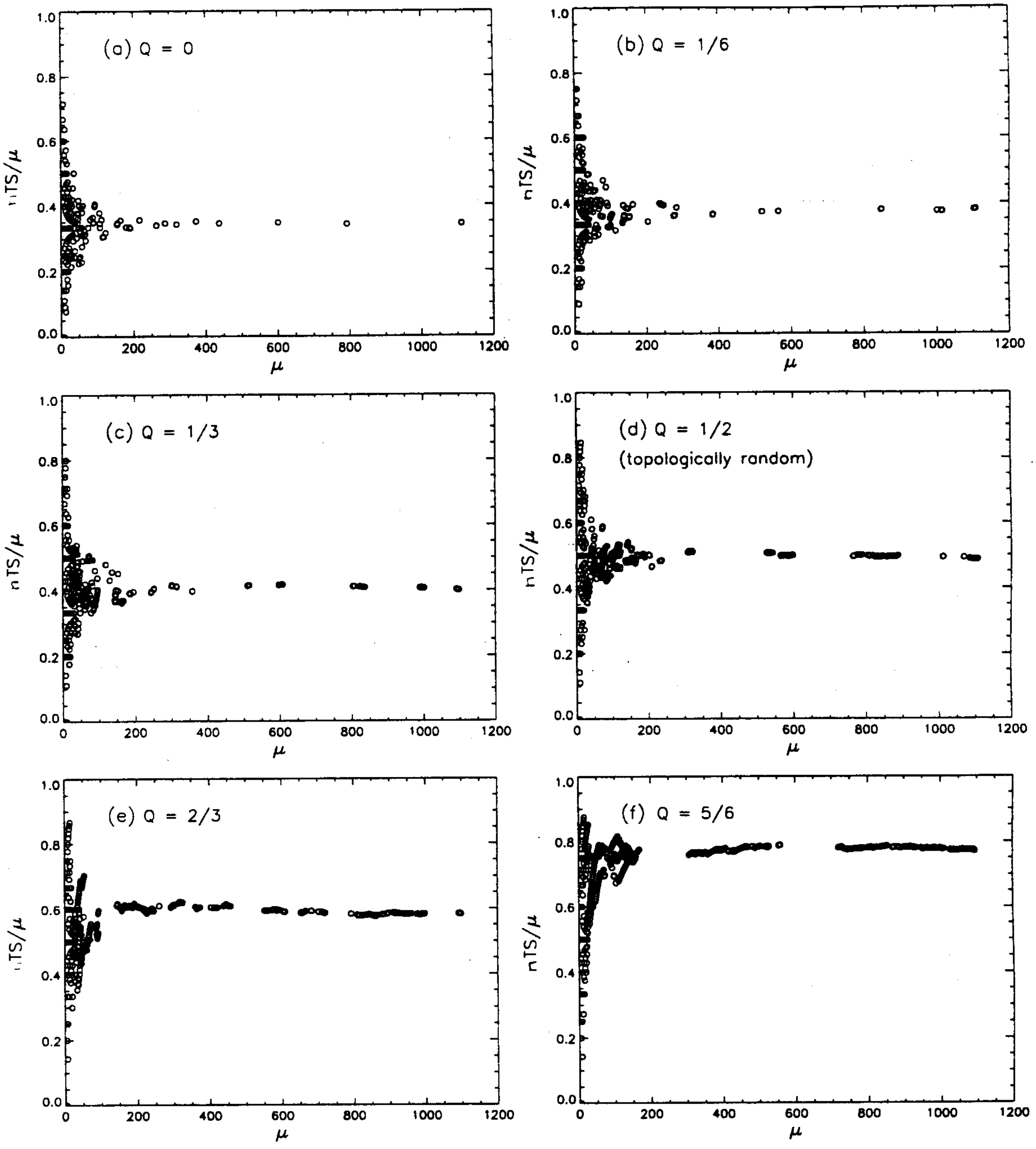

Figure C.4. Number of tributary-source links, nTS, divided by network magnitude, μ, for each subnetwork of TM test sample networks created with various Q values, plotted against μ. Ratio nTS/μ increases from 0.343 for the complete network created with Q=0, to 0.772 for the complete network created with Q=5/6 (Table 3.9).

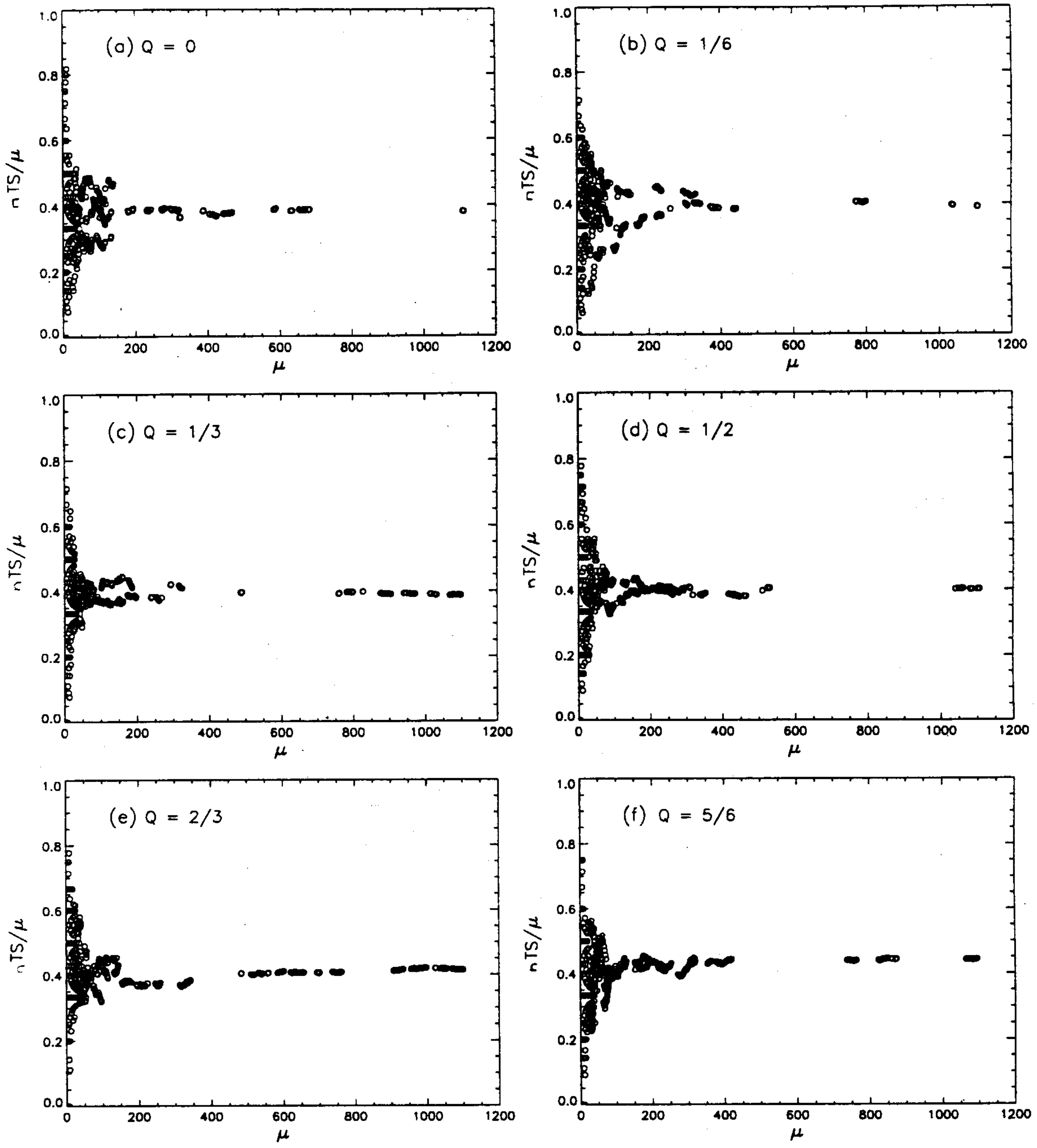

Figure C.5. Number of tributary-source links, nTS, divided by network magnitude, μ, for each subnetwork of SM dendritic test sample networks having α=70°, created with various Q values, plotted against μ. Ratio nTS/μ increases from 0.381 for the complete network created with Q=0, to 0.443 for the complete network created with Q=5/6 (Table 3.9).

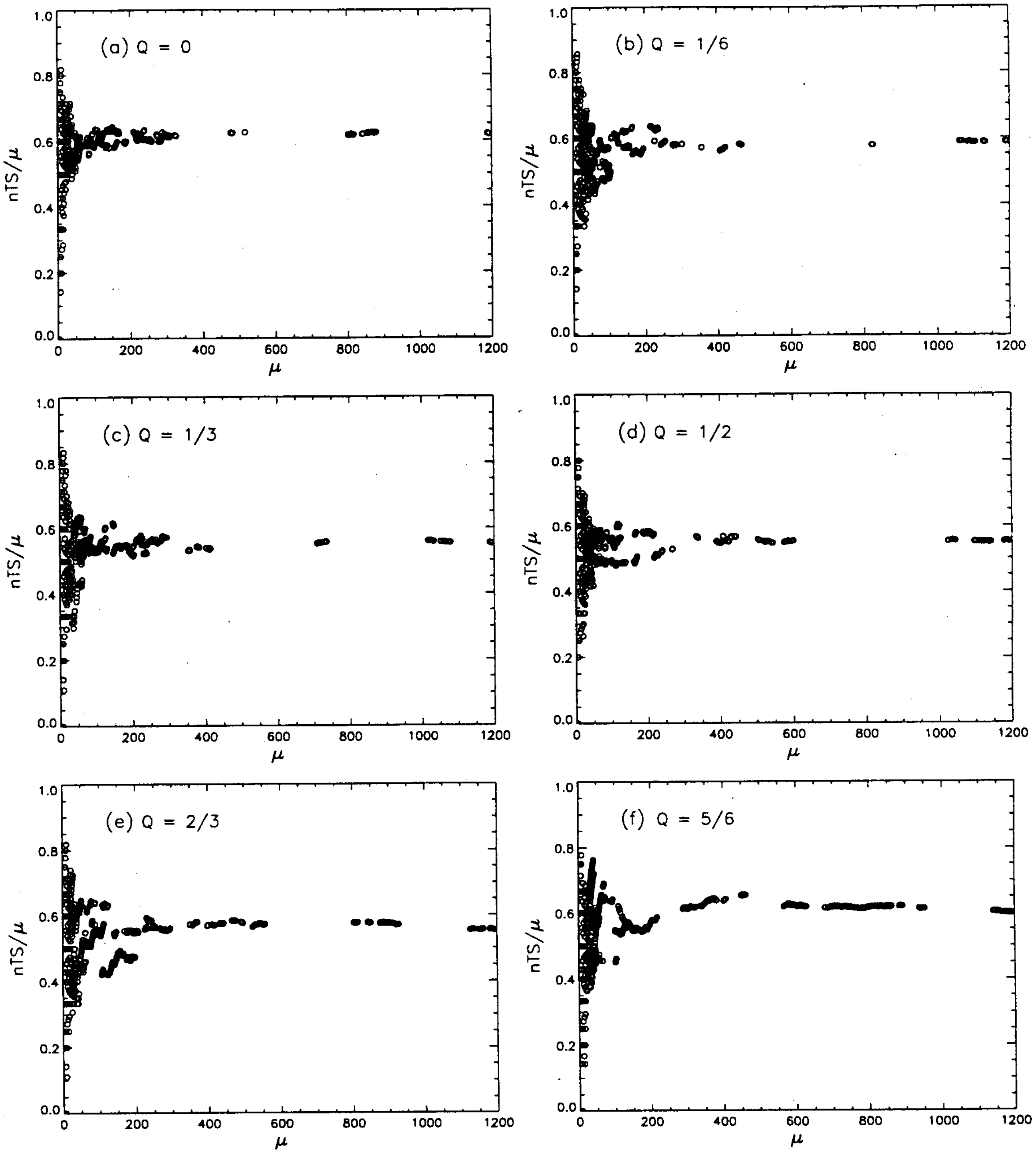

Figure C.6. Number of tributary-source links, nTS, divided by network magnitude, μ, for each subnetwork of SM trellis test sample networks having $\alpha=90°$, created with various Q values, plotted against μ. Ratio nTS/μ varies in the range [0.698, 0.746], and does not vary consistently with Q (Table 3.9).

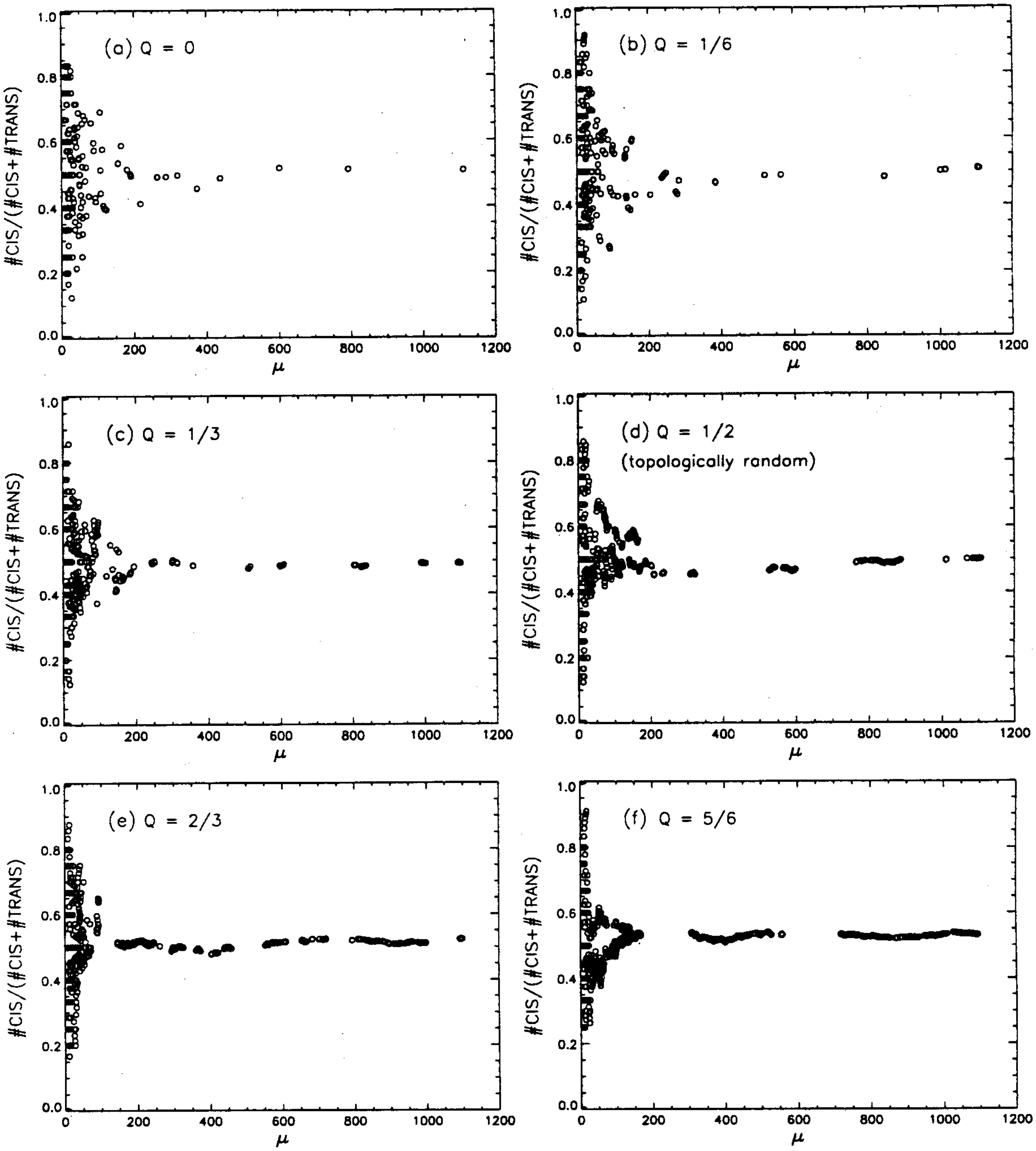

Figure C.7. Fraction of CIS links, nCIS/(nCIS+nTRANS), for each subnetwork of TM test sample networks created with various Q values, plotted against μ. Fraction nCIS/(nCIS+nTRANS) in the complete networks varies about the theoretic expectation value of 0.5, in the range [0.492, 0.532] (Table 3.9).

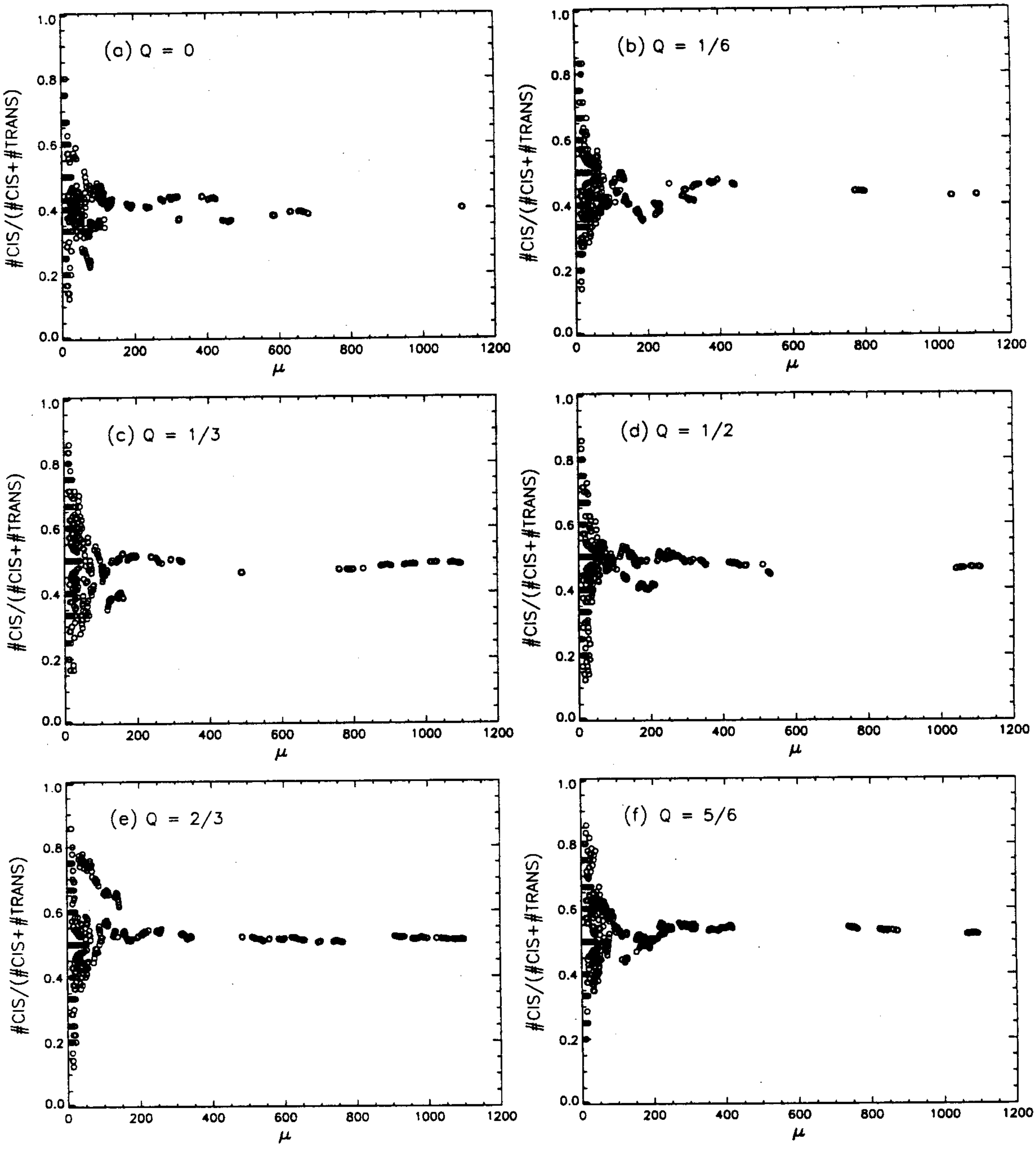

Figure C.8. Fraction of CIS links, nCIS/(nCIS+nTRANS), for each subnetwork of SM dendritic test sample networks having α=70°, created with various Q values, plotted against μ. Fraction nCIS/(nCIS+nTRANS) in the complete networks increases from 0.400 for the complete network created with Q=0, to 0.520 for the complete network created with Q=5/6 (Table 3.9).

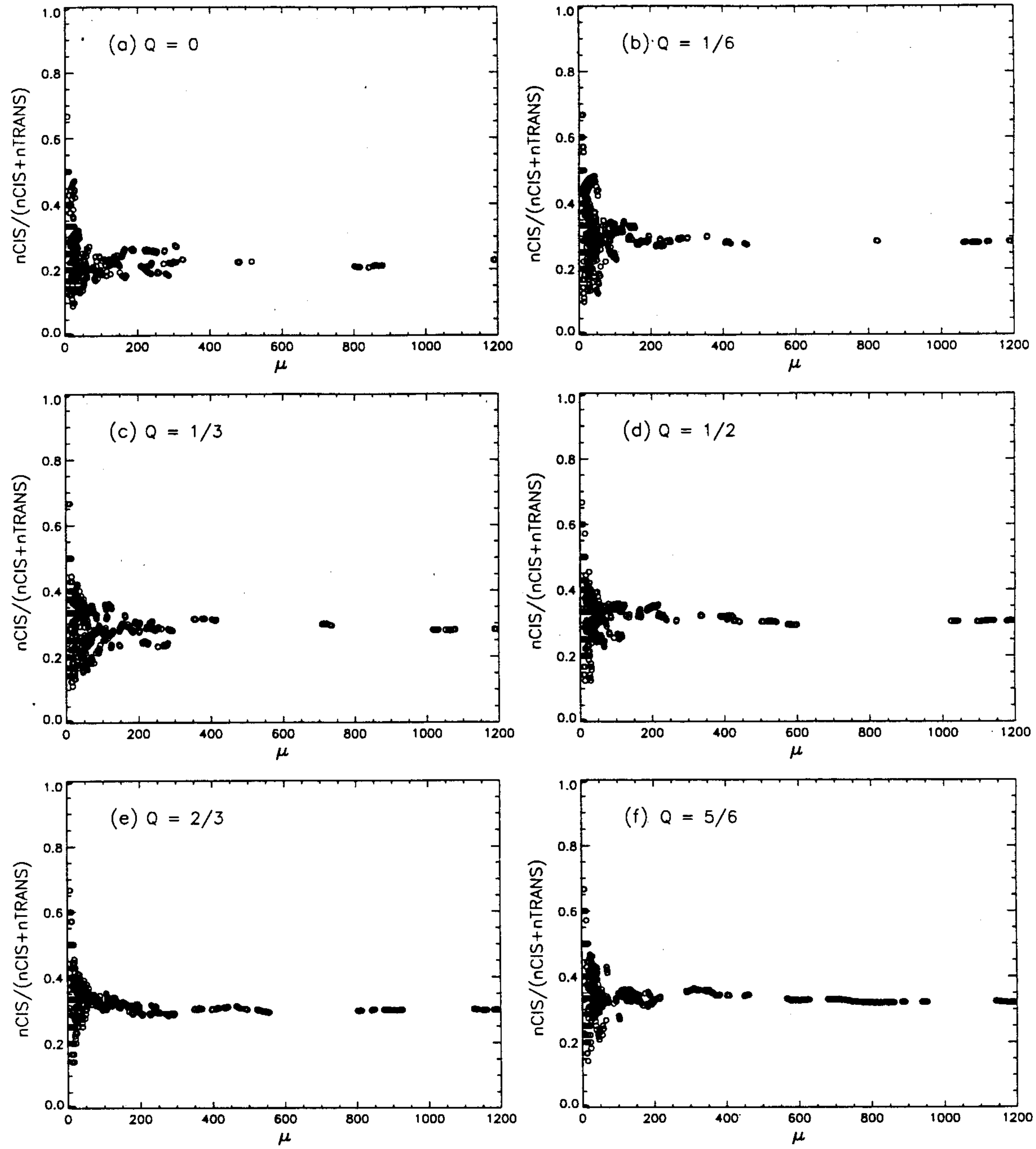

Figure C.9. Fraction of CIS links, nCIS/(nCIS+nTRANS), for each subnetwork of SM trellis test sample networks having α=90°, created with various Q values, plotted against μ. Fraction nCIS/(nCIS+nTRANS) in the complete networks increases from 0.285 for the complete network created with Q=0, to 0.321 for the complete network created with Q=5/6 (Table 3.9), a range of variation below the theoretical value of 0.5 for TM networks.

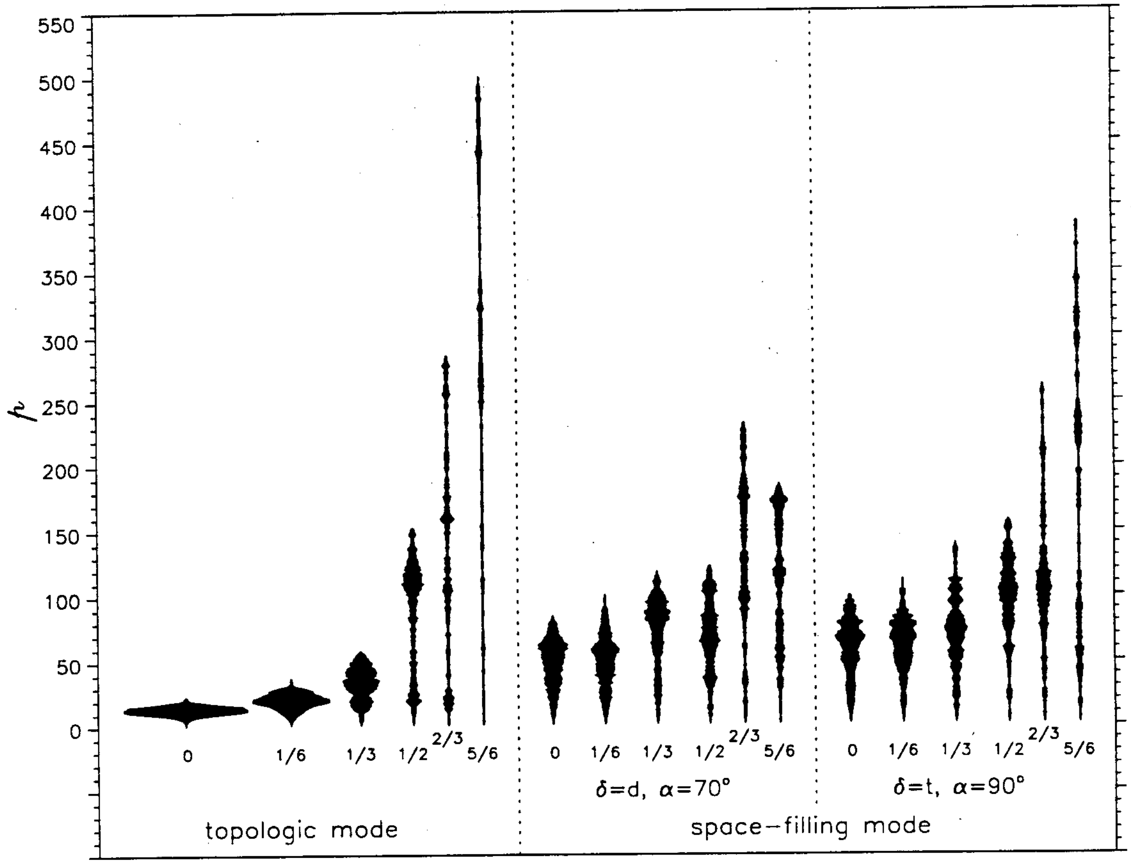

Figure C.10. Path length distribution histograms for TM and SM dendritic and trellis test sample networks, using a bin size of 1. For each sample the vertical reference axis extends from the minimum to the maximum value observed (the diameter, d), and the width about the axis is proportional to frequency. The maximum width about the axis is proportional to network width, w. Where there is no thickness about the reference axis, there are no observed values. The corresponding Q value is indicated at the bottom of each histogram. Variables d and w are given in Table 3.1. Sensitivity to Q is reduced in both dendritic and trellis sample networks, relatively to TM sample networks.

Appendix D

Digital Elevation Model Networks (DEMON): A model of flow over hillslopes for computation of contributing and dispersal areas

Reprinted from *Water Resources Research*, vol. 30, no. 6, pp. 1681-1692, 1994.

WATER RESOURCES RESEARCH, VOL. 30, NO. 6, PAGES 1681–1692, JUNE 1994

Digital elevation model networks (DEMON): A model of flow over hillslopes for computation of contributing and dispersal areas

Mariza C. Costa-Cabral and Stephen J. Burges
Department of Civil Engineering, University of Washington, Seattle

Abstract. Current algorithms for computing contributing areas from a rectangular grid digital elevation model (DEM) use the flow-routing model of O'Callaghan and Mark (1984), which has two major restrictions: (1) flow which originates over a two-dimensional pixel is treated as a point source (nondimensional) and is projected downslope by a line (one dimensional) (Moore and Grayson, 1991), and (2) the flow direction in each pixel is restricted to eight possibilities. We show that large errors in the computed contributing areas result for any terrain topography: divergent, convergent, or planar. We present a new model, called digital elevation model networks (DEMON), which avoids the above problems by representing flow in two dimensions and directed by aspect. DEMON allows computation of both contributing and dispersal areas. DEMON offers the main advantage of contour-based models (e.g., Moore et al., 1988), the representation of varying flow width over nonplanar topography, while having the convenience of using rectangular grid DEMs.

1. Introduction

The specific contributing area (SCA), and the specific dispersal area (SDA) (Figure 1), are distributed variables with important hydrological, geomorphological, and geological significance. The total contributing area (TCA) of a contour segment is the plan area of terrain that contributes flow to the contour segment. The SCA (designated often by "a" in the literature) of a contour segment is the TCA divided by the contour segment length. Because it is a plan area, the concept of SCA relies on the assumption that the plan view projection of flow directions does not change with depth below the land surface and is determined by surface topography. This assumption provides a valid approximation where the terrain permeability is small relative to the rainfall rate or where subsurface flow lines are approximately parallel in plan view to surface flow lines. The SCA is the plan area located topographically upstream from the unit contour length of interest. The SCA may be interpreted as an equivalent flow path length, because when upslope flow lines are parallel in plan view, the SCA equals the upslope flow path length.

In hydrology and geomorphology, the SCA is used extensively as an indicator of discharge. This assumes that the rate of flow generation r is uniform spatially and that the discharge rate is steady, in which case the specific discharge equals SCA times r. While these conditions of uniformity and equilibrium seldom are met in nature, they are assumed often to approximate natural conditions. Uses of the SCA as an indicator of discharge include studies of hillslope hydrologic response, channel location, long-term basin evolution, landslide risk, soil water content, and vulnerability to pollution, among others. Indexes that combine the SCA as a discharge indicator with other variables are used widely in hydrology and geomorphology. Examples of such indexes are ln(SCA/S), where S is slope, used to predict the soil moisture deficit [*Beven and Kirkby*, 1979], and S^2SCA, used to predict channel initiation by overland flow [*Montgomery and Dietrich*, 1989, 1992; *Montgomery and Foufoula-Georgiou*, 1993]. Use of the SCA as an indicator of discharge for prediction of the location and extent of channel networks is widespread. Reviews of channel network location based on SCA values obtained from rectangular digital elevation models (DEMs) include those by *Mark* [1988] and *Tarboton et al.* [1989, 1991].

The total dispersal area (TDA) of a contour segment is the plan area of terrain that drains flow from that contour segment. The SDA of a contour segment is the TDA divided by the contour segment length. The underlying assumption is the same as for the SCA definition, and the SDA is then the plan area topographically downstream from the unit length of contour. The SDA extends over the hillslope and may terminate at a location of topographic convergence or at a receiving water body. The SDA indicates the area of influence of flow generated at the given location and may be used, for example, to predict the influence zone of upslope pollution sources or of any development affecting terrain permeability. *Speight* [1974, 1980] interpreted the SDA as an indicator of soil drainage rate. Present uses of the SDA are more limited than those of the SCA.

The SCA and the SDA were defined originally for a segment of a contour line, and *Speight* [1974] pioneered the computation of these variables for landform classification, using a terrain partition based on contours and flow lines. Given the convenience of representing distributed variables for grid cells, or pixels, of rectangular digital elevation models (DEMs), the concept of the SCA was transferred from contour segments to DEM pixels and has joined the list of geomorphometric parameters that are computed routinely in the analysis of a DEM. Various models for flow routing in rectangular DEMs have been proposed for the computation

Paper number 93WR03512.
0043-1397/94/93WR-03512$05.00

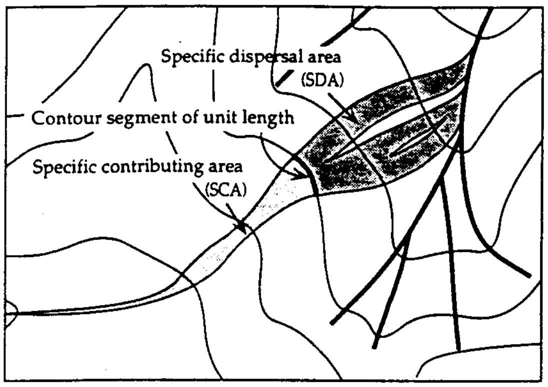

Figure 1. Illustration of the concepts of specific contributing area and specific dispersal area of a contour segment of unit length. The channel network drains to the top right of the figure.

of SCAs. These models have not been used, however, to compute SDAs, given their inappropriate (one-dimensional) downslope projection of flow. The same limitations that render current grid-based models unsuitable for computing SDAs make them equally inappropriate for computing SCAs. The major fault of most current models is their point source representation of flow generation and the resulting one-dimensional representation of flow paths [*Moore and Grayson*, 1991].

In digital elevation model networks (DEMON), flow is generated areally, not at point sources. Flow generated over a pixel is projected downslope over a two-dimensional flow strip, analogous to a flow tube. Flow direction is determined by the local aspect angle, in a manner similar to that used by *Lea* [1992]. The computed width of a "flow tube" increases over divergent topography, decreases over convergent topography, and remains constant over plane surfaces. DEMON offers the main advantage of contour-based models [e.g., *Moore et al.*, 1988], the representation of flow width variation as a function of local topography, and the benefits of rectangular grid DEMs. In addition, it permits computation of both SCAs and SDAs.

2. Review of Existing Methods and Their Limitations

Several methods exist for computing the SCA of a DEM pixel. We are unaware of methods for computing the SDA of a pixel. Computation of SDA values was possible previously only for the areal segments of a contour-based terrain partition [*Moore and Grayson*, 1991]. A review of the principal methods for computing SCAs for DEM pixels and what in our view are their limitations is presented below.

2.1. D8 [*O'Callaghan and Mark*, 1984]

The methods used most for SCA computation for DEM pixels are based on the flow-routing model introduced by *O'Callaghan and Mark* [1984]. We refer to them collectively as method D8. In method D8, pixels are centered on the DEM grid points, and each pixel discharges, or "spills," into one of its eight neighbors: the one located in the direction of steepest descent. The total contributing area (TCA) of a pixel is the number of pixels whose flow reaches the pixel of interest following a path of steepest descents, multiplied by one pixel area, $\Delta x \Delta y$. The SCA of a pixel is given by the TCA divided by the length of the segment orthogonal to flow direction in the pixel, either a pixel side, Δx or Δy, or the diagonal, $(\Delta x^2 + \Delta y^2)^{1/2}$.

Efficient algorithms for computing TCAs search upslope from a pixel and involve recursion. Examples include, among others, the algorithm of *Mark* [1988] and those of *Tarboton et al.* [1989, 1991].

The D8 method allows flow from each pixel to discharge to only one receiving neighbor. This amounts to treating flow which originated over a two-dimensional pixel as a point source (nondimensional) and projecting it downslope by a line (one dimensional) instead of a flow tube (two dimensional). This limitation has been pointed out by *Moore and Grayson* [1991]. The single receiving neighbor also imposes restrictions on possible flow path configurations because flow can occur only in either a cardinal or diagonal direction. The errors resulting from these limitations are different for areas where flow is divergent (where flow tube width increases downslope), convergent (flow tube width decreases downslope), or parallel (flow tube width is constant).

For parallel flow the true SCA is equal numerically to the flow path length. Method D8 computes the SCA correctly for parallel flow only when flow is in the x or y direction. When flow is at an angle to the principal grid orientation, two kinds of errors arise: errors that affect flow path direction and errors of SCA underestimation for a given flow path. The first source of error results when flow is at an angle different from a multiple of 45°. For example, if flow is at an angle of 30° (measured counterclockwise from east), then the steepest descent direction given by the D8 method will be toward the NE, and each pixel will discharge into its NE neighbor. This amounts to approximating the angle of flow to 45°, and modeled flow is diverted from its true path by 15°.

The second source of error results from the one-dimensional projection of flow. Consider parallel flow at an angle of 315° (a multiple of 45°), shown in Figure 2. The computed TCA is underestimated by a factor of 2 when using method D8. When using D8, the computed SCAs for parallel flow are correct for flow that is entirely in a cardinal direction (0°, 90°, 180°, or 270°), are underestimated by a factor of 2 for flow that is entirely in a diagonal direction (45°, 135°, 225°, or 315°), and are less than the correct value by a factor between 1 and 2 for flow that changes along its path between cardinal and diagonal directions. A simple correction by a factor of 2 is possibly only if the entire TCA of the

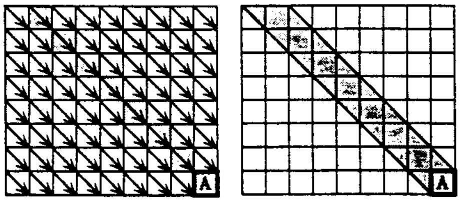

(a) (b)

Figure 2. TCA of a pixel on a planar slope with aspect angle 315° (a) predicted by method D8 and (b) true TCA. Method D8 underestimates the TCA of pixel A by a factor of 2.

pixel is in a diagonal direction. In cases where flow paths have both cardinal and diagonal directions a correction factor between 1 and 2 must be determined.

For divergent flow over a right circular cone mountain (Figure 3), the true TCA of any pixel includes the pixel itself and a triangle with one vertex at the cone center and two vertices at pixel corners. The SCA of a pixel at a distance r from the cone center is numerically close to $\frac{1}{2} r$, and the SCA has radial symmetry (Figure 3d). Divergent flow cannot be represented by a linear path of steepest descents, hence the SCA values computed by method D8 do not have radial symmetry (Figure 3c). Modeled flow is concentrated arbitrarily on eight preferential paths oriented in the cardinal and diagonal directions, while avoiding other paths. Consequently, at any given distance r from the cone center, some pixels drain all pixels between themselves and the cone center and have an SCA close to r, an overestimation by a factor of 2; while other pixels drain only themselves and have an SCA equal to a pixel side (Δx or Δy), an underestimation that approaches 100% at large r. Similar problems arise for convergent flow, such as over a right circular cone crater (Figure 4). Again, modeled flow is concentrated along eight preferential paths (Figure 4c), although overestimation and underestimation of the SCA magnitudes are not as large as for a cone mountain.

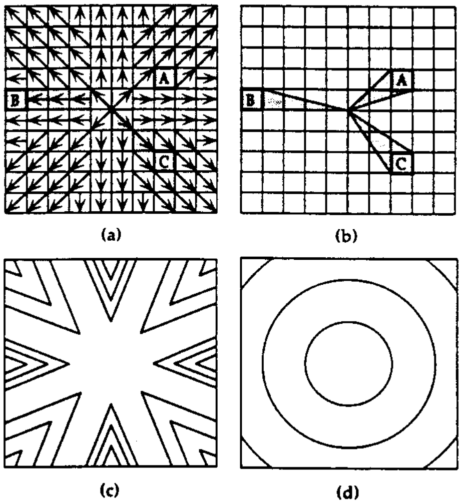

Figure 3. TCA of pixels on a right circular cone mountain surface (or TDA of pixels on a right circular cone crater surface): (a) TCA of pixels A, B, and C predicted by method D8, (b) true TCA of pixels A, B, and C, (c) SCA contours for method D8, and (d) true SCA contours. Radial symmetry is not conserved with method D8. With D8, pixel A drains only itself.

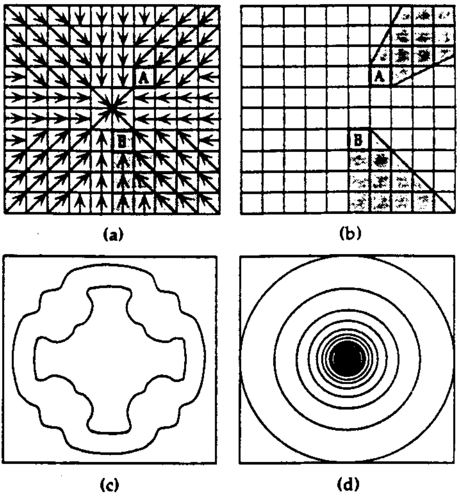

Figure 4. TCA of pixels on a right circular cone crater surface (or TDA of pixels on a right circular cone mountain surface): (a) TCA of pixels A and B predicted by method D8, (b) true TCA of pixels A and B, (c) SCA contours for method D8, and (d) true SCA contours. Radial symmetry is not conserved with method D8. The TCA of pixel A is underestimated greatly.

2.2. Rho8 [*Fairfield and Leymarie*, 1991]

Method Rho8 attempts to solve one of the problems of method D8: the diversion of modeled flow paths toward a cardinal or diagonal direction, resulting arbitrarily from grid orientation. Method Rho8 introduces a stochastic component into method D8, yielding flow paths that reflect more closely the true aspect of hillslopes. As in method D8, each pixel discharges into one of its eight neighbors. (A variation, called method Rho4, considers only the four cardinal neighbors.) The choice of the receiving pixel among the neighbors is made stochastically. One of the neighbors is assigned a probability p of being chosen and another neighbor is assigned a probability $1 - p$.

The scheme for assigning probabilities and the objective of this method are illustrated in the following example. Consider a plane surface with an aspect angle of 30° (measured counterclockwise from east). Method D8 makes every pixel discharge into its NE neighbor, resulting in a path direction that is wrong by 15°. Method Rho8 assigns a probability p to any given pixel discharging to its NE neighbor and a probability $(1 - p)$ to it discharging to its eastern neighbor. Therefore some pixels will discharge to their NE neighbor, and the remainder will discharge to their eastern neighbor. If the number of pixels discharging to the NE versus the eastern neighbor is in the right proportion (the expected proportion is $p/(1 - p)$), then the resulting flow lines will have an overall direction of 30°. The value of p should be such that the expected value of the flow path direction is equal to the aspect angle.

While this method provides, in mathematical expectation, appropriate flow path directions, all other problems identified above remain. Method Rho8 introduces problems of its own: randomness does not ensure reproducible results; and in locations of parallel flow, adjacent flow paths are not parallel but wiggle randomly and therefore often converge laterally with one another. Lateral convergence of flow paths on plane surfaces, where flow should be parallel, concentrates upslope flow on only some pixels. Once two flow paths have merged due to their random wiggling, there is no mechanism that can make them diverge again, hence errors increase downslope as flow becomes more and more concentrated. Some pixels will have overestimated TCA values, while others that were missed by the wiggling flow paths have underestimated TCAs.

2.3. *Lea* [1992]

This method solves the problem attempted by *Fairfield and Leymarie* [1991] by routing flow according to local aspect angle. The surface of each pixel is approximated by a best fit plane, and the direction of steepest slope (or the aspect angle) is computed (section 3.2 below). Flow is routed downslope along a path comprising straight segments with different directions, according to the aspect angle of each pixel. The algorithm models the entry and exit points of flow on the perimeter of each pixel along the flow path. Flow is modeled as a "rolling ball" (point source assumption) moving across the topographic surface in the direction of local aspect. Hence the major limitation of method D8, the one-dimensional representation of flow, remains.

2.4. Multiple-Direction Methods

Multiple-direction methods attempt to solve the major limitation of method D8, the one-dimensional representation of flow, by distributing flow from a pixel among all of its lower-elevation neighbor pixels, according to some specified rule. *Quinn et al.* [1991] proposed that the fraction of flow allocated to each lower neighbor i be determined by

$$f_i = \frac{S_i L_i}{\sum S_j L_j} \qquad (1)$$

where the summation is for all lower neighbors, S is the directional slope, and L is an "effective contour length" that acts as a weighting factor. The values of L used by *Quinn et al.* [1991] were $\frac{1}{2}$ of the pixel side for cardinal neighbors and a fraction 0.354 of the pixel diagonal for diagonal neighbors.

Freeman [1991] proposed that the fraction of flow allocated to each lower neighbor i be determined by

$$f_i = \frac{S_i^p}{\sum S_j^p} \qquad (2)$$

where S is the directional slope and p is a nonphysical parameter. This method was tested for flow over a right circular cone mountain, for different values of parameter p. Since $p = 1.1$ provided drainage contours which approached circles, this value was recommended for use. Freeman applied the method exclusively to divergent topography and used a different algorithm for convergent topography.

Figure 5 represents schematically the contributing area of a pixel, labeled "A," located on three different surfaces: a plane, a right circular cone mountain, and a right circular cone crater. The contributing areas shown are those that result from use of any multiple-direction algorithm, such as those of *Quinn et al.* [1991] or *Freeman* [1991]. For an inclined plane surface each pixel discharges to three or four other pixels (depending on plane aspect), and only a fraction of the discharge pixel surface area belongs to the contributing area of a receiving pixel. Therefore the contributing area of a pixel does not include any full pixel but instead is composed of portions of different pixels and is discontiguous. The flow direction over the plane in Figure 5a is top to bottom, and the true TCA of pixel A is the full area of the four pixels immediately above pixel A. Multiple-direction algorithms predict that the contributing area is composed of portions of pixels inside a triangular region. The computed TCA value of a pixel is correct if it is located far enough from the plane's lateral edges, otherwise the triangular region is incomplete and the TCA is underestimated. For the plane represented in Figure 5a, 70 of the 100 pixels represented have an underestimated TCA value (e.g., the TCA of pixels labeled "B" and "C"). Thus results are affected by boundary proximity. For a right circular cone mountain (Figure 5b) and a cone crater (Figure 5c) the TCA of pixel A is, again, discontiguous and includes portions of pixels located far outside the true (triangular) contributing area. Parameter calibration may yield predicted TCA values that are correct (e.g., $p = 1.1$ in (2) for a right circular cone mountain). The approximation relies on surface geometric symmetry and will suffer to the extent that a natural terrain surface will diverge from the symmetric geometric surfaces used for parameter calibration. Due to their misplacement of contributing areas, multiple-direction algorithms are not appropriate for contaminant tracing nor can they represent distributed runoff rates.

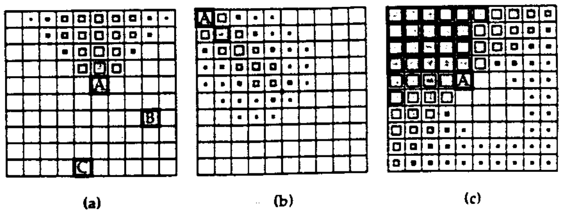

(a) (b) (c)

Figure 5. Schematic representation of the TCA of a pixel that is estimated by any multiple-direction algorithm. The size of the shaded square inside each pixel is proportional to the size of that pixel's portion that drains to pixel A. (a) Predicted TCA of pixel A located on a plane surface where flow is from top to bottom. (b) Predicted TCA of pixel A located on a right circular cone mountain. (c) Predicted TCA of pixel A located on a right circular cone crater.

2.5. Summary

The D8 family of methods, used to compute SCAs for DEM pixels, contains limitations which can result in large errors for any terrain configuration, including planar, divergent, and convergent topographies. More recent methods attempt to overcome some of the problems of method D8. *Lea* [1992] provides a sound scheme for aspect-driven routing which is an improvement over D8 routing. However, no satisfactory solution has been presented for the most important limitation of method D8, the point source assumption and one-dimensional routing. This problem has been addressed with partial success by multiple-direction models. In our view, the most important limitations of multiple-direction models are that the computed contributing areas are discontiguous, and the quality of the approximation of the computed values relies on geometric symmetry and is affected by boundary proximity.

We present an alternative approach which attempts to overcome the problems identified in this section by modeling downslope flow in two dimensions and in well-defined flow tubes.

3. DEMON

In this section we define the SCA and SDA of a pixel (or, in general, any terrain discretization element), discuss our representation of the flow field, and describe the DEMON algorithms used to compute the SCA and SDA matrices.

3.1. Definitions

The total contributing area (TCA) of a DEM pixel is the plan-view area draining to that pixel. Implicit in this definition is the assumption that the plan-view projection of the flow field does not change with depth below the land surface and is determined by surface topography. The TCA of a pixel is then the plan-view area of the collection of all points located upstream topographically from the pixel. A point is located upstream topographically from a pixel if the surface flow line passing through that point enters the pixel downstream. The SCA of a DEM pixel (or any terrain discretization element) is defined as the average value of contributing area per unit flow width as flow exits the pixel and is obtained by division of the pixel's TCA by the total exiting flow width, ω, that is,

$$\mathrm{SCA} = \frac{\mathrm{TCA}}{\omega} \tag{3}$$

The TDA of a DEM pixel is the plan-view area draining flow from the pixel. The implicit assumption is the same as in the TCA definition. The TDA of a pixel is the plan-view area of the collection of all points located topographically downstream from the pixel. A point is located topographically downstream from a pixel if there is a flow line that passes through the pixel and also through the point downstream. The SDA is the TDA per unit flow width ω:

$$\mathrm{SDA} = \frac{\mathrm{TDA}}{\omega} \tag{4}$$

The total flow width ω in (3) and (4) is the flow width orthogonal to the flow direction along the portion of the pixel boundary through which flow exits the pixel. For a DEM grid with x and y axes pointing east and north, respectively, and pixel dimensions Δx and Δy,

$$\begin{aligned} \omega &= \int_{l_N} \frac{\partial \omega}{\partial l}\, dl + \int_{l_E} \frac{\partial \omega}{\partial l}\, dl + \int_{l_S} \frac{\partial \omega}{\partial l}\, dl + \int_{l_W} \frac{\partial \omega}{\partial l}\, dl \\ &= \int_{l_N} \sin \alpha(x, y = \Delta y)\, dx + \int_{l_E} \cos \alpha(x = \Delta x, y)\, dy \\ &\quad - \int_{l_S} \sin \alpha(x, y = 0)\, dx - \int_{l_W} \cos \alpha(x = 0, y)\, dy \end{aligned} \tag{5}$$

where l_N, l_E, l_S, and l_W designate the lengths of the exit segments lying on the northern, eastern, southern, and western boundary segments, respectively, and $\alpha(x, y)$ is the flow direction angle, measured counterclockwise from east. Here l_N and l_S take values between zero and Δx, and l_E and l_W take values between zero and Δy.

3.2. Surface Fitting to the DEM and Determination of Flow Direction Angles

The SCA and SDA variables are determined entirely by the flow field, that is, the field of flow direction angles, $\alpha(x, y)$. Flow at a point is in the direction of maximal surface slope and is obtained from the reverse direction of the elevation tensor at that point. Thus determination of the flow angle field requires prior knowledge of the elevation field. Given that the DEM provides only a point sampling of elevations, it is necessary to fit an elevation surface to the DEM. This may be thought of as an attempt to reconstruct the topographic surface after it had been stored in the image-compressed form of a DEM. How well the reconstructed surface represents the true topographic surface will depend on the size of the DEM grid relative to the roughness of the terrain and on the surface-fitting method.

The simplest surface-fitting method approximates the surface of each pixel by a best fit plane using local interpolation. In this case the fitted terrain surface consists of planar mosaics and, in general, will be discontinuous (i.e., with finite jumps from one pixel to the next). The approximation is best for Δx and Δy small relative to topographic roughness.

DEMON uses planar surfaces because a single-flow direction within each pixel is simpler computationally. Pixels are defined by grid lines, having grid points at the corners. The elevation tensor in each pixel is given by vector $a\mathbf{i} + b\mathbf{j}$ ($\mathbf{i}$ and $\mathbf{j}$ are unit vectors in the x and y directions, respectively), with

$$\begin{aligned} a &= \frac{1}{2\Delta x}(-z_1 + z_2 + z_3 - z_4) \\ b &= \frac{1}{2\Delta y}(z_1 + z_2 - z_3 - z_4) \end{aligned} \tag{6}$$

where z_1, z_2, z_3, and z_4 are the elevations at the upper left, upper right, lower right, and lower left pixel corners, respectively. Flow is in the direction of vector $-(a\mathbf{i} + b\mathbf{j})$, indicated by the aspect angle α.

For planar pixels, if the flow direction is parallel to the grid orientation, the exit portion of the boundary is a single full boundary segment. If the flow direction is not parallel to the grid orientation, the exit portion of the boundary consists of two full adjacent boundary segments. The general expression (5) for the flow width becomes

$$\omega = |\sin \alpha|\Delta x + |\cos \alpha|\Delta y \tag{7}$$

3.3. DEMON-Downslope and DEMON-Upslope Algorithms for Computing the SCA and SDA Matrices

DEMON-downslope is a particle-tracking algorithm that projects flow downslope using the matrix of flow angles and allows computing both the SCA and SDA matrices. DEMON-upslope traces the boundary of a pixel's contributing area and calculates the size of the area enclosed by that line. DEMON-upslope computes the SCA matrix faster than DEMON-downslope but does not calculate the SDA matrix because the TDA cannot always be bounded by a single connected line (Figure 1). While different, the two algorithms, DEMON-downslope and DEMON-upslope, provide the same SCA values. The information required by either algorithm is the matrix of flow angles.

3.3.1. DEMON-downslope: SCA computation. If a unit flow depth is generated uniformly everywhere over the area covered by the DEM, the total flow volume drained by any given pixel equals the pixel's TCA. DEMON-downslope

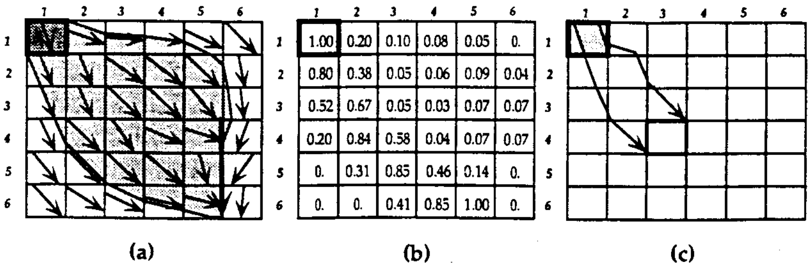

	1	2	3	4	5	6
1	1.00	0.20	0.10	0.08	0.05	0.
2	0.80	0.38	0.05	0.06	0.09	0.04
3	0.52	0.67	0.05	0.03	0.07	0.07
4	0.20	0.84	0.58	0.04	0.07	0.07
5	0.	0.31	0.85	0.46	0.14	0.
6	0.	0.	0.41	0.85	1.00	0.

Figure 6. (a) Example of two-dimensional, aspect-driven (arrow directions) flow movement. Flow originates over pixel (1,1). The area shaded is the TDA of pixel (1,1). (b) Influence matrix of pixel (1,1). Each entry in the influence matrix represents the fraction of the area within pixel (1,1) that is drained by a pixel. (c) Illustration of the physical meaning of the value 0.58 of pixel (4,3) in Figure 6b.

considers that a unit flow depth is generated uniformly over the surface of every pixel in the DEM. The flow generated over each pixel is tracked downslope in two dimensions (i.e., as a flow tube) according to local terrain aspect, until the flow either leaves the DEM or enters a sink pixel (a "pit"). The total flow drained by a given pixel equals that pixel's TCA.

DEMON-downslope takes one pixel at a time and makes it a source pixel. A unit flow depth is considered to be generated uniformly over the source pixel and is followed downslope. Figure 6a shows two-dimensional aspect-driven flow movement from source pixel (1,1) (we use (i, j) to indicate the pixel corresponding to row i and column j of the DEM). As we track the flow downslope, we compute the flow volume drained by each pixel that the flow traverses. The influence matrix of a source pixel contains the flow volume from the source pixel that is drained by each pixel in the DEM. If a pixel receives no flow from the source pixel, its entry in the influence matrix is zero; if it drains all of the flow, its entry is $\Delta x \Delta y$; and if it drains part of the flow, its entry is a fraction of $\Delta x \Delta y$. Figure 6b is the influence matrix of pixel (1,1) (in this example, $\Delta x = \Delta y = 1$). The entries on any cross diagonal of the influence matrix, before flow convergence to a line occurs, sum to unity. Figure 6c shows the physical location of the portion of the source pixel (shaded area) associated with the entry of pixel (4,3) in the influence matrix of pixel (1,1). Pixel (4,3) drains 58% of the area of pixel (1,1).

The TCA matrix is computed by successive addition of the influence matrix of every pixel in the DEM. In the example DEM of Figure 6, 36 influence matrices, one for each source pixel, are computed and added. The SCA matrix is computed by division of the TCA matrix by the flow width matrix, which is obtained from the matrix of flow angles using (7).

We use Figure 6 to illustrate the three-step procedure for computing the influence matrix of a pixel.

Step 1: Flow generated over the source pixel flows over the pixel surface in the direction indicated by α. If α is a multiple of 90°, all flow goes to a single neighbor. For example, if α is equal to 180°, all flow will enter the western neighbor. If α is not a multiple of 90°, then flow will be split between two cardinal neighbors (S and E in Figure 7). There can be no flow to a diagonal neighbor because contact with diagonal neighbors is through a point (width of flow is infinitesimally small), not a segment. For flow to reach a diagonal neighbor it must cross through a cardinal neighbor. Therefore a diagonal neighbor cannot be a direct receiving pixel. Figure 7 illustrates how flow is split among the eastern and southern neighbors for $\alpha = 292°$ (the flow angle of pixel (1,1) in Figure 6). A flow particle generated in the upper right shaded triangular area, moving at an angle of 292°, must cross the eastern border and enter the eastern neighbor. The area of the triangular section and the fractions f_E and f_S are, for $\alpha = 292°$,

$$f_E = \frac{A_\Delta}{A} = -\frac{1}{2}\frac{\Delta y}{\Delta x}\frac{1}{\tan(292°)} = 0.20; \quad f_S = 1 - f_E = 0.80 \qquad (8)$$

where A_Δ represents the triangular area in Figure 7, and A represents the pixel area ($\Delta x \Delta y$). Twenty percent of the flow generated over pixel (1,1) is delivered to the E neighbor and 80% to the S neighbor.

Step 2: In Figure 6a, source the S neighbor. has two receiving pixels. To follow flow downslope we must step to one of these two receiving pixels, while the other one is put on a waiting list for later consideration. Consider pixel (2,1), with pixel (1,2) on the waiting list.

Step 3: Figure 8 illustrates the definition of the eight

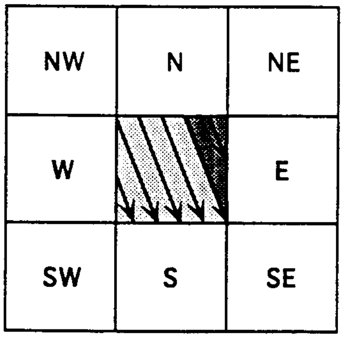

Figure 7. Illustration of how flow from the source pixel is partitioned between two cardinal neighbors. In this case the flow angle in the source pixel is 292°, and flow is partitioned between the eastern and southern neighbor pixels. The fraction of flow that enters the eastern neighbor is the fraction of the area of the source pixel represented by the darker shaded triangular area.

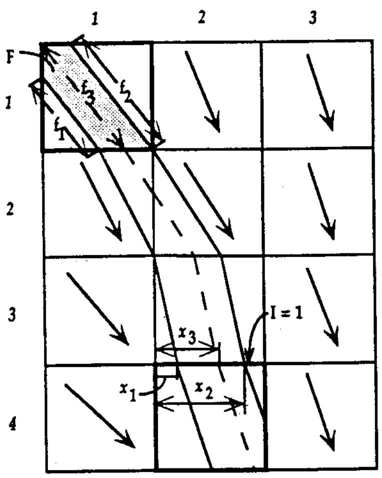

Figure 8. Illustration of the definition of variables F, f_1, f_2, f_3, x_1, x_2, x_3, and I, needed for projecting flow across pixel (4,2). F is the flow entering pixel (4,2) (the shaded area); f_1 and f_2 are the lengths drained by the flow lines bounding the flow tube; I = 1, 2, 3, 4 indicates flow entering from the north, east, south, and west, respectively; x_1 and x_2 indicate the points of entry of the bounding flow lines; x_3 indicates the point of entry of the flow line generated at the corner of the source pixel (dashed curve); $f_3 = f_2$ indicates that all points inside the flow tube to the right of the dashed curve drain the same amount of flow, while the flow drained by any point to the left of the dashed curve varies linearly across the flow tube.

variables (F, f_1, f_2, f_3, I, x_1, x_2, and x_3) required to describe the geometry of flow movement across a pixel (pixel (4,2) in Figure 8). (The DEM in Figure 8 is different from that in the previous figures to facilitate displaying the eight variables.) The source pixel being considered in Figure 8 is (1,1). The flow tube shown is the flow tube that has the path (1,1)-(2,1)-(2,2)-(3,2)-(4,2). Part of the flow carried by this flow tube will enter pixel (4,3) and the remainder will enter pixel (5,2), that is, this flow tube will be split into two flow tubes. The fractions entering (4,3) and (5,2) are computed from geometry, using f_1, f_2, and f_3.

Topographic convergence converts a flow strip (two dimensional) into a line (one dimensional). The vertical bold arrow in the lower right of Figure 6a is an example of one-dimensional flow. One-dimensional flow need not be along pixel boundaries but may cross through pixels. Projecting a line according to flow angle requires only the variables I and x_1 to keep track of the point of entry of the flow line in each pixel [*Lea*, 1992].

The algorithm used to compute the influence matrix of a pixel can follow one flow path at a time, that is, the dispersal area of the pixel is dissected into several flow tubes so that the path of each flow tube can be written as a path from one pixel to the next. The flow tube in Figure 8 can be written as (1,1)-(2,1)-(2,2)-(3,2)-(4,2), which is a directed graph. Figure 9a represents all the (directed graph) flow tube paths that can be written for the example DEM shown in Figure 6. Figure 9b represents these paths schematically; each branch in Figure 9b corresponds to one flow tube in Figure 9a.

3.3.2. DEMON-downslope: SDA computation. The SDA is computed simultaneously with the SCA. As we step to each pixel downslope and project flow through it, the size of the area within the pixel occupied by the flow tube is computed. The summation of all these areas is the TDA of the source pixel (the shaded area in Figure 6a). The SCA matrix is obtained from the TCA matrix through division by the flow width matrix.

3.3.3. DEMON-upslope. The DEMON-upslope algorithm computes the TCA directly for each pixel by tracing the boundary of the pixel's contributing area and calculating the size of the area enclosed by that line. Most pixels have a single source area, whose boundary intercepts two corners of the pixel of interest. It is not possible to start at one pixel corner and trace the entire boundary line until the second pixel corner is reached. This is because for part of the way the tracing direction is against the flow (going upslope), while for the second part, movement is with the flow (going downslope), and it is not known a priori which is the right location to switch from upslope to downslope. Hence it is necessary to trace the boundary line starting at each of its two ends at the pixel corners and always move upslope, until

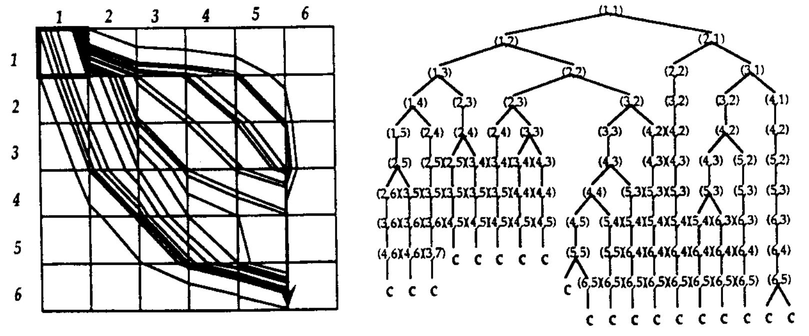

(a) (b)

Figure 9. (a) Flow tubes that must be considered to compute the influence matrix of pixel (1,1) in Figure 6. (b) Schematic representation of the flow tubes defined in Figure 9a. Branching corresponds to flow being split between two neighbor pixels. All paths exit the DEM in concentrated form, indicated by "c."

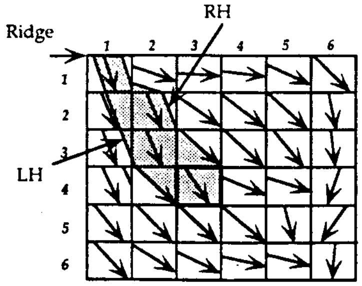

Figure 10. Illustration of the right-hand side (RH) and left-hand side (LH) flow lines that must be traced uphill in the DEMON-upslope algorithm.

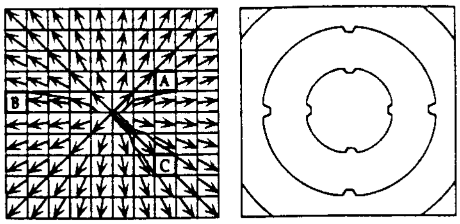

(a) (b)

Figure 12. TCA of pixels on a right circular cone mountain surface (or TDA of pixels on a right circular cone crater surface) predicted by DEMON. (a) TCA of pixels A, B, and C. The prediction is poorest for pixel B, which is overestimated as a result of allowing for a single flow direction in each pixel. (b) SCA contours.

the point where the two traced lines meet (Figure 10). Some pixels may receive flow from two source areas, in which case four lines must be traced. The three-step procedure for computing the TCA of a pixel is as follows:

Step 1: Determine which of the four cardinal neighbors discharge some flow to the pixel of interest. If a cardinal neighbor drains into the pixel of interest, an indicator variable for that neighbor is set to 1 (0 otherwise). Next, the indicator variables of the four neighbors are checked in clockwise order, and if a switch from 0 to 1 or from 1 to 0 from one neighbor to the next is found, then there is a boundary line that starts at the corner point shared by those two neighbors.

Step 2: Trace the TCA boundary lines uphill. If a pixel has more than one contributing area, this procedure is repeated for each. The boundary line consists of two lines that join uphill; the left-hand (LH) line bounds the contributing area from the left, and the right-hand (RH) line bounds the contributing area from the right as paths are followed upslope from the pixel. The RH line is traced from the pixel of interest by moving continuously against the flow direction. The coordinates of the points at which the line intercepts the boundary of each pixel are stored. The RH line is traced for some large, preestablished, number of pixels n_p (e.g., equal to 3 times the typical hillslope length for the study area). The LH line is traced uphill in the same way, until the RH line is met. While tracing the RH or LH line, often a local elevation maximum is found. In such cases it is not possible to move further upslope, so the path follows a line of divergence, that is, a line where flow directions oppose each other on each side.

Step 3: After the RH and LH lines have been mapped, the TCA boundary is known. The TCA is calculated from the area enclosed by the boundary lines which is determined from the stored coordinates that describe their paths.

4. Results

We present results from use of DEMON for a plane, a right circular cone mountain, and a right circular cone crater (Figures 11–13, respectively) to illustrate model performance for parallel, convergent, and divergent flow conditions. Figures 11–13 may be compared with Figures 2–4, which show the corresponding results using D8; and Figures 11, 12a, and 13a may be compared with Figures 5a–5c, which show the corresponding results using multiple-direction algorithms. For the plane, computed SCAs correspond correctly to the distance to the top of the plane. True SDAs for a right circular cone mountain are the same as the SCAs for a right circular cone crater and vice versa. For both cones the predicted SCA and SDA isolines are approximately circular with indentations to the north, east, south, and west. These indentations are larger for the crater cone than for the mountain cone, and in both cases they become more pronounced with distance to the cone center. The indentations result from the approximation of the conical surface by a mosaic of planes, which generates a bias toward the N-S and E-W directions. The indentations can be avoided only if a

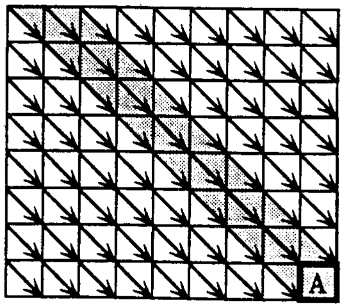

Figure 11. TCA of a pixel on a planar slope with aspect angle 315° predicted by DEMON.

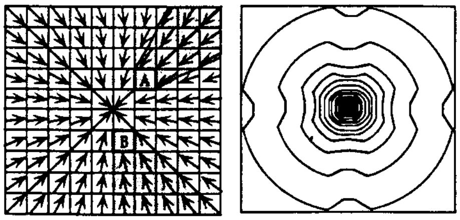

(a) (b)

Figure 13. TCA of pixels on a right circular cone crater surface (or TCA of pixels on a right circular cone mountain surface). (a) TCA of pixels A and B predicted by DEMON. (b) SCA contours.

curved rather than a planar surface is fitted to each pixel; using DEMON, the computational expense for nonplanar surface fitting would be large. Significant errors may result on concave or convex hillslopes that are long relative to grid size, that is, comprising a large number of pixels. For a conical surface the magnitude of the error a distance of 40 pixels away from the cone center is approximately 15%. For a 10-m grid DEM, 40 pixels represents a physical distance of 400 m.

To illustrate model performance for natural topography, we present results of computed SCAs and SDAs for the pixels of a DEM for Mettman Ridge, in southern Oregon [*Zhang and Montgomery*, 1994]. This DEM has a 2 × 2 m grid covering an area of 720 × 900 m^2 (360 × 450 pixels) and was obtained by interpolation of a 1:4800 scale topographic map [*Montgomery*, 1991]. Field mapping of the channel network revealed that the land surface differed locally from the DEM [*Montgomery and Dietrich*, 1994, Figure 4(b)]. The SCA and SDA matrices obtained with DEMON are represented as images in Figures 14 and 15. Figure 16 shows the SCAs computed using D8. DEMON represents hillslope aspect better, while in D8 the erroneous tendency toward preferred directions is obvious. Also, curved flow paths are represented by DEMON but not D8.

In Figure 17 we plot the computed SCA values for each pixel using DEMON and D8. Only pixels belonging to basins that lie fully inside the DEM are represented, to eliminate any DEM boundary effects. The disagreement between computed SCAs spans 5 orders of magnitude at the hillslope scale. The two methods agree in many pixels with a high SCA value because no flow is lost in either routing model, so

Figure 15. Image of the SDA matrix for the Mettman Ridge study area obtained with DEMON. A logarithmic scale of gray shades is used; lighter shades correspond to higher values.

Figure 14. Image of the SCA matrix for the Mettman Ridge study area obtained with DEMON. A logarithmic scale of gray shades is used; lighter shades correspond to higher values.

Figure 16. Image of the SCA matrix for the Mettman Ridge study area obtained with D8. A logarithmic scale of gray shades is used; lighter shades correspond to higher values.

that topographic convergence eventually leads to the same value at the outlet of each basin. The large differences found at the hillslope scale are attributed principally to D8 errors similar to those illustrated in Figures 2–4.

Figure 18 shows the histograms of the SCAs smaller than 100 m computed with D8 and DEMON. The D8 histogram is discontinuous, while the DEMON histogram is continuous and smooth, as is to be expected over natural hillslopes. The discontinuous D8 histogram reflects the fact that D8 TCAs are integers, and flow width has only three possible values (Δx, Δy, or $(\Delta x^2 + \Delta y^2)^{1/2}$).

Figure 19 shows pixels with SCAs smaller than 4 m (i.e., draining themselves and one other pixel), for DEMON and for D8. DEMON gives low values almost exclusively at or near hillslope tops, while D8 gives low values at many locations on the hillslopes. This is because some pixels are missed by the one-dimensional flow paths of method D8 where flow is divergent (such as pixel A in Figure 3a).

Figure 20 shows pixels with SCAs higher than 1000 m, for DEMON and for D8. There are significant differences between the two drainage configurations. Overall, the D8 network has straighter segments. Network structure is different at a location near the lower left-hand corner (see arrow). Two D8 flow paths run parallel at a very short distance from each other at a location in the central upper half of the study area (see arrow). The high-SCA network configuration computed with DEMON is in better agreement with the field-surveyed channel network [*Montgomery and Dietrich*, 1994, Figure 4(b)].

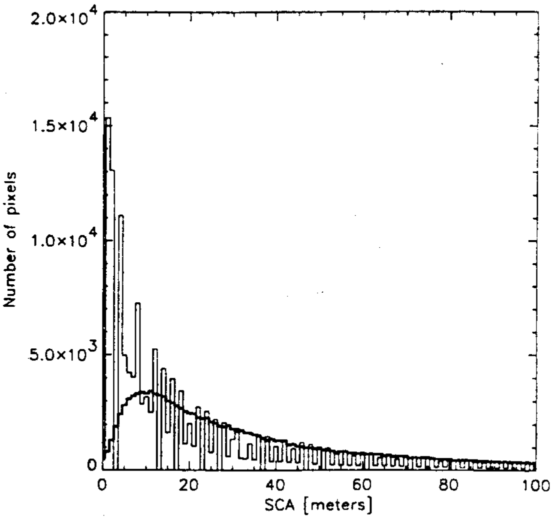

Figure 18. Histogram of SCA values obtained with methods D8 (finer curve) and DEMON (heavier curve) for values lower than 100 m.

5. Conclusions

We have shown that the models presently in widest use for computing the specific contributing area of rectangular grid DEM pixels, those based on flow-routing method D8 [*O'Callaghan and Mark*, 1984], can produce seriously erroneous results for either planar, convergent, or divergent topography. The most important source of errors is the point source assumption and the resulting one-dimensional flow routing (each pixel discharges into only one neighbor pixel). Another source of error is the restriction on the flow direction in each pixel to only eight possibilities (multiples of 45°), established by the orientation of the sampling grid. More recent models reviewed attempt to overcome the limitations of method D8, with partial success. *Lea* [1992] provides a sound scheme for aspect-driven routing which is an improvement over D8 routing. However, no satisfactory solution has been presented for the most important limitation of method D8, the point source assumption and one-dimensional routing. This problem has been addressed with partial success by multiple-direction models. The most important limitations of multiple-direction models are that the computed contributing areas are discontiguous, and the quality of the approximation of the computed values relies on surface geometric symmetry and is affected by boundary proximity.

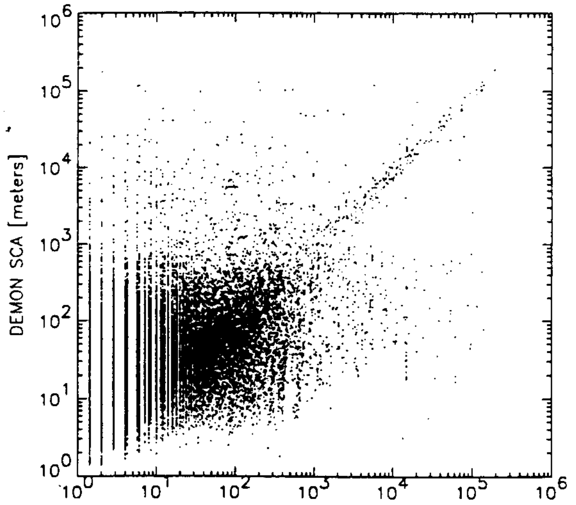

Figure 17. Plot of SCA values for the Mettman Ridge study area: D8, horizontal axis, and DEMON, vertical axis. One fifth (32,400) of all pixels are shown to avoid clutter.

DEMON computes the specific contributing areas and specific dispersal areas of DEM pixels. Assignment of flow directions is according to aspect angle, as given by *Lea* [1992]. Flow path routing is two dimensional, allowing representation of the effect of terrain topography on flow path width. Flow path width remains constant over planar terrain, increases over divergent topography, and decreases over convergent topography. Thus the proposed model has capabilities which at present are offered only by contour-based flow models, while having the convenience of using rectangular grid DEMs.

Results for geometric surfaces for which SCAs can be computed analytically show that DEMON approximates analytic values, while D8 has large errors for either parallel, convergent, or divergent flow. Computed SCAs for the Mettman Ridge DEM using D8 and DEMON differ by 5 orders of magnitude at the hillslope scale. The two methods have better agreement at high SCA values, because flow conservation leads to similar values after flow is concentrated into linear paths by terrain convergence. The large errors at the hillslope scale indicate that D8 is inappropriate for hillslope applications, including studies of hillslope hydrologic response, channel head location, long-term basin evolution, landslide risk, and soil water content.

We presented two equivalent algorithms for computing SCAs: DEMON-downslope and DEMON-upslope. DEMON-downslope provides more information than DEMON-upslope. The particle-tracking approach of DEMON-downslope may be used for surface sediment or pollutant tracking. While both algorithms can be adapted to accommodate distributed values of runoff generation, only DEMON-downslope can permit reinfiltration. DEMON-downslope can also provide SDA values for individual flow tubes within a pixel, which may constitute useful information for a large grid size. Finally, DEMON-downslope distinguishes between dispersed (two dimensional in plan view) and concentrated (one-dimensional) flow, information with potential utility for models of rainfall-runoff, soil water content, and other applications.

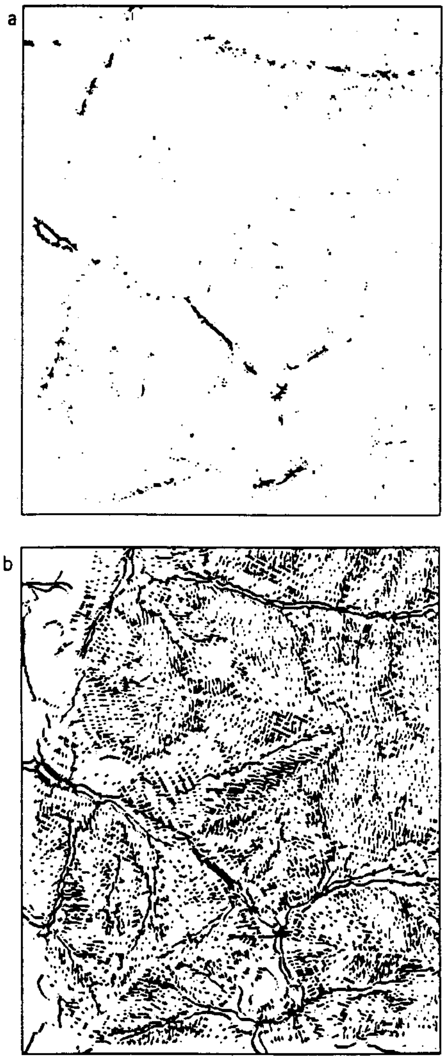

Figure 19. Image of the SCA values less than 4 m, that is, pixels that drain no more than the area of one pixel other than themselves for (a) DEMON and (b) D8. Low values of SCA are located over large ridges for DEMON but are ubiquitous on the hillslopes for D8.

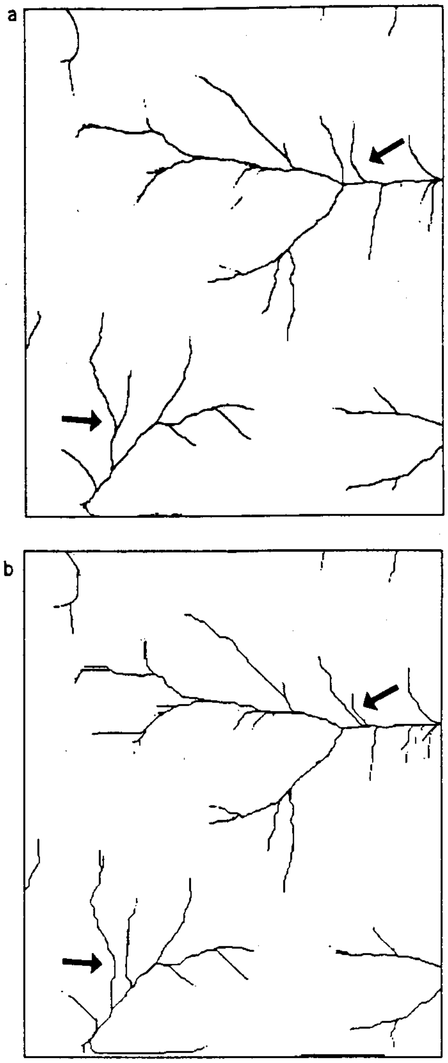

Figure 20. Image of the SCA values larger than 1000 m for (a) DEMON and (b) D8. (In some locations the networks are discontinuous because the pits in the original DEM were not removed.)

Acknowledgments. This work is dedicated to the memory of Ian Moore (1951–1993). We appreciated his generosity and selflessness in the help he provided during preparation of our manuscript. We are all the richer for the many contributions he made during his too short professional life. We are all the poorer for the loss of his intellectual leadership, energy, enthusiasm, and collegiality. This work has been supported in part by the "Junta Nacional de Investigação Científica e Tecnológica," Portugal, under award BD-1480-91, and by the U.S. Geological Survey (USGS), Department of the Interior, under USGS award 14-08-0001-G1887. The views and conclusions contained in this document are those of the writers and should not be interpreted as necessarily representing the official policies, either expressed or implied, of either the U.S. or Portuguese governments. We thank David Montgomery, of the University of Washington, for helpful discussion and providing the Mettman Ridge DEM. We thank David Tarboton and an anonymous reviewer for their valuable critiques of this manuscript. The DEMON codes are available from the authors upon request to colleagues who provide an e-mail address.

References

Beven, K. J., and M. J. Kirkby, A physically-based variable contributing area model of basin hydrology, *Hydrol. Sci. Bull., 24,* 43–69, 1979.

Fairfield, J., and P. Leymarie, Drainage networks from grid digital elevation models, *Water Resour. Res., 27*(5), 709–717, 1991. (Correction, *Water Resour. Res., 27*(10), 2809, 1991.)

Freeman, T. G., Calculating catchment area with divergent flow based on a regular grid, *Comput. Geosci., 17*(3), 413–422, 1991.

Lea, N. L., An aspect driven kinematic routing algorithm, in *Overland Flow: Hydraulics and Erosion Mechanics,* edited by A. J. Parsons and A. D. Abrahams, Chapman and Hall, New York, 1992.

Mark, D. M., Network models in geomorphology, in *Modelling Geomorphological Systems,* edited by M. G. Anderson, pp. 73–97, John Wiley, New York, 1988.

Montgomery, D. R., Channel initiation and landscape evolution, Ph.D. dissertation, 421 pp., Dep. of Geol. and Geophys., Univ. of California, Berkeley, 1991.

Montgomery, D. R., and W. E. Dietrich, Source areas, drainage density, and channel initiation, *Water Resour. Res., 25*(8), 1907–1918, 1989.

Montgomery, D. R., and W. E. Dietrich, Channel initiation and the problem of landscape scale, *Science, 255,* 826–830, 1992.

Montgomery, D. R., and W. E. Dietrich, A physically based model for the topographic control of shallow landsliding, *Water Resour. Res., 30*(4), 1153–1171, 1994.

Montgomery 1R., and E. Foufoula-Georgiou, Channel network source representation for digital elevation models, *Water Resour. Res., 29*(12), 3925–3934, 1993.

Moore, I. D., and R. B. Grayson, Terrain-based catchment partitioning and runoff prediction using vector elevation data, *Water Resour. Res., 27*(6), 1177–1191, 1991.

Moore, I. D., E. M. O'Loughlin, and G. J. Burch, A contour-based topographic model for hydrological and ecological applications, *Earth Surf. Processes Landforms, 13,* 305–320, 1988.

O'Callaghan, J. F., and D. M. Mark, The extraction of drainage networks from digital elevation data, *Comput. Vision Graphics Image Process., 28,* 323–344, 1984.

Quinn, P., K. Beven, P. Chevalier, and O. Planchon, The prediction of hillslope flow paths for distributed hydrological modelling using digital terrain models, *Hydrol. Processes, 5,* 59–79, 1991.

Speight, J. G., A parametric approach to landform regions, *Spec. Publ. Inst. Br. Geogr., 7,* 213–230, 1974.

Speight, J. G., The role of topography in controlling throughflow generation: A discussion, *Earth Surf. Processes Landforms, 5,* 187–191, 1980.

Tarboton, D. G., R. L. Bras, and I. Rodriguez-Iturbe, The analysis of river basins and channel networks using digital terrain data, *Tech. Rep. 326,* 251 pp., Ralph M. Parsons Lab., Dep. Civ. Eng., Mass. Inst. of Technol., Cambridge, 1989.

Tarboton, D. G., R. L. Bras, and I. Rodriguez-Iturbe, On the extraction of channel networks from digital elevation data, *Hydrol. Processes, 5,* 81–100, 1991.

Zhang, W., and D. R. Montgomery, Digital elevation model grid size, landscape representation, and hydrologic simulations, *Water Resour. Res., 30*(4), 1019–1028, 1994.

S. J. Burges and M. C. Costa-Cabral, Department of Civil Engineering, FX-10, University of Washington, Seattle, WA 98195.

(Received May 19, 1993; revised November 30, 1993;
accepted December 13, 1993.)

VITA

Mariza Castanheira de Moura da Costa Cabral was born on November 29, 1963, in Lisboa, Portugal. She received her "Licenciatura" in Environmental Engineering from the "Universidade Nova de Lisboa", Portugal, in 1986. She received a Master of Arts in Energy and Environmental Studies from Boston University, in 1988, and a Master of Science in Civil Engineering from the Massachusetts Institute of Technology, Ralph M. Parsons Laboratory, in 1990. For part of 1990 and 1991 she worked as a Research Assistant at the Portuguese National Laboratory of Civil Engineering, Hydraulics Department. She entered the Department of Civil Engineering at the University of Washington in the Fall of 1991, from which she received her Ph.D. in 1997.